NOTICE

The quality of this microform is heavily dependent upon the quality of the original thesis submitted for microfilming. Every effort has been made to ensure the highest quality of reproduction possible.

If pages are missing, contact the university which granted the degree.

Some pages may have indistinct print especially if the original pages were typed with a poor typewriter ribbon or if the university sent us an inferior photocopy.

Reproduction in full or in part of this microform is governed by the Canadian Copyright Act, R.S.C. 1970, c. C-30, and subsequent amendments.

AVIS

La qualité de cette microforme dépend grandement de la qualité de la thèse soumise au microfilmage. Nous avons tout fait pour assurer une qualité supérieure de reproduction.

S'il manque des pages, veuillez communiquer avec l'université qui a conféré le grade.

La qualité d'impression de certaines pages peut laisser à désirer, surtout si les pages originales ont été dactylographiées à l'aide d'un ruban usé ou si l'université nous a fait parvenir une photocopie de qualité inférieure.

La reproduction, même partielle, de cette microforme est soumise à la Loi canadienne sur le droit d'auteur, SRC 1970, c. C-30, et ses amendements subséquents

Canada

UNIVERSITY OF ALBERTA

Laminar Flow and Heat Transfer
in Helical Pipes with Finite Pitch

by

Shijie Liu

A thesis

submitted to the Faculty of Graduate Studies and Research

in partial fulfillment of the requirements for the degree of

Doctor of Philosophy

Department of Chemical Engineering

Edmonton, Alberta

Spring, 1992

The author has granted an irrevocable non-exclusive licence allowing the National Library of Canada to reproduce, loan, distribute or sell copies of his/her thesis by any means and in any form or format, making this thesis available to interested persons.

The author retains ownership of the copyright in his/her thesis. Neither the thesis nor substantial extracts from it may be printed or otherwise reproduced without his/her permission.

L'auteur a accordé une licence irrévocable et non exclusive permettant à la Bibliothèque nationale du Canada de reproduire, prêter, distribuer ou vendre des copies de sa thèse de quelque manière et sous quelque forme que ce soit pour mettre des exemplaires de cette thèse à la disposition des personnes intéressées.

L'auteur conserve la propriété du droit d'auteur qui protège sa thèse. Ni la thèse ni des extraits substantiels de celle-ci ne doivent être imprimés ou autrement reproduits sans son autorisation.

ISBN   0-315-73075-7

Canada

UNIVERSITY OF ALBERTA

RELEASE FORM

Name of Author: **Shijie Liu**

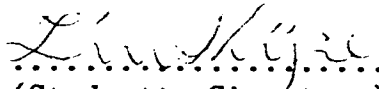Title of thesis: **Laminar Flow and Heat Transfer**
                                    in Helical Pipes with Finite Pitch

Degree: Doctor of Philosophy

Year this degree granted: Spring 1992

(Student's Signature)
Anning 5–4, Santai county
Sichuan Province, China

Date: March 26, 1992

University of Alberta

Faculty of Graduate Studies and Research

The undersigned certify that they have read, and recommend to the Faculty of Graduate Studies and Research for acceptance, a thesis entitled **Laminar Flow and Heat Transfer in Helical Pipes with Finite Pitch** submitted by **Shijie Liu** in partial fulfillment of the requirements for the degree of **Doctor of Philosophy**.

J. H. Masliyah (supervisor)

M. Van Dyke

K.C. Cheng

W. Finlay

K. Nandakumar

R. Hayes

Date: March 26, 1992.

To

my father

and

in memory of my mother

ABSTRACT

A first order non—confirming numerical method for fluid flow problems with a three—point exponential interpolation has been developed. The flow problem is decoupled into multiple one—dimensional subproblems and assembled to form the solution. A fully staggered grid and a conservational domain centered at each node of interest make the decoupling scheme to be first order accurate. It is shown that the ordinary upwind (or exponentially weighted upstream) scheme is of zeroth order accuracy. The pressure is decoupled from the velocity field through the perturbation method due to Patankar. Thomas algorithm is used to solve the resulting algebraic equations iteratively. In addition, a 2—dimensional direct solver has been developed based on block matrix inversion to tackle the difficulty that may arise from the perturbation of the pressure. The 2—dimensional solver uses less memory storage than band solvers and the component matrices are inverted to allow fast solutions. The numerical advantage of the proposed method is tested for the laminar flows in a torus and in a square driven cavity.

Steady axially—invariant (fully—developed) incompressible flow of Newtonian fluids in helical pipes of constant circular cross—section with arbitrary pitch and arbitrary radius of coil is studied. A loose coiling analysis leads to two dominant parameters, namely Dean number, $Dn = Re \sqrt{\lambda}$, and Germano number, $Gn = Re\ \eta$, where Re is the Reynolds number, λ is the normalized curvature ratio and η is the normalized torsion. The Germano number is embedded in the body—centered azimuthal velocity which appears as a group in the governing equations. When studying the importance of the Germano number effects on the helical flow of large Dn, a third dimensionless group is evolved, $\gamma = \eta/\sqrt{\lambda Dn}$. It is found that γ is the controlling parameter governing the flow pattern transition between one— to two—vortex flows. For $Dn < 20$, the group $\gamma^* = Gn\ Dn^{-2} = \eta/(\lambda Re)$ takes the place of γ.

Numerical simulations with the full Navier–Stokes equations confirmed the theoretical findings. It is revealed that the torsion effect on the helical flow can be neglected when $\gamma \leq 0.01$ for moderate Dn. The critical value for which the secondary flow pattern changes from two vortices to one vortex is $\gamma^* > 0.039$ for Dn < 20 and $\gamma > 0.2$ for Dn $\geq$ 20. For a fixed high Dean number and λ flows, increasing the torsion has the effect of changing the relative position of the secondary flow vortices and the eventual formation of a flow having a Poiseuille type axial velocity with a superimposed swirling flow. In the orthogonal coordinate system, the secondary flow is generally of two vortices with sources and sinks. In the small γ limit, it is of the usual two–vortex. In the large γ limit, it is of a two–vortex type but the orientation the two vortices turned 90° towards the helical axis. In the intermediate range of γ, the secondary flow may have only one (lower) vortex. The flow friction factor is correlated to account for Dn, λ and γ effects for Dn $\leq$ 5000 and $\gamma < 0.1$.

The stability of the flow is investigated through parabolized governing equations. It is found that the four–vortex solution can be observed by a perturbation of the flow field for $\gamma < 0.01$ and Dn > 130. However, the four–vortex solution is not stable and it eventually degenerates to the stable two–vortex flow.

Simultaneous developing laminar flow and heat transfer of Newtonian fluids in the helical pipes of constant circular cross–section are numerically studied. The governing equations are fully parabolized Navier–Stokes equations written in the orthogonal helical coordinate system. They are shown to be a good approximation in the limiting case of loose coiling.

Numerical simulations of shear rates, axial velocity and Nusselt number agree well with published data of toroidal flow in the developing region. In the limit of large torsion, the flow and heat transfer characteristics tend to correspond to the straight pipe case. Both the hydrodynamic and thermal entrance lengths and the fully–developed heat transfer Nusselt number are correlated for Dn < 5000.

Acknowledgements

The author owes much thanks to his family and friends for their love, support and encouragement throughout this study. Special thanks to his wife, Chunmei, and his new son, Jimmy, for their love, support and understanding through what must have seemed to be a never ending task.

The author wishes to thank his supervisor Killam Professor Jacob H. Masliyah for whose support throughout the author's entire stay at this university paved the way for the success of this project. Dr. Masliyah's patience, understanding, encouragement and guidance were the key to uncover the author's creativity and potential.

The author is very much indebted to the former and current teachers who also helped to develop his skills. Among them, special thanks should be given to Ms. Hu, Shuochun; Prof. Fu, Youjie and Prof. Zhou, Zhaoyi; and Prof. K. Nandakumar.

Table of Contents

Abstract

Acknowledgements

List of Tables

List of Figures

Nomenclature

Chapter 3. Axially–Invariant Laminar Flow in Helical Pipes with a Finite Pitch

Part 1 Theory and Loosely Coiled Pipes   88

Chapter 4. Axially–Invariant Laminar Flow in Helical Pipes with a Finite Pitch

Part 2 Torsion and Curvature Effects   137

Chapter 5. Developing Laminar Flow and Heat Transfer in Helical Pipes

201

Chapter 6. General Conclusions and Discussions

Appendix: Derivation of Orthogonal Helical Coordinates

List of Tables

List of Figures

Nomenclature

A, A_e	area
A_1, A_2, A_3	constants or regression coefficients
a	the radius of the pipe
a_i, b_i	coefficients
$a(\cdot; \cdot, \cdot)$	tri— and bi— linear form, $a_1(\cdot; \cdot, \cdot) + a_0(\cdot, \cdot)$
$a_1(\cdot; \cdot, \cdot)$	tri–linear form, defined by equation (1–15)
$a_0(\cdot, \cdot)$	bi–linear form, defined by equation (1–16)
B	pitch number, $\sqrt{\tau H / 2\pi}$
B	differential operator
$B, C\phi$	coefficients
$b(\cdot, \cdot)$	linear divergence (weak) form, defined by equation (1–18)
C_P	specific heat, or heat capacity
D	Dean number, $K/4$
d	diagonal term
Dn	Dean number, $Re\sqrt{\lambda}$
E	decomposed one–dimensional momentum terms
ESN	error in continuity equation with axial directional change removed
F	relaxation factor
f	Fanning friction factor, $-\dfrac{a}{\rho U^2}\dfrac{\partial p'}{\partial s'}$
g	gravity
g_{ij}	metric coefficients, i=1,2,3 and j=1,2,3
G	axial pressure gradient, $\dfrac{\partial p}{\partial s}$
Gn	Germano number, $Re\ \eta$
h	radius of conservational domain
h	local wall heat transfer coefficient, $-\dfrac{a}{T_{av}} k \left(\dfrac{\partial T}{\partial r}\right)_{r=1}$

$\bar{h}$	peripherally averaged wall heat transfer coefficient
h_1, h_2, h_3	metric coefficients
H	pitch of the helical coil
H_1, H_2	grid spacing
i,j,k	index
I,J,K	index
inf	infimum
k	thermal conductivity
K	Dean number, $2\lambda(\frac{\rho a^3}{4\mu^2}\frac{\partial p'}{\partial s'})^2$
K	stiffness matrix or algebraic equation coefficient matrix
L	developing length, $s'/(2aRe)$, or side length of the square cavity
L	linear space
L	differential operator
l_e	length of a conservational domain
Lu	hydrodynamic developing length measured by center axial velocity
Lp	hydrodynamic entrance length measured by axial pressure gradient
LNu	thermal developing length measured by peripherally averaged Nusselt number
M	momentum/energy operator
$Nu(\theta)$	Local Nusselt number, 2 a h / k
Nu	Nusselt number, 2 a $\bar{h}$ / k
p,P	pressure
Pe	Peclet number
PIJK	diagonal term of the discrete pressure perturbation equation
PMJK	coefficient for P_{i-1jk} of the discrete pressure perturbation equation
PPJK	coefficient for P_{i+1jk} of the discrete pressure perturbation equation
PIMK	coefficient for P_{ij-1k} of the discrete pressure perturbation equation
PIPK	coefficient for P_{ij+1k} of the discrete pressure perturbation equation

PIJM	coefficient for P_{ijk-1} of the discrete pressure perturbation equation
PIJP	coefficient for P_{ijk+1} of the discrete pressure perturbation equation
PRH	right—hand—side of the discrete pressure perturbation equation
Pr	Prandtl number, $\mu C_p/k$
Q	flow rate
Q	square integrable functional space
Q_s	flow rate scale, $\pi a^2 W$
q	weighting function or a function in a square integrable space
q	$(Dn^2 Pr)^{-\frac{1}{4}}$
q$'$	peripherally averaged heat flux at pipe wall
q_1, q_2, q_3	curvilinear coordinate
r	radial coordinate
Rc	radius of coil
Re	Reynolds number, $2aU/\nu$ or LU_0/ν
RSD	residual
s	axial coordinate
s^+	non—dimensional axial length, s$'$ / (2 a Re)
S	source term
sup	supremum
t	time
T	temperature
u	x—velocity component
u, u_1	axial velocity
U	average axial velocity
U_0	plate moving velocity of the square cavity
V	functional space of velocity field
V$\cdots$	coefficient of the discrete v—equation, for example

VIJK	diagonal coefficient of the discrete v–equation
v	y–velocity component
v, u_2	radial or x–directional velocity component
W	velocity scale, $\frac{a^2}{8\mu}\left(-\frac{\partial p'}{\partial s'}\right)$
W$\cdots$	coefficient of the discrete w–equation, for example
WIJK	diagonal term of the discrete w–equation
w_i	weighting function
w, u_3	azimuthal or y–velocity component
x,y,z	coordinate, cartesian or rectangular
z	non–dimensional axial length, $s' \lambda^{3/4} Re^{1/2} / a$

Superscripts

$'$	denotes dimensional quantity
$'$	denotes a different version
*	denote small Dn, Dn < 20
c	normalized by average
h	interpolated

Subscripts

av	average
c	conservational domain
d	discrete
fd	fully developed
i	inlet bulk
i,j,k,I,J	nodal index

m	average
max	maximum
min	minimum
Nu	peripherally averaged Nusselt number
o	orthogonal
p	average axial pressure gradient
s	straight pipe
u	axial velocity at the center
w	wall
0	divergence—free
0,0	the center of the pipe
0,1,2,3,..	orders of approximation in the form of a polynomial
1	axial direction
2	radial or x direction
3	azimuthal or y direction
85%	up to 85% fully—developed
95	up to 95% fully—developed

Greek

α, β, φ	angle
α, β	constants or coefficients
β	global index with special interest in the parallel direction
γ	flow transition group, $\eta/\sqrt{\lambda Dn}$
γ^*	flow transition group, $\eta/(\lambda Re)$
δ	Dirac delta
Δ, δ	difference

η	normalized torsion, $(\frac{H}{2\pi})$ a / $[Rc^2 + (\frac{H}{2\pi})^2]$
θ	azimuthal coordinate
θ'	orthogonal azimuthal coordinate
κ	curvature ratio, Rc / $[Rc^2 + (\frac{H}{2\pi})^2]$
λ	normalized curvature ratio, Rc a / $[Rc^2 + (\frac{H}{2\pi})^2]$
μ	dynamic viscosity
ν	kinematic viscosity
ξ	body–centered azimuthal velocity
ρ	density
Σ	summation
τ	torsion, $(\frac{H}{2\pi})$ / $[Rc^2 + (\frac{H}{2\pi})^2]$
ϕ	physical variable
ϕIJK	diagonal term of the discrete ϕ–equation
ϕMJK	coefficient for ϕ_{i-1jk} of the discrete ϕ–equation
ϕPJK	coefficient for ϕ_{i+1jk} of the discrete ϕ–equation
ϕIMK	coefficient for ϕ_{ij-1k} of the discrete ϕ–equation
ϕIPK	coefficient for ϕ_{ij+1k} of the discrete ϕ–equation
ϕIJM	coefficient for ϕ_{ijk-1} of the discrete ϕ–equation
ϕIJP	coefficient for ϕ_{ijk+1} of the discrete ϕ–equation
ϕRH	right–hand–side of the discrete ϕ–equation
ψ	pseudo–secondary flow stream function
Ω	domain of computation

symbols

∇	gradient
∂	partial derivative of
$\partial\Omega$	boundary of domain Ω
$\exists$	exists
$\forall$	for all
$\|\cdot\|$	norm
$\|v\|_{r\theta}$	Secondary flow strength in the orthogonal coordinate system,

$$\int_0^1 r\,dr \int_0^{2\pi} (1 + \lambda\, r \sin\theta)\, (v^2 + w^2)^{\frac{1}{2}}\, d\theta$$

Chapter 1.

General Introduction

1.0 Thesis Layout

This study is set to investigate the problem of laminar incompressible Newtonian fluid flow and forced convective heat transfer in circular helical pipes of finite pitch.

Chapter 1 gives a general review and re—examination of the related previous literature studies.

In Chapter 2, a novel numerical method is developed. The new method is based on a 3—point exponential interpolation scheme. The multi—dimensional flow problem is subdivided into multiple one—dimensional problems. The resulting discrete equations are solved iteratively using a tri—diagonal solver. The toroidal flow problem and a square driven cavity flow problem are solved in Chapter 2.

Chapter 3 deals with the fully—developed laminar flows in helical pipes of finite pitch. A loose coiling approximation is performed to single out the dominant flow parameters. With the numerical simulations, conditions for which the torsion effect is negligible are investigated. The flow pattern transition from two— to one—vortex flows is characterized for small Dean number flows.

Chapter 4 is a continuation of Chapter 3. The curvature ratio and torsion effect are examined. The flow pattern transition is characterized for large Dean number flows. The stability of the helical flows is also numerically experimented to look for possible bifurcations. The orthogonal secondary flow strength and the representation of the secondary flow are addressed. A correlation equation for the flow friction factor is developed.

In Chapter 5, the simultaneous developing laminar flow and convective heat transfer of incompressible Newtonian fluids in helical pipes with a uniform wall temperature is studied. The parabolization of the governing equations is derived. Correlations for the fully—developed peripherally averaged Nusselt number and the

hydrodynamic and thermal developing lengths are presented.

Chapter 6 gives a short summary and general conclusions to this study. Some recommendations are also given for possible future studies on this subject.

A detailed derivation of the governing equations is given in the Appendix.

1.1 Numerical Methods in Fluid Dynamics

The convergence of a numerical scheme is often mistaken by one's ability to obtain a solution from the numerical analysis without any concern over the quality of the solution. A convergent numerical scheme is defined as a scheme in which all values of the numerical solution approach the exact differential equation solution as the mesh size approaches zero. This definition stresses that the limit behavior is the limit of the whole solution of the differential equation, not merely the individual terms of the equation. Hence apart from the ability to obtain a solution, the numerical discretization must be consistent.

Consistency is defined as the limit behavior of the discrete equation used in a numerical scheme to approach the governing differential equation as the mesh size approaches zero. All the standard discretizations such as central difference, standard finite element, spectral method, etc. are consistent.

Stability is defined by O'Brien, et al. (1950) and Eddy (1949) in terms of the growth or decay of roundoff errors. This definition tells us that if a numerical scheme is stable, then the roundoff error will not grow. Lax & Richtmyer (1956) define the stability in a more general sense by requiring a bounded extent to which any component of the initial data can be amplified in the numerical procedure. For stability analysis, there is a vast amount of literature available, see Richtmyer & Morton (1967), Holt (1984), Roache (1985), and Sod (1985). The most commonly used technique to check the linear stability is the von Neumann analysis, which employs discrete Fourier transformation and checks the amplification factor. Stability of a non–linear problem is much more difficult to analyze.

The Lax equivalent theorem for a linear system of equations is of fundamental importance. It states that, for a consistent finite–difference scheme, stability is a necessary and a sufficient condition for convergence. Actually, this

theorem can be generalized to any discretizations, hence one may replace "finite difference" with "numerical". When this theorem applies to a non–linear problem, however, one must make sure that the problem is well–posed. Even for a linear problem, one cannot construct a stable discretization for an ill–posed problem.

So far, no definition has been given for a numerical scheme in the text. A numerical scheme is a mathematical transformation of original continuous problem into a set of discrete algebraic equations. Consider the differential equation,

$$Lu = f, \quad x \in \Omega \tag{1-1}$$

with a boundary condition:

$$Bu = g, \quad x \in \partial\Omega \tag{1-2}$$

where $\partial\Omega$ is the boundary of the domain Ω and is required to be Lipschitz continuous. L and B are differential operators.

A numerical discretization with a numerical scheme is generally done by first forming the following weak form of the original differential equation,

$$\int_{\Omega_e} w^h \, Lu^h \, d\Omega = \int_{\Omega_e} w^h f \, d\Omega \tag{1-3}$$

and

$$\int_{\partial\Omega_e} q^h \, Bu^h \, ds = \int_{\partial\Omega_e} q^h g \, ds \tag{1-4}$$

where w^h and q^h are the weighting functions. u^h is the approximated form of u based on the discretized domain Ω_e of Ω.

A standard finite element method would interpolate both u^h and w^h in the same way. When the value of w^h at each node on the discretized domain Ω_e is set to be arbitrary, the original problem, equations (1–1) and (1–2), reduces to a set of algebraic equations involving the values of u^h at each node on Ω_e.

1.1.1 Elliptic Problems and Stability

"Wiggles", or spatial oscillations in a flow solution, have been encountered in many works where elliptic problems are treated. Even for a linear elliptic type of equation, the stability of a particular discretization should also be of concern. This type of stability problem has been extensively studied for one and two dimensions. The interested reader is referred to Roache (1985), Leonard (1981 & 1987) and Neuberger (1987). An illustration is presented here to show the instability of a boundary value problem with a given numerical discretization. Consider the "one–dimensional flow" equation with a constant velocity in dimensionless form,

$$\text{Re} \frac{d\phi}{dx} - \frac{d^2\phi}{dx^2} = 0 \qquad (1-5)$$

where Re is the Reynolds number. The boundary conditions are

$$\phi(0) = 0, \qquad \phi(1) = 1 \qquad (1-6)$$

This is a relatively simple problem, the exact solution can be obtained as

$$\phi(x) = \frac{1 - e^{x\text{Re}}}{1 - e^{\text{Re}}} \qquad (1-7)$$

Since our purpose here is to show the instability of a numerical scheme, we discretize equation (1–5) by either a central difference or a standard linear finite element (Galerkin) method. Both numerical methods can render the following reduced discrete equation centered at the node i:

$$\frac{\Delta x}{2}\text{Re}(\phi_{i+1} - \phi_{i-1}) - (\phi_{i+1} - 2\phi_i + \phi_{i-1}) = 0 \qquad (1-8)$$

For simplicity, a uniform mesh is assumed. $\Delta x = 1 / (N - 1)$, $N > 2$, $1 < i < N$, $\phi_i = \phi(x_i)$, $x_i = (i - 1)\Delta x$. It is easy to show that equation (1–8) is

consistent with equation (1–5) by an order of $(\Delta x)^2$, i.e., the discretization is second order accurate. Let

$$Pe = \Delta x\, Re \qquad (1\text{--}9)$$

be the "cell Peclet number". Define

$$\alpha = -\frac{Pe\ -\ 2}{Pe\ +\ 2} \qquad (1\text{--}10)$$

The discrete equation (1–8) together with the boundary conditions

$$\phi_1 = 0, \qquad \phi_N = 1 \qquad (1\text{--}10)$$

can be solved directly to yield

$$\phi_i = \alpha^{N-i}\,\frac{1\ -\ \alpha^{i-1}}{1\ -\ \alpha^{N-1}} \qquad (1\text{--}12)$$

Equation (1–12) is the "numerical" solution of the problem given by equations (1–5) and (1–6). By solving the discrete equations (1–8) and (1–11) analytically, we have avoided the issue of the ability to obtain a solution. From equation (1–12), we can observe that the "numerical" solution is oscillatory when $\alpha < 0$, i.e., $Pe > 2$. The exact solution, equation (1–3), on the other hand, is monotonic in the entire domain, $0 \le x \le 1$. In this regard, the "numerical" solution is not the solution of the original problem when $Pe > 2$.

However, as $N \to \infty$, equation (1–12) reduces to equation (1–7). It follows that the schemes are convergent. Since it is not always possible to have a fine enough grid, this theoretical convergence may be not achievable.

Of course, the effect of spatial varying flow velocity and higher dimensions may quantitatively change such a stability behavior, but the analysis presented here can occur in multi–dimensional real flow problems as well, for example, Zhong &

Olson (1989). In particular, "wiggles" are present in the solution of the toroidal flow problem given by Van de Vosse (1987) and Van de Vosse et al. (1989). Needless to mention that such a type of instability may cause numeric divergence if a good solver is not used.

1.1.2 The Navier–Stokes equations

Laminar incompressible fluid flow is governed by the dimensionless momentum and continuity equations. They are given as

$$\frac{\partial u}{\partial t} + \text{Re } u \cdot \nabla u - \nabla^2 u = - \nabla p \qquad (1-13)$$

$$\nabla \cdot u = 0 \qquad (1-14)$$

with

$$x \in \Omega$$

Re is the flow Reynolds number, u is the velocity vector, p is the dynamic pressure and t is the time. The non–dimensionalized variables are defined as follows:

$$u = \frac{u'}{<U>}, \qquad \nabla = \frac{\partial}{\partial x_i} = <L> \frac{\partial}{\partial x_i'}, \qquad p = \frac{\text{Re } P'}{\rho <U>^2},$$

$$t = \frac{\mu \ t'}{\rho <L>^2}, \qquad \text{Re} = \frac{\rho <L> <U>}{\mu} \qquad (1-15)$$

The primed variables are the corresponding dimensional variables, $<U>$ is the characteristic velocity scale, $<L>$ is the characteristic length, ρ is the density of the fluid, μ is the dynamic viscosity.

For the case of steady state, i.e., $\frac{\partial u}{\partial t} = 0$, the existence and the uniqueness of solutions of equations (1–13) and (1–14) with a Dirichlet boundary condition for u have been proven, see Thomasset (1981), Girault & Raviart (1986) and Temam (1979). The interested reader is referred to the original books for proofs.

We define the trilinear form and the bilinear form as follows:

$$a_1(w;u,v) = \text{Re} \int_\Omega w_j \frac{\partial u_i}{\partial x_j} v_i \, dx \qquad (1\text{--}15)$$

$$a_0(u,v) = \int_\Omega \left(\frac{\partial u_i}{\partial x_j} + \frac{\partial u_j}{\partial x_i} \right) \frac{\partial v_i}{\partial x_j} \, dx \qquad (1\text{--}16)$$

The combined advection and diffusion operator is

$$a(w;u,v) = a_1(w;u,v) + a_0(u,v) \qquad (1\text{--}17)$$

The linear divergence form is defined by

$$b(u,q) = -\int_\Omega \frac{\partial u_i}{\partial x_j} q \, dx \qquad (1\text{--}18)$$

Define the following Hilbert Space,

$$V = \{ v \in L^2(\Omega); \, \partial v \in L^2(\Omega); \, v|_{\partial\Omega} = 0 \} \qquad (1\text{--}19)$$

and its subspace $V_0 \subset V$

$$V_0 = \{ v \in V \,|\, b(v,q) = 0, \, \forall q \in Q \} \qquad (1\text{--}20)$$

where Q is simply the square integrable space, i.e.,

$$Q = \{ q \in L^2(\Omega) \} \qquad (1\text{--}21)$$

When the following conditions are met

i) $b(v,q)$ satisfies the inf–sup condition:

$$\underset{\beta>0}{\exists} \, \underset{q \in Q}{\inf} \, \underset{v \in V}{\sup} \, \frac{b(v,q)}{\|v\|_V \|q\|_Q} \geq \beta \qquad (1\text{--}22)$$

and ii) $a(w;u,v)$ is V_0 coercive, i.e.,

$$\underset{\substack{\alpha>0 \\ v\in V_0}}{\exists \quad \forall} \ a(v;v,v) \geq \alpha \, \|v\|_V^2 \tag{1-23}$$

then the flow equations (1–13) and (1–14), together with a Dirichlet boundary condition for u, exist at least one pair of solution $(u,p) \in V \times Q$.

When the following condition holds,

iii) $Re < Re_0$ $\hfill$ (1–24)

then the Navier–Stokes equations have a unique solution. Here Re_0 is a critical flow Reynolds number for which a flow bifurcation may occur.

Theoretically, conditions i) and ii) can be shown to be satisfied for a Dirichlet problem. However, numerically, deliberation must be made to satisfy the two conditions. For a dynamic problem, a Crank–Nicolson or backward Euler for the time evolution term will yield a stable scheme by applying any standard discretization on the rest of the terms. For proofs, see Temam (1979). It seems that the easy way to check the stability for a nonlinear problem is to use the energy norm method, i.e., requiring the boundedness of the energy norm to be independent of the mesh size, Temam (1979).

1.1.3. Velocity–pressure coupling and inf–sup condition

A numerical discretization must satisfy the inf–sup condition in order to render a stable scheme. If the inf–sup condition is not satisfied, the pressure solution will contain spurious modes. One such an example has been outlined by Patankar (1980), as the checkerboard effect.

The inf–sup condition was carefully studied in the past two decades and was implemented in numerical discretizations. For a finite element method and a

spectral method, it is satisfied by choosing different functional spaces for the velocity and the pressure. The procedure, however, is rather complicated. For stable elements, the reader is referred to Fortin & Fortin (1985), Arnold et al. (1984), Raviart (1984), Fortin (1981), Bercovier (1977), Taylor & Hood (1973) and Crouzeix & Raviart (1973). Some numerical analysts take a different approach by discretizing the domain and the governing equations and then filter the spurious pressure modes out after each iteration.

Owing to the simple discretization strategy used for the finite difference and finite volume methods, one must deal with the inf—sup condition in a way other than imposing it directly. The fully staggered grid of Welch & Hallow (1965) has been very successful in this regard. For details on the grid staggering, see Patankar (1980). The staggered grid technique has also been used in the spectral method as well. If a non—staggered grid is used, the momentum equations must be used recursively to assist in the elimination of spurious pressure modes. It is also possible to simply use an upwind scheme on the pressure discretization to avoid the checkerboard effect, see Temam (1979). The spurious pressure filtering can also be applied to these methods.

1.1.4 Upwind and a(w;u,v) coercive

Apart from the inf—sup condition, the tri— and bi—linear forms of a(w;u,v) must be V_0—coercive, i.e., the left—hand—side of the equation (1–13) with $\frac{\partial u}{\partial t} = 0$ must be weakly elliptic. Theoretically, this is true for a Dirichlet condition for u, see Temam (1979). However, numerical discretization with a centered scheme does not satisfy this condition for large Re. When Re is small or the mesh size is fine enough, then this condition can be satisfied.

Actually, the coercive condition is the same as the stability condition of section 1.1.1. What is important is that this condition is required by the

Navier–Stokes equation and it is not only a numerical requirement. It makes the "wiggle–free" stability condition a sufficient condition for the convergence of a scheme as applied to the Navier–Stokes equation.

There are many upwind schemes in use in the computational fluid dynamics. One can name a few for the finite element method: they are Petrov–Galerkin method, artificial viscosity method, streamline diffusion method, see Brooks & Hugues (1982), Fortin & Thomasset (1979), Girault & Raviart (1982 & 1986), Thomasset (1981), Glowinski (1984) and Johnson (1987).

For finite difference and finite volume methods, the upwinding schemes are first order upwind, second order upwind, third order upwind (QUICK), two–point exponential upwind, exponential weighted with source specification, and the less commonly used three point exponential without imposing length scale. The reader is referred to Allen & Southwell (1955), Raithby & Torrance (1974), Patankar (1980), Leonard (1981 & 1987), Neuberger (1987) and De Henau et al. (1989). The two–point exponential or exponentially weighted, see Patankar (1980) are commonly used. All the higher order schemes are subject to instability and divergence, see Leonard (1981 & 1987) and Neuberger (1987). However, the exponentially weighted scheme is subject to large error due to the source–free specification. On the other hand, the source term specification can only be applied to one dimensional problems. For multi–dimensional problems, care must be taken to use any of the schemes mentioned.

1.2 Fully Developed Flows in Helically Coiled Circular Pipes

Curved pipes are often used in the chemical process industry to enhance the heat and mass transfer in chemical reactors, heat exchangers and mixers. In health sciences, they are used in blood oxygenators and in dialysis equipment.

Curved pipes of interest to chemical process industry are helical pipes. Helical pipes are spirally coiled pipes. A helical pipe having a zero pitch is termed a torus. Experimental fluid flow in a torus is limited to a single turn. However, theoretical analysis for fluid flow in a torus can apply as many turns as is desired. To date most of the studies for fluid flow are for a flow through a torus. The reason is that there exists a simple orthogonal coordinate system for the case of a torus. Flow through a helical pipe of finite pitch is of more practical use.

1.2.1 The toroidal flow

The milestone study of the flow in a toroidal pipe is that of Dean (1927 & 1928). Most of the studies for fluid flow in a torus deal with the case of the curvature ratio $\lambda = a/Rc$ close to zero, where a is the radius of pipe and Rc is the radius of coil.

The perturbation series has offered an excellent solution approach to the toroidal flow problem for very small Dn number flows. The perturbation series solution to the problem started since the initial Dean's work. We define the dimensionless velocity field as:

$$u = \frac{2\mu}{(-\frac{\partial p'}{\partial s'})a^2} u', \quad v = \frac{a}{\nu} v', \quad w = \frac{a}{\nu} w' \quad (1\text{--}25)$$

where a is the radius of the pipe. $\frac{\partial p'}{\partial s'}$ is the pressure gradient. μ is the viscosity of the fluid. p′ is the pressure. s′ is the axial length variable. ν is the dynamic

viscosity of the fluid. u, v, w are the axial, radial and circumferen

components and the primed variables are the corresponding dimensiona

The perturbation solutions for the axial velocity u and the secondary

function ψ are written respectively as

$$u = 1 - r^2 + K u_1 + K^2 u_2 + ...$$

and

$$\psi = K\psi_1 + K^2\psi_2 + ...$$

where

$$K = (2a/Rc)(2Wa/\nu)^2 = 2\lambda(-\frac{\rho a^3}{4\mu^2}\frac{\partial p'}{\partial s'})^2$$

W is the average axial velocity in a straight pipe of the same radius un

axial pressure gradient $(\partial p'/\partial s')$. ρ is the density of the fluid. K is

Dean number, in the form first used by Dean. u is the axial velocity. T

of such a solution is that it is only valid for small K flows. The transve

are obtained from the secondary flow stream function as given by

$$v = \frac{1}{rh_1}\frac{\partial\psi}{\partial\theta}$$

$$w = -\frac{1}{h_1}\frac{\partial\psi}{\partial r}$$

where h_1 is the metric coefficient of the axial direction It was found, D

1928), that

$$\psi_1 = \frac{1}{576}(4r - 9r^3 - r^7)\cos\theta$$

and

$$u_1 = \frac{1}{576}(\frac{19}{40}r - r^3 + \frac{3}{4}r^5 - \frac{1}{4}r^7 + \frac{1}{40}r^9)\sin\theta$$

Hence the series solution gives rise to a two—vortex secondary flow according to equation (1–31).

It is found that the dimensionless volume flux in the pipe depends only on Dean number and for small Dean number is given by

$$\frac{Q}{Q_s} = 1 - 0.0306(\frac{K}{576})^2 + 0.0120(\frac{K}{576})^4 + O(\frac{K}{576})^6 \qquad (1-33)$$

where Q is the flow rate in the curved pipe and $Q_s = \pi\, a^2\, W$ is the flow rate in the straight pipe with the same axial pressure gradient. We see that the effect of curvature is to reduce the flux.

For a finite coil radius, the perturbation solution was obtained by Topakoglu (1967) and is given by

$$\frac{Q}{Q_s} = 1 - 0.030575\,(\frac{K}{576})^2 - \frac{11}{60}\,\lambda\,(\frac{K}{576}) + \frac{\lambda^2}{48} \qquad (1-34)$$

It can be seen that for very small K and large λ, the flow rate in a curved pipe can be larger than that in the straight pipe.

One outstanding feature of Dean's series solution is that the flow rate ratio is not affected by the first order term $O(K)$, and is decreased by the second order term $O(K^2)$ for a pipe of an almost zero curvature.

The Fanning friction factor is defined by

$$f = -\frac{a}{\rho U^2}\frac{\partial p'}{\partial s'} \qquad (1-35)$$

where U is the average axial velocity. p' is the pressure and s' is the axial length variable.

To convert the flow rate ratio to the friction factor ratio, we must consider the formulation of the perturbation series instead of using equation (1–35) directly.

The perturbation series is based on the parameter K, which is defined by equation (1-28). The more acceptable variant of Dean number is defined by White (1929) as

$$Dn = \lambda^{\frac{1}{2}} Re = \lambda^{\frac{1}{2}} \frac{2aU\rho}{\mu} \tag{1-36}$$

The immediate concern is to relate K with the flow rate ratio and the friction factor ratio. From equations (1-28) and (1-35), we obtain

$$K = 8\lambda \left(\frac{Q_s}{\pi \, a \, \nu}\right)^2 = 2\lambda \left(\frac{1}{16} Re^2 f\right)^2 \tag{1-37}$$

On the other hand, if we define f_s as the friction factor of a straight pipe Poiseuille flow having the same flow rate Q as that of the curved pipe, i.e., $f_s Re = 16$, then we obtain from the equation (1-36)

$$Dn^2 = \lambda \left(\frac{2Q}{\pi \, \nu \, a}\right)^2 = \lambda \left(\frac{1}{16} Re^2 f_s\right)^2 \tag{1-38}$$

Comparing equations (1-37) and (1-38), we obtain

$$\frac{1}{2} \frac{K}{Dn^2} = \left(\frac{Q_s}{Q}\right)^2 = \left(\frac{Re^2 f}{Re^2 f_s}\right)^2 \tag{1-39}$$

Hence, the flow rate ratio for a given pressure gradient and the friction factor ratio of a given flow rate are related by the following equation:

$$\left(\frac{Q_s}{Q}\right)_{\text{constant pressure drop}} = \left(\frac{f}{f_s}\right)_{\text{constant flow rate}} \tag{1-40}$$

Hence the friction factor ratio is just the reciprocal of the flow rate ratio. It follows then from equations (1-34) and (1-40) that

$$\frac{f}{f_s} = \left(\frac{Q}{Q_s}\right)^{-1} = 1 + 0.03058(1 + 1.141\lambda^2)\left(\frac{K}{576}\right)^2 + 0.1833\lambda(1 + \frac{\lambda^2}{24})\left(\frac{K}{576}\right) - \frac{\lambda^2}{48} \tag{1-41}$$

Since expression (1—34) is only valid for very small K, the discussion is restricted to a small K. We see that the friction factor in the curved pipe can be smaller than the straight pipe for reasonably large curvature pipe. For larger K flows, the friction factor increases with the curvature ratio.

For creeping flow, i.e., K = 0, Chadwick (1985) and Van Dyke (1990) formed a much longer series for the flow rate ratio. In particular, Van Dyke (1990) worked out a series convergent in the full range of λ ($0 \leq \lambda \leq 1$). These investigators found that the friction factor in a curved pipe is smaller than that in a straight pipe except when λ is greater than 0.85.

As we have mentioned, the perturbation series given by equations (1—26) and (1—27) are only valid for very small K. In order to have a convergent series for a larger K, deliberation must be made to eliminate the singularities in the series (Van Dyke, 1978). In searching for higher order terms, Larrain & Bonilla (1970) and Van Dyke (1978) have tried to extend the perturbation series indefinitely. In particular, Van Dyke attempted to extract the higher K convergent series from his first 12 terms of the Taylor series by extrapolation through Domb—Sykes plots. The final friction factor ratio in the high Dean number limit obtained by Van Dyke is given by

$$\frac{f}{f_s} = 0.47136 \; \mathrm{Dn}^{\frac{1}{4}} \tag{1—42}$$

Van Dyke suggested that equation (1—42) may be valid for Dn → ∞. However, comparing with experimental results of White and others, we see that equation (1—42) is valid for 25 < Dn < 250 only.

The numerical solutions of the Navier—Stokes equations for fully developed laminar flow flow in a torus were conducted extensively in the past twenty years, starting with McConalogue & Scrivastava (1968). The most comprehensive

calculations for very large values of Dean numbers for arbitrary values of λ were carried out by Yang & Keller (1986) who obtained solutions for D (= K/4) up to 30 000 and λ up to 0.3. The solutions are obtained by Fourier expansion on θ direction and finite (central) difference on the radial direction. The symmetry condition is implied and the continuation technique is used with D as a parameter. The solution family has four folds or limit points, i.e., five branches of solutions. Yang & Keller (1986) speculated that there may be countless solutions for reasonably large D flows bearing a secondary flow pattern of 2n—vortex, where $n = 1, 2, \cdots$. Two— to eight— vortex patterns have been obtained. As they refined the grid size, the limit points moved towards a higher D. This suggests that all the solution branches might be separated and no real turning points exist.

Following Nandakumar & Masliyah (1982), Daskopoulos & Lenhoff (1989) used a geometrical change to study the possible isolated solution branches. The continuation technique is involved to follow each solution branch with the parameter D. The symmetry is imposed and λ is set to be zero. The spectral method is applied to solve the flow problem with the secondary flow stream function and axial velocity formulation. Owing to the difficulty in discretizing the bi—harmonic equation of the secondary flow stream function equation, they encountered spurious modes in the solution. The spurious modes were removed artificially. The bifurcation map of Daskopoulos & Lenhoff is rather different from that of Yang & Keller. Furthermore, Daskopoulos & Lenhoff found that only two— and four— vortex solutions are stable. This explains that only two— and four— vortex solutions can be obtained with a prescribed symmetry formulation.

The four—vortex solution were first obtained by Nandakumar & Masliyah and Dennis & Ng (1982). Nandakumar & Masliyah used finite λ and documented the solutions with respect to the physical parameters. Dennis & Ng set λ to be zero and used D as the Dean number. Dennis (1980) correlated his two- vortex flow

friction factor against Dn. His relationship of

$$\frac{f}{f_s} = 0.388 + 0.105 \; \text{Dn}^{\frac{1}{2}} \qquad (1\text{--}43)$$

is accepted as an accurate expression for large Dn flows.

Using a spectral method, Yanase et al. (1988) found only two— and four—vortex solutions similar to those of Nandakumar & Masliyah and Dennis & Ng. They found further that the four—vortex solution is not stable with respect to asymmetrical disturbances. This leads to a conclusion that only two—vortex solution is stable. Although with the same line of discretization as Daskopoulos & Lenhoff, Yanase et al. did not mention any spurious modes in their solution.

The numerical solutions and experimental results support the relationship of the type (1—43), which was first proposed by Adler (1934) through his boundary layer analysis. Adler's solution is given by

$$\frac{f}{f_s} = 0.1064 \; \text{Dn}^{\frac{1}{2}} \qquad (1\text{--}44)$$

which is valid for large Dn but still in laminar flow regime. The same relationship was used to correlate the experimental data of White by Hasson (1955). Hasson's correlation is given by

$$\frac{f}{f_s} = 0.556 + 0.0969 \; \text{Dn}^{\frac{1}{2}} \qquad (1\text{--}45)$$

which is the now accepted friction factor relation for small curvature and large Dn flows. There are many other correlations, but none of them improved much about the valid range of Dn.

However, a more recent experimental work by Ramshankar & Sreenivasan

(1988) claimed to have resolved the "Paradox" of the relationships of the friction factor versus the Dean number in the large Dn range between Van Dyke's 1/4 power and the accepted square root. Ramshankar & Sreenivasan attempted to show that Van Dyke's relation was the correct one.

The "paradox" was addressed by Jayanti & Hewitt (1991) once again numerically, after Dennis (1980). The claim by Ramshankar & Sreenivasan (1988) was dismissed by Jayanti & Hewitt through direct numerical evaluation of the friction factor. The pressure drop measurements of Ramshankar & Sreenivasan were suspected to be in error. Even if the pressure drop measurements were conducted properly, Ramshankar & Sreenivasan did not seem to analyze their results correctly.

Dennis & Riley (1991) took a different approach to resolve the paradox by proving the validity of the boundary layer analysis in the limit of very large Dean number and zero curvature.

It should be noted that the argument between Van Dyke's 1/4 and every one else's 1/2 power dependence of the friction factor ratio on the Dean number is essentially theoretical. When $\lambda = 0$, the flow is of Poiseuille type as long as it is laminar. When λ is finite but very small, the Dean number should not be very large prior to the flow becoming turbulent. In any event, Van Dyke (1978) revolutionized the series solutions from his first 12 terms by pushing the validity range to a practically useful region. More terms should lead to a better closed form solution.

For small Dn flows, Akiyama and Cheng (1971) obtained a numerical solution for $\lambda \to 0$. They observed both numerically and experimentally that the relative constant behavior of the friction factor ratio for Dn < 16 is due to the compensation of the increasing resistance on the outer bend surface and the decreasing friction on the inner bend surface.

For more detailed review of the previous studies, the reader can refer to Berger et al. (1983), Nandakumar & Masliyah (1986) and Berger (1991).

1.2.2 Laminar flow in a helical pipe of non—zero pitch

The study of fluid flow in helical pipes of a circular cross section with an arbitrary pitch has not been dealt as extensively as its counterpart, the flow in a torus, i.e., helical pipe of zero pitch in the literature.

The solution of helical flow was first attempted by Truesdell & Adler (1970). Truesdell & Adler suggested ad hoc quantitative arguments that their numerical solutions of the toroidal flow were applicable to a helically coiled pipe of moderate pitch if the curvature ratio is correctly used. The question was addressed more properly by Manlapaz & Churchill (1980), Murata et al. (1981), Wang (1981), Germano (1982 & 1989), Kao (1987) and Tuttle (1990). Orthogonal helical coordinates were first introduced by Germano (1982), and subsequently are used to solve helical flow problems.

Kao (1987) used the orthogonal coordinates and computed three cases of helical flows having small torsion and small Dn (Dn < 200). Kao presented velocity plots and did not make use of the pseudo—secondary flow stream function to show more clearly the flow pattern. Kao mentioned that only a two—vortex type solution is present.

Wang (1981), Murata et al. (1981), Germano (1982 & 1989), Kao (1987) and Tuttle (1990) obtained perturbation solutions in the curvature ratio λ and torsion η. The curvature ratio for a helical pipe is defined as $\lambda = \text{Rc a} / [\text{Rc}^2 + (\text{H}/2\pi)^2]$. The torsion η for a helical pipe is defined as $\eta = (\text{H}/2\pi) \text{a} / [\text{Rc}^2 + (\text{H}/2\pi)^2]$. Wang found that the torsion effect is of first order. Murata et al. and Tuttle found that the torsion effect is of $O(\lambda\eta)$. Germano (1982) stated that the torsion has second order effect and in a later study, Germano (1989) stated that no pure torsion of any order effect is present for a circular helical pipe. Kao stated that the parameter $\beta^{\frac{1}{2}} = \eta/\sqrt{2\lambda}$ determines whether the torsion can exert a $1\frac{1}{2}$ order effect.

The perturbation series solutions for helical flow can be extended from the

toroidal flow solution with the parameter K. The pseudo—secondary flow secondary stream function and the transverse velocities are related as

$$v = \frac{1}{rh_1}\frac{\partial \psi}{\partial \theta}$$

(1—46)

$$w - \frac{\eta r}{h_1}u = -\frac{1}{h_1}\frac{\partial \psi}{\partial r}$$

(1—47)

where u, v and w are the dimensionless axial, radial and azimuthal velocity components in the orthogonal coordinate system, respectively. The dimensionless quantities are defined by equation (1—25). The perturbation series can be written from Topakoglu (1967), Wang (1981) and Tuttle (1990) as

$$u = (1 - r^2)(1 + \frac{3}{4}\lambda r \sin\theta) + \frac{r}{40}(\frac{K}{576})(r^8 - 10r^6 + 30r^4 - 40r^2 + 19)\sin\theta +$$

$$\frac{\sqrt{2}}{48}\lambda^{\frac{1}{2}}\eta(\frac{K}{576})^{\frac{1}{2}}r(3r^6 - 8r^4 - 24r^2 + 29)\cos\theta +$$

$$\frac{\sqrt{2}}{8400}(\frac{K}{576})^{3/2}\lambda^{-\frac{1}{2}}\eta r(20r^{12}-294r^{10}+1575r^8-4550r^6+7630r^4-7350r^2+2969)\cos\theta$$

(1—48)

and

$$\psi = -(\frac{K}{576})r(r^6-6r^4+9r^2-4)\cos\theta + 6\sqrt{2}(\frac{K}{576})^{\frac{1}{2}}\lambda^{-1/2}\eta(1 - r^2)^2(1 - \frac{2}{3}\lambda r\sin\theta) +$$

$$\frac{\sqrt{2}}{10}\lambda^{-1/2}\eta(\frac{K}{576})^{3/2}r(r^{10} - 9r^8 + 30r^6 - 50r^4 + 41r^2 - 13)\sin\theta$$

(1—49)

From equation (1—49) we observe that the secondary flow consists of two recirculating cells when $(\eta \cdot \lambda^{-\frac{1}{2}}K^{-\frac{1}{2}})$ is small. When the torsion is large, the secondary flow degenerates to one vortex pattern as Wang noted that the transition is $(\frac{\eta}{\lambda Re} > \frac{1}{24})$.

It is clear that the controversy on the torsion effect is simply a difference in

viewpoint as noted by Tuttle. Germano, Murata et al. and Tuttle looked at torsion effect on the secondary flow velocity components v and w. Wang, however, considered the torsion effect from the point of pseudo—secondary flow stream function, or the body—centered transverse velocity components. Kao, on the other hand, expanded the series in the same manner but omitted the lowest order terms of $K^{1/2}$. Instead of factoring out the lowest order effect of the torsion, Kao gave the lowest order in K where the lowest order torsion term appears. For a fixed K, Kao obtained a $1\frac{1}{2}$ order in K at which the torsion effect contributes to the secondary flow.

The flow rate ratio can then be obtained as

$$\frac{Q}{Q_s} = 1 - 0.030575(\frac{K}{576})^2 - \lambda\frac{11}{60}(\frac{K}{576}) + \frac{\lambda^2}{48} - \frac{\eta^2}{288}[9.2575(\frac{K}{576})^2 + 616.92\lambda(\frac{K}{576}) - \frac{31\lambda^2}{8}]$$

(1–50)

The friction factor ratio can then be obtained by taking the inverse of the flow rate ratio. This leads to

$$\frac{f}{f_s} = 1 + 0.03058(1 + 1.141\lambda^2)(\frac{K}{576})^2 + 0.1833\lambda(1 + \frac{\lambda^2}{24})(\frac{K}{576}) - \frac{\lambda^2}{48} +$$
$$\frac{\eta^2}{288}[(9.258 - 0.6227\lambda^2)(\frac{K}{576})^2 + 616.92\lambda(1 + \frac{11}{30}\lambda)(\frac{K}{576}) - \frac{31\lambda^2}{8}]$$

(1–51)

From equation (1–51), we observe than the friction factor for flow in a small curvature helical pipe increases with the pipe torsion. For very small Dean number flows, i.e. K is very small, the friction factor can be smaller than that of the straight pipe Poiseuille flow.

The experimental studies were conducted mostly in coiled pipes having a finite pitch. But none of the experimental studies were conducted under the

condition of large torsion. The friction factors were then fitted into the category of toroidal flow as long as the curvature is calculated appropriately. A wide range of pitch was covered in the experimental work of Mishra & Gupta (1979). They correlated the friction factor in the following manner:

$$\frac{f}{f_s} = 1 + 0.033 \, (\log Dn)^4 \qquad (1\text{--}52)$$

for the range of $1 < Dn < 3000$, $Rc > 0.02 \, Dn$ and $H/Rc \leq 26.6$.

1.3. Steady Laminar Developing Flow in Helical Pipes

The developing fluid flow was studied only for the toroidal pipes. Solutions were obtained by Singh (1974), Yao & Berger (1975 & 1988), Yeung (1980) and Stewartson et al. (1980) using a boundary layer formulation. Berger (1991) gave a full review on the boundary layer results.

Austin (1971), Humphrey (1977) and Van de Vosse F.N. (1987) carried out a numerical study for the flow development in curved pipes having a Poiseuille flow at the inlet with the full Navier–Stokes equations. Patankar et al. (1974) studied the flow evolvement from a Poiseuille flow in curved pipes. Their results compared reasonably well with the experimental data. Smith (1976) investigated the transition of a parabolic flow (Poiseuille flow) in a straight pipe to a curved one near their junction. Liu (1977) and Soh & Berger (1984) studied the flow development in a circular torus with a flattish velocity profile (or free–vortex) entry.

Although only half a domain was used in the numerical calculations, none of the above investigators found a flow development into a four–vortex solution.

Cheng & Mok (1986) and Cheng & Yuen (1987) experimentally observed the flow development into a four–vortex solution from a disturbed velocity field. The laminar flow development in a torus was also experimentally studied by Hawthorne (1951), Austin & Seader (1974), Agrawal et al. (1978), Choi et al. (1979), Olson & Snyder (1983), Olson & Snyder (1985) and Bovendeerd et al. (1987).

Austin & Seader (1974) observed experimentally the hydrodynamic entrance length and correlated their results by

$$Lu = \frac{49\pi}{360} Dn^{-2/3} \lambda^{-1/6} \qquad (1-53)$$

where $Lu = s'_{95\%} / (2 \, a \, Re)$ is the hydrodynamic entrance length for the axial

velocity to reach 95% of the fully—developed value.

For a torus with a free—vortex inlet, Singh (1974) observed that for a developing laminar flow, the maximum axial wall shear rate was initially at the inner wall and crossed over to the outer wall at $s' / a = 1.9$, s' is the axial length evaluated from the pipe inlet. For a uniform axial velocity inlet, Singh found that the crossover occurred at a distance half that of a free—vortex inlet flow.

For a uniform axial velocity entry, Yao & Berger (1975) found that the secondary boundary layer separated at the inner wall in the developing region of a torus. They also observed that the hydrodynamic entrance length is proportional to $\sqrt{Dn/\lambda}$.

From boundary layer analysis in the developing region of a toroidal flow, Stewartson et al. (1980) found that the axial inner wall shear stress vanished at $Dn \, s' / (a \, Re) = 0.943$. Based on their analysis, a boundary layer collision theory was conjectured.

Yao & Berger (1988) discovered that the crossover point of the axial shear stress was strongly dependent on the curvature ratio λ and that the crossover point moved downstream as λ was increased.

1.4. Heat Transfer in Helical Pipes

Numerical solutions and experimental studies have been extensively conducted for convective heat transfer in a torus and finite elbows. Representative studies are: Abul—Hamayel & Bell (1979), Akiyama & Cheng (1974), Berg & Bonilla (1950), Dravid et al. (1971), Janssen & Hoogendoom (1978), Kalb & Seader (1972), Kubair & Kuloor (1966), Mori & Nakayama (1965 & 1967), Oliver & Asghar (1976), Owhadi et al. (1968), Patankar et al. (1974), Prusa & Yao (1982), Seban & McLaughlim (1963), Shchukin (1969), Simon et al. (1977), Singh & Bell (1974), Tarbell & Samuels (1973), Yao & Berger (1978) and Zapryanov et al. (1980). A summary of this subject can be found in Manlapaz & Churchill (1981), Nandakumar & Masliyah (1986) and Berger (1991). There are no extensive studies for the case of the heat transfer in helical pipes of finite pitch. Manlapaz & Churchill (1981) attempted to solve the problem for a helical pipe of finite pitch. However, they obtained very limited results. Their correlations of Nu were based on the previous studies of a torus.

Akiyama & Cheng (1971) were the first to numerically study heat transfer in toroidal pipes. They used the boundary vorticity finite difference method to solve the full axially—invariant transport equations subject to the boundary conditions of axially uniform heat flux with peripherally constant temperature. They found that the Nusselt number is a function of the parameter Dn^2Pr alone when $Pr > 1$ and $\lambda \to 0$. $Pr = \mu C_p/k$ is the Prandtl number and C_p is the heat capacity. In a subsequent study, Akiyama & Cheng (1972) presented similar results for the thermal boundary condition of axially and peripherally uniform wall temperature. Akiyama & Cheng's correlation for the Nusselt number with a uniform wall temperature is given by

$$\text{Nu} = \frac{0.987}{q} (1 - 1.48q + 23.2q^2 - 120q^3 + 212q^4) \qquad (1-\text{!}$$

where $\text{Pr} \geq 1$, $q = (Dn^2 Pr)^{-\frac{1}{4}} \leq \frac{1}{3}$ and $\lambda < 0.1$. $\text{Nu} = \frac{2 \, a \, \bar{h}}{k} = \frac{2 \, a \, q'}{k \, (T_w - T_m)}$ is

average Nusselt number. $\bar{h}$ is the peripherally averaged heat transfer coefficient. k

the thermal conductivity. q' is the peripherally averaged heat flux at the pipe w;

T_w and T_m are the wall and the average bulk fluid temperatures, respectively.

Kalb & Seader (1972 & 1974) also studied the same problem for the t

boundary conditions. However, Kalb & Seader did not invoke the loose coili

condition for a torus. Kalb & Seader (1974) correlated the heat transfer Nuss

number for the uniform wall temperature as:

$$\text{Nu} = 0.836 \, Dn^{0.5} \, Pr^{0.1} \qquad (1-\text{!}$$

for $0.01 \leq \lambda \leq 0.1$, $80 < Dn < 1200$ and $0.7 < Pr < 5$.

Dravid et al. (1971) studied both experimentally and numerically lamii

heat transfer in the thermal entrance region of a torus subject to the boundi

condition of axially uniform flux with peripherally uniform wall temperature. Tl

observed an oscillatory variation in wall temperature and Nusselt number. 7

amplitude of the oscillation decreases with the axial distance. An asymptotic va

is reached at low values of Graetz number. Similar oscillatory behavior v

observed by Balejova et al. (1977) in their experimental work using Newtonian a

non—Newtonian fluids. The cyclic variation was observed by Tarbell & Samu

(1973) in their numerical solutions of the thermally developing convective h

transfer starting with a fully—developed flow under axially and peripherally unifo:

wall temperature condition.

Janssen & Hoogendoorn (1978) presented experimental Nusselt numl

development in the laminar developing flow region ($20 < \text{Re} < 4000$) of a torus :

a wide range of Pr ($5 \leq \text{Pr} \leq 500$). They found no significant difference between 1

two thermal boundary conditions, i.e., uniform wall temperature and uniform axial heat flux. They also observed the oscillatory variation in Nusselt number in the entrance region. They were the first to give a bound for the thermal entrance length and it is given by

$$LNu = s'_{85\%} / (2 \ Re \ a) \leq 20 \ Pr^{0.2}/ \ Dn \qquad (1{-}56)$$

where $s'_{85\%}$ is the axial length from the inlet at which the heat transfer Nusselt number reached 85% of the fully—developed value. They found that the thermal entrance length is much shorter than that for a straight pipe. This was the reason that Dravid et al. (1971) suggested that the entrance region for a torus be omitted.

References

Abul–Hamayel M.A. and Bell K.J., "Heat transfer in helically–coiled tubes with laminar flow", ASME Pap. No. 79–WA/HT–11, 1979.

Adler M., "Strömung in gekrümmten Rohren", Z. Angew. Math. Mech., 14, 257–275(1934).

Agrawal Y., Talbot L. and Gong K., "Laser anemometer study of flow development in curved circular pipe", J. Fluid Mech., 85, 497–518(1978).

Akiyama M. and Cheng K.C., "Boundary vorticity method for laminar forced convection heat transfer in curved pipes", Int. J. Heat Mass Transfer, 14, 1659–1675(1971).

Akiyama M. and Cheng K.C., "Laminar forced convection heat transfer in curved pipes with uniform wall temperature", Int. J. Heat Mass Transfer, 15, 1426–1431(1972).

Akiyama M. and Cheng K.C., "Graetz problem in curved pipes with uniform wall heat flux", Appl. Sci. Res., 29, 401–418(1974).

Allen D.N. de G. and Southwell R.V., "Relaxation methods applied to determine the motion in two dimensions of a viscous fluid past a fixed cylinder", Q. J. Mech. Appl. Math., 8, 129(1955).

Arnold D.N., Brezzi F. and Fortin M., "A stable finite element for the Stokes equations", Calcolo, 21, 337–344(1984).

Austin L.R., The development of Viscous Flow within Helical Coils, PhD Thesis, University of Utah, Salt Lake, U.S.A., 1971.

Austin L.R. and Seader J.D., "Entry region for steady viscous flow in coiled circular pipes", AIChE J., 20, 820–822(1974).

Bercovier M., "A family of finite elements with penalisation for the numerical solution of Stokes and Navier–Stokes equations", in Information Processing

77, IFIP, ed. by Gilcrist B., North–Holland Publishing Company, 1977.

Berg R.R. and Bonilla C.F., "Heating of fluids in coils", *Trans. NY Acad. Sci.*, 13, 12–18(1950).

Berger S.A., "Flow and heat transfer in curved pipes and tubes", AIAA 91–0030, 1991.

Bovendeerd P.H.M., Van Steenhoven A.A., Van de Vosse F.N. and Vossers G., "Steady entry flow in a curved pipe", *J. Fluid Mech.*, 177, 233–246(1987).

Brooks A.N. and Hugues T.J.R., "Streamline upwind/Petrov–Galerkin formulations for convection dominated flows with particular emphasis on the incompressible Navier–Stokes equations", *Comp. Meth. Appl. Mech. Eng.* 32, 199–259(1982).

Chadwick R.S., "Slow viscous flow inside a torus——the resistence of small tortuous blood vessels", *Q. Appl. Math.*, 43, 317–323(1985).

Cheng K.C. and Mok S.Y., "Flow visualization studies on secondary flow patterns and centrifugal instability phenomena in curved tubes", in: *Fluid Control Measurement*, Vol. 2, ed. M. Harada, p.756–773, Pergamom, Oxford, 1986.

Cheng K.C. and Yuen F.P., "Flow visualization studies on secondary flow patterns in straight tubes downstream of a 180 deg bend and in isothermally heated horizontal tubes", *J. Heat Transfer*, 109, 49–54(1987).

Choi U.S., Talbot L. and Cornet I., "Experimental study of wall shear rates in the entry region of a curved pipe", *J. Fluid Mech.*, 93, 465–489(1979).

Crouzeix M. and Raviart P.A., "Confirming and non–confirming finite element methods for solving the stationary Stokes equations I.", *RAIRO Anal. Num.*, 7, 33–76(1973).

Daskopoulos P. and Lenhoff A.M., "Flow in curved ducts: bifurcation structure for stationary ducts", *J. Fluid Mech.*, 203, 125–148(1989).

Dean W.R., "Note on the motion of fluid in a curved pipe", *Phil. Mag. J. Sci.*, IV,

208–223(1927).

Dean W.R., "The stream–line motion of fluid in a curved pipe", *Phil. Mag. J. Sci.*, V, 673–695(1928).

De Henau V.D., Raithby G.D. and Thompson B.E., "A total pressure correction for upstream weighted schemes", *Int. J. Numer. Meth. Fluids*, 9, 855–864(1989).

Dennis S.C.R., "Calculation of the steady flow through a curved tube using a new finite–difference method", *J. Fluid Mech.*, 99, 449–467(1980).

Dennis S.C.R. and Ng M., "Dual solutions for steady laminar flow through a curved tube", *Q. J. Mech. Appl. Math.*, 35, 305–324(1982).

Dennis S.C.R. and Riley N., "On the fully developed flow in a curved pipe at large Dean number", *Proc. R. Soc. London*, A434, 473–478(1991).

Dravid A.N., Smith K.A., Merrill E.W. and Brian P.L.T., "Effect on secondary fluid motion of laminar flow heat transfer in helically coiled tubes", *AIChE J.*, 17, 1114–1122(1971).

Eddy E.P., "Stability in numerical solution of initial value problems in partial differential equations", NOLM 10232, Naval Ordnance Laboratory, White Oak, Silver Spring, Maryland, 1949.

Fortin M, "Old and new finite elements for incompressible flows", *Int. J. Num. Meth. Fluids.*, 1, 347–364(1981).

Fortin M. and Fortin A., "Newer and newer elements for incompressible flow", in *Finite Elements in Fluids,*, ed. by Gallagher R.H., Carey G.F., Oden J.T. and Zienkiewicz O.C., John Wiley & Sons Ltd., 1985.

Fortin M. and Thomasset F., "Mixed finite element methods for incompressible flow problems", *J. Comput. Phys.*, 31, 173–215(1979).

Germano M., "On the effect of torsion in a helical pipe flow", *J. Fluid Mech.*, 125, 1–8(1982).

Germano M., "The Dean equations extended to a helical pipe flow", *J. Fluid Mech.*,

203, 289–305(1989).

Girault V. and Raviart P.A., "An analysis of upwind schemes for the Navier–Stokes equations", *SIAM J. Numerical Analysis*, 9(2), 312–333(1982).

Girault V. and Raviart P.A., *Finite Element Methods for Navier–Stokes equations, Theory and Algorithms*, Springer–Verlag, 1986.

Glowinski R., *Numerical Methods for Nonlinear Variational Problems*, Springer–Verlag, 1984.

Hasson D., "Streamline flow resistance in coils", *Res. Corresp.*, 1, s1(1955).

Harlow F.H. and Welsh J.E., "Numerical calculation of time–dependent viscous incompressible flow of fluids with free surface", *Physics of Fluids*, 8, 2182–2189(1965).

Hawthorne W.R., "Secondary circulation in fluid flow", *Proc. R. Soc. London*, A206, 374–387(1951).

Janssen L.A.M. and Hoogendoorn C.J., "Laminar convective heat transfer in helical coiled tubes", *Int. J. Heat Mass Transfer*, 21, 1179–1206(1978).

Jayanti S. and Hewitt G.F., "On the paradox concerning friction factor ratio in laminar flow in coils", *Proc. R. Soc. London*, A432, 291–299(1991).

Johnson C., *Numerical Solution of Partial Differential Equations by the Finite Element Method*, Cambridge University Press, 1987.

Kalb C.E. and Seader J.D., "Heat and Mass transfer phenomena for viscous flow in curved circular tubes", *Int. J. Heat Mass Transfer*, 15, 801–817 and Errata 2680(1972).

Kalb C.E. and Seader J.D., "Fully developed viscous flow, heat transfer in curved circular tubes with uniform wall temperature", *AIChE J*, 20, 340–346(1974).

Kao H.C., "Torsion effect on fully developed flow in a helical pipe flow", *J. Fluid Mech.*, 184, 335–356(1987).

Kubair V. and Kuloor N.R., "Heat transfer to Newtonian fluids in coiled pipes in

laminar flow", *Int. J. Heat Mass Transfer*, 9, 63–75(1966).

Lax P.D. and Richtmyer R.D., "Survey of the stability of linear finite difference equations", *Communications on Pure and Applied Mathematics*, 9, 267–293(1956).

Larrain J. and Bonilia C.F., "Theoretical analysis of pressure drop in the laminar flow of fluid in a coiled pipe", *Trans. Soc. Rheol.*, 14, 135–147(1970).

Leonard B.P., "A survey of finite differences with upwinding for numerical modelling of the incompressible convective diffusion equation", in *Computational Techniques in Transient and Turbulent Flow*, ed. by Taylor C. and Morgan K., Pineridge Press Limited, 1981.

Leonard B.P., "Locally modified QUICK scheme for highly convective 2–D and 3–D flows", in *Numerical Methods in Laminar and Turbulent Flow*, Taylor C., Habashi W.G. and Hafez M.M. ed., Vol. 5, part 1, 35–47(1987).

Liu N.S., "Developing flow in a curved pipe", *INSERM–Euromech 92*, 71, 53–64(1977).

Manlapaz R.L. and Churchill S.W., "Fully developed laminar convection from a helical coil", *Chem. Eng. Commun.*, 9, 185–200(1981).

McConalogue D.J. & Srivastava C.F., "Motion of a fluid in a curved tube", *Proc. Roy. Soc. A.* 307, 37–53(1968).

Mishra P. and Gupta S.N., "Momentum transfer in curved pipes", *Ind. Eng. Chem. Proc. Des. Dev.*, 18, 130–142(1979).

Mori Y. and Nakayama W., "Study on forced convective heat transfer in curved pipes (1st report, laminar region)", *Int. J. Heat Mass Transfer*, 8, 67–82(1965).

Mori Y. and Nakayama W., "Study on forced convective heat transfer in curved pipes (3rd report)", *Int. J. Heat Mass Transfer*, 10, 681–695(1967).

Murata S., Miyake Y., Inaba T. and Ogawa H., "Laminar flow in a helically coiled

pipe", *Bull. JSME*, **24**, 355–62(1981).

Nandakumar K. and Masliyah J.H., "Bifurcation in steady laminar flow through curved tubes", *J. Fluid Mech.*, **119**, 475–490(1982).

Nandakumar K. and Masliyah J.H., "Swirling flow and heat transfer in coiled and twisted pipes", in *Advances in Transport Processes*, vol IV, ed. by Mujumdar A.S. and Mashelkar R.A., Wiley Eastern Ltd., New Delhi, India, 1986.

Neuberger A.W., "Error estimates and convergence acceleration of different discretization schemes", in *Numerical Methods in Laminar and Turbulent Flow*, Taylor C., Habashi W.G. and Hafez M.M. ed., Vol. 5, part 1, 91–101(1987).

O'Brien G.G., Hyman M.A. and Kaplan S., "A study of the numerical solution of partial differential equations", *J. Math. and Phys.*, **29**, 223–251(1950).

Oliver D.R. and Asghar S.M., "Heat transfer to Newtonian and viscoelastic liquids during laminar flow in helical coils", *Trans. Inst. Chem. Eng.*, **54**, 218–24(1976).

Olson D.E. and Snyder B., "The growth of swirl in curved circular pipes", *Physics of Fluids*, **56**, 347–349(1983).

Olson D.E. and Snyder B., "The upstream scale of flow development in curved circular pipes", *J. Fluid Mech.*, **150**, 139–158(1985).

Owhadi A., Bell K.J. and Crain B., Jr., "Forced convection boiling inside helically coiled tubes", *Int. J. Heat Mass Transfer*, **11**, 1779–1793(1968).

Patankar S.V., *Numerical Heat Transfer and Fluid Flow*, Hemisphere Publishing Company, 1980.

Patankar S.V., Pratap V.S. and Spalding D.B., "Prediction of laminar flow and heat transfer in helically coiled pipes", *J. Fluid Mech.*, **62**, 539–551(1974).

Prusa J. and Yao L.S., "Numerical solution of fully–developed flow in heated

curved tubes", *J. Fluid Mech.*, **123**, 503–522(1982).

Raithby G.D. and Torrance K.E., "Upstream weighted differencing schemes and their applications to elliptic problems involving fluid flows", *Computers and Fluids*, **2**, 191–206(1974).

Ramshankar R. and Sreenivasan K.R., "A paradox concerning the extended Stokes series solution for the pressure drop in coiled pipes", *Physics of Fluids*, **31**(6), 1339–1347(1988).

Raviart P.A., "Mixed finite element methods", in *The Mathematical Basis of Finite Element Methods*, ed. by Griffiths D.F., Clarendon Press, Oxford, 1984.

Richtmyer R.D. and Morton K.W., *Difference Methods for Initial–Value Problems*, 2nd ed., Interscience Publishers, J. Wiley and Sons, New York, 1967.

Roache P.J., *Computational Fluid Dynamics*, Hermosa Publishers, Albuquerque, 1985.

Seban R.A. and Mclaughlim E.F., "Heat transfer in tube coils with laminar and turbulent flow", *Int. J. Heat Mass Transfer*, **6**, 387–395(1963).

Shchukin V.K., "Correlation of experimental data on heat transfer in curved pipes", *Therm. Eng.*, **16**, 72–76(1969).

Simon H.A., Chang M.H. and Chow J.C.F., "Heat transfer in curved tubes with pulsatile, fully developed, laminar flows", *J. Heat Transfer*, **99**, 590–595(1977).

Singh M.P., "Entry flow in a curved pipe", *J. Fluid Mech.*, **65**, 517–539(1974).

Singh S.P.N. and Bell K.J., "Laminar flow heat transfer in a helically coiled tube", *Proc. 5th Int. Heat Transfer Conf.*, Tokyo, **2**, 193–197(1974).

Sod G.A., *Numerical Methods in Fluid Dynamics, Initial and Initial Boundary–value Problems*, Cambridge University Press, 1985.

Soh W.Y. and Berger S.A., "Laminar entrance flow in a curved tube", *J. Fluid Mech.*, **148**, 109–135(1984).

Smith F.T., "Fluid flow into a curved pipe", *Proc. R. Soc. London*, *A*351, 71–87(1976).

Stewartson K., Cebeci T. and Chang K.C., "A boundary–layer collision in a curved duct", *Q. J. Mech. Appl. Math.*, **33**, 59–75(1980).

Tarbell J.M. and Samuels M.R., "Momentum and heat transfer in helical coils", *Chem. Eng. J.*, **5**, 117–127(1973).

Taylor C. and Hood P., "A numerical solution of the Navier–Stokes equations using the finite element technique", *Comp. Fluids*, **1**, 73–100(1973).

Temam R., *Navier–Stokes Equations, Theory and Numerical Analysis*, North–Holland Publishing Company, 1979.

Thomasset F., *Implementation of Finite Element Methods for Navier–Stokes Equations*, Springer–Verlag, 1981.

Topakoglu H.C., "Steady laminar flows of an incompressible viscous fluid in curved pipes", *J. Math. Mech.*, **16**(2), 1321–1337(1967).

Truesdell L.C. and Adler R.J., "Numerical treatment of fully developed laminar flow in helically coiled tubes", *AIChE J.*, **16**, 1010–1015(1970).

Tuttle E.R., "Laminar flow in twisted pipes", *J. Fluid Mech.*, **219**, 545–570(1990).

Van de Vosse F.N., *Numerical Analysis of Carotid Artery Flow*, PhD Thesis, University of Technology, Eindhoven, The Netherlands, 1987.

Van de Vosse, Van Steenhoven A.A., Segal A. and Janssen J.D., "A finite element analysis of the steady laminar entrance flow in a 90° curved tube", *International Journal for Numerical Methods in Fluids*, **9**, 275–287(1989).

Van Dyke M., "Extended stokes series: laminar flow through a loosely coiled pipe", *J. Fluid Mech.*, **86**, 129–145(1978).

Van Dyke M., "Creeping flow in a coiled pipe by computer–extended series", in *Yung–huai Kuo Memorial Volume*, ed. by Zheng et al., Science Publishing Co., Beijing, China, p.35, 1990.

Wang C.Y., "On the low—Reynolds—number flow in a helical pipe", *J. Fluid Mech.*, **108**, 185—194(1981).

White C.M., "Streamline flow through curved pipes", *Proc. R. Soc. London*, **A123**, 645—663(1929).

Yanase S., Goto N. and Yamamoto K., "Dual solutions of the flow through a curved tube", *Fluid Dynamics Research*, **5**, 191—201(1989).

Yang Z.H. and Keller H.B., "Multiple laminar flows through curved pipes", *Appl. Num. Math.*, **2**, 251—271(1986).

Yao L.S. and Berger S.A., "Entry flow in a curved pipe", *J. Fluid Mech.*, **67**, 177—196(1975).

Yao L.S. and Berger S.A., "Flow in heated curved pipes", *Journal of Fluid Mechanics*, **88**, 339—354(1978).

Yeung W.S., "Laminar boundary—layer flow near the entry of a curved circular pipe", *J. Appl. Mech.*, **47**, 697—702(1980).

Zapryanov Z., Christov C. and Toshev E., "Fully developed laminar flow and heat transfer in curved tubes", *Int. J. Heat Mass Transfer*, **23**, 873—880(1980).

Zhong Q. and Olson M.D., "Finite element—algebraic closure modeling of turbulent separated flows", in *Numerical Methods in Laminar and Turbulent Flow*, Taylor C., Gresho P., Sani R.L. and Haüser J. ed., Vol. 6, part 1, 473—483(1989).

Chapter 2

The Separation Method

2.0 SUMMARY

A first order non—conforming numerical method, SEPARATION METHOD, for fluid flow problems with a 3—point exponential interpolation scheme has been developed. The flow problem is decoupled into multiple one—dimensional subproblems and assembled to form the solution. A fully staggered grid and a conservational domain centered at the node of interest make the decoupling scheme first order accurate. The discretization of each one—dimensional subproblem is based on a 3—point interpolation function and a conservational domain centered at the node of interest. The proposed scheme gives a guaranteed first order accuracy. It is shown that the traditional upwind (or exponentially weighted upstream) scheme is actually of zeroth order accuracy. The pressure is decoupled from the velocity field using the pressure correction method of SIMPLE. Thomas algorithm (tri—diagonal solver) is used to solve the algebraic equations iteratively. In addition, a 2—dimensional direct solver has been developed based on block matrix inversion to tackle the difficulty that may arise from the perturbation of the pressure. The 2—dimensional solver uses less memory storage than the band solvers and the component matrices are inverted to allow fast solutions. The numerical advantage of the proposed scheme is tested for laminar fluid flows in a torus and in a square driven cavity. Both two and four vortices solutions for a torus are computed to show the convergence of the proposed scheme. The convergence rates are compared with the traditional schemes for the square driven cavity problem. Good behavior of the proposed scheme is ascertained.

2.1. INTRODUCTION

The numerical study of fluid flow through direct formulations, i.e. primitive variable approach, needs special attention. Great strides have been made in the past two decades. All the methodologies, e.g., finite element, finite difference and finite volume, gave rise to new issues to be studied. Some of the issues are: the inf–sup condition of the finite element method (Babuška 1973, Brezzi 1974, Ladyzhenskaya 1969), the checkerboard effect of the finite difference method (Patankar 1980), the Petrov–Galerkin or streamline weighted scheme (Carey & Oden 1986) and the upwind differencing scheme (Raithby & Torrance 1974). However, any practical scheme must use at least a partially direct algebraic equations solution strategy in order to obtain a meaningful solution. This largely restricted the development of numerical schemes, especially for three dimensional problems, where the full storage of the coefficient matrices is sometimes beyond the reach of computer memory required by a direct solver. In this regard, the pressure distribution cannot be easily solved as it appears in the momentum equations. This gave the formation of the pressure correction method of Patankar (1980).

It is well known that a convergent numerical scheme must be both consistent and stable. The consistency is defined as the limit behavior of the discrete equations used in a numerical scheme to approach the governing differential equation as the mesh size approaches zero. The stability of a numerical scheme is related to the solution behavior of the discrete equations. When an iterative method is used, an unstable scheme may have difficulty in generating solution.

This study intends to develop a scheme which is spurious modes free and stable. Our attention on the stability will be directed to an accurate representation of the flow behavior (wiggle–free) rather than the ability to obtain a solution alone. The strategy of the scheme is focused on making a complex problem easy to deal

with. At each step, the flow problem is subdivided into multi—subproblems an best possible choice is used to obtain convergence.

The pressure field is solved with the pressure correction method due Patankar (1980) to avoid the painstaking solution of the standard finite elem approach. The popular finite difference and finite volume schemes suffer fr spurious pressure modes. For higher Reynolds number flows, even the solution of pressure correction equation is not an easy job (Macharthur & Patankar 19 without a carefully chosen solution algorithm. This will be fully addressed here. separating the multi—dimensional dependence into multi—subproblems ; introducing some extrapolation or first order accuracy—guaranteed exponen interpolation, we eliminate the stability problem of a traditional centered sche and simplify the solution procedure without sacrificing too much in accuracy. Ow to the strategy of the method, we call it the Separation Method.

To obtain a meaningful solution, we decided to give up the conform property. Instead, the scheme is checked against consistency. It should be no that a conforming scheme yields a globally consistent interpolation for the varial under consideration. Hence, the variable under consideration at a given point only one unique interpolation equation no matter to how and/or from where refers the value at that point. The conforming methods pay full attention to consistency in the interpolation of the variables and their fluxes. However t introduce excessive errors when the flow Reynolds number is large. We work froi different perspective which leads to a good local behavior and a better glc solution. A three—point interpolation scheme is introduced in this study. accommodate the three—point interpolation scheme a conservational domain is us

The following two sections serve as a general guideline for the propo scheme. More details are given in the first numerical example.

2.2. DOMAIN DISCRETIZATION AND NODAL ARRANGEMENTS

Our primary goal here is to establish a centered conservational scheme and to use fully staggered grid (Harlow & Welch 1965) to maintain both simplicity and inf—sup condition requirement. For a relatively simple geometry, we discretize the domain into a relatively uniform mesh where the mesh lines are parallel to the coordinate lines, i.e., undistorted mesh. The non—equal spacing does not need a mapping. However, a centered conservational scheme can be obtained by simply placing the node of interest in the center of the symmetrically chosen domain even though the actual nodes are not symmetrical with the coordinate axes. We make the undistorted non—uniform mesh as the general case for discussion in this study.

The numbering of the nodes is based on an appropriate book—keeping. A good choice of node numbering can be expressed as follows. First, identify the three curvilinear directions and secondly, number each direction independently, and record the nodes by a three indexed (i, j, k) tensor related to the three curvilinear directions. In this way no special attention is needed to keep tracking the neighboring nodes.

The exact conservational domain for each node on or near a boundary, however, will be considered in the light of the specified boundary condition in order to avoid the introduction of error by requiring values outside the computational domain. If Dirichlet condition is specified. the nodes next to the boundary will have a conservational domain bounded by the boundary. For a Neumann boundary, a node on the boundary will have a symmetrically extrapolated conservational domain. The above treatment of boundaries can achieve consistency and avoid the non—consistent accuracy match for finite difference and for finite volume methods.

To fully address the arrangement of nodes for the different primitive variables, we establish the following convention: when the direction of the velocity

component of interest (the center nodal variable) coincides with a given coordinate axis, we denote that direction as the parallel direction, while all other directions become perpendicular directions. We name the parallel velocity as the velocity of the coincident axis, while the perpendicular velocity stands for the velocity that is not in the direction of the axis. This convention will be very convenient as we deal with the axes one at a time.

The inf—sup condition can be represented as follows:

$$\exists \quad \inf_{\substack{a>0 \\ q \in Q}} \quad \sup_{\tilde{u} \in V} \quad \frac{-\int_Q \nabla \cdot \tilde{u} \; q}{\|\tilde{u}\|_V \|q\|_Q} \geq \alpha \tag{2-1}$$

Where α is a positive number independent of the mesh size. $\tilde{u}$ is the velocity field. V is the functional space of $\tilde{u}$ and q is a variable taking its value from the functional space of the pressure, Q.

It is known that equation (2—1) can be satisfied by a proper choice of (match between) V and Q. It is independent of the choice of coordinate system. Equation (2—1) can be satisfied by arranging the velocity and pressure nodes in the following manner:

As shown in Figure 2.1, the pressure nodes are located only on the parallel direction (in one element), exactly at the center of two adjacent velocity nodes. In other words, when the continuity equation is treated (pressure is the variable of interest), all the velocity components are presented symmetrically on the nodal axis away from the center, and only the parallel velocity is present on each axis.
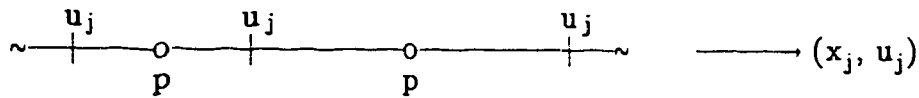
Fig. 2.1.   Pressure nodes placement.

2.3. FORMAL DISCRETIZATION

To carry out the discretization of the flow equation, the problem of interest must be initially written either in an orthogonal coordinate or a non—orthogonal coordinate system prior to domain discretization. For a steady flow problem, the Navier—Stokes equation, in a cartesian coordinate system for a given x_i direction, is given by

$$\sum_j \frac{\partial}{\partial x_j}(p\delta_{ij} + \rho u_i u_j - \mu \frac{\partial u_i}{\partial x_j}) = 0 \qquad (2\text{--}2)$$

where x_j is the cartesian coordinate, p is the pressure and u_i is the velocity field.

The governing equations can be rewritten in the weak form with an added weighting function. The weak form governing equation is:

$$\frac{1}{V_e}\iiint_{\Omega_e} \sum_j \frac{\partial}{\partial x_j}(p\delta_{ij} + \rho u_i u_j - \mu \frac{\partial u_i}{\partial x_j}) \, w_i \, dv = 0 \qquad (2\text{--}3)$$

where V_e is the volume of the conservation domain and w_i is a weighting function. We take w_i as

$$w_i \in \{w_i = 1 \text{ if } x \in \text{conservational domain}; \quad w_i = 0 \text{ for all other cases}\}$$

The multi—dimensionality of equation (2–3) is the most significant obstacle in developing a good numerical scheme. To achieve a good behavior, one dimensional problems are easy to deal with and better understood. To tackle the multi—dimensionality, we introduce an approximation strategy that allows us to separate the multi—dimensional problem into multiple one—dimensional subproblems. Since the node of interest is at the center of the conservational domain, we can quadratically approximate the integration over a dimension using the center value when a derivative is not involved in that dimension. Hence,

equation (2–3) can be decoupled further to reduce the multi–dimensional problem into multiple pseudo–one–dimensional problems. Before the decoupling is performed, the governing equation is regrouped in the following manner:

$$\sum_j E_{ij} = -\frac{1}{V_e} \iiint\limits_{\Omega_e} w_i \frac{\partial p}{\partial x_i} \, dv \tag{2-4a}$$

$$E_{ij} = \frac{1}{V_e} \iiint\limits_{\Omega_e} w_i \frac{\partial}{\partial x_j}(\rho u_i u_j - \mu \frac{\partial u_i}{\partial x_j}) \, dv \tag{2-4b}$$

The decoupling of the multi–dimensional problem is achieved by approximating equation (2–4b) by

$$E_{ij} \simeq \frac{1}{\ell_e} \int w_i \frac{\partial}{\partial x_j}(\rho u_i u_j - \mu \frac{\partial u_i}{\partial x_j}) \, d\ell \tag{2-4c}$$

where ℓ_e is the length of the conservational domain in the x_i direction. E_{ij} is the x_j–component of the x_i–momentum. Equations (2–4a) and (2–4b) are a multiple dimensional problem. After using the approximation to the integration over the dimensions of x_k's (k ≠ j) by the center nodal value, the multiple integration in equation (2–4b) is approximated by a single integration as shown by equation (2–4c), which represents a one–dimensional problem. This leads us to consider one dimensional discretization only and the resulting discrete equation coefficient (stiffness) matrix consists of only the node of interest and its two neighbors. This approximation of equation (2–4b) by (2–4c) is a key element of the method presented in this Chapter.

For example, the weak form of the two–dimensional Navier–Stokes equation is given by

$$\left\{ \begin{array}{l} \dfrac{1}{A_e} \displaystyle\iint_{xy} w_x \left[\rho \frac{\partial p}{\partial x} + \frac{\partial}{\partial x}(\rho u_x u_x - \mu \frac{\partial u_x}{\partial x}) + \frac{\partial}{\partial y}(\rho u_x u_y - \mu \frac{\partial u_x}{\partial y})\right] dx\ dy = 0 \\[4ex] \dfrac{1}{A_e} \displaystyle\iint_{xy} w_y \left[\rho \frac{\partial p}{\partial y} + \frac{\partial}{\partial x}(\rho u_x u_y - \mu \frac{\partial u_y}{\partial x}) + \frac{\partial}{\partial y}(\rho u_y u_y - \mu \frac{\partial u_y}{\partial y})\right] dx\ dy = 0 \end{array} \right.$$

$$(2\text{--}5a)$$

The separation of space variables for the x–momentum equation is given by

$$E_{xx} + E_{xy} = - \iint_{xy} \frac{w_x}{A_e} \frac{\partial p}{\partial x}\ dx\ dy \qquad (2\text{--}5b)$$

and the momentum components are defined by

$$E_{xx} = \frac{1}{A_e} \iint_{xy} w_x \frac{\partial}{\partial x}(\rho u_x u_x - \mu \frac{\partial u_x}{\partial x})\ dxdy \qquad (2\text{--}5c)$$

$$E_{xy} = \frac{1}{A_e} \iint_{xy} w_y \frac{\partial}{\partial y}(\rho u_y u_x - \mu \frac{\partial u_x}{\partial y})\ dxdy \qquad (2\text{--}5d)$$

E_{xx} and E_{xy} are approximated, respectively, by

$$E_{xx} \simeq \frac{1}{\Delta x} \int_x w_x \frac{\partial}{\partial x}(\rho u_x u_x - \mu \frac{\partial u_x}{\partial x})\ dx \qquad (2\text{--}5e)$$

$$E_{xy} \simeq \frac{1}{\Delta y} \int_y w_x \frac{\partial}{\partial y}(\rho u_y u_x - \mu \frac{\partial u_x}{\partial y})\ dy \qquad (2\text{--}5f)$$

where $A_e = \Delta x\ \Delta y$, Δx and Δy are the widths of the conservational domain in x and y directions, respectively. Equations (2–5e) and (2–5f) are one–dimensional problems if E_{xx} and E_{xy} are regarded as source terms.

The quadratic interpolation function in a non–uniform one dimensional grid can be written as follows:

$$\phi = \phi_i + \frac{(\phi_{i+1}-\phi_i)(h_1+x)h_1 - (\phi_{i-1}-\phi_i)(h_2-x)h_2}{h_1 h_2(h_1 + h_2)} x \qquad (2-6)$$

where h_1 and h_2 are the two grid spacings of the node of interest. A brief illustration of a one dimensional nodal arrangement is shown in Figure 2.2.
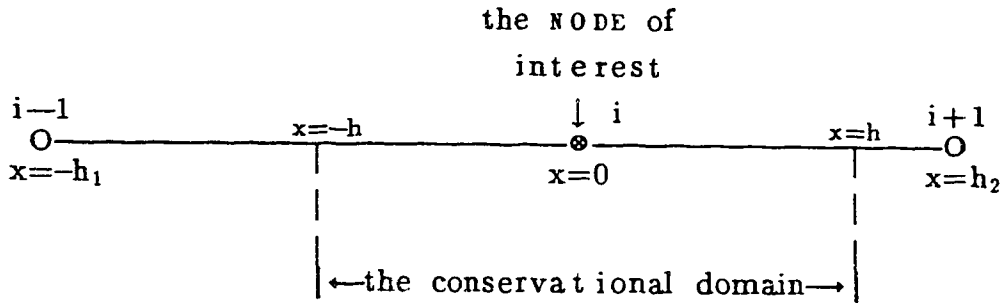
Fig. 2.2. Nodal arrangement for a non—uniform one dimensional mesh.

The space variable x has its origin at the node of interest. The radius of the conservational domain is h.

The discretization of a one dimensional problem is simple to handle and to enforce stability. The general conservational domain can be described as follows:

1. For the perpendicular direction, as shown in Figure 2.3, we use the intersection with the corresponding perpendicular mesh lines of the parallel velocity as the conservational domain boundary.
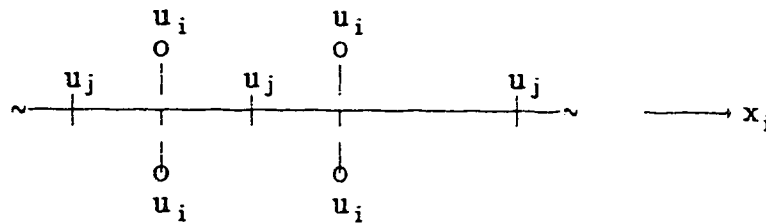
Fig. 2.3. Conservational domain setup in a perpendicular direction.

2. For the parallel direction, however, the conservational domain can be arbitrary. A viable choice would be using the half length of the shorter side as the conservational radius. An illustration of this situation is shown in Figure 2.2, where the variable of interest is u_j and the space variable x is actually x_j.

3. If the node of interest is on the perpendicular direction and next to a Dirichlet boundary (no–slip or known entrance–exit), we can choose the side length towards the boundary as the radius of the conservational domain. This is shown in Figure 2.4.
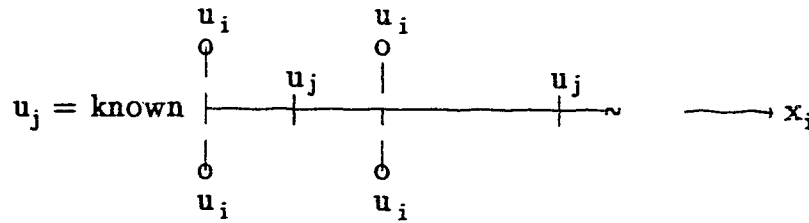
Fig. 2.4. Conservational domain setup next to a Dirichlet boundary for a perpendicular direction.

Equation (2–4c) is treated using an appropriate interpolation function based on the three available nodes, such as equation (2–6). Special attention, however, will be given to the advection dominated subproblems. Since no simple normal mode exists (although Patankar 1980 claimed to be exact) and the quadratic interpolation, equation (2–6), cannot be used, we employ the following type 3–point exponential interpolation

$$\phi = \phi_i + a_i e^{Re u_i x} + b_i x \qquad (2–7)$$

where ϕ is the velocity of interest and u_i is the parallel velocity of the x direction evaluated at the center of the conservational domain or the node of interest, i.

Leonard (1987) proposed a 3–point exponential scheme and it has the following form:

$$\phi' = \phi_i + a_i'[\exp(b_i'x) - 1] \tag{2-8}$$

However, equation (2–8) is rather difficult to work with and it leads to unstable solutions when advection is dominant (Leonard 1987).

Corresponding to equation (2–7), the interpolation function can be obtained using the three available nodes as

$$\phi = \phi_i + \frac{h_1(e^{ReU_i x} - 1) + x\,(e^{-ReU_i h_1} - 1)}{h_1(e^{ReU_i h_2} - 1) + h_2(e^{-ReU_i h_1} - 1)}(\phi_{i+1} - \phi_i) +$$

$$\frac{h_2(e^{-ReU_i x} - 1) - x\,(e^{ReU_i h_2} - 1)}{h_1(e^{ReU_i h_2} - 1) + h_2(e^{-ReU_i h_1} - 1)}(\phi_{i-1} - \phi_i) \tag{2-9}$$

The interpolation equation (2–9) reduces to a standard upwind scheme (but not the traditional one) for $Re \cdot u_i \to +$ or $- \infty$ with the sign taken to be the same as that of u_i in the above equation. It can be shown that when $Re \cdot u_i \to 0$, equation (2–9) reduces to the quadratic interpolation equation (2–6). For a simple upwind scheme, we can combine the quadratic interpolation equation (2–6) by setting the off–diagonal terms to be no greater than zero in the resulting stiffness matrices. By doing so, we can dampen the oscillations while not altering the solution. It is worth to mention that a traditional centered treatment of the right hand side of equation (2–4b) for the stiffness matrix does not lead to absolute divergence As a matter of fact, it can be solved quite successfully with careful arrangements (Nandakumar et al. 1985).

It is clear that the above strategy results in a quadratic accuracy for a small flow Reynolds number flow, i.e., $\phi = \phi_0 + a\,x + b\,x^2 + O(x^3)$, and linear accuracy

for a large Reynolds number flow, i.e., $\phi = \phi_0 + a\,x + O(x^2)$. It should be noted that for the latter case, an ordinary upwind / exponentially weighted implementation gives only zeroth order accuracy, i.e., $\phi = \phi_0 + O(x)$, in the interpolation.

An interesting by–product of this 3–point exponential implementation is that we are able to produce an accuracy equivalent to a total pressure corrected exponentially weighted scheme of De Henau et al. (1989), while treating a problem in a multi–dimensional situation. The complexity of the proposed scheme is not more than the original concepts advanced by Raithby & Torrance (1974) and Patankar (1980).

The discrete momentum equation can be obtained for an undistorted mesh as

$$
\begin{aligned}
&\phi IJK_{ijk}\ \phi_{ijk} + \phi MJK_{ijk}\ \phi_{i-1jk} + \phi PJK_{ijk}\ \phi_{i+1jk} + \phi IMK_{ijk}\ \phi_{ij-1k} + \\
&\phi IPK_{ijk}\ \phi_{ij+1k} + \phi IJM_{ijk}\ \phi_{ijk-1} + \phi IJP_{ijk}\ \phi_{ijk+1} \\
&= - C\phi_{ijk}\ (p_\beta - p_{\beta-1}) + B\phi_{ijk}
\end{aligned}
\tag{2-10}
$$

where ϕ_{ijk} stands for any velocity component at the node (i, j, k). ϕIJK, ϕMJK, ϕPJK, ϕIMK, ϕIPK, ϕIJM, ϕIJP, $C\phi$ and $B\phi$ are coefficients. (i, j, k) is the global index for the node of interest. β is the global index of the parallel direction with all the perpendicular directional indices fixed. For example for the velocity component in the direction of i, i.e., $\phi = u_i$, the pressure term $(p_\beta - p_{\beta-1})$ is equivalent to $(p_{i-1jk} - p_{i-1jk})$. The pressure p has been treated linearly in order to satisfy the inf–sup condition. The formulation as described above renders the coefficients to be similar to that of a 7–point stencil. With the present nodal arrangement, the required interpolations for the variables that are not currently under consideration can be made linearly. Best of all, a given interpolation involves only two points and no extrapolation is used. For example, the coefficient of the pressure gradient term is,

$$C\phi_{ijk} = \frac{1}{x_\beta - x_{\beta-1}} \qquad (2-11)$$

where x_β is the coordinate location with x being of the parallel direction of the variable of interest.

It is important to note that, for the boundary, the treatment must be consistent with the interior domain and the boundary condition over—specification must be avoided. To summarize, we list the treatment of the boundary as follows:

1. Only when the gradient is known can one use a symmetrically extrapolated grid outside of the domain of interest. Under no other circumstances should one use a grid point outside the domain of interest.

2. For a Dirichlet velocity boundary condition, all the velocity components must have a grid point on the boundary. However, the pressure node is not necessarily placed on the boundary. As a matter of fact, only the interior nodes for the pressure are present in this scheme for a Dirichlet velocity boundary.

3. In case where the velocity gradient is known on a boundary, the pressure node can be placed on the boundary, however, the normal velocity component should not be placed on the boundary.

4. The pressure node must be present on the pressure known boundary, where the normal velocity is not present. Here we should point out that the boundary condition for the normal velocity component should not be imposed when the pressure is known on the boundary. Instead, one must use a deduced boundary condition (gradient type) from the continuity equation to fulfill both the boundary condition requirement of the momentum equation and the continuity equation.

Finally, to solve the discretized equations, we introduce some under—relaxation F_ϕ, where

$$(1+F_\phi) \; \phi IJK_{ijk} \; \phi_{ijk} + \phi MJK_{ijk} \; \phi_{i-1jk} + \phi PJK_{ijk} \; \phi_{i+1jk} + \phi IMK_{ijk} \; \phi_{ij-1k} +$$

$$\phi IPK_{ijk} \; \phi_{ij+1k} + \phi IJM_{ijk} \; \phi_{ijk-1} + \phi IJP_{ijk} \; \phi_{ijk+1}$$

$$= F_\phi \cdot \phi IJK_{ijk} \; \phi^0_{ijk} - C\phi_{ijk} \; (p_\beta - p_{\beta-1}) + B\phi_{ijk} \qquad\qquad (2\text{--}12)$$

ϕ^0_{ijk} is the currently available value of ϕ_{ijk}. The formed matrix structure is a 7—point difference module.

Owing to the complexity of flow problems, the above treatise is merely a guideline for the proposed scheme. A more detailed discretization can be found in the first numerical example.

2.4. ACCURACY AND CONVERGENCE

The accuracy of a numerical scheme depends on the order of interpolation scheme used and the consistency of the discretization. Since all the non—derivative terms of the direction under consideration are evaluated at the center node, the integration is quadratic. The consistency is then of only first order for the weak form of the Navier—Stokes equation, i.e., equation (2–3). Hence, the accuracy for the advective (nonlinear) term is linear. Based on past experience, a higher order approximation could lead to instability (most likely to have oscillation) (Leonard 1987, Neuberger 1987). On the other hand, a lower order approximation, although may be stable, gives a lower overall accuracy.

The accuracy of the current scheme is to be discussed relatively to the existing popular upwind / exponentially weighted schemes. Let us first examine the upwind scheme and the exponential scheme of Raithby & Torrance (1974), which was claimed to be exact by Patankar (1980). For simplicity, we consider a one dimensional analogy and assume an advection dominated flow:

The interpolation formula due to Raithby & Torrance (1974) is given by

$$u = u_i + [a_i \exp(Reu^+x) - a_i \exp(Reu^+x_i) +] \; O(x) \tag{12}$$

with $x_i < x < x_{i+1}$ and $a_i = f(u_i, u_{i+1})$ being a constant.

The consistency for the advective term becomes

$$\frac{duu}{dx} \sim \frac{u^+ \, u_i - u^- \, u_{i-1}}{2h}$$

$$= \frac{(u_i + u_{i+1})u_i - (u_{i-1} + u_i)u_{i-1}}{4h}$$

$$= \frac{(u + \frac{du}{dx}h + \frac{d^2u}{dx^2}h^2)u - 2(u - \frac{du}{dx}h + \frac{d^2u}{dx^2}h^2)(\frac{u}{2} - \frac{du}{dx}h + \frac{d^2u}{dx^2}h^2)}{4h} + \cdots$$

$$= \frac{d \; uu}{dx} - \left[\frac{d^2u}{dx^2}u + (\frac{du}{dx})^2\right]h + O(h^2) \tag{2-14}$$

Where h is the radius of the conservational domain, i.e. $h = \Delta x/2$, $u^+ = u_{i+\frac{1}{2}}$ and $u^- = u_{i-\frac{1}{2}}$. All the treatments above are traditional except that Taylor expansion is introduced here to examine the consistency.

The advective term appears to be of a first order consistency if one does not look at the details of the contents in the square bracket of the equation (2–14). It is, however, obvious to note that, if

$$u = \alpha + \beta x \tag{2-15}$$

neither the interpolation, equation (2–13), nor the consistency, equation (2–14), can satisfy equation (2–15). Hence the scheme is actually of only constant convergence, or based on the appearance one may call it a pseudo–first order convergent scheme. The scheme is likely to experience large error in the boundary layers having sharp gradients due to the large amount of the numerical dispersion that is evident in the

equation (2–14). However, we are aware that it is customary to call the traditional upwind / exponentially weighted schemes as being first order.

A reduction in the numerical dispersion present in the 2–point schemes (traditional upwind / exponentially weighted schemes) could be achieved by introducing the same interpolation scheme for both the variable of interest and the parallel velocity u_j.

The proposed scheme described here has the interpolation formulae

$$\phi_I = \phi_i + a_i \exp(\text{Reu}_i x_I) + b_i x_I + O(x_I^2) \tag{2–16}$$

with $x_{i-1} - x_i \leq x_I \leq x_{i+1} - x_i$ and a_i and b_i being constant.

The consistency is given by

$$\frac{du\phi}{dx} \sim \frac{u^+(3\phi_i - \phi_{i-1}) - u^-(\phi_{i-1} + \phi_i)}{4h}$$

$$= \frac{u^+(\phi + \frac{d\phi}{dx}h - \frac{d^2\phi}{dx^2}h^2) - u^-(\phi - \frac{d\phi}{dx}h + \frac{d^2\phi}{dx^2}h^2)}{2h} + \cdots$$

$$= \frac{d\ u\phi}{dx} - u\frac{d^2\phi}{dx^2}h + O(h^2) \tag{2–17}$$

The above consistency equation (2–17) not only looks like but it is indeed first order convergent where only the higher order derivative (second order being the lowest) is contained in the leading truncated term. It is easy to verify that equation (2–15) can be exactly satisfied. The current scheme gives the same order of accuracy as the traditional upwind or exponential scheme would give for a constant coefficient linear equation. To distinguish from the customary convention of calling the 2–point schemes first order, the current scheme may be regarded as a second order scheme. However, we still consider the proposed scheme first order.

By forcing the off–diagonal terms in the stiffness matrices (or difference

molecule) not to be larger than zero, this scheme has guaranteed stability optimum convergence. The interpolation and consistency evaluation are accurat to the second order derivative of the variable of interest. Although a r sophisticated upwind scheme can reduce the numerical dissipation, it is more t likely that this would introduce the symptom of an unstable scheme, an oscilla alien to the exact solution behavior (Neuberger 1987). A quadratic or higher o scheme for the advective terms alone does not improve the accuracy drasticall; quadratic scheme will have to make use of at least full 27 nodes and hence it add complexity.

It should be noted that a conforming scheme for this particular setup can at most two—point interpolation functions. For a multi—dimensional problem, use of a two—point interpolation function does not yield a conforming scheme. ' is a limitation of existing finite volume and control volume methods.

2.5. PRESSURE ITERATION

The solution strategy of the pressure is that of the pressure correc method (Patankar 1980). By perturbing the pressure field, the resulting chang velocities is obtained simply by using Gauss—Seidel iteration. The new pertu velocity field is then applied to satisfy the continuity. By forcing the contir equation to be satisfied, we are able to solve for the appropriate pres perturbation. This procedure can be illustrated as follows:

$$\Delta\phi = \frac{1}{\phi IJK} \cdot \frac{\partial \Delta p}{\partial x} = \frac{C\phi}{\phi IJK} (\Delta p_\beta - \Delta p_{\beta-1})$$

$$\nabla \cdot (u + \Delta u) = 0$$

$$\nabla_d^2 (\Delta p) = - \nabla \cdot u$$

where Δ denote the perturbation i.e. a numeric difference and ∇_d^2 is the discrete Laplacian.

Since the pressure is corrected (perturbed) through the enforcement of the continuity equation and the velocity field is solved by satisfying the momentum equations, the order of the approximation on the velocity and the pressure must be fixed such that the scheme is stable and spurious mode free. It is well known that schemes which are at least slightly more accurate in velocity interpolation than in pressure interpolation can give rise to a stable approximation, Arnold et. al., 1984 [1]. In view of the type of approximation we use here, a quadratic approximation of velocity and linear pressure would give a stable scheme. The proof of satisfying the inf—sup condition is extremely difficult for a staggered grid. Our intention is simply to approach the condition. By placing the pressure node of interest exactly in the symmetric position with the velocity nodes surrounding it, one can ensure that the continuity is second order accurate in velocity. In the case of a non—uniform grid, a velocity element has two asymmetric pressure nodes. The pressure approximation is linear. For the case of a uniform grid, even though the pressure approximation is second order, past experience tells us that such a setup does converge. And above all, the checker board effect is eliminated by the staggering.

After the justification of the pressure—velocity approximation, we can now discuss the practical part of the scheme, which is the solution for the pressure. Owing to the behavior of the Gauss—Seidel iteration, the pressure equation itself needs special attention. If storage permitting, a direct solver is advised. In some cases, the initial guess is not good and we have to combine a direct solver with an iterative solver since the round—off error could destroy the convergence at the initial stage of the iteration. To ease the storage requirement of a direct solver, we have developed a 2—dimensional 5—point direct solver based on block matrix inversion without any pivoting The solution found by the direct solver is then used as the

initial guess for the sweeping (iterative) solver combined with a tri–diagonal algorithm.

Finally, we must apply some under relaxation when perturbing the pressure. We have been successful in using self–adjusting relaxation factor in correcting the pressure. The relaxation factor range is different from problem to problem. In general, a more complex problem is likely to require a smaller relaxation factor. The relaxation factor in the pressure perturbation equation is, however, different from that in the velocity field evaluation. Since the initial value (before perturbation) of the pressure perturbation is uniformly zero, the relaxation factor is introduced in the following way:

$$PIJK_{ijk} \, \Delta p_{ijk} + PMJK_{ijk} \, \Delta p_{i-1jk} + PPJK_{ijk} \, \Delta p_{i+1jk} +$$

$$PIMK_{ijk} \, \Delta p_{ij-1k} + PIPK_{ijk} \, \Delta p_{ij+1k} + PIJM_{ijk} \, \Delta p_{ijk-1} + PIJP_{ijk} \, \Delta p_{ijk+1}$$

$$= - F_p \cdot (\nabla \cdot u)_{ijk} \tag{2–21}$$

Equation (2–21) can also be written as:

$$K \cdot \Delta p = F_p \cdot PRH$$

where the pressure perturbation equation is arranged in the same manner as that for the momentum equations. PIJK is a coefficient of the same type as that of ϕIJK, the notation is the same as that of equation (2–10).

In the formulation above, we have directly linked the SIMPLEc and SIMPLE in the pressure iteration. Our approach towards the pressure correction is close to that of SIMPLEc.

2.6. NUMERICAL PROCEDURE

An important step for a numerical method is the execution of the solution procedure of the discretized equations. This is a most time/space consuming step. We adopt an approach that requires minimum storage while using as much direct solution strategy as possible. The solution procedure is summarized as follows:

1. Initialize the velocity and pressure fields.

2. Discretize the domain as described in the domain discretization section.

3. Establish the matrices for the x_1 — momentum equation while keeping all the other components and coefficients unchanged as described in the formal discretization section.

4. Solve the discretized equations through sweeping direction with a tri—diagonal solver and update the velocity component for the purpose of the pressure correction (step 6).

5. Repeat 1~3 but for the x_2 and x_3 — velocity components.

6. Calculate the perturbation of pressure and update the pressure if the continuity is not satisfied.

7. Repeat 2~6 for a given number of inner loop iterations or until a certain criteria is met. Updating the velocity field.

8. Repeat 7 until the continuity is satisfied up to a preset tolerance at the first inner loop iteration.

9. Interpolate to obtain the desired values. Store the results and stop.

The inner loop (step 7) is necessary in order to separate the nonlinearity from velocity—pressure coupling, especially when the Reynolds number is high and the initial guess is poor. If storage permitting, store the coefficient matrices and step 7 becomes a repetition of step 4 to step 6.

2.7. SOME COMMENTS ON PRESSURE PERTURBATION AND 2–D SOLVER

The pressure correction equation needs more care than the momentum equations. If the initial guess is smooth in error, the sweeping among three dimensions with Thomas algorithm can fit the solution strategy quite well. If the initial guess is poor, a direct solver becomes essential. Without using a direct solver, even using the sweeping strategy may require hundreds of sweeps while still leaving a marginal error. In some cases, it is even very difficult to have the error under control.

When a good initial guess of the velocity field can be found and used, the pressure perturbation alone may not be the best approach (Patankar 1980). A Gauss–Seidel iterated velocity (pseudo–velocity field) can be used in the continuity equation of the pressure correction equation so that the pressure can be solved exactly from the given velocity field through the pressure correction equation (now denoted as the pressure equation). In this case, a direct solver is a must.

To this end, we developed a two–dimensional five–point direct solver based block matrices inversion. The full stiffness matrix is written in view of one direction, say, i (index notation) with m grid points as follows.

$$K = \begin{bmatrix} A_1 & \beta_1 & 0 & ... & 0 \\ \alpha_2 & A_2 & \beta_2 & ... & 0 \\ . & ... & ... & ... & . \\ 0 & 0 & 0 & ... & A_m \end{bmatrix}$$

(2.22)

where, α_i and β_i's are vectors containing the off–diagonal terms (lower and upper hand coefficients) in i–direction. A_i's are the block matrices (again tri–diagonal, but with only scalar quantities) of n×n, with n being the mesh points of the j–direction. A_i's are first inverted, so that the overall storage required is

$m \times n^2$. The inversion of A_i's is performed one at a time starting with A_1. A_1 is inverted as A_1 is appeared alone. When inverting A_i ($i \neq 1$), the inverted A_{i-1}, i.e., A_{i-1}^{-1}, must be used first to complete the forward elimination of the global matrix K, that is, $A_i^{-1} = (A_i - \alpha_i \beta_{i-1} A_{i-1}^{-1})^{-1}$. After inversion, A_i's become, in general, full matrices of $n \times n$. This solution strategy not only requires less storage than the band solver, but is more economic as well. Since the pressure equation is solved intensively, an efficient inversion of the matrix becomes essential.

When solving the pressure correction equation, the direct solver is employed first to obtain a globally smooth solution. This solution is then used as the initial guess to the sweeping algorithm. The sweeping algorithm is used to smooth the round—off errors and reduce the global error. The pressure equation or pressure correction equation solved in this manner will not have any difficulty in keeping the convergence under control.

2.8. NUMERICAL EXAMPLE 1.

Laminar flow in curved (toroidal) pipes

A numerical flow problem will be solved to demonstrate the use of the proposed numerical scheme. In our group, the problem of laminar fluid flow in helical ducts has been solved with a zero pitch i.e., a torus (Masliyah & Nandakumar 1979, Nandakumar & Masliyah 1982, Sankar et al. 1988). We shall treat this flow problem once again using the proposed numerical scheme.

The laminar fluid flow will be that of a developing Newtonian fluid in a torus having a circular cross section. The momentum equations are parabolized in the axial flow direction. A sketch of the coordinate set-up and the parameter scaling is shown in Figure 2.5.
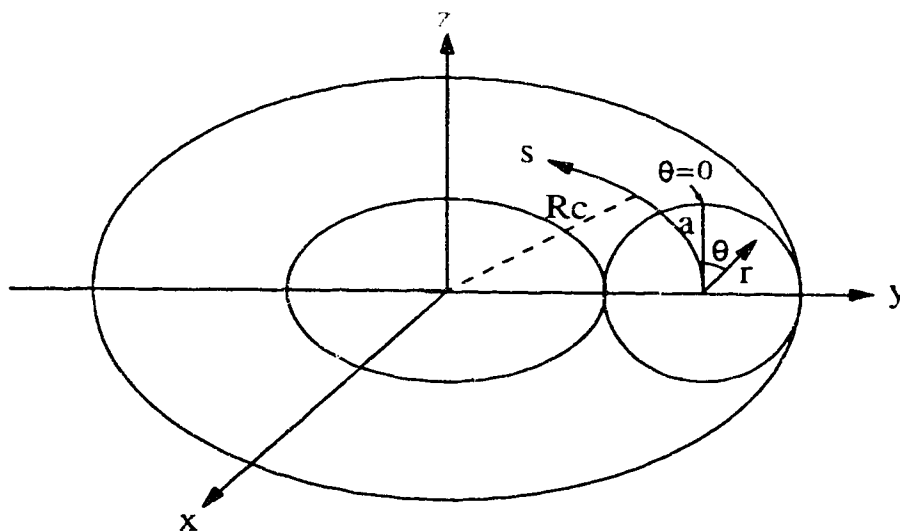
Fig. 2.5. Toroidal coordinate set up

The Navier–Stokes equations are written in the generic toroidal coordinate system. The radius of the pipe, a, and the average axial velocity, U, are used to render the various variables dimensionless, that is,

$$s = \frac{r'}{a}, \quad r = \frac{r'}{a}, \quad \theta = \theta', \quad u = \frac{u'}{2U}, \quad v = \frac{v'}{2U}, \quad w = \frac{w'}{2U}, \quad p = \frac{Re}{4\rho}\frac{p'}{U^2}$$

$$\text{and} \quad \lambda = \frac{a}{Rc}, \quad Re = \frac{2aU}{\nu}, \quad Dn = Re\ \lambda^{1/2}$$

where Re is the Reynolds number, Dn is the Dean number, Rc is the radius of the coil, λ is the curvature ratio, u is the dimensionless axial velocity, v is the dimensionless radial velocity, w is the dimensionless angular velocity and the primed variables are the corresponding dimensional quantities.

The dimensionless governing equations become

Continuity equation:

$$\frac{1}{h_1}\cdot\frac{\partial u}{\partial s} + \frac{1}{rh_1}\cdot\frac{\partial(rh_1 v)}{\partial r} + \frac{1}{rh_1}\cdot\frac{\partial(h_1 w)}{\partial \theta} = 0 \qquad (2\text{--}23)$$

The general form of the momentum equations:

$$\frac{1}{h_1}\cdot\frac{\partial}{\partial s}(u Re\ \phi) + \frac{1}{rh_1}\cdot\frac{\partial}{\partial r}[rh_1(v Re\ \phi - \frac{\partial \phi}{\partial r})] +$$

$$\frac{1}{rh_1}\cdot\frac{\partial}{\partial \theta}(h_1 w Re\ \phi - \frac{h_1}{r}\cdot\frac{\partial \phi}{\partial \theta}) + d_\phi \phi$$

$$= S_\phi \qquad (2\text{--}24)$$

For the various directions, the corresponding quantities ϕ, d_ϕ and S_ϕ take the form:

s—momentum: $\phi = u$

$$d_\phi = \frac{v\sin\theta + w\cos\theta}{h_1}\lambda Re + \frac{\lambda^2}{h_1^2}$$

(2–25a)

$$S_\phi = -\frac{1}{h_1}\cdot\frac{\partial p}{\partial s} + \frac{2\lambda}{h_1^2}(\sin\theta\cdot\frac{\partial v}{\partial s} + \cos\theta\cdot\frac{\partial w}{\partial s})$$

(2–25b)

r—momentum: $\phi = v$

$$d_\phi = \frac{1}{r} \cdots \sin\theta$$

(2–26a)

$$S_\phi = -\frac{\partial p}{\partial r} + Re(\frac{\lambda\sin\theta}{h_1}u^2 + \frac{w^2}{r}) - \frac{2\lambda\sin\theta}{h_1^2}\cdot\frac{\partial u}{\partial s} - \frac{2}{r^2}\cdot\frac{\partial w}{\partial\theta} - \frac{2h_1-1}{rh_1^2}\lambda\cos\theta w$$

(2–26b)

θ—momentum: $\phi = w$

$$d_\phi = Re\frac{v}{r} + \frac{1}{h_1^2}(\lambda^2 + \frac{2h_1-1}{r})$$

(2–27a)

$$S_\phi = -\frac{\partial p}{\partial\theta} + Re\frac{\lambda\cos\theta}{h_1}u^2 - \frac{2\lambda\cos\theta}{h_1^2}\cdot\frac{\partial u}{\partial s} + \frac{3h_1-1}{r^2h_1^2}\frac{\partial v}{\partial\theta} + \frac{1}{rh_1^2}\lambda\cos\theta v$$

(2–27b)

where h_1 is the metric coefficient, $h_1 = 1 + \lambda r \sin\theta$.

Together with the boundary conditions:

$r = 1$, $u = v = w = 0$

$p = 0$ at a certain interior point (reference).

And the average u across the pipe is half a unit, i.e.,

$$\frac{\int u \, dA}{\int dA} = 0.5$$

The secondary flow pattern is obtained when the flow is fully developed by the following:

$$h_1 w = \frac{\partial \psi}{\partial r}$$

(2–28)

where ψ is the secondary flow stream function.

2.8.1. Domain Discretization

Since the domain is regular, we use undistorted non–uniform mesh to maintain the best results. The three curvilinear directions are those of the three coordinate axes. Since the governing equations are parabolized, the problem reduces to a two dimensional problem with extra time–like variable in the axial flow direction. Hence, the nodal arrangement thereafter is the same as that of a two dimensional problem. A sketch of the nodal arrangement is shown in Figure 2.6. Where p and u share the same grid points, w grid is placed symmetrically surrounding each p grid point in the θ direction while v grid points are placed to symmetrically surround each p grid point in the r direction, i.e., $\theta_j = \frac{1}{2}(\theta_{J+1} + \theta_J)$ and $r_i = \frac{1}{2}(r_{I-1} + r_I)$. The index notations of I and J are used for bookkeeping the mesh lines of the parallel velocity components of the directions of r and θ of the staggered grid.

On the boundary (pipe wall), the pressure grid point is not present. The v grid is regularly placed (the same rule as that of the interior nodes) and w and u are placed on the boundary as if half of the r mesh spacing was chopped. The nodal layout is shown in Figure 2.8.

At the center of the pipe, the θ direction is not defined. To avoid this type of singularity, we simply avoid placing any grid point at the center. The resulting mesh near the center looks as if a v node were present at the center. A sketch of
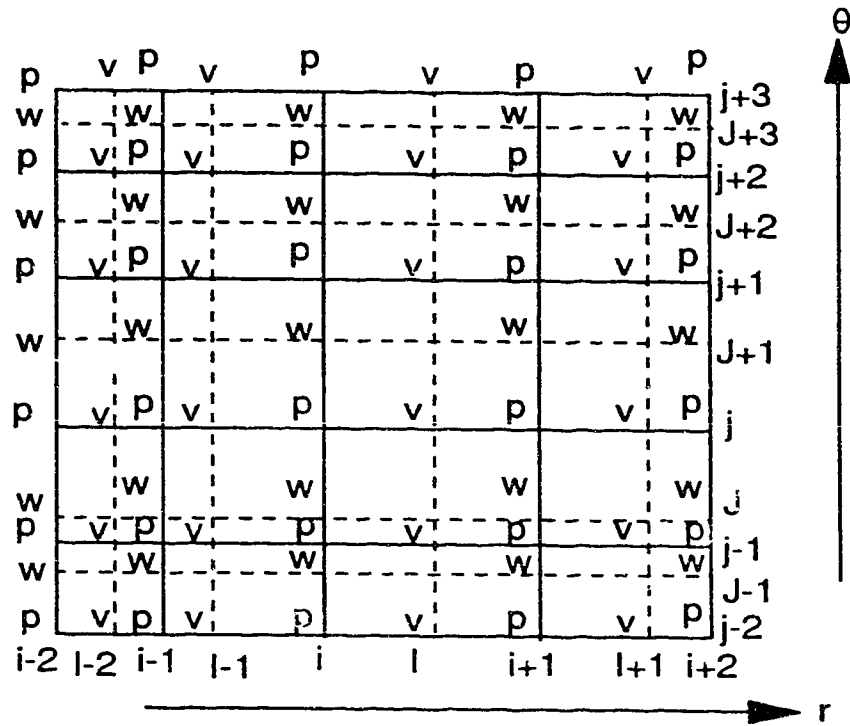
Fig. 2.6 The mesh layout in the domain.
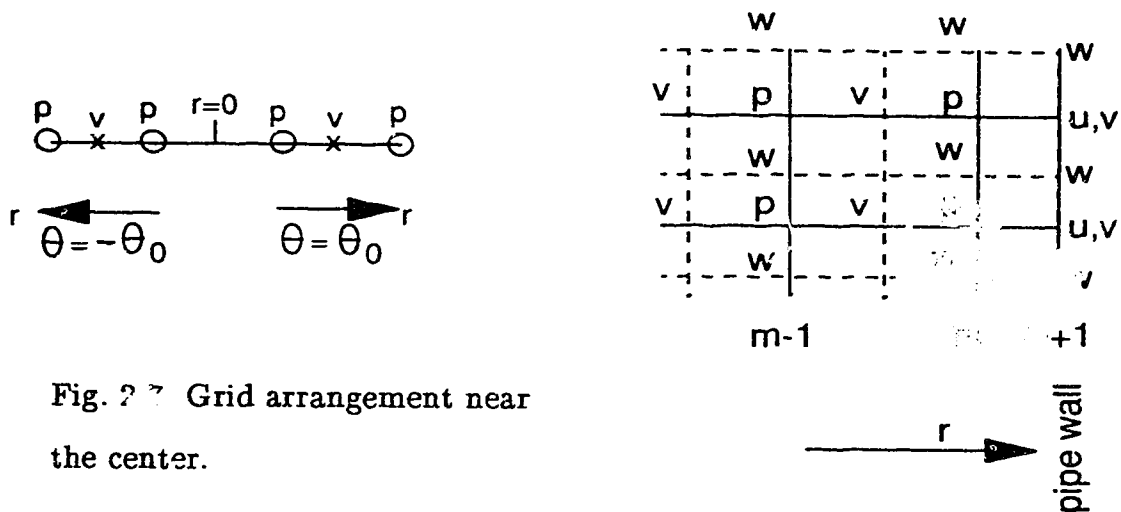
Fig. 2 7 Grid arrangement near the center.

Fig. 2.8 Grid layout near the wall.
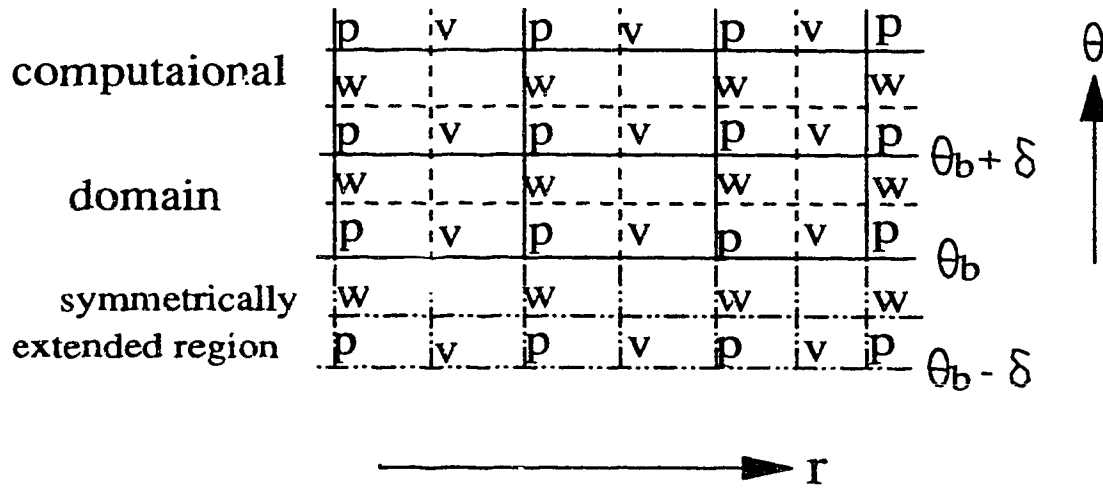
Fig. 2.9 Mesh layout near a symmetrical pseudo–boundary.
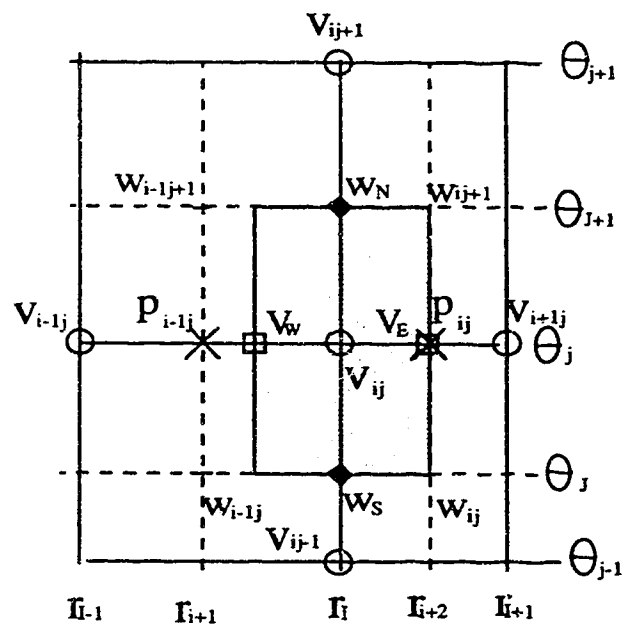
Fig. 2.10 Conservational domain for node v_{ij}.

such a setup is shown in Figure 2.7. When discretizing the nodes near the center, the variables r, v, and w are assigned their opposite sign when referred cross the center to the other side.

If we are to compute only half the domain, the horizontal line ($\theta = -\frac{\pi}{2}$ and $\theta = \frac{\pi}{2}$) is the breaking line to form a pseudo—boundary, where the flow is symmetrical. On such a symmetrical boundary, (u, p) and v grids are arranged regularly and w grid point is absent. The conservational domain is, however, symmetrically extended outside of the computational domain. A sketch of the mesh arrangement is shown in Figure 2.9. This setup allows us to impose the following type of weak symmetrical conditions easily:

$$\phi_{\theta_b+\delta} = \phi_{\theta_b-\delta} \quad \text{and} \quad w_{\theta_b+\delta/2} = -w_{\theta_b-\delta/2}$$

where $\phi = $ u, v, p. However, the symmetrical condition for p needs not be imposed in the numerical computation. θ_b is the angle of the symmetry $-\pi/2$ or $\pi/2$. δ is the angular incremental of the grid lines cross the symmetry line.

The global numbering of the nodes is shown in Figure 2.6. Locally, the conservational domain is formed for the best interest of the computation. A sketch of such setup for a v_{ij} node is shown in Figure 2.10.

2.8.2. Formal Discretization

Since the governing equations can be written in the form of equation (2–8), we need only to identify the decoupling. To illustrate the proposed method, we take the r—momentum equation and discretize it at the node of v_{ij} in a general undistorted non—uniform mesh. A sketch of the conservational domain is shown in Figure 2.10.

The first step is to discretize in the axial direction by using a similar

approach as that of Patankar & Spalding (1972). The final governing equation (r—momentum) after discretizing in the s—direction and separating r and θ directions is shown as:

$$r(h_1 d_v + \frac{Re}{\Delta s} u^U)v + E_{vr} + E_{v\theta} = \frac{1}{A_e} \int_{r_W}^{r_E} \int_{\theta_S}^{\theta_N} (h_1 S_v + \frac{Re}{\Delta s} u^U v^U) r \, dr \, d\theta \quad (2\text{--}29a)$$

where

$$E_{vr} = \frac{1}{r_E - r_W} \int_{r_W}^{r_E} \{\frac{\partial}{\partial r}[rh_1(v^U \, Re \, v - \frac{\partial v}{\partial r})] - v\frac{\partial(rh_1 v^U)}{\partial r} Re\} dr \quad (2\text{--}29b)$$

and

$$E_{v\theta} = \frac{1}{\theta_N - \theta_S} \int_{\theta_S}^{\theta_N} \{\frac{\partial}{\partial\theta}[\frac{h_1}{r}(rw^U \, Re \, v - \frac{\partial v}{\partial\theta})] - v\frac{\partial(h_1 w^U)}{\partial\theta} Re\} d\theta \quad (2\text{--}29c)$$

The superscript U stands for the upstream, $A_e = (r_E - r_W)(\theta_N - \theta_S)$, the subscripts E, W, N and S stand for the r increasing side, r decreasing side, θ increasing side and θ decreasing side of the conservational domain surfaces, respectively, $r_E = \frac{1}{2}(r_I + r_{I+1})$, $r_W = 2r_I - r_E$, $\theta_N = \theta_{J+1}$, $\theta_S = \theta_J$ and Δs is the axial step size. The evaluation of the right hand side of equation (2—29a) is straightforward. Discretization of equations (2—29b) is given in the Supplement of this Chapter.

The discretized v—momentum equation can be assembled from the individual one—dimensional subproblems to yield:

$$VIJ_{ij}v_{ij} + VMJ_{ij}v_{i-1j} + VPJ_{ij}v_{i+1j} + VIM_{ij}v_{ij-1} + VIP_{ij}v_{ij+1}$$
$$= VRH_{ij} - r_I h_{1Ij} \cdot \frac{p_{ij} - p_{i-1j}}{r_{i+2} - r_{i+1}} \quad (2\text{--}30)$$

where $h_{1Ij} = 1 + \lambda r_I \sin\theta_j$ and the coefficient matrix and the right hand side are given in the Supplement following this Chapter.

2.8.3. Pressure Perturbation

When the pressure field is perturbed by Δp, the velocity fields will result in a change. To estimate the velocity change, we apply Gauss–Seidel iteration on the discretized momentum equations:

$$\Delta v_{ij} = -\frac{r_I h_{1j}}{VIJ_{ij}} \cdot \frac{\Delta p_{i+1j} - \Delta p_{ij}}{r_{i+2} - r_{i+1}} \tag{2-31}$$

$$\Delta w_{ij} = -\frac{h_{1iJ}}{WIJ_{ij}} \cdot \frac{\Delta p_{ij} - \Delta p_{ij-1}}{\theta_j - \theta_{j-1}} \tag{2-32}$$

Hence, the resulting perturbed velocity field is:

$$v_{ij}^{new} = v_{ij} + \Delta v_{ij}$$

$$w_{ij}^{new} = w_{ij} + \Delta w_{ij}$$

By forcing the continuity equation to be satisfied, we can solve for the pressure perturbation, i.e.,

$$\iint [\frac{\partial}{\partial r}(rh_1\Delta v) + (h_1\Delta w)] = -\iint [r\frac{\partial u}{\partial s} + \frac{\partial(rh_1v)}{\partial r} + \frac{\partial(h_1w)}{\partial \theta}] \tag{2-33}$$

With some under–relaxation, the above equation can be rendered to the standard 5–point module pressure perturbation equation after substituting in the velocity perturbation:

$$PIJ_{ij}\Delta p_{ij} + PMJ_{ij}\Delta p_{i-1j} + PPJ_{ij}\Delta p_{i+1j} + PIM_{ij}\Delta p_{ij-1} + PIP_{ij}\Delta p_{ij+1} = F_p \cdot PRH_{ij} \tag{2-34}$$

where

$$PIJ_{ij} = -PMJ_{ij} - PPJ_{ij} - PIM_{ij} - PIP_{ij} \; ; \quad PMJ_{ij} = -\frac{(r_{I-1}h_{1I-1j})^2}{(r_I-r_{I-1})(r_i-r_{i-1})VIJ_{i-1j}}$$

$$PPJ_{ij} = -\frac{(r_I h_{1Ij})^2}{(r_I - r_{I-1})(r_{i+1} - r_i)VIJ_{ij}} \; ; \qquad PIM_{ij} = -\frac{h_{1iJ}^2}{(\theta_{J+1} - \theta_J)(\theta_j - \theta_{j-1})WIJ_{ij}}$$

$$PIP_{ij} = -\frac{h_{1iJ+1}^2}{(\theta_{J+1} - \theta_J)(\theta_{j+1} - \theta_j)WIJ_{ij+1}} \; ; \qquad PRH_{ij} = FLOWIN_{ij} - FLOWOUT_{ij}$$

$$FLOWIN_{ij} = \frac{r_{I-1} h_{1I-1j} v_{i-1j}}{r_I - r_{I-1}} + \frac{h_{1iJ} w_{ij}}{\theta_{J+1} - \theta_J} + \frac{r_i u_{ij}^U}{\Delta s}$$

$$FLOWOUT_{ij} = \frac{r_I h_{1Ij} v_{ij}}{r_I - r_{I-1}} + \frac{h_{1iJ+1} w_{ij+1}}{\theta_{J+1} - \theta_J} + \frac{r_i u_{ij}}{\Delta s}$$

When a good initial guess in the velocity field is used, the pressure perturbation alone is not the best approach to take for the pressure evaluation (see Patankar 1980). Following the same method as that of SIMPLER (Patankar 1980), we can solve for the pressure directly.

Although the pressure is solved by using the above strategy, SIMPLER type pressure iteration is not recommended. Without the pressure perturbation, the scheme would be like a simple iteration switching between various variables. The simple iteration scheme is usually not favorable. Instead, the above pressure evaluation is used only once to initiate the iteration for a few matching steps at the start or after we disturbed the velocity field substantially.

The 2–D solver we developed is especially useful in solving the pressure perturbation equation. When using the sweeping strategy alone, we found that it is extremely difficult to obtain convergence.

2.8.4. Termination of Iteration

The stopping criterion for the iteration is crucial in knowing the quality of the solution obtained. At each iteration, we have controlled the solutions out of the directional sweeping solver to a relative tolerance of 10^{-6}. Hence the momentum

equations are satisfied as long as the pressure field is correct.

In order to have a correct pressure field, the velocity field must satisfy the continuity equation. This gives rise to a stopping criterion which is related to of the continuity equation.

We use a normal relative error in continuity to define the error index as follows:

$$
RSD = \frac{\displaystyle\sum_{i,j} \frac{2|PRH_{ij}|}{|FLOWIN_{ij}| + |FLOWOUT_{ij}|}}{\displaystyle\sum_{i,j} 1}
$$

where PRH_{ij} is the error in the flow in and out of the conservational domain of p_{ij} and $FLOWIN_{ij}$ is the flow into the conservational domain. In this example, we set the stopping criterion to be $RSD < 10^{-5}$.

A close look at the definition of RSD, we can see that RSD can be considered as an estimate of the L_1 norm of the normalized continuity equation error distribution.

2.8.5. Computational Results

Table 2.1 shows the grid dependence and the computational time required for the fluid flow development from a flat flow profile to the primary two—vortex

Table 2.1. Grid test for Re = 1723, λ = 1 / 30

Grid	u10×20fu	n10×20fu	n15×24fu	n20×28fu	n25×32fu	n30×40fu	n40×48fu
fRe	38.30	37.42	35.82	36.38	36.10	36.24	36.19
cpu,s	3161.4	2954.9	6506.9	9646.8	19282.1	43150	123530*

Note that the literature value found is fRe = 37.15 by Tarbell & Samuels 1972.

* 2000 axial steps are used for this case.

Computational domain

$\theta = -90°$

$\theta = 90°$

symmetrically extented

symmetrically extented
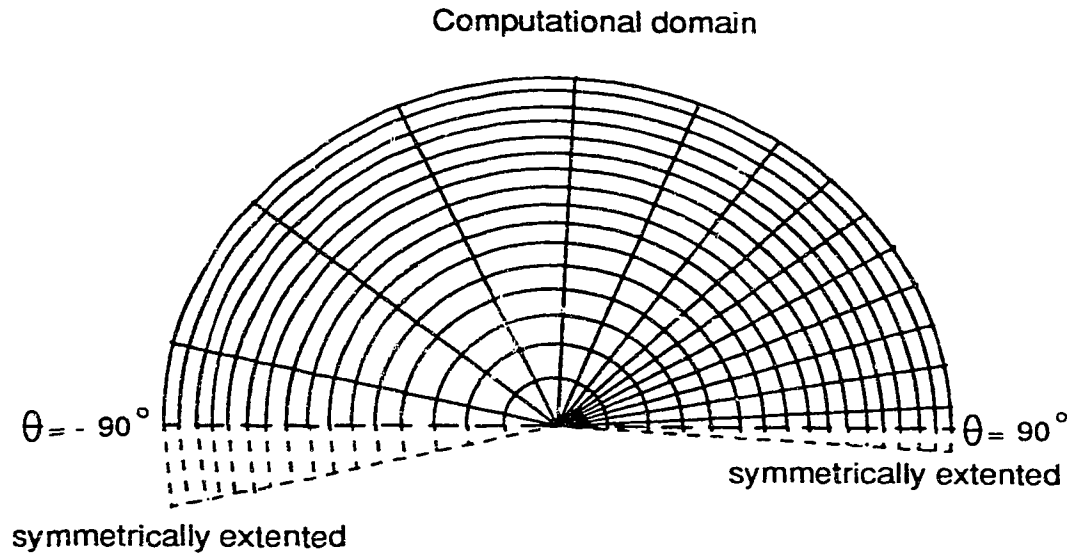
Fig. 2.11   Mesh layout for n16×14hn.

solution by a NeXT station for 1200 axial steps.

The grid notation used is given as aM×Nbc, where a=n stands for non—uniform mesh in the radial direction, a=u stands for uniform mesh in the radial direction. M is the number of grid points in the radial direction. N is the number of grid points in the peripheral direction, b=f stands for the full domain formulation (no symmetry is assumed), b=h stands for a half domain formulation (the symmetry is imposed), c=n stands for the non—uniform mesh in the peripheral direction and c=u stands for the uniform mesh in the peripheral direction. A typical mesh n16×14hn is shown in Figure 2.11. The non—uniform mesh in the radial direction is accomplished by interpolating between the uniform mesh in r and the uniform mesh in r^2. The non—uniform mesh in the azimuthal direction is made by choosing a fine uniform mesh in the outer wall region $(-\frac{1}{4}\pi \leq \theta \leq \frac{3}{4}\pi)$ with nearly half of the total mesh points. A coarse uniform mesh

is used in the inner wall region ($-\pi \lesssim \theta \lesssim 0$). The regions connecting the two uniform mesh regions are uniform exponentially changing meshes to match the mesh sizes at the ends. The change in mesh size is gradual to avoid extra error due to mesh size change and is controlled by $0.5 < (\Delta\theta)_j / (\Delta\theta)_{j-1} < 2$.

In Figure 2.11, the mesh lines parallel to the peripheral direction are the perpendicular mesh lines of the variable v and those lines parallel to the radial direction are the perpendicular mesh lines of the variable w. The cells formed by the mesh lines are the conservational domains for the variables of u and p. The center of the pipe has no grid points. $\theta = -\pi/2$ and $\theta = \pi/2$ lines are the computational domain boundaries and not the perpendicular mesh lines for w.

To serve as a comparison, we choose $\lambda = 0.01$ to generate some solutions to compare with the literature where the loose coiling was used as that was done by Nandakumar & Masliyah (1982).

Table 2.2 shows the grid dependence and the computational time required for the flow developing from a geometrically disturbed straight pipe Poiseuille flow to a secondary four—vortex solution with the axial steps of 1600. The literature data for a loose coiling is also included in the Table 2.2.

From Table 2.1 and Table 2.2, one can observe that the proposed scheme converges very well. The grid of n16×14hn is adequate for the four—vortex solution

Table 2.2. Grid test for Re = 1928.5, λ = 0.01 i.e., Dn = 192.85

Grid	n10×12hu	n10×12hn	n16×14hn	n20×16hn	n20×20hn	n30x25hn	n30×30hn
fRe	30.64	29.10	29.35	29.50	29.40	29.36	29.36
cpu,s	4563.7	6472.1	10936.3	17049.2	20946.8	49123.2	61480.0

Literature	Grid	fRe	Dn	λ
Dennis & Ng 1982	60×30	29.33	192.9	0.0
Yang & Keller 1986	60×20	29.34	192.8	0.0

of Dn = 192.85, whereas in the literature, a very large number of grid points were required despite their use of global interpolation (or collocation) in the numerical discretization. Even the solution from the grid of n10×12hn is within the range of 1%. Owing to the location of the second vortex, the grid points concentrated in the region of the second vortex have a better result than the uniform one for the case of small number of grid points.

The solutions were found not to be grid sensitive once the grid size is sufficiently small as is shown in both Tables 2.1 and 2.2.

Figure 2.12 shows the secondary flow pattern of the four—vortex solution used in Table 2.2. The numbers denote the ψ values of the secondary flow stream function as defined by equation (2—25).

Figure 2.13 shows the axial velocity profile corresponding to the four—vortex solution of Figure 2.12.
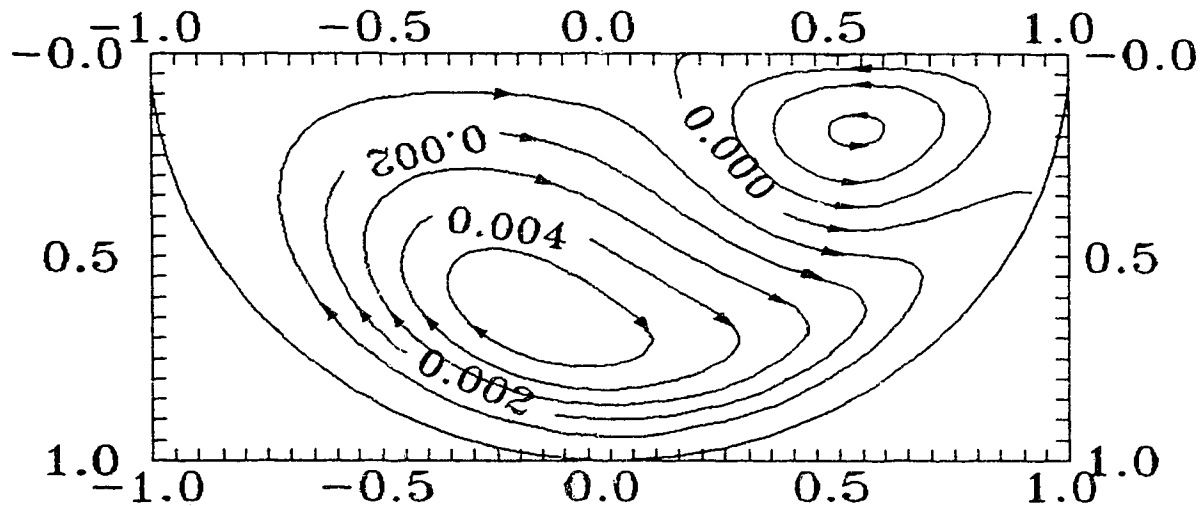
Fig. 2.12. Four—vortex secondary flow pattern for Dn = 192.85 and $\lambda = 0.01$ for half of the flow domain.
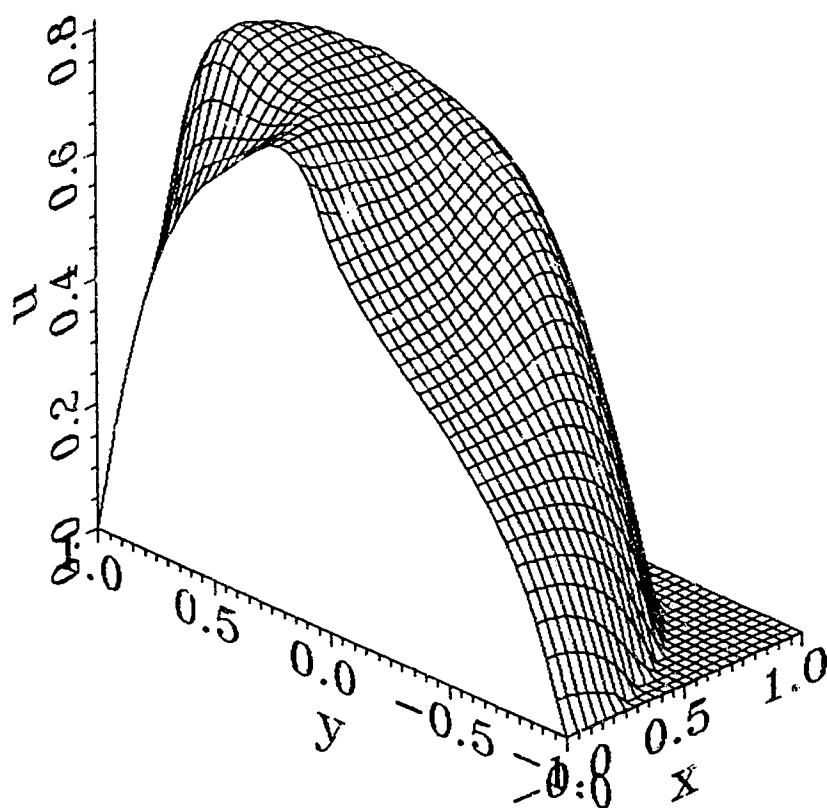
Fig. 2.13. Axial velocity profile for the flow shown in Figure 2.12.

2.9. NUMERICAL EXAMPLE 2

Square driven cavity flow

In the first example, we have shown the implementation of the proposed method. To show more clearly the convergence and the advantage of the 3—point exponential scheme over 2—point schemes, we chose the problem of a square driven cavity flow. The system setup and the boundary conditions are shown in Figure 2.14. The velocity components are normalized by the velocity of the moving plate U_0 (located at the topmost), i.e., $u = \frac{u'}{U_0}$ and $v = \frac{v'}{U_0}$. The geometrical variables are normalized by the side length of the square, L, i.e., $x = \frac{x'}{L}$ and $y = \frac{y'}{L}$.

The governing equations are

$$
\left\{
\begin{array}{l}
\frac{\partial u}{\partial x} + \frac{\partial v}{\partial y} = 0 \\[2mm]
Re(\frac{\partial uu}{\partial x} + \frac{\partial vu}{\partial y}) - \frac{\partial^2 u}{\partial x^2} - \frac{\partial^2 u}{\partial y^2} = -\frac{\partial p}{\partial x} \\[2mm]
Re(\frac{\partial uv}{\partial x} + \frac{\partial vv}{\partial y}) - \frac{\partial^2 v}{\partial x^2} - \frac{\partial^2 v}{\partial y^2} = -\frac{\partial p}{\partial y}
\end{array}
\right.
\qquad (2\text{--}35)
$$
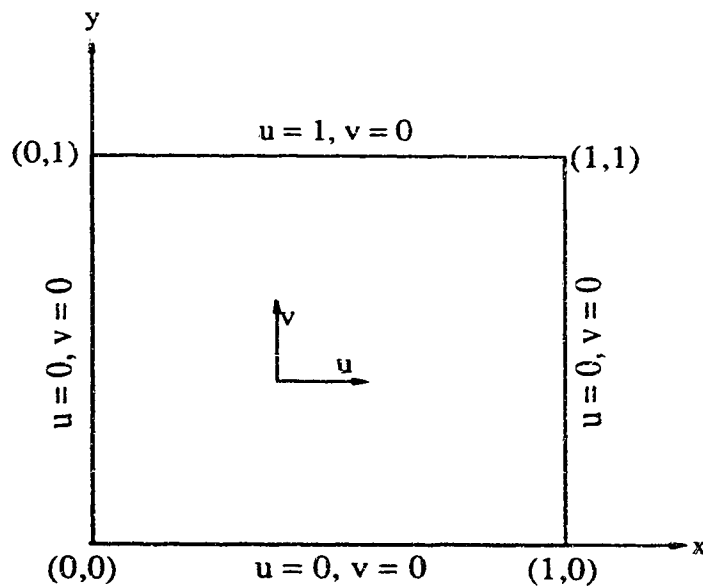
Fig. 2.14. Square Driven Cavity.

where $Re = \dfrac{LU_0}{\nu}$ and $p = \dfrac{Re}{4\rho}\dfrac{p'}{U_0^2}$.

Although a good approach to this problem would be to use a non—uniform mesh, we choose to use uniform meshes for the sake of comparison. When a 2—point interpolation function is used, the current method may be identical to a finite volume method by a proper choice of the conservational domain for a uniform mesh. The initial guess of zero is used for all variables in all cases.

Figure 2.15. shows the convergence rate of using different interpolation functions. It can be seen that the 3—point interpolation schemes do not differ much from the 2—point schemes in terms of convergence rate, except that the 2—point exponential scheme showed difficulty at very low RSD.

Table 2.3 shows clearly the cpu time requirement of the various schemes by a NeXT machine. The use of exponential functions does not increase the cpu time dramatically. A small increase of less than 2% is observed for the case of 3—point
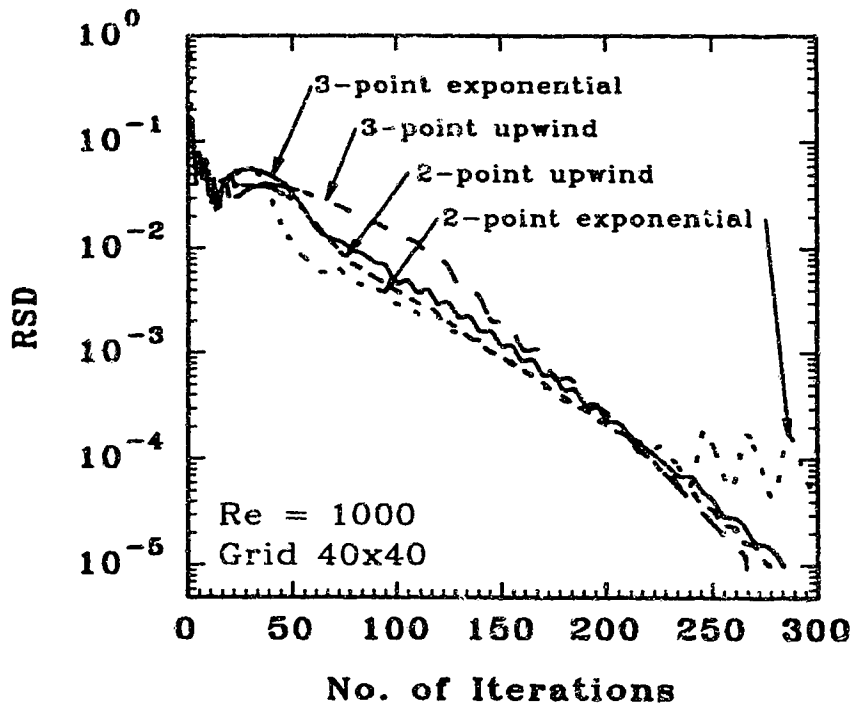
Fig. 2.15. Convergence rate of the proposed method.

Table 2.3.   Cpu time requirement for various schemes and mesh.

Re	scheme	Mesh	ITER	RSD	cpu, s
1000	2—p upwind	40x40	278	1.0×10^{-5}	5193.9
1000	2—p exponential	40x40	300	4.4×10^{-5}	7238.7
1000	3—p upwind	40x40	266	9.1×10^{-6}	6418.8
1000	3—p exponential	40x40	284	9.6×10^{-6}	6528.8
1000	3—p exponential	20x20	69	9.7×10^{-6}	550.6
1000	3—p exponential	80x80	765	7.9×10^{-6}	111784.8

ITER stands for the number of iterations performed.

exponential over 3—point upwind which derived from equation (2—9) by specifying $Re \to \infty$.

Figure 2.16 shows the present solutions by utilizing uniform grids of 80x80 and 140x140 together with the 3—point exponential interpolation function. Results from Schreiber & Keller (1983) are also included for comparison. From Figure 2.16, we observe that the proposed method works fairly good.
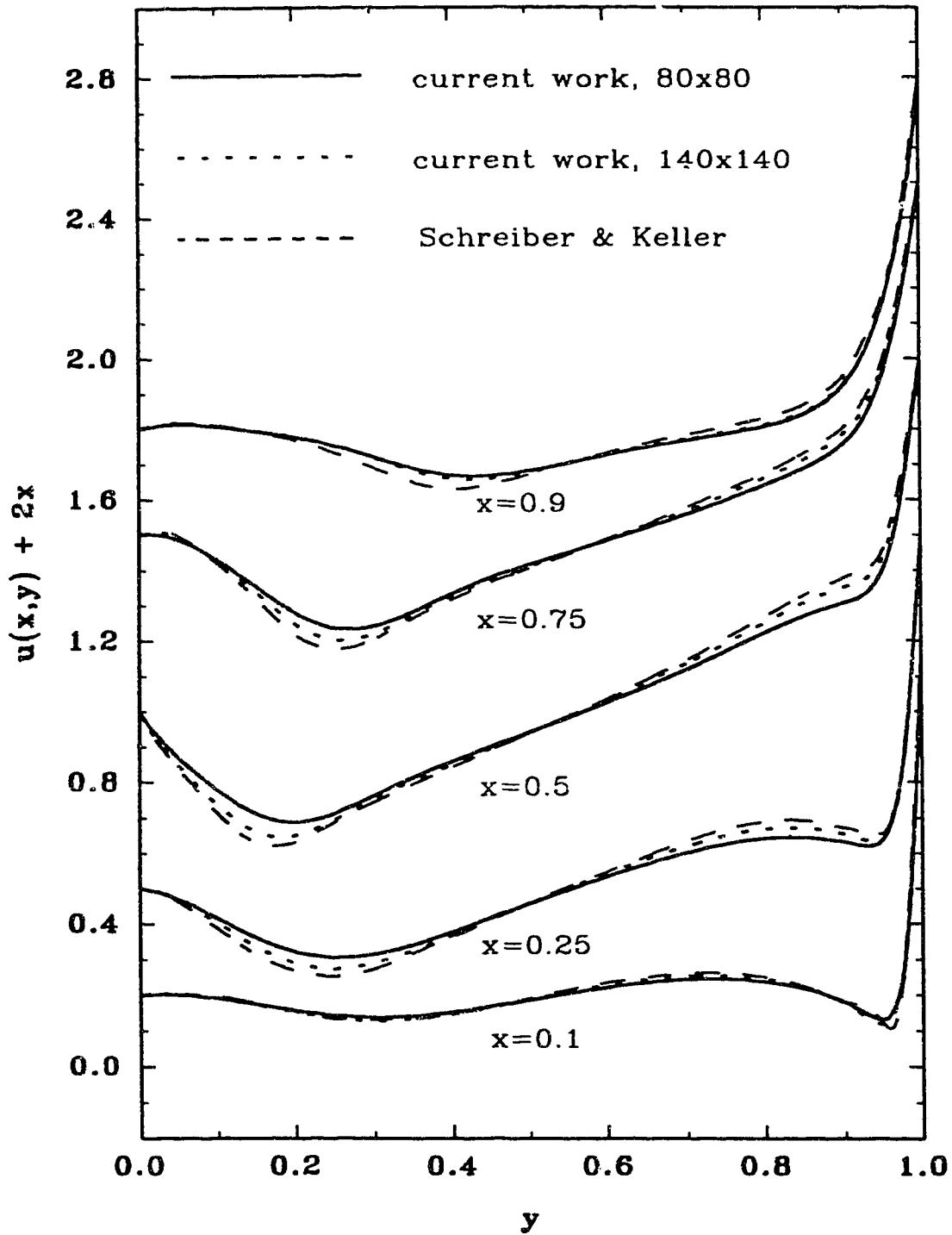
Fig. 2.16. Velocity profiles for u at Re = 1000 of current work with the 3–point exponential scheme and meshes of 80x80 and 140x140. The solution of Schreiber & Keller (1983) with a grid of 141x141 and a stream function approach is also included.

2.10. CONCLUSIONS

A first order non—conforming numerical method for fluid flow with a 3—point exponential interpolation has been developed. It is achieved by decomposing a multi—dimensional problem to multiple one—dimensional subproblems. The multi—dimensional problem is first decoupled into multiple one—dimensional subproblems upon discretizing. After assembling the multiple one dimensional subproblems to form the algebraic equations, the resulting algebraic equations are solved with a tri—diagonal solver iteratively. The velocity and pressure are decoupled at each iteration using the pressure correction method of Patankar.

The accuracy of the traditional upwind / exponentially weighted schemes has been investigated to compare with the proposed 3—point scheme for both interpolation and consistency. It is found that the proposed 3—point exponential interpolation scheme together with the multi—dimensional separating strategy render a guaranteed first order convergence. It is shown that the use of the traditional exponential or upwind scheme renders a scheme less than first order accurate due to the presence of numerical dispersion in the non—linear terms.

A two—dimensional direct solver has been developed with minimum storage requirement (less than a band solver) and with a partial inversion strategy. It is written for the best interest of the pressure perturbation equation.

The computational results for the laminar fluid flows in a torus and in a square driven cavity show good agreement with the literature. The convergence rate is similar to the traditional upwind schemes. The use of exponential functions do not influence much the computational time.

Supplement

Discretization of the separated r–directional r–momentum component can be illustrated as follows:

$$(r_E - r_W)E_{vr} =$$
$$[rh_i(v^U Re\ v - \frac{\partial v}{\partial r})]_{r=r_E} - [rh_i(v^U Re\ v - \frac{\partial v}{\partial r})]_{r=r_W} - v_{ij}(r_E h_{iE} v_E - r_W h_{iW} v_W)Re$$

where

$$v_E = v^U|_{r=r_E} = \frac{v^U_{i+1j}(r_E - r_I) + v^U_{ij}(r_{I+1} - r_E)}{r_{I+1} - r_I} \quad \text{and}$$

$$v_W = v^U|_{r=r_W} = \frac{v^U_{ij}(r_I - r_W) + v^U_{i-1j}(r_W - r_{I-1})}{r_I - r_{I-1}}.$$

The subscript E and W are defined in the paper following equation (2–28).

The momentum fluxes at the conservational surface can further be written as follows:

$$[rh_i(v^U Re\ v - \frac{\partial v}{\partial r})]_{r=r_E} = \alpha_E v_{i-1j} + (r_E h_{iE} v_E Re - \alpha_E - \beta_E)v_{ij} + \beta_E v_{i+1j}$$

$$[rh_i(v^U Re\ v - \frac{\partial v}{\partial r})]_{r=r_W} = \alpha_W v_{i-1j} + (r_W h_{iW} v_W Re - \alpha_W - \beta_W)v_{ij} + \beta_W v_{i+1j}$$

Hence, the discretized one–dimensional module can be written as:

$$(r_E - r_W)E_{vr} = (r_E h_{iE} \alpha_E - r_W h_{iW} \alpha_W)v_{i-1j} + (r_E h_{iE} \beta_E - r_W h_{iW} \beta_W)v_{i+1j} - $$
$$[r_E h_{iE}(\alpha_E + \beta_E) - r_W h_{iW}(\alpha_W + \beta_W)]v_{ij} \qquad (2\text{--}S1)$$

α and β's are obtained by using the interpolation equation (2–9). In this case,

$H_1 = r_I - r_{I-1}$, $H_2 = r_{I+1} - r_I$ and $Re\, u_i = v_{ij}^U Re$. Here the use of uppercase H is to avoid any confusion with the metric coefficients. Owing to the numeric limitation of the computers, we take $Re\, u_i = \min\{v_{ij}^U\, Re\, H_1,\ 80.0\}\ /\ H_1$. To simplify the notations, we use:

$$a = v^U Re, \quad b = Re\, u_i, \quad H = r_E - r_I = r_I - r_W$$

We apply the 3–point exponential interpolation equation (2–9) to obtain

$$[rh_1(av - \tfrac{\partial v}{\partial r})]_{r=r_E} = a_E v_{ij} + \frac{H_1(e^{bH}-1)+H\,(e^{-bH_1}-1)}{H_1(e^{bH_2}-1)+H_2(e^{-bH_1}-1)}\, a_E(v_{i+1j}-v_{ij}) +$$

$$\frac{H_2(e^{-bH}-1)-H\,(e^{bH_2}-1)}{H_1(e^{bH_2}-1)+H_2(e^{-bH_1}-1)}\, a_E(v_{i-1j}-v_{ij}) -$$

$$\frac{bH_1\ e^{bH} + e^{-bH_1} - 1}{H_1(\,e^{bH_2}-1)+H_2(e^{-bH_1}-1)}\,(v_{i+1j}-v_{ij}) -$$

$$\frac{bH_2\ e^{-bH} - e^{bH_2} + 1}{H_1(\,e^{bH_2}-1)+H_2(\,e^{-bH_1}-1)}\,(v_{i-1j}-v_{ij})$$

Hence, we obtain

$$\alpha_E = \frac{(a_E+b)H_2(e^{-bH}-1)+bH_2-(a_EH-1)\,(e^{bH_2}-1)}{H_1(e^{bH_2}-1)\ +\ H_2(\,e^{-bH_1}-1)} \tag{2–S2a}$$

$$\beta_E = \frac{(a_E-b)H_1(e^{bH}-1)-bH_1+(a_EH-1)\,(e^{-bH_1}-1)}{H_1(e^{bH_2}-1)\ +\ H_2(\,e^{-bH_1}-1)} \tag{2–S2b}$$

Similarly,

$$\alpha_W = \frac{(a_W+b)H_2(e^{-bH}-1)+bH_2-(a_WH-1)(e^{bH_2}-1)}{H_1(e^{bH_2}-1) + H_2(e^{-bH_1}-1)} \qquad (2-S2c)$$

$$\beta_W = \frac{(a_W-b)H_1(e^{bH}-1)-bH_1+(a_WH-1)(e^{-bH_1}-1)}{H_1(e^{bH_2}-1) + H_2(e^{-bH_1}-1)} \qquad (2-S2d)$$

In the above expressions for α, β's, we have taken care of the large Reynolds number flow limit. When $b \to 0$, i.e., almost creeping flow, computationally equation (2–S2) is of $\frac{0}{0}$ type. In order to avoid this numeric difficulty in the computation, we take the limit of $b \to 0$ in equation (2–S2) to obtain the following expressions for small Reynolds number flows:

$$\alpha_E = \frac{(a_E H-1)(H-H_2)-H}{H_1(H_1+H_2)} \qquad (2-S3a)$$

$$\beta_E = \frac{(a_E H-1)(H+H_1)-H}{H_1(H_1+H_2)} \qquad (2-S3b)$$

$$\alpha_W = \frac{(a_W H+1)(H+H_2)+H}{H_1(H_1+H_2)} \qquad (2-S3c)$$

$$\beta_W = \frac{(a_W H+1)(H-H_1)+H}{H_1(H_1+H_2)} \qquad (2-S3d)$$

Equation (2–S3) can also be obtained by applying the quadratic interpolation function, equation (2–10) instead of the exponential interpolation function, equation (2–9). In practice, we can use equation (2–S3) when the cell Peclet number bH_1 and $bH_2 < 2$.

One can discretize the other direction in the manner. The final discretized r—momentum is shown by equation (2–4), where the coefficients are defined as follows:

$$VRH_{ij} = Re \left(\lambda r_I \sin\theta_j \ U_C^2 + h_{1Ij} W_C^2 \right) -$$

$$\frac{2\lambda r_I \sin\theta_j}{h_{1Ij}} \cdot \frac{U_C - U_C^U}{\Delta s} - \frac{2}{r_I} \cdot \frac{W_N - W_S}{\theta_{J+1} - \theta_J} - (2 - \frac{1}{h_{1Ij}})\lambda \cos\theta_j \ W_C$$

$$VIJ_{ij} = \frac{1+2h_{1Ij}\lambda r_I \sin\theta_j}{r_I h_{1Ij}} - VMJ_{ij} - VPJ_{ij} - VIM_{ij} - VIP_{ij}$$

$$VMJ_{ij} = \frac{r_E h_{1E} \alpha_E - r_W h_{1W} \alpha_W}{r_E - r_W} ; \qquad VPJ_{ij} = \frac{r_E h_{1E} \beta_E - r_W h_{1W} \beta_W}{r_E - r_W}$$

$$U_C = \frac{u_{ij}(r_I - r_{i+1}) + u_{i-1j}(r_{i+2} - r_I)}{r_{i+2} - r_{i+1}} ; \qquad U_C^U = \frac{u_{ij}^U(r_I - r_{i+1}) + u_{i-1j}^U(r_{i+2} - r_I)}{r_{i+2} - r_{i+1}}$$

$$W_C = \frac{W_N + W_S}{2} ; \qquad W_N = \frac{w_{ij+1}(r_I - r_{i+1}) + w_{i-1j+1}(r_{i+2} - r_I)}{r_{i+2} - r_{i+1}}$$

$$W_S = \frac{w_{ij}(r_I - r_{i+1}) + w_{i-1j}(r_{i+2} - r_I)}{r_{i+2} - r_{i+1}} ,$$

and VIP_{ij} and VIM_{ij} are similar to VMJ_{ij} and VPJ_{ij}.

REFERENCES

Arnold D.N., Brezzi F. and Fortin M., "A stable finite element for the Stokes equations", *Calcolo*, 21, 337–344(1984).

Babuška I., "The finite element method with Lagrange multipliers", *Numer. Math.*, 20, 179–192(1973).

Brezzi F., "On the existence, uniqueness and application of saddle point problems arising from Lagrangian multipliers", *RAIRO*, 8, 129–151(1974).

Carey G. and Oden J.T., *Finite Elements: Fluid Mechanics*, Vol. VI, Prentice–Hall Canada Inc., Toronto, 1986.

De Henau V.D., Raithby G.D. and Thompson B.E., "A total pressure correction for upstream weighted schemes", *Int. J. Numer. Meth. Fluids*, 9, 855–864(1989).

Dennis S.C.R. and Ng M., "Dual solutions for steady laminar flow through a curved tube", *Q. J. Mech. Appl. Math.*, 35, 305–324(1982).

Harlow F.H. and Welch J.E., "Numerical calculation of time–dependent viscous incompressible flow of fluids with free surface", *Physics of Fluids*, 8, 2182–2189(1965).

Ladyzhenskaya O.A., *Mathematical Theory of Viscous Incompressible Flow*, Gordon and Breach, New York, 1969.

Leonard B.P., "Locally modified QUICK scheme for highly convective 2–D and 3–D flows", *Numerical Methods in Laminar and Turbulent Flow*, Vol. 5, 35–47, ed. by Taylor C., Habashi U.G. and Haffez M.M., Pineridge Press Ltd., Swansea, U.K., 1987.

Macharthur J.W. and Patankar S.V., "Robust semidirect finite difference methods for solving the Navier–Stokes and energy equations", *Int. J. Numer. Meth. Fluids*, 4, 517–537(1984).

Masliyah J.H. and Nandakumar K., "Fully developed viscous flow and heat transfer in curved semicircular sectors", *AIChE J.*, 25(3), 478—487(1979).

Nandakumar K. and Masliyah J.H., "Bifurcation in steady laminar flow through curved tubes", *J. Fluid Mech.*, 119, 475—490(1982).

Nandakumar K., Masliyah J.H. and Law H., "Bifurcation in steady laminar mixed convection flow in horizontal ducts", *J. Fluid Mech.*, 152, 145—161(1985).

Neuberger A.W., "Error estimates and convergence acceleration of different discretization schemes", *Numerical Methods in Laminar and Turbulent Flow*, Vol. 5, 91—101, ed. by Taylor C., Habashi W.G. and Haffez M.M., Pineridge Press Ltd., Swansea, U.K., 1987.

Patankar S.V., *Numerical Heat Transfer and Fluid Flow*, Hemisphere Publishing Co., New York, 1980.

Patankar S.V. and Spalding D.B., "A calculation procedure for heat, mass and momentum transfer in three—dimensional parabolic flows", *Int. J. Heat Mass Transfer*, 15, 1787—1806(1972).

Raithby G.D. and Torrance K.E., "Upstream weighted differencing schemes and their applications to elliptic problem involving fluid flows", *Computers and Fluids*, 2, 191—206(1974).

Sankar S.R., Nandakumar K. and Masliyah J.H., "Oscillatory flows in coiled square ducts", *Physics of Fluids*, 31(6), 1348—1358(1988).

Schreiber R. and Keller H.B., "Driven cavity flows by efficient numerical techniques", *J. Comp. Phys.*, 49, 310—333(1983).

Tarbell J.M. and Samuels M.R., "Momentum and heat transfer in helical coils", *Chem. Eng. J.*, 5, 117—127(1972).

Yang Z. and Keller H.B., "Multiple laminar flows through curved pipes", *Appl. Numer. Math.*, 2, 257—271(1986).

Chapter 3.

Axially–Invariant Laminar Flow in Helical Pipes
with a Finite Pitch

Part 1. Theory and Loosely Coiled Pipes

88

3.0. SUMMARY

Axially—invariant incompressible flows of Newtonian fluids in helical pipes of constant circular cross—section with a finite pitch and a radius of coil are formulated and numerically studied by the Separation Method. The loose coiling analysis leads to two dominant parameters, namely Dean number $Dn = Re \sqrt{\lambda}$ and Germano number $Gn = Re\, \eta$, where Re is the Reynolds number, λ is the normalized curvature ratio and η is the normalized torsion. When studying the importance of the Germano number effects on the helical flow of large Dn, a third dimensionless group is evolved, $\gamma = \dfrac{Gn}{Dn^{3/2}} = \dfrac{\eta}{\sqrt{\lambda\, Dn}} = \dfrac{\eta}{\lambda^{3/4} Re^{\frac{1}{2}}}$.

For $Dn < 20$, the group $\gamma^{*} = \dfrac{Gn}{Dn^{2}} = \dfrac{\eta}{\sqrt{\lambda}\, Dn} = \dfrac{\eta}{\lambda Re}$ becomes the controlling parameter governing the flow transition between one— and two—vortex flows.

Numerical simulations with the full Navier—Stokes equations confirmed the theoretical findings. It is revealed that the torsion effect on the helical flow can be neglected when $\gamma \leq 0.01$. The critical value for which the secondary flow pattern changes from two vortices to one vortex is $\gamma^{*} > 0.039$ for $Dn < 20$.

3.1. Introduction

Laminar flow in helical pipes of constant circular cross—section is of practical importance in many branches of engineering in which pipe systems are used for transport and treatment of gases and liquids. The problem of the flow in a toroidal pipe, i.e., a helical pipe with a zero pitch, was dealt with extensively and drew great interest after the initial work by Dean (1927 & 1928). Most of the studies dealing with laminar flow in a torus concentrated on the limiting case of loose coiling where a/Rc approaches zero. Rc is the radius of the coil and a is the radius of the pipe. The mathematical limit of this case is of great interest as the flow is governed by a single parameter, namely Dean number, $D = \frac{G\rho a^3}{\mu^2}(\frac{2a}{Rc})^{1/2}$ with the axial pressure gradient G, fluid density ρ and dynamic viscosity of the fluid μ. Several different versions of Dean number have been defined. Since D involves the pressure gradient G, it is hardly a physical controlling parameter to be considered for a flow problem. A more common version of Dean number is defined by $Dn = Re \sqrt{a/Rc}$, where Re is the Reynolds number. For details, the reader is referred to the review articles dealing with the flow in a torus by Nandakumar & Masliyah (1986) and more recently, Berger (1991).

One of the interesting features of the flow through a toroidal pipe (torus) has been that dual or more solutions appear if Dn exceeds a certain critical value. It has been a challenge to compute the secondary solutions. The stationary four—vortex solution with the symmetry prescribed was obtained accidentally by Dennis & Ng (1982) and Yanase et al. (1989); through gradual geometrical change by Nandakumar & Masliyah (1982) and Daskopoulos & Lenhoff (1989) and with the method of continuation by Yang & Keller (1986). Nandakumar & Masliyah (1982) documented the flow properties with Dn and Rc. Doubts are shadowed on the work of Daskopoulos & Lenhoff (1989) and Yanase et al. (1989), in which the spectral

method was employed to solve the bi—harmonic type stream function equation. Not only is it difficult to justify any conditions at the center of the pipe to be imposed by a numerical scheme, but spurious modes appear (Daskopoulos & Lenhoff 1989) as well. Additional solutions are also presented by Yang & Keller (1986) and Daskopoulos & Lenhoff (1989) without the confirmation of each other. The characteristics of the developing flow is, however, still unknown.

Laminar flow in helical pipes of finite pitch was treated less extensively. Starting with Truesdell & Adler (1970), suggestion was made that an appropriate approximation might be obtained by replacing the curvature for a toroidal pipe by the curvature for the helical pipe under consideration, at least for coils of small pitch. This was continued by Manlapaz & Churchill (1980), who assumed the effects of non—orthogonality to be negligible in the limit of small pitch. Non—orthogonal helical systems were studied by Wang (1981) and Murata et al. (1981). Owing to the non—orthogonality of the coordinates, one must be specially careful in interpreting their results. To avoid the complexity associated with the non—orthogonal helical coordinate system as that noted by Murata et al. (1981), Germano (1982 & 1989) introduced a helical orthogonal coordinate system.

The complexity of the system drew many different explanations. Often apparently opposing results were obtained, which were resolved by Tuttle (1990). Wang (1981) found that for Re $= O(1)$ the torsion effect on the secondary flow is of $O(\eta)$. However, Murata et al. (1981) and Tuttle (1990) found that the torsion effect on the secondary flow is of $O(\lambda\eta)$. Germano (1982) stated that the torsion effect is of second order. In a later study, Germano (1989) found that the pipe torsion influences the secondary flow through the dimensionless group ηRe (denoted by T in his paper) for a non—circular geometry. For a circular geometry, Germano stated that no pure torsion effect of any order is to be expected. Kao (1987) found that $\eta \cdot (2\lambda)^{-\frac{1}{2}}$ is a controlling parameter determining whether the torsion can exert a $1\frac{1}{2}$

order effect and that for $\lambda \geq 0.4$ the nonlinear interactions become important.

For Re $= O(1)$, Wang (1981) found that the two recirculating cells become one when $\eta/\lambda \mathrm{Re} \geq 1/24$. The two recirculating cells (vortices) were in an up—and—down position when the helix axis is vertical. Kao's attempt to compute four—vortex type solutions failed. The state of understanding of laminar flow in helical pipes with finite pitch is relatively immature especially for large Reynolds number flows, where little work has been done.

The representation of the secondary flow is controversial, although Tuttle (1990) stated that the (pseudo—) secondary flow stream function is preferable. Murata et al. (1981) and Kao (1987) stated that no stream function—like property exists, which results in that the velocity vector plots must be introduced to represent the secondary flow. Wang (1981) was able to define a (pseudo—) secondary flow stream function using the physical covariant velocity components in the non—orthogonal coordinate system. This pseudo—secondary flow stream function was used by Germano (1982 & 1989) and by Tuttle (1990). However, Germano (1982 & 1989) preferred to present the secondary flow with the orthogonal velocity vectors. Wang (1981) and Tuttle (1990) presented the secondary flow with the pseudo—secondary flow stream function. Tuttle (1990) further qualified that the pseudo—secondary flow stream function is indeed a stream function property. Hence, as far as the secondary flow pattern is to be concerned, the pseudo—secondary flow stream function is a better choice than the orthogonal velocity vector.

However, one strong argument against the use of the pseudo—secondary flow stream function is that the value in the pseudo—secondary flow stream function can not represent the secondary flow strength when the torsion of the helical pipe is important. Germano (1989) noted that there is no pure torsion effect on the helical flow. The flow in a twisted straight full circular pipe is of Poiseuille type. The artificial torsion in the straight pipe results in an artificial swirling secondary flow.

Although the pseudo—secondary flow stream function can present the rotation imposed by the "twisted straight pipe" setup, the true secondary flow strength should be zero. However, the orthogonal velocity vectors cannot represent this setup as one is interested in.

In this study, the Separation Method (Chapter 2, or Liu & Masliyah 1992) is used to solve the problem of laminar Newtonian fluid flows in helical pipes having a non—zero pitch. The flow simulations are made with the Navier—Stokes equations constructed from the orthogonal helical coordinates after Germano (1982). A scale analysis is performed for the limiting case of loose coiling and the dominant dimensionless groups are identified. The argument over the representation of the secondary flow should be left for Chapter 4.

3.2. Mathematical formulations

A coordinate setup of the helical system is shown in Figure 3.1.
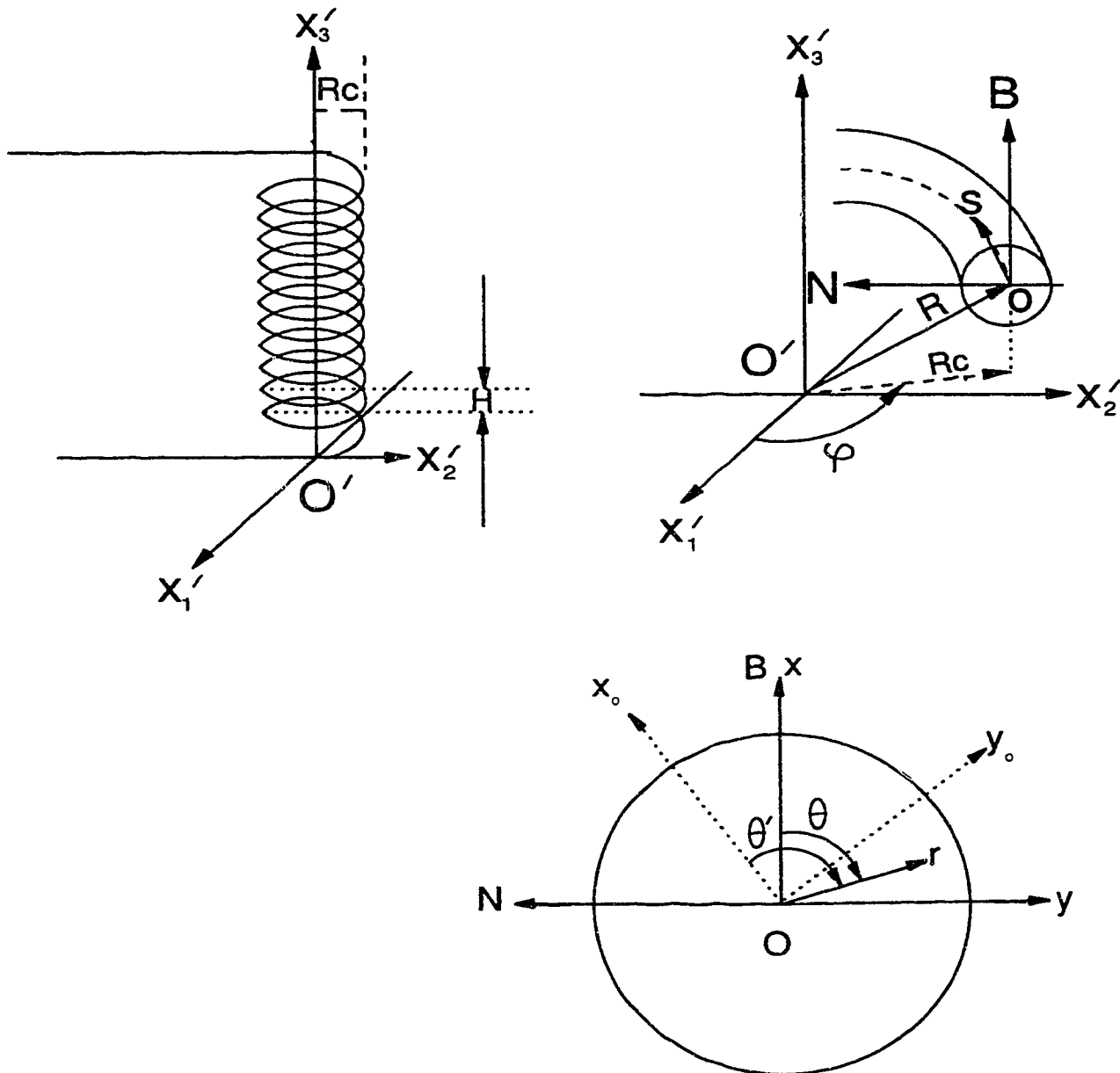
Fig. 3.1 The helical system set up.

A helical system can be established in reference to the master cartesian coordinate system $\vec{x}'$ (x'_1, x'_2, x'_3) and the local vectors originated on the generic curve of the helix as follows:

$$\vec{R} = (R_c \cos\varphi, \ R_c \sin\varphi, \ B \ s) \tag{3-1}$$

$$\vec{T} = \frac{d\vec{R}}{ds} = (-\sqrt{\kappa R_c} \sin\varphi, \ \sqrt{\kappa R_c} \cos\varphi, \ B) \tag{3-2}$$

$$\vec{N} = \frac{1}{\kappa} \frac{d\vec{T}}{ds} = (-\cos\varphi, -\sin\varphi, \ 0) \tag{3-3}$$

$$\vec{B} = \vec{T} \times \vec{N} = (B \sin\varphi, \ -B \cos\varphi, \ \sqrt{\kappa R_c}) \tag{3-4}$$

$$\varphi = \frac{s}{\sqrt{R_c^2 + (H/2\pi)^2}} \tag{3-5}$$

Where $B = (H/2\pi)/\sqrt{R_c^2 + (H/2\pi)^2}$; $\vec{R}$ is the global coordinate vector at the point of consideration O on the generic curve; the generic curve is the track of a particle moving along the center of the cross section of the helical pipe; $\vec{T}$ (shown as $\vec{s}$ in Figure 3.1); $\vec{N}$ and $\vec{B}$ are the tangent, normal and binormal to the generic curve at the point of consideration on the generic curve respectively; s is the curve length along the generic curve; κ and τ are the curvature and torsion; Rc and H are the radius of coil and the pitch of the helix respectively. The orthogonality of a helical system can be achieved by rotating the basis formed by $\vec{B}$ and $\vec{N}$ around the s axis.

A given point in the pipe can be mapped to the master cartesian system as follows:

$$\vec{x}' = \vec{R} + r\cos\theta' \ \vec{N} + r\sin\theta' \ \vec{B} \tag{3-6}$$

The metrics for the transformation are given by

$$g_{ij} = \frac{\partial x'_k}{\partial q_i} \cdot \frac{\partial x'_k}{\partial q_j}$$

(3–7)

where $q_1 = s$, $q_2 = r$, $q_3 = \theta$ and $\theta = \theta' + f(s)$. The basic equations of the curve theory

$$\frac{d\vec{N}}{ds} = \tau\vec{B} - \kappa\vec{T}$$

(3–8)

and

$$\frac{d\vec{B}}{ds} = -\tau\vec{N}$$

(3–9)

can be applied to derive the metrics of the orthogonal helical system. Here the curvature ratio is defined as

$$\kappa = \frac{Rc}{Rc^2 + (H/2\pi)^2}$$

(3–10)

and the torsion is given by

$$\tau = \frac{H/2\pi}{Rc^2 + (H/2\pi)^2}$$

(3–11)

By forcing $g_{ij} = 0$, for $i \neq j$, $i,j = 1, 2, 3$, we obtain the metrics:

$$\begin{cases} h_1 = g_{11}^{1/2} = 1 + \kappa r\sin\theta \\ h_2 = g_{22}^{1/2} = 1 \\ h_3 = g_{33}^{1/2} = r \end{cases}$$

(3–12)

where $\theta = \theta' - \tau s$, (s, r, θ') and its corresponding rectangular coordinates (s, x_o, y_o) are orthogonal. For details, the reader should refer to Appendix A.

The governing equations are first derived in the orthogonal system (s, r, θ') and transformed to the non—orthogonal system (s, r, θ) leaving the velocity components untouched. The transformation is necessary to eliminate the s—dependent coefficients and variable $\theta' - \tau s$ which always appears in place of θ. This allows an axially—invariant solution to be realizable if it exists. The variables are non—dimensionalized in the following manner:

$$s = \frac{s'}{a}, \quad r = \frac{r'}{a}, \quad t = \frac{\nu t'}{a^2}, \quad u = \frac{u'}{2U}, \quad v = \frac{v'}{2U}, \quad w = \frac{w'}{2U}, \quad p = \frac{ReP'}{4\rho U^2}$$

$$\text{and} \quad \lambda = \kappa a, \quad \eta = \tau a, \quad Re = \frac{2aU}{\nu}$$

Where a is the radius of the pipe, U is the average axial velocity, t is time, ν is kinematic viscosity, u is the axial velocity component (orthogonal s—directional component), v is the radial velocity component (r—direction), w is the angular velocity component (orthogonal θ'—directional component), λ is the curvature, η is the torsion, Re is the Reynolds number, p is the pressure. The primed variables are the dimensional quantities.

The final governing flow equations, after all the necessary substitution and rearrangement, become:

The continuity,

$$\frac{1}{h_1}(\frac{\partial u}{\partial s} - \eta\frac{\partial u}{\partial \theta}) + \frac{1}{rh_1}\cdot\frac{\partial(rh_1 v)}{\partial r} + \frac{1}{rh_1}\cdot\frac{\partial(h_1 w)}{\partial \theta} = 0 \qquad (3\text{--}13)$$

where h_1 is the metric coefficient in the axial (s—) direction and it is given by

$$h_1 = 1 + \lambda r \sin\theta \tag{3-14}$$

The general form of the momentum equations,

$$(M + d_\phi)\phi = S_\phi \tag{3-15a}$$

$$M\,\phi = \frac{\partial\phi}{\partial t} + \frac{1}{h_1}\frac{\partial}{\partial s}\left[(Re\,u - \lambda\,\eta\,r\,\frac{\cos\theta}{h_1^2})\phi - \frac{1}{h_1}\frac{\partial\phi}{\partial s}\right] + \frac{1}{rh_1}\cdot\frac{\partial}{\partial r}[rh_1(Re\,v\,\phi - \frac{\partial\phi}{\partial r})] +$$

$$\frac{1}{rh_1}\cdot\frac{\partial}{\partial\theta}[Re(h_1 w - \eta\,r\,u)\phi - \frac{h_1}{r}(1 + \frac{\eta^2 r^2}{h_1^2})\frac{\partial\phi}{\partial\theta}] + \frac{2\eta}{h_1^2}\frac{\partial^2\phi}{\partial s\,\partial\theta}$$

$$\tag{3-15b}$$

where ϕ stands for any velocity component, M denotes the momentum operator. The individual momentum equations are obtained by a specification of the velocity component ϕ, extra diagonal term d_ϕ and the source term S_ϕ.

s—momentum

$$\phi = u \tag{3-16a}$$

$$d_\phi = \frac{v\sin\theta + w\cos\theta}{h_1}\lambda\,Re + \frac{\lambda^2}{h_1^2} \tag{3-16b}$$

$$S_\phi = -\frac{1}{h_1}(\frac{\partial p}{\partial s} - \eta\frac{\partial p}{\partial\theta}) + \frac{1}{h_1^2}[2\lambda\sin\theta(\frac{\partial v}{\partial s} - \eta\frac{\partial v}{\partial\theta}) + 2\lambda\cos\theta(\frac{\partial w}{\partial s} - \eta\frac{\partial w}{\partial\theta}) +$$

$$\frac{\lambda\eta\cos\theta}{h_1}v - \frac{\lambda r + \sin\theta}{h_1}\lambda\eta w] \tag{3-16c}$$

r—momentum

$$\phi = v \tag{3-17a}$$

$$d_\phi = \frac{1 + 2h_1\lambda r\sin\theta}{r^2 h_1^2} \tag{3-17b}$$

$$S_\phi = -\frac{\partial p}{\partial r} + Re(\frac{\lambda\sin\theta}{h_1}u^2 + \frac{w^2}{r}) - \frac{2\lambda\sin\theta}{h_1^2}(\frac{\partial u}{\partial s} - \eta\frac{\partial u}{\partial\theta}) + \frac{\lambda\eta\cos\theta}{h_1^2}u -$$

$$\frac{2}{r^2}\frac{\partial w}{\partial\theta} - \frac{2h_1 - 1}{rh_1^2}\lambda\cos\theta w \tag{3-17c}$$

θ—momentum

$$\phi = w \qquad (3\text{--}18a)$$

$$d_\phi = Re\frac{v}{r} + \frac{1}{h_1^2}(\lambda^2 + \frac{2h_1-1}{r}) \qquad (3\text{--}18b)$$

$$S_\phi = -\frac{\partial p}{\partial \theta} + Re\frac{\lambda\cos\theta}{h_1}u^2 - \frac{2\lambda\cos\theta}{h_1^2}(\frac{\partial u}{\partial s} - \eta\frac{\partial u}{\partial \theta}) - \frac{\lambda r+\sin\theta}{h_1^3}\lambda\eta u +$$

$$\frac{3h_1-1}{r^2h_1^2}\frac{\partial v}{\partial \theta} + \frac{1}{rh_1^2}\lambda\cos\theta v \qquad (3\text{--}18c)$$

The boundary is defined by the pipe wall. Although a numerical scheme with a polar coordinate system would prefer to have a condition set at the center of the pipe, there are no conditions that can fit such a need. We can only say that the properties are continuous at the center. Hence, the center point of the pipe is simply an interior point of the computational domain and is not treated differently. The boundary and necessary conditions are:

$$u = v = w = 0 \qquad \text{at } r = 1;$$

$p = 0$ at one reference point inside the computational domain;

$$\frac{\int_0^{2\pi}d\theta\int_0^1 r\ u\ dr}{\pi} = \frac{1}{2} \qquad \text{(from the nondimensionalization)} \qquad (3\text{--}19)$$

When the flow reaches the fully—developed (i.e., axially—invariant) stage, the transverse velocity field can be represented by a field scalar quantity, ψ, as follows:

$$rh_1v = -\frac{\partial \psi}{\partial \theta} \qquad (3\text{--}20a)$$

$$h_1w - \eta ru = \frac{\partial \psi}{\partial r} \qquad (3\text{--}20b)$$

To the same extent as ordinary two—dimensional flows, the field scalar quantity ψ can be called the pseudo—secondary flow stream function. To compute the pseudo—secondary flow stream function, we integrate equation (3—20b) after the velocity field is obtained.

The contour presentation of the numerical simulations can be explained as follows with the setup shown in Figure 3.2. The scales are shown on the rectangles. The directions are indicated as x and y of the non—orthogonal coordinate system. However, the directions x and y and the other texts, such as inner wall, outer wall, etc. and pipe origin are not shown on the actual contour plots. The same directions are implied by the setup. The pipe boundary is shown as a full circle. The contour lines are equally spaced in the variable of interest (the axial velocity u, the pressure p or the pseudo—secondary flow stream function ψ), unless otherwise specified.
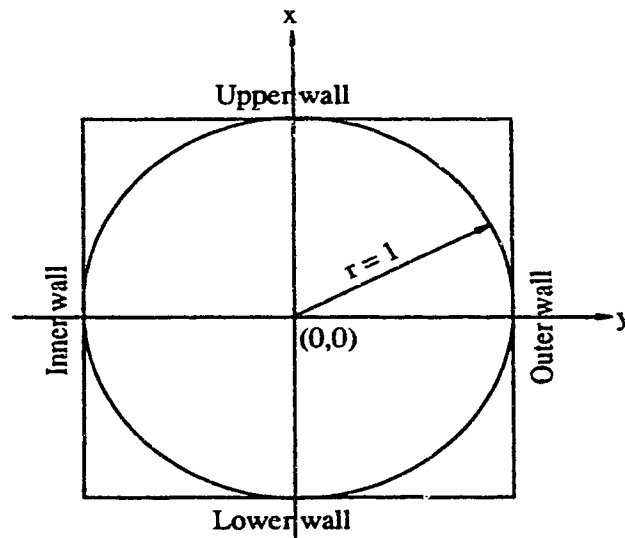
Fig. 3.2. Orientation layout for contour plots.

3.3. Loose coiling analysis

The formulation of the flow in a helical pipe indicates that there are three dimensionless parameters involved, namely, the curvature ratio λ, the torsion η and the Reynolds number Re. To identify the dominant parameters, we consider loosely coiled pipes under high Reynolds number, i.e.,

$$\lambda \rightarrow 0 \quad \text{and} \quad \eta \rightarrow 0, \quad \text{while} \quad \text{Re} \rightarrow +\infty, \ \lambda \neq 0$$

The above loose coiling conditions can be obtained by having either a large radius of coil Rc or a large pitch H. Under the above conditions, we can rearrange the governing equations to obtain the dominant parameters. Let's introduce the following rescaled velocity field:

$$u_1 = u, \quad u_2 = \text{Re } v, \quad u_3 = \text{Re } w, \quad P = \text{Re } p \tag{3-21}$$

The above rescaling is necessary since for a smaller λ, the secondary flow field is weaker for a given main flow, i.e. Re = fixed. For a fixed secondary flow and $\lambda \rightarrow 0$, Re $\rightarrow \infty$, the above rescaling can make the new secondary flow field variables to be comparable with the main flow field variables.

In this study, our focus is on the axially–invariant flows. Hence, we omit the axial variation and introduce the following pressure gradient parameter:

$$G = -\frac{\partial p}{\partial s} \tag{3-22}$$

For $\lambda \rightarrow 0$, $\eta \rightarrow 0$ and Re $\rightarrow +\infty$, we obtain:

The metrics of the axial axis: $\quad h_1 = 1 + \lambda r \sin\theta \rightarrow 1$

The continuity:

$$- \mathrm{Re}\ \eta \frac{\partial u_1}{\partial \theta} + \frac{1}{r} \cdot \frac{\partial (r u_2)}{\partial r} + \frac{1}{r} \cdot \frac{\partial u_3}{\partial \theta} = 0 \qquad (3\text{--}23)$$

Momentum equation:

$$(\mathbf{M} + \mathrm{d}_\phi)\ \phi = S_\phi \qquad (3\text{--}15a)$$

$$\mathbf{M}\phi = \frac{\partial \phi}{\partial t} + \frac{1}{r}\frac{\partial}{\partial r}[r(u_2 \phi - \frac{\partial \phi}{\partial r})] + \frac{1}{r}\cdot\frac{\partial}{\partial \theta}[(u_3 - \mathrm{Re}\ \eta\ r\ u_1)\phi - \frac{1}{r}\frac{\partial \phi}{\partial \theta}]$$

$$(3\text{--}24)$$

s—momentum

$$\phi = u_1, \qquad \mathrm{d}_\phi = 0, \qquad S_\phi = G \qquad (3\text{--}25)$$

r—momentum

$$\phi = u_2, \qquad \mathrm{d}_\phi = \frac{1}{r^2}, \qquad S_\phi = -\frac{\partial P}{\partial r} + \mathrm{Re}^2 \lambda \sin\theta\ u_1^2 + \frac{u_3^2}{r} + \mathrm{Re}\lambda\eta\cos\theta u_1 - \frac{2}{r^2}\cdot\frac{\partial u_3}{\partial \theta}$$

$$(26)$$

θ—momentum

$$\phi = u_3, \qquad \mathrm{d}_\phi = \frac{u_2}{r} + \frac{1}{r^2}, \qquad (27a)$$

$$S_\phi = -\frac{\partial P}{\partial \theta} + \mathrm{Re}^2 \lambda \cos\theta\ u_1^2 - \mathrm{Re}(\lambda r + \sin\theta)\lambda\eta u_1 + \frac{2}{r^2}\frac{\partial u_2}{\partial \theta} \qquad (27b)$$

From equations (3–23) ~ (3–27), we can see that four groups emerge: namely, Re η, Re$^2\lambda$, Re $\eta\,\lambda$ and Re $\lambda^2\,\eta$. The latter two groups are of lower magnitude for $\lambda \to 0$, $\eta \to 0$ and Re $\to +\infty$. The two groups that are of higher magnitude are Re η and Re$^2\lambda$. The first group can be identified as the contribution of the "twisting" forces in a helical pipe and the second group can be related to the centrifugal forces. We define the first group as Germano number, Gn, where

$$Gn = Re\ \eta = Re\ \frac{a\left(\frac{H}{2\ \pi}\right)}{Rc^2 + \left(\frac{H}{2\ \pi}\right)^2} \tag{3–28}$$

Since the "twisting" forces that make a rotating fluid element twist are proportional to $\rho\eta U^2$ and the viscous forces are proportional to $\frac{\mu\ U}{a}$, it follows that the Germano number Gn is a direct measure of the ratio of the "twisting" forces to the viscous forces. In other words, Germano number is a measure of the torsion effect. When Germano number Gn is small enough to be negligible, the helical system reduces to the Dean problem.

We define a generalized Dean number as

$$Dn = Re\ \sqrt{\lambda} = Re\ \left[\frac{a\ Rc}{Rc^2 + \left(\frac{H}{2\ \pi}\right)^2}\right]^{\frac{1}{2}} \tag{3–29}$$

The parameter Dn is sometimes referred to as Helical number (He) or a modified Dean number in the literature. For simplicity, we will refer to it as the Dean number. In the limiting case of H = 0 ($\eta \equiv 0$), Dn becomes exactly the same as the Dean number defined by early investigators. Since the inertia forces are proportional to ρU^2, the centrifugal forces are proportional to $\rho\lambda U^2$ and the viscous forces are proportional to $\frac{\mu\ U}{a}$, it follows that the square of the Dean

number, as it appears in the equations, is a direct measure of the product of the ratio of the centrifugal forces to the viscous forces and the ratio of the inertia forces to the viscous forces. The centrifugal forces make the fluid element move toward the outer wall. To bring the fluid element back toward inner wall, the viscous forces take the effect at the inertial and the centrifugal forces negligible region (near the wall). Hence, the flow Dean number is also measure of the secondary flow strength.

After introducing Germano number and the generalized Dean number and making the loose coiling assumption, the reduced flow equations become:

The continuity,

$$\frac{1}{r}\cdot\frac{\partial(r u_2)}{\partial r} + \frac{1}{r}\cdot\frac{\partial(u_3 - Gn\ r\ u_1)}{\partial \theta} = 0 \tag{3-30}$$

Momentum operator,

$$M\phi = \frac{\partial\phi}{\partial t} + \frac{1}{r}\cdot\frac{\partial}{\partial r}[r(u_2\ \phi - \frac{\partial\phi}{\partial r})] + \frac{1}{r}\cdot\frac{\partial}{\partial \theta}[(u_3 - Gn\ r\ u_1)\ \phi - \frac{1}{r}\frac{\partial\phi}{\partial \theta}] \tag{3-31}$$

s—momentum

$$\phi = u_1, \qquad d_\phi = 0, \qquad S_\phi = G \tag{3-32}$$

r—momentum

$$\phi = u_2, \qquad d_\phi = \frac{1}{r^2}, \qquad S_\phi = -\frac{\partial P}{\partial r} + Dn^2 u_1^2 \sin\theta + \frac{u_3^2}{r} + \frac{2}{r^2}\cdot\frac{\partial u_3}{\partial \theta} \tag{3-33}$$

θ—momentum

$$\phi = u_3, \qquad d_\phi = \frac{u_2}{r} + \frac{1}{r^2}, \qquad S_\phi = -\frac{\partial P}{\partial \theta} + Dn^2 u_1^2 \cos\theta + \frac{2}{r^2}\frac{\partial u_2}{\partial \theta} \tag{3-34}$$

Hence, from equations (3–30) – (3–34), we observe that only two newly defined parameters Gn and Dn are present in the governing flow equations. It is now obvious that, if Germano number is negligible, the loosely coiled helical problem reduces to the original Dean problem.

It is of interest to note that Germano number always appears in the form of $(u_3 - Gn\ r\ u_1)$ as seen from equations (3–30) ~ (3–34). Since the norm of u_3 and u_1 are functions of Dn, it becomes necessary to relate the Germano number and the Dean number in order to find out when the Germano number is important. To fulfill this task, we let

$$\xi = u_3 - Gn\ r\ u_1 \tag{3–35}$$

where ξ can be considered as a body–centered angular velocity component. As noted by Tuttle (1990), ξ is a transverse velocity component defined by the pseudo–secondary flow stream function ψ. Although ξ is not an orthogonal velocity component, it is nevertheless the momentum / energy advection velocity in the azimuthal direction. Hence, the importance of the Germano number is to be detected from the momentum equations. We apply the M operator as defined by equation (3–31) on equation (3–35) and take the norm of both sides, we obtain

$$||M\xi|| = ||Mu_3 - Gn\ M\ ru_1|| \tag{3–36}$$

From equation (3–34), we have

$$||Mu_3|| = ||S_{u_3}|| \propto Dn^2 \tag{3–37}$$

From equation (3–32), we have

$$||Mru_1|| = ||rS_{u_1}|| \propto G \tag{3–38a}$$

Since the normalized pressure gradient $G \propto Dn^{\frac{1}{2}}$ for large Dn and negligible

torsion effect, see Nandakumar & Masliyah (1986), equation (3–38a) becomes

$$||Mru_1|| \propto Dn^{\frac{1}{2}} \qquad (3\text{–}38b)$$

The absolute values of individual momentum norms are not of concern. However, the relative order is important to elucidate the significance of Gn. Combining equations (3–36) − (3–38b) yields

$$||M\xi|| = A_1(Dn^2 - A_2 \, Gn \, Dn^{\frac{1}{2}}) \qquad (3\text{–}39)$$

or

$$||M\xi|| = A_1 \, Dn^2(1 - A_2 \, Gn \, Dn^{-3/2}) \qquad (3\text{–}40)$$

Hence, the importance of Gn for a given Dn becomes obvious from equation (3–40). In order for the Germano number to have a noticeable influence on the helical flow field, $Gn \, Dn^{-3/2}$ must be large, the magnitude of which is to be determined by the flow field simulations. To account for this relative importance, we define a new helical flow group γ

$$\gamma = \frac{Gn}{Dn^{3/2}} = \frac{\eta}{\sqrt{\lambda \, Dn}} \qquad (3\text{–}41)$$

It is now obvious that the Dean problem becomes a special case of the loose coiling approximation with $\gamma << 1$. Note that the analysis is based on the premise that the secondary flow is present, i.e., centrifugal forces cannot be neglected. Hence, we would hope to qualitatively describe the helical flow field with the Dean flow (toroidal flow) field in the limit of

$$\lambda \to 0, \quad Re > O(\lambda^{-1/2}) \quad \text{and} \quad \gamma \to 0 \qquad (3\text{–}42)$$

where $Re > O(\lambda^{-1/2})$ reads that Re is of order greater than $\lambda^{-\frac{1}{2}}$, which means that the Dean number is large. $\gamma \to 0$ means that the Germano number is very small

as compared with the Dean number. It is understood that the curvature ratio can be small but not identically zero, at which the pipe is straight.

The expression for γ at large Dn was determined using the fact that G is proportional to the square root of Dn. The uniqueness of γ to govern the torsion effect on the helical flow is expected to fail when Dn is small. For very small Dn, the axial pressure gradient is relatively constant with respect to Dn. Hence, the equation (3–38a) must be reconsidered to reflect the variation of G with Dn at low Dean number flows.

Using the fact that G is relatively constant for small Dn flows, equations (3–36) ∼ (3–38a) can be combined to yield

$$||\mathbf{M}\xi||^* = A_1^* \, Dn^2(1 - A_2^* \, Gn \, Dn^{-2}) \tag{3--43}$$

where * denotes small Dn. Hence, for very small Dn the torsion effect is governed by

$$\gamma^* = \frac{Gn}{Dn^2} = \frac{\eta}{\sqrt{\lambda} \, Dn} = \frac{\eta}{\lambda \, Re} \tag{3--44}$$

It is not surprising that for low Dn flows, the parameter γ^* turned out to be the flow transition controlling group as was found by Wang (1981).

For large Dn flows, it is then expected that γ would characterize the transition from a torus–like flow to a swirl–like flow. For small γ, the flow is torus–like and for large γ the flow is swirl–like (or saddle flow, Germano 1989). For a given helical pipe geometry, i.e., fixed η and λ, equation (3–41) indicate that the type of flow is then influenced by the flow Dean number. For large Dn, γ becomes small and hence the flow should be a torus–like type. On the other hand, when Dn is small, γ becomes large and the flow can be of a swirl–like (or saddle flow) type. The torus–like flow can be identified as a two–vortex flow and the swirl–like is a one–vortex flow. Such profiles may be found in Wang (1981) and Tuttle (1990) for small Dn flows. Similar arguments can be stated for γ^*.

It can be drawn from the above derivation that γ is proportional to $\frac{Gn}{Dn^2} fRe$. It follows that the flow pattern transition parameter γ is a direct measure of the product of the ratio of the twisting forces to the centrifugal forces and the ratio of the viscous forces to the inertial forces and the ratio of the flow driving forces to the inertial forces. This physical implication of γ makes it clear that when γ is large, the centrifugal forces and the inertial forces become less important. Hence, similarity of helical flow structure is expected to relate to γ rather than η or Gn when the torsion effect is of concern.

3.4. Numerical Results and Discussions

The numerical method used here is the Separation Method of Chapter 2 (or Liu & Masliyah 1991). The advantage of this technique is that a m—dimensional problem is divided into m one—dimensional subproblems upon each treatment. The spurious pressure modes are eliminated by a careful nodal and interpolate arrangement. For details, the reader is to refer to Chapter 2 (or Liu & Masliyah 1992). The mesh size used in the computations is: n25x26fu for $Dn \leq 20$ and $Dn = 50$, n25x32fu for $20 < Dn \leq 1000$, n60x40fu for $Dn = 2000$ and n100x50fu for $Dn = 5000$, unless otherwise mentioned specifically. See the appendix for the nomenclature. It should be stressed that all the numerical results are based on the governing equations with the full range of λ and η, i.e., no loose coiling is introduced to the governing equations.

In this Chapter, we focus on small torsion and small curvature ratio (including loose coiling) helical flows. The large torsion and curvature ratio effects are treated in Chapter 4.

3.4.1 λ and γ effects on helical flows of $Dn = 100$, $\lambda \leq 0.01$, $\gamma \leq 0.01$.

It has been shown analytically in the previous section for loose coiling analysis that under the conditions of $\lambda \rightarrow 0$, $\gamma \rightarrow 0$ and $Re > O(\lambda^{-1/2})$, the Dean number ($Dn = Re\sqrt{\lambda}$) has the dominant effect on the axially—invariant flow behavior. In this section, selected numerical simulations will be made to reveal the significance of Dn.

The solution characteristics for small torsion and small curvature ratio helical pipes for $Dn = 100$, $\lambda \leq 0.01$ and $\gamma \leq 0.01$ are shown in Table 3.1. fRe is defined as

$$fRe = -4\frac{dp}{ds} = -\frac{aRe}{\rho U^2}\frac{dp'}{ds'} \qquad (3\text{--}45)$$

where f is the Fanning friction factor. $u_{0,0}$ is the axial velocity at the center of the pipe, u_{max}, r_{max} and θ_{max} are the maximum axial velocity and its location. p_{max} and p_{min} are the maximum and the minimum (infimum) pressure difference from the pipe center across the pipe.

It is clear from Table 3.1 that the numerical results show good agreement with the theoretical analysis. The axial pressure gradient fRe, $u_{0,0}$, u_{max}, r_{max} and θ_{max} are relatively constant at a given Dn value despite the changes in Re, λ and η. Owing to scale difference in the pressure and the pseudo--secondary flow stream

Table 3.1. Helical flow properties for Dn = 100, $\gamma \leq 0.01$, and $\lambda \leq 0.01$.

Rc	H	η	100γ	fRe	$u_{0,0}$	u_{max}	r_{max}	θ_{max}	p_{max}	$-p_{min}$
for $\lambda = 0.01$, Re=1000										
100	0	0	0	23.90	.6306	.8755	.6110	1.571	5.348	1.666
99.99	6.283	.0001	.01	23.90	.6305	.8756	.6110	1.570	5.348	1.666
99.01	62.21	.001	.1	23.90	.6305	.8756	.6111	1.567	5.344	1.665
96.15	120.8	.002	.2	23.91	.6305	.8756	.6110	1.562	5.349	1.665
80	80π	.005	.5	23.91	.6304	.8755	.6110	1.549	5.352	1.664
50	100π	.01	1	23.92	.6301	.8750	.6111	1.527	5.363	1.660
for $\lambda = 0.0025$, Re=2000										
400	0	0	0	23.85	.6301	.8783	.6130	1.571	2.693	.8251
320	320π	0.5λ	.25	23.85	.6301	.8783	.6130	1.560	2.694	.8251
for $\lambda = 0.000625$, Re=4000										
1600	0	0	0	23.83	.6300	.8790	.6135	1.571	1.349	.4117
1280	1280π	0.5λ	.125	23.83	.6300	.8790	.6135	1.565	1.349	.4117

a. $\lambda=.01$, $\gamma=0$, $\eta=0$

b. $\lambda=.01$, $\gamma=.005$, $\eta=.005$

c. $\lambda=.01$, $\gamma=.01$, $\eta=.01$

d. $\lambda=.0025$, $\gamma=0$, $\eta=0$

e. $\lambda=.0025$, $\gamma=0.0025$, $\eta=0.00125$

f. $\lambda=.000625$, $\gamma=0$, $\eta=0$
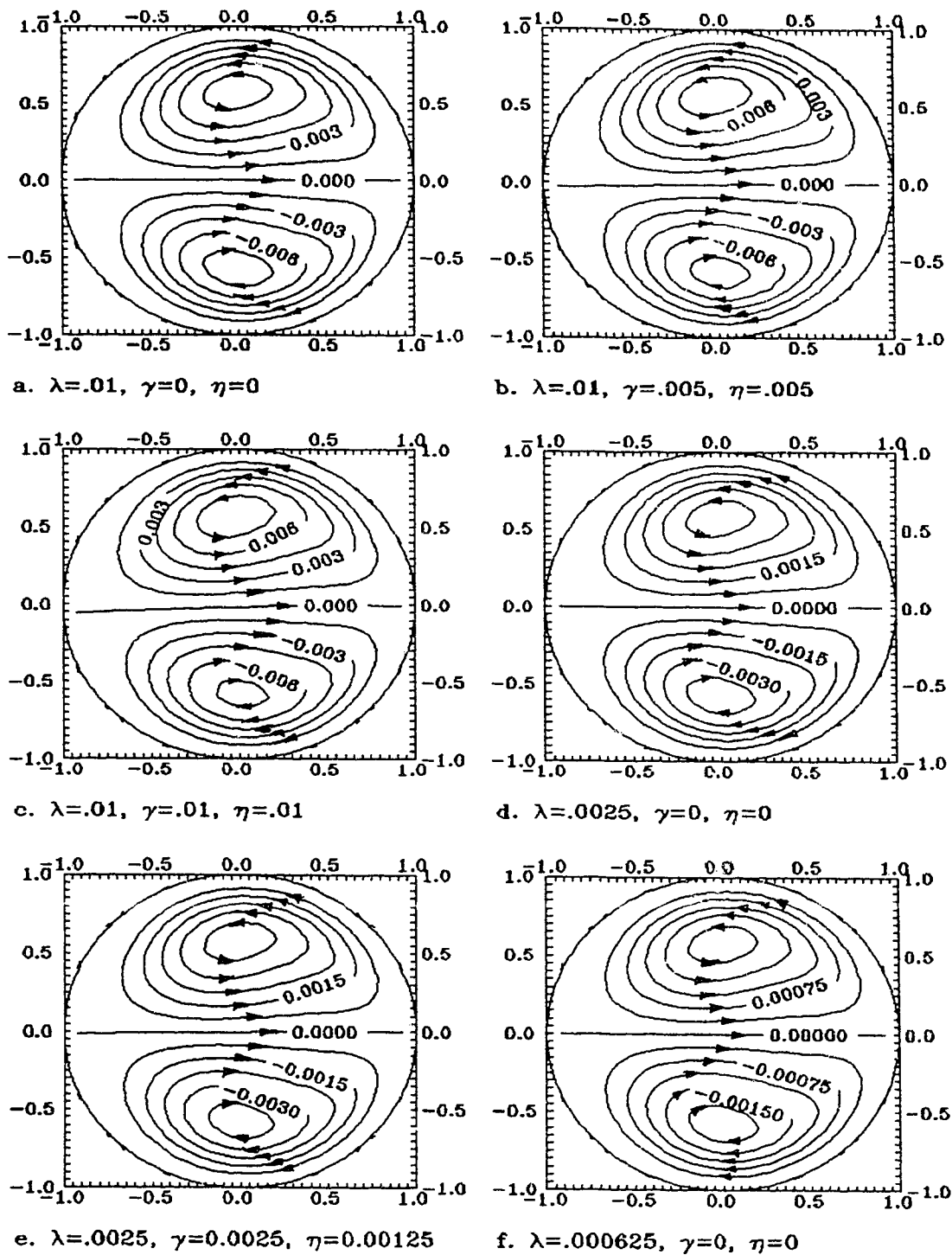
Fig. 3.3.   Effect of variation of η and λ on secondary flow patterns for Dn = 100, $\gamma \leq 0.01$, $\lambda \leq 0.01$. (Rc, H) = a. (100, 0); b. (80, 80π); c. (50, 50π); d. (400,0); e. (320, 320π); f. (1600,0).

a. $\lambda=.01$, $\gamma=0$, $\eta=0$

b. $\lambda=.01$, $\gamma=0.005$, $\eta=0.005$

c. $\lambda=.01$, $\gamma=0.01$, $\eta=0.01$

d. $\lambda=.0025$, $\gamma=0$, $\eta=0$

e. $\lambda=.0025$, $\gamma=.0025$, $\eta=.00125$

f. $\lambda=.000625$, $\gamma=0$, $\eta=0$
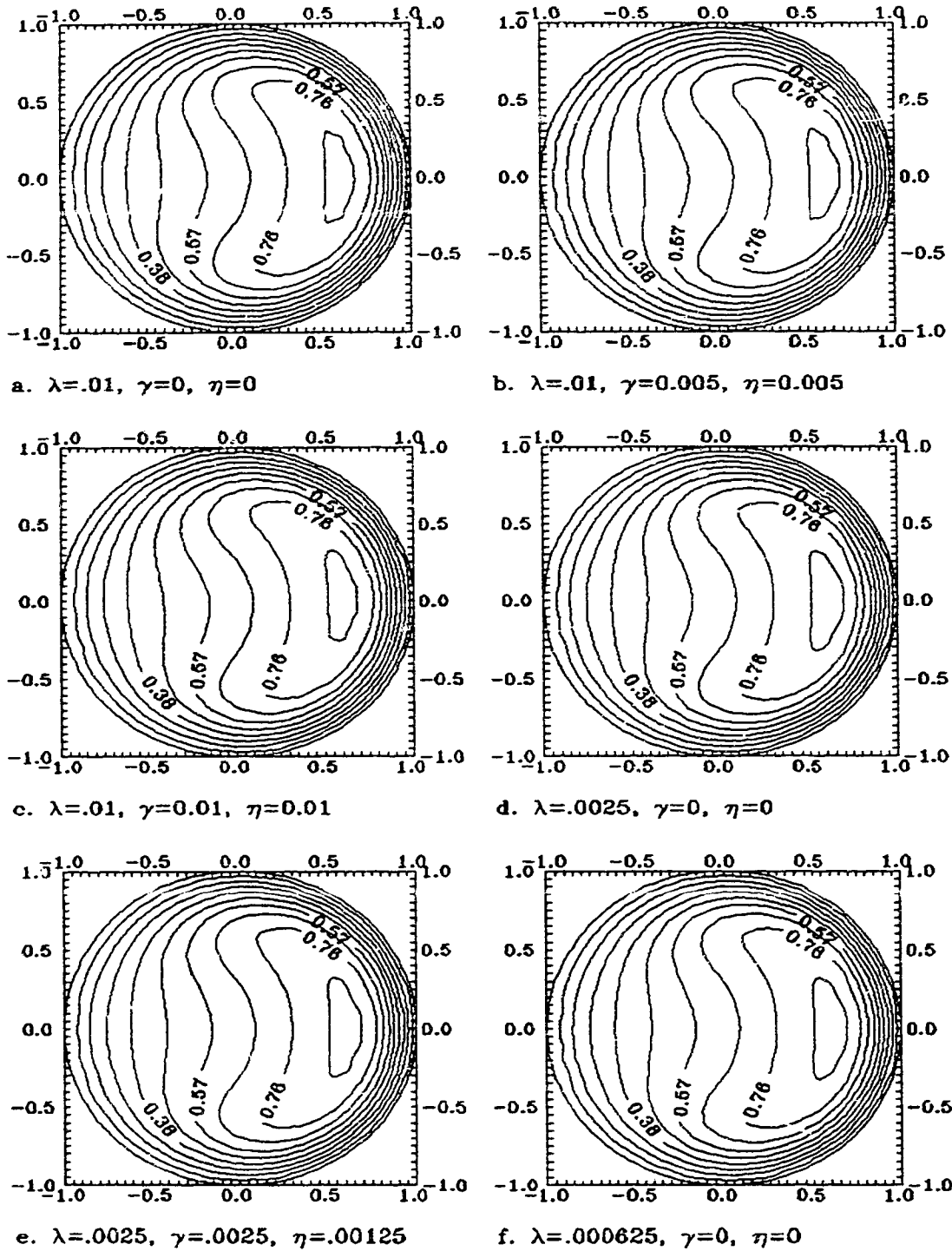
Fig. 3.4. Effect of variation of η and λ on axial velocity isoplethes for $Dn = 100$, $\gamma \leq 0.01$, $\lambda \leq 0.01$. (Rc, H) = a. (100, 0); b. (80, 80π); c. (50, 100π); d. (400, 0); e. (320, 320π); f. (1600, 0).

a. $\lambda=.01$, $\gamma=0$, $\eta=0$

b. $\lambda=.01$, $\gamma=.005$, $\eta=.005$

c. $\lambda=.01$, $\gamma=.01$, $\eta=.01$

d. $\lambda=.0025$, $\gamma=0$, $\eta=0$

e. $\lambda=.0025$, $\gamma=.0025$, $\eta=.00125$
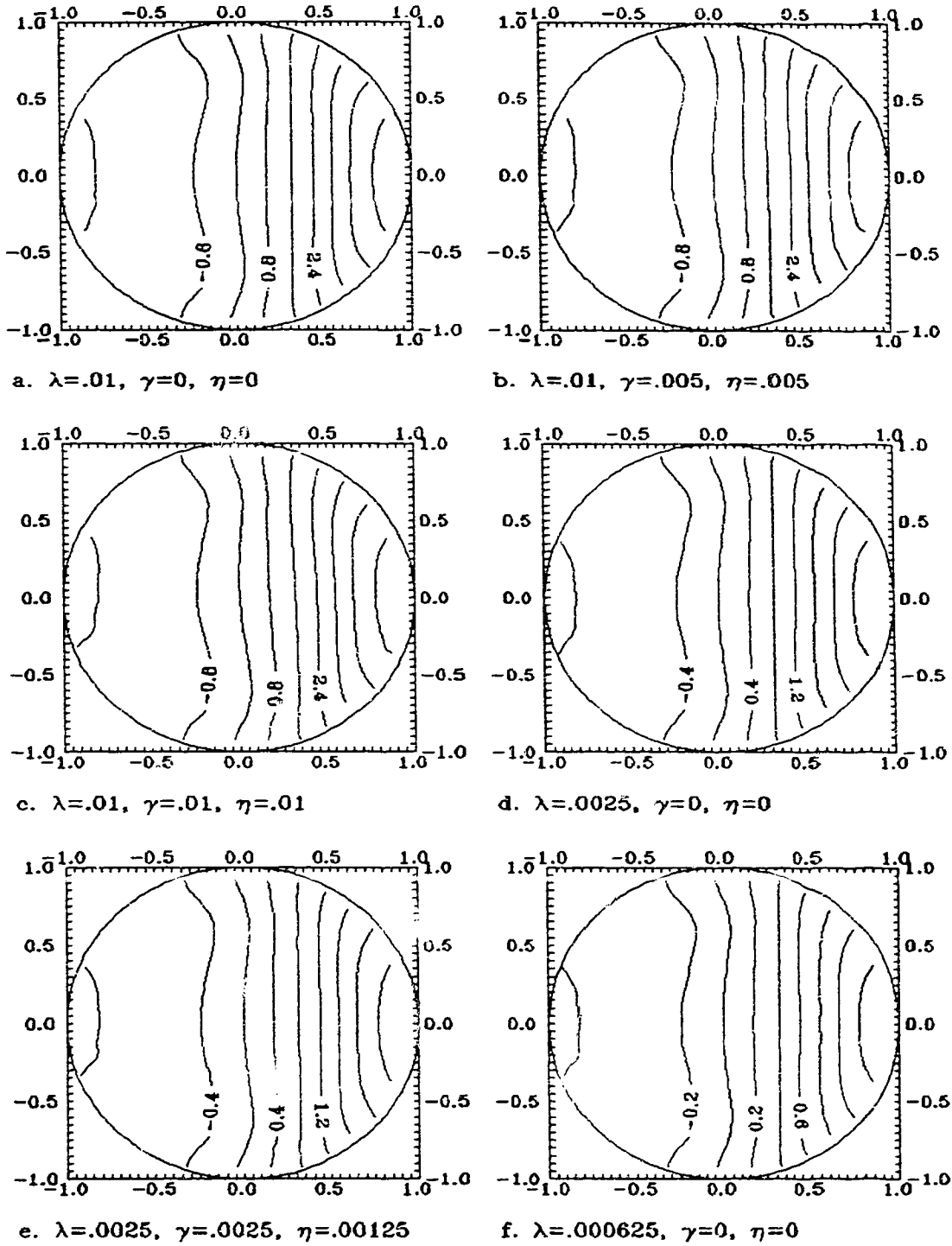
f. $\lambda=.000625$, $\gamma=0$, $\eta=0$

Fig. 3.5. Effect of variation of η and λ on pressure contours for $Dn = 100$, $\gamma \leq 0.01$ and $\lambda \leq 0.01$. (Rc, H) = a. (100, 0); b. (80, 80π); c. (50, 100π); d. (400, 0); e. (320, 320π); f. (1600, 0).
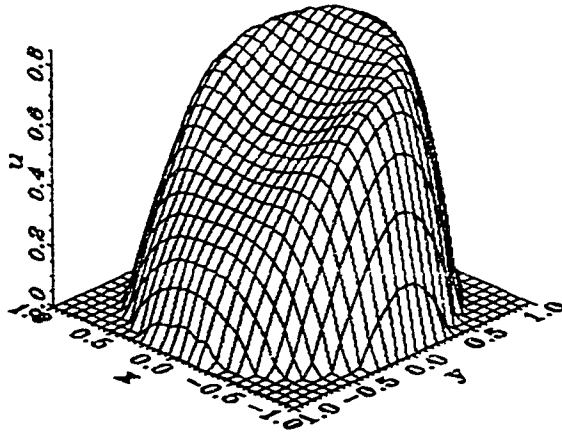
a. $\lambda=.01$, $\gamma=0$, $\eta=0$
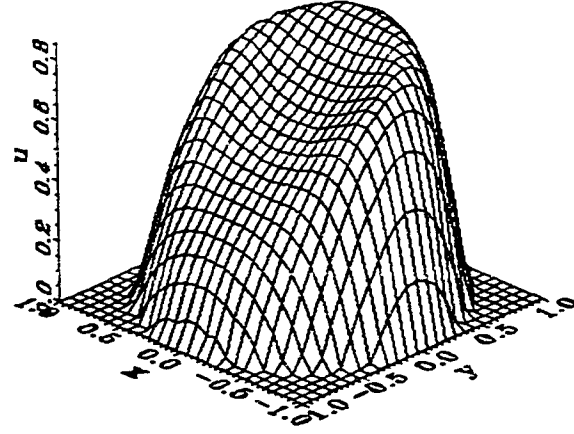
b. $\lambda=.01$, $\gamma=.005$, $\eta=.005$
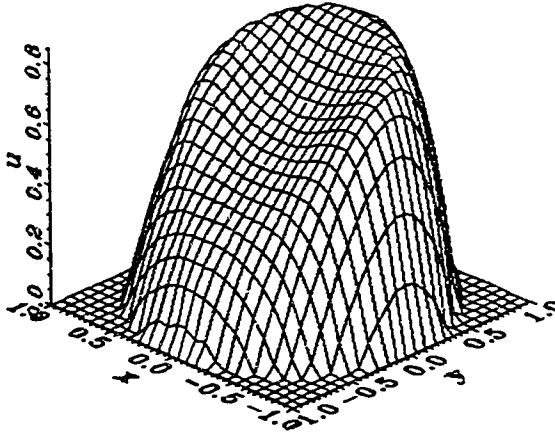
c. $\lambda=.01$, $\gamma=.01$, $\eta=.01$
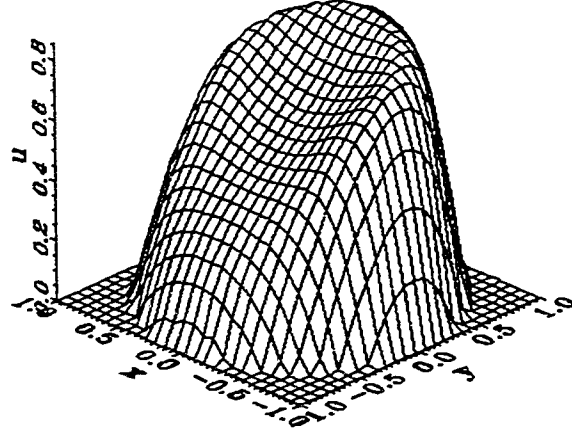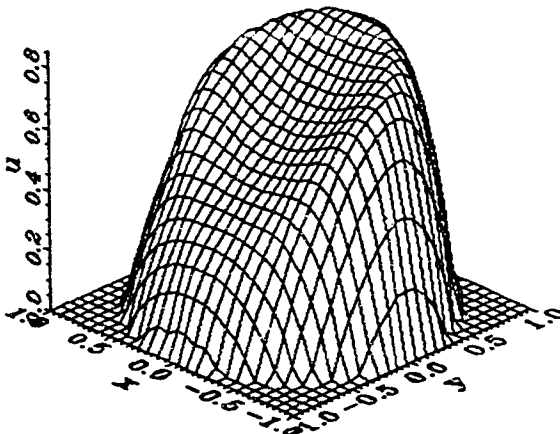
d. $\lambda=.0025$, $\gamma=0$, $\eta=0$

e. $\lambda=.0025$, $\gamma=.0025$, $\eta=.00125$
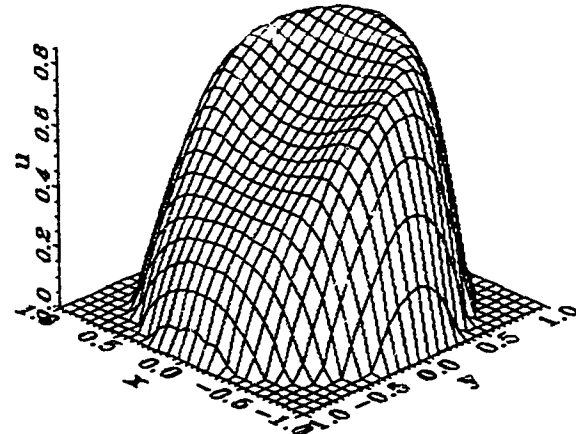
f. $\lambda=.000625$, $\gamma=0$, $\eta=0$

Fig. 3.6. Effect of variation of η and λ on axial velocity profiles for $Dn = 100$, $\gamma \leq 0.01$ and $\lambda \leq 0.01$.

function, the values of p_{max} and p_{min} presented in Table 3.1 are different as λ changes. Had we rescaled the secondary velocity and pressure fields by multiplying them with $\lambda^{-1/2}$ or Re as that was indicated in the loose coiling analysis section, all the quantities in Table 3.1 would look almost identical, irrespective of the individual values of λ and η. This is obvious by comparing the product of the pressure and Re for different values of Re.

Under the condition of loose coiling and small γ, Figures 3.3 to 3.6 show the contours of various flow characteristics of the flow in a helical pipe. The Dean number is Dn = 100. The range of λ, η and γ is similar to that shown in Table 3.1. In all the cases, the flow patterns are very similar indicating once again that as long as the loose coiling approximation is met and $\gamma \leq 0.01$, the flow corresponds to a torus–like flow.

For example, if one is to compare Figures 3.3d–3.6d for a helical pipe having a geometry of a torus with Rc=400 with the respective Figures 3.3e–3.6e for a helical pipe having Rc = 320 and H = 320π, one would notice similar flow behavior even though the second case has H/Rc = π. In all cases, a = 1 is implied.

3.4.2 Dean number effect on helical flows of a fixed pipe geometry.

To proceed with the examination of the Dean number effect on the helical flow, the solution properties for small torsion helical pipes with various Dean numbers and helical geometries are shown in Table 3.2. Δp_{max} is the maximum pressure difference across the pipe. For a comparison, some friction factor values from the literature are listed and denoted by fRe,prv.

In the limit of zero pitch, $\eta = 0$, i.e., for toroidal flow, one calculation is made with the same conditions as that of Truesdell & Adler (1970) at Dn = 122.9, $\lambda = 0.01$, $\eta = 0$. The agreement between our result and that of Truesdell & Adler (1970) is relatively good, with a deviation of about 2%. More comparisons are made

with the study of Austin & Seader (1973). It is found that at small Dn, the results are in better agreement with those of Austin & Seader and Manlapaz & Churchill (1980). However, the results of Austin & Seader are on the higher side and the results of Manlapaz & Churchill are on the lower side. To compare with the more accepted fRe values, we calculated the case of Dn = 371.4, λ = 0.01, η = 0 to

Table 3.2. Dean number effect under small torsion

Rc	H	Re	λ	η	100γ	Dn	fRe	u_{max}	Δp_{max}	fRe,prv
16	4	.9588	.0624	.0025	4*15	.2395	16.00	.9999	.0493	
16	4	1.103	.0624	.0025	3*606	.2756	16.00	1.000	.0567	
100	100	3.835	.0098	.0016	4*15	.3787	16.00	1.000	.0308	
100	100	4.414	.0098	.0016	3*606	.4359	16.00	.9999	.0354	
50	500	38.35	.0057	.0090	4*15	2.882	16.00	.9999	.1786	
50	500	44.14	.0057	.0090	3*606	3.321	16.00	1.000	.2055	
20	400	76.70	.0045	.0143	4*15	5.140	16.00	.9998	.2834	
20	400	88.27	.0045	.0143	3*606	5.916	16.01	.9989	.3263	
4	40	38.35	.0708	.1126	4*15	10.20	16.13	.9950	2.222	
4	40	44.14	.0708	.1126	3*606	11.74	16.18	.9947	2.555	
4	2	1.003	.2484	.0198	7*933	.5	15.98	1.002	.2111	
4	2	1.918	.2484	.0198	4*15	.9557	15.98	1.002	.4035	
4	2	2.006	.2484	.0198	3*966	1	15.98	1.002	.4221	
4	2	2.207	.2484	.0198	3*606	1.1	15.98	1.002	.4642	
4	2	2.408	.2484	.0198	3*305	1.2	15.98	1.001	.5064	
4	2	4.013	.2484	.0198	1*983	2	15.99	1.001	.8434	
4	2	8.026	.2484	.0198	*9916	4	16.02	.9992	1.683	
4	2	10.03	.2484	.0198	1.774	5	16.05	.9978	2.110	
40.00	2	200	.025	.0002	.04	10	16.08	.9980	1.307	
4	2	20.06	.2484	.0198	1.254	10	16.40	.9641	4.128	
40.00	2	300	.025	.0002	.0327	15	16.29	.9957	1.954	
20	20π	300	.025	.025	4.082	15	16.30	.9939	1.956	
5	5	50.98	.1951	.031	1.479	22.52	17.54	.9475	7.883	17.54[1]
4	2	50.16	.2484	.0198	.7931	25	18.03	.9288	9.749	

Table 3.2. Dean number effect under small torsion, contd.

Rc	H	Re	λ	η	100γ	Dn	fRe	u_{max}	Δp_{max}	fRe,prv
4	2	100.3	.2484	.0198	.5609	50	21.27	.8458	17.68	
4	2	200.6	.2484	.0198	.3966	100	25.47	.7995	31.93	
100	0	1003	.01	0	0	100.3	23.89	.8753	7.028	23.92 [5]
100	0	122.9	.01	0	0	122.9	25.47	.8745	8.482	26.00 [2]
10	5	468.9	.0994	.0079	.2061	147.8	27.89	.8422	30.41	26.9 [1]
10	0	468	.1	0	0	148.0	27.91	.8420	40.52	27.0 [1]
5	2.5	543	.1987	.0158	.2278	242.1	34.59	.8011	65.51	33.0 [1]
4	2	501.6	.2484	.0198	.2508	250	35.37	.7874	74.14	
100	0	3714	.01	0	0	371.4	38.27	.8592	24.03	38.03 [3]
80	80π	3714	.01	.005	.2594	371.4	38.28	.8590	24.03	38.13 [4]
50	100π	3714	.01	.01	.5188	371.4	38.30	.8586	24.08	
10	10	1295	.0975	.0155	.2468	404.4	40.81	.8173	75.87	39.0 [1]
4	2	1003	.2484	.0198	.1774	500	46.53	.7579	140.9	
3.846	4.833	1000	.25	.05	.4472	500	47.00	.7606	141.8	
3.448	8.666	1000	.25	.1	.8944	500	47.28	.7592	142.4	
2	4π	1000	.25	.25	2.236	500	49.24	.7494	146.4	
40	0	3957	.025	0	0	625.6	47.44	.8379	61.67	48.27 [5]
5	5	1648	.1951	.031	.2602	727.8	53.95	.7744	182.8	51.8 [1]
9.06	0	2500	.1104	0	0	830.6	55.14	.8015	162.0	56.69 [5]
4	2	2006	.2484	.0198	.1254	1000	62.56	.7519	274.1	
4	0	2000	.25	0	0	1000	63.06	.7555	274.1	
3.974	2	2000	.25	.02	.1265	1000	63.14	.7561	274.1	
3.846	4.833	2000	.25	.05	.3162	1000	63.27	.7552	274.7	
3.448	8.666	2000	.25	.1	.6324	1000	63.70	.7537	276.2	
2	4π	2000	.25	.25	1.581	1000	66.62	.7433	283.9	
9.06	0	3034	.1104	0	0	1008	59.98	.8019	195.3	62.58 [5]
3.974	2	4000	.25	.02	.0894	2000	85.85	.7459	536.2	
3.974	2	10000	.25	.02	.0566	5000	130.7	.7377	1260	
3.448	8.666	10000	.25	.1	.2828	5000	131.9	.7354	1268	

Note, the sources of fRe,prv are: [1] Manlapaz & Churchill (1980); [2] Truesdell & Adler (1970); [3] Dennis & Ng (1982) for λ=0, η=0; [4] Yang & Keller (1986) for λ=0, η=0; [5] Austin & Seader (1973).

* denote both the decimal point and the number listed being 100γ

a. Dn=0.5, γ^*=0.07933   b. Dn=1, γ^*=0.03966

c. Dn=1.1, γ^*=0.03606   d. Dn=1.2, γ^*=0.03305

e. Dn=2, γ^*=0.01983   f. Dn=4, γ^*=0.009916
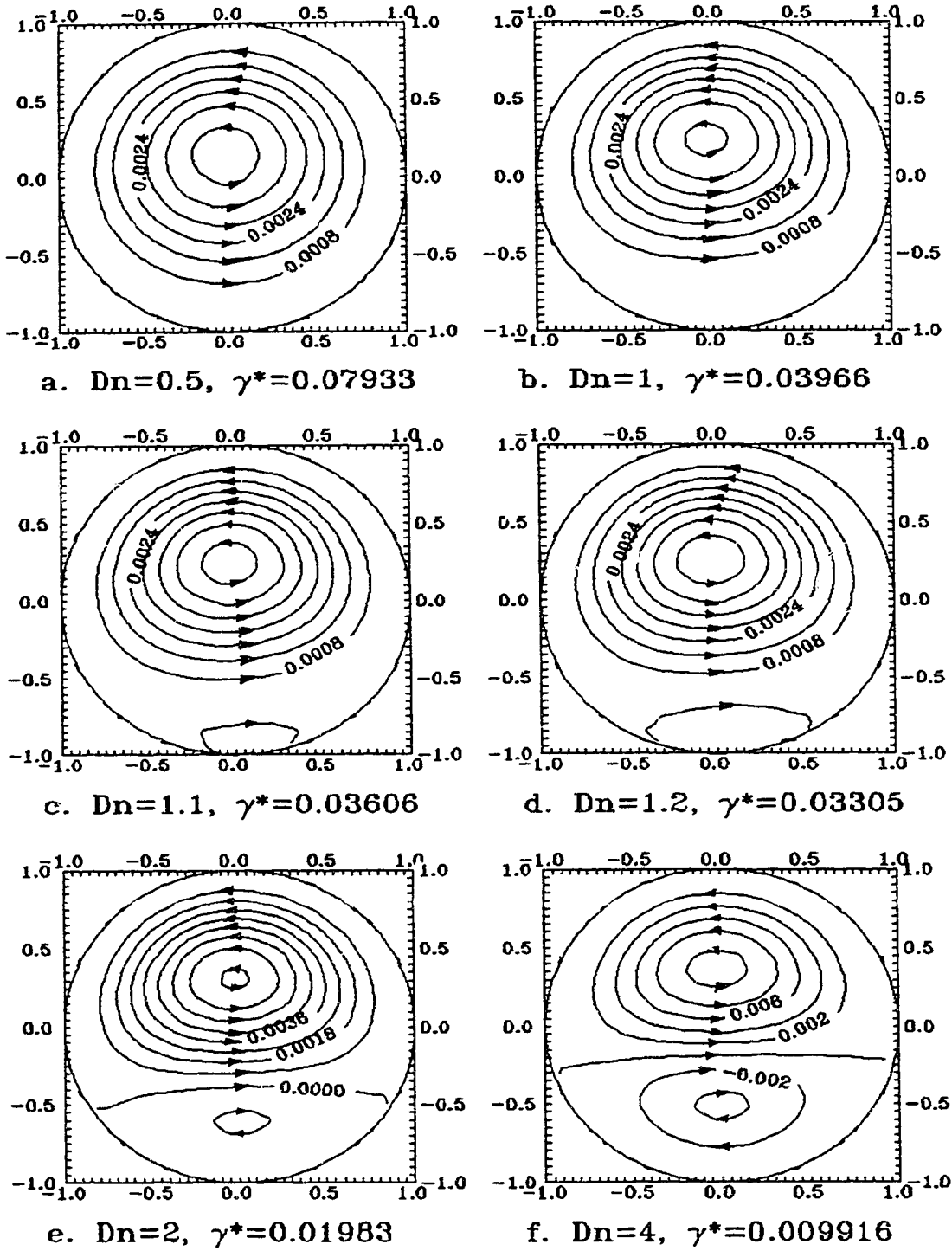
Fig. 3.7. Dean number effect on secondary flow patterns for a fixed helical pipe geometry of Rc = 4 and H = 2 and Dn < 5.
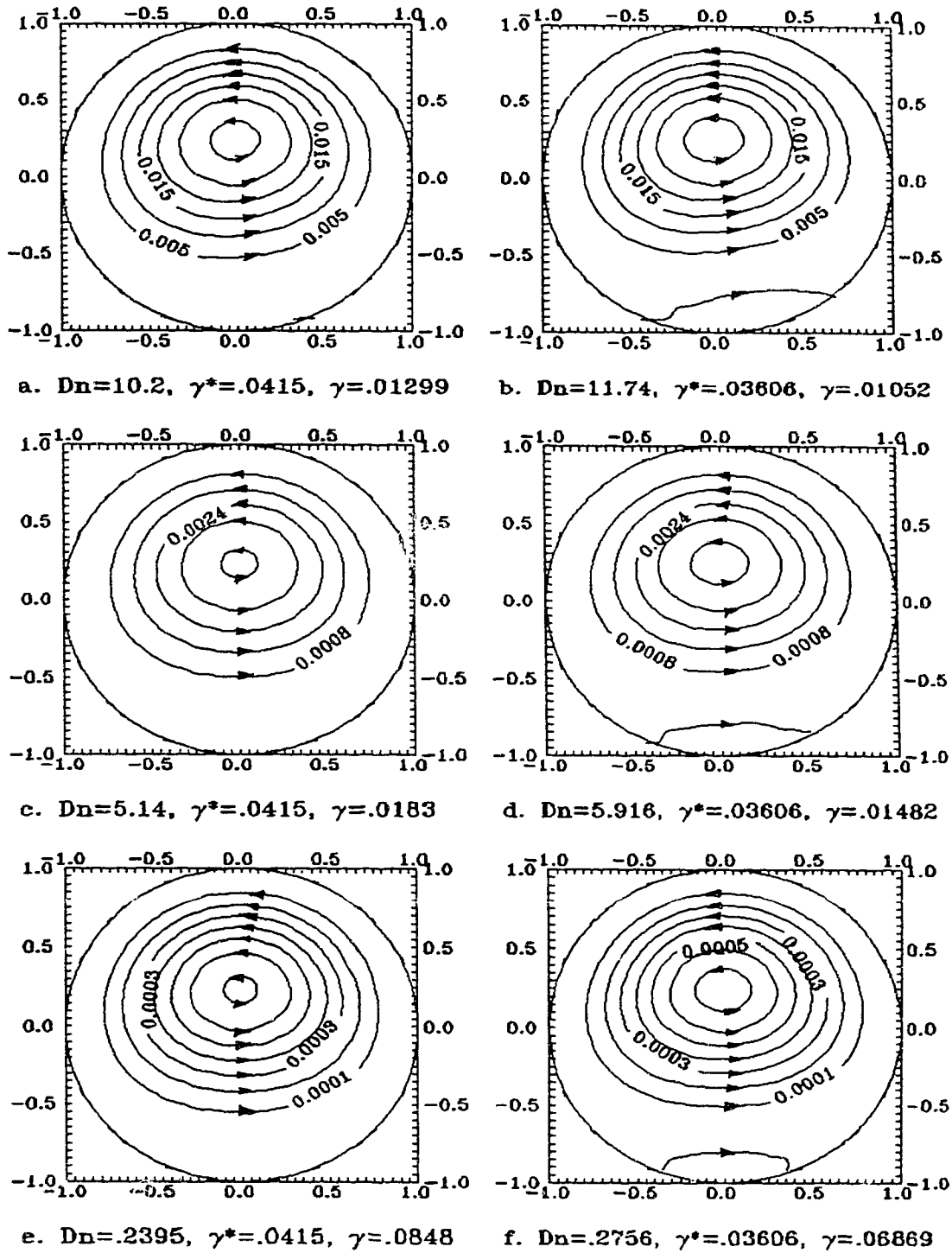
Fig. 3.8. Flow transition from two–vortex to one–vortex for Dn < 20. (Rc, H, Re) = a. (4, 40, 38.35); b. (4, 40, 44.14); c. (20, 400, 76.70); d. (20, 400, 88.27); e. (16, 4, 0.9588); f. (16,4, 1.103).

simulate the loose coiling solution of Dennis & Ng (1982) and Yang & Keller (1986). It is found that the fRe value is in very good agreement with the work of Dennis & Ng (1982), with a deviation less than 0.7% and that of Yang & Keller (1986), with a deviation of less than 0.4%.

Manlapaz & Churchill (1980) also studied flow in a helical pipe with small pitch, H $\leq$ Rc. Albeit, their solution used a non—orthogonal coordinate system. It should be mentioned that the helical flow problems calculated by Manlapaz and Churchill (1980) have a γ of less than 0.015 for Dn > 20. The deviation for fRe values is up to 5%. The higher deviation from Manlapaz & Churchill at higher Dn could be due to their extrapolation which was based on the solutions of too coarse grid size.

For very small Dean number flows, the current calculations in Table 3.2 show the same behavior as that of the toroidal flow findings in the literature (see Manlapaz & Churchill 1980). When Dn < 20, the friction factor exhibits a very small dependence on the Dn number. The friction factor can be smaller than its counterpart of the straight pipe flow as Reynolds number is very small.

In the previous section, the relative torsion or Gn importance on the helical pipe flow at very small Dean numbers was shown to be governed by $\gamma^* = \frac{\eta}{\lambda Re}$. Figure 3.7 shows the secondary flow patterns for a fixed helical pipe of Rc = 4 and H = 2 with Dn < 5. As we expected, at very small Dn the flow is swirl—like, or saddle flow as it is called by Germano (1989), which is a one—vortex flow. As Dn increases, an additional vortex appears from the bottom of the pipe (the geometry is shown in Figure 3.2). The threshold point for which the second vortex appears is $\gamma^* = 0.039$. The size and the strength of the second vortex increase as Dn increases.

Figure 3.8 shows the validity of γ^* as the flow transition parameter for Dn < 20. As shown in Figure 3.8, changes in Dn and γ or Re do not reflect the flow pattern transition. However, the secondary flow pattern has two vortices at
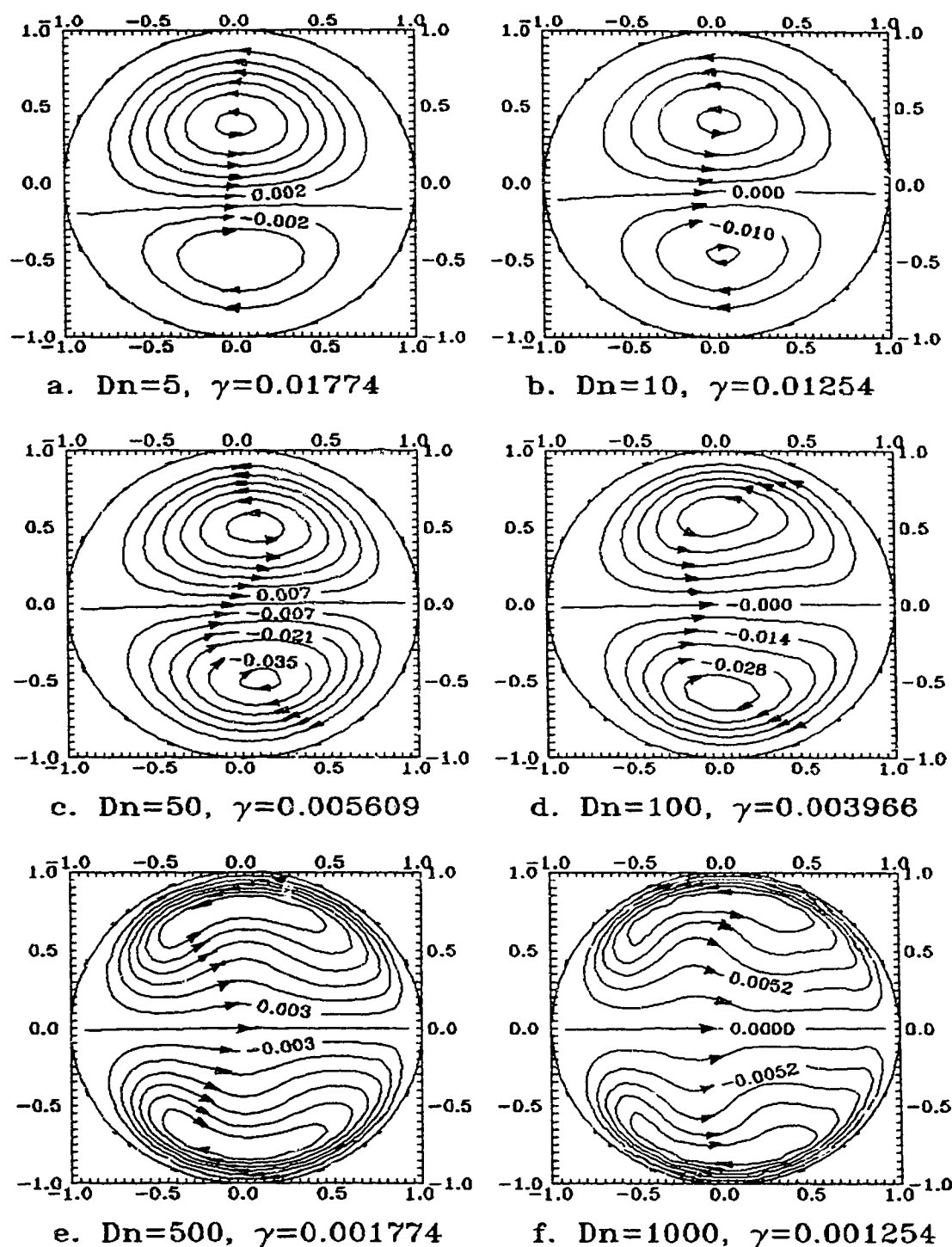
Fig. 3.9.   Dean number effect on secondary flow patterns for a fixed helical pipe geometry of Rc = 4, H = 2.

a. Dn=5, γ=0.01774

b. Dn=10, γ=0.01254

c. Dn=50, γ=0.005609

d. Dn=100, γ=0.003966

e. Dn=500, γ=0.001774

f. Dn=1000, γ=0.001254
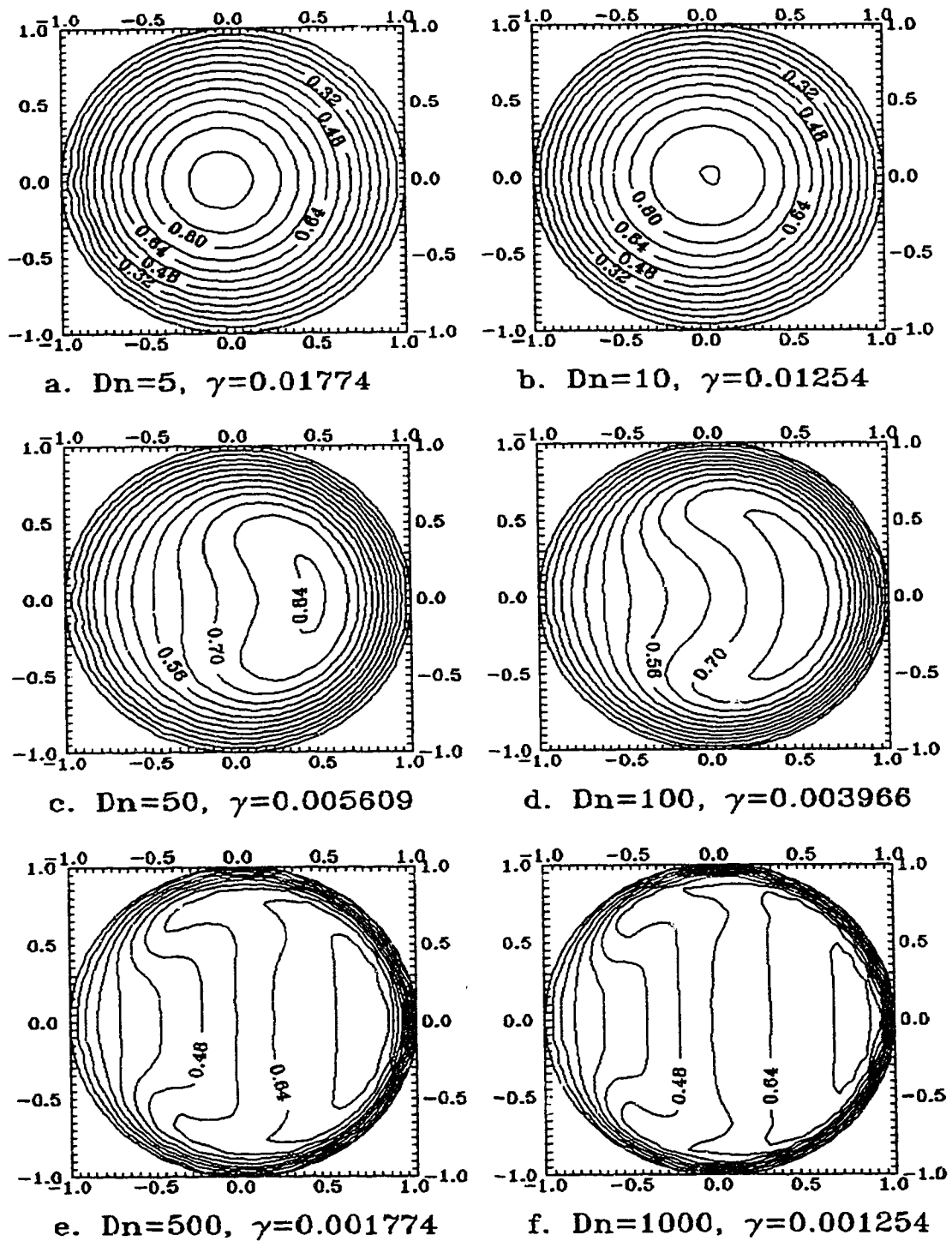
Fig. 3.10. Dean number effect on iso—axial velocity contours for a fixed helical pipe geometry of Rc = 4, H = 2.

123
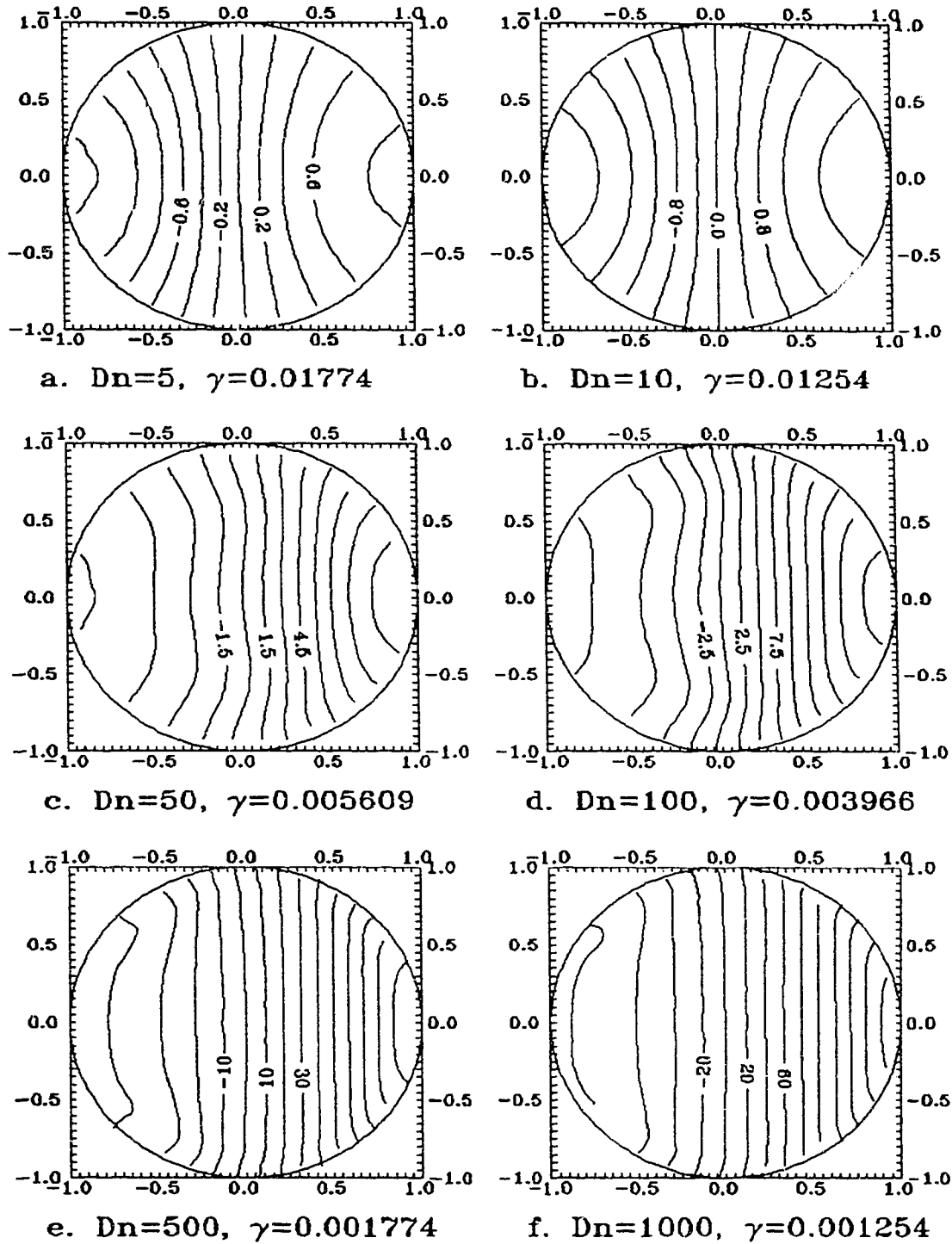
Fig. 3.11. Dean number effect on pressure contours for fixed helical pipe geometry of Rc = 4, H = 2.
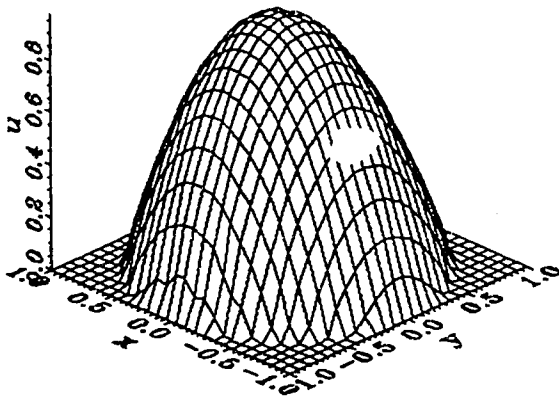
a. Dn=5, γ=0.01774

b. Dn=10, γ=0.01254
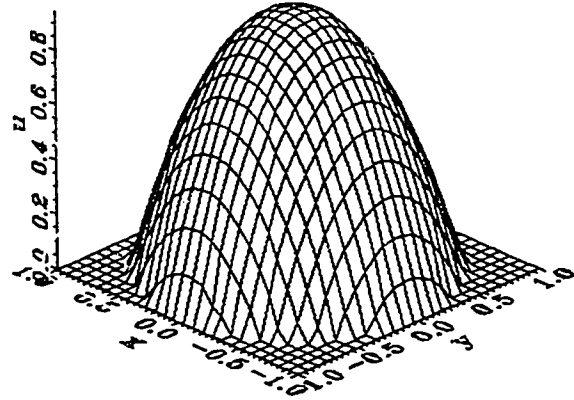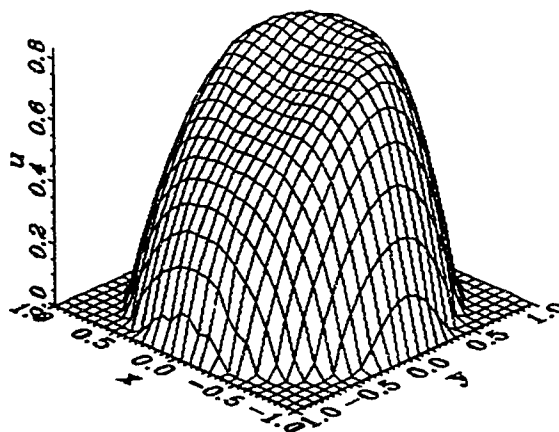
c. Dn=50, γ=0.005609
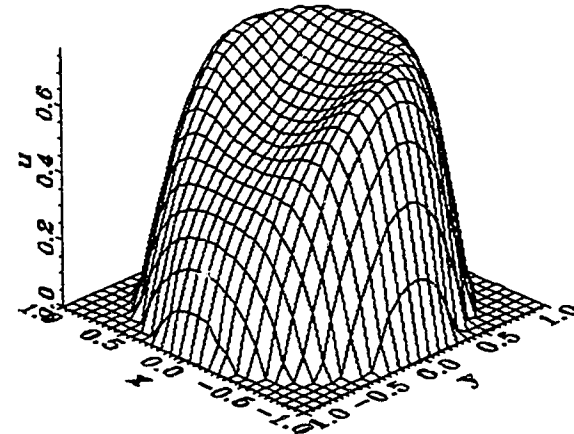
d. Dn=100, γ=0.003966
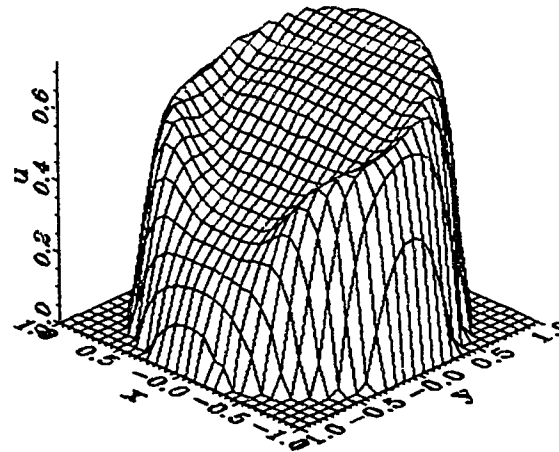
e. Dn=500, γ=0.001774
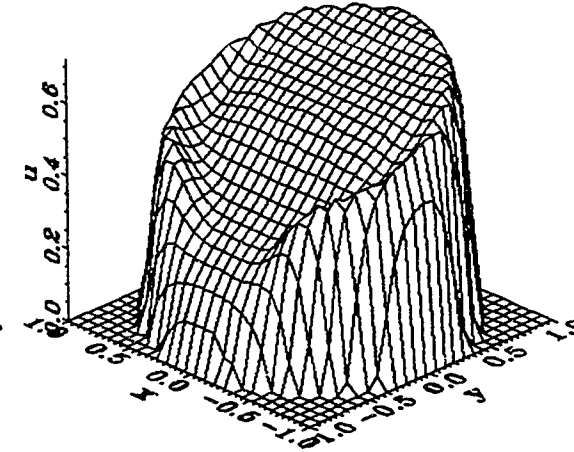
f. Dn=1000, γ=0.001254

Fig. 3.12. Dean number effect on axial velocity distribution for fixed helical pipe geometry of Rc = 4, H = 2.

a. Dn=5, γ=0.01774

b. Dn=10, γ=0.01254

c. Dn=50, γ=0.005609

d. Dn=100, γ=0.003966

e. Dn=500, γ=0.001774

f. Dn=1000, γ=0.001254
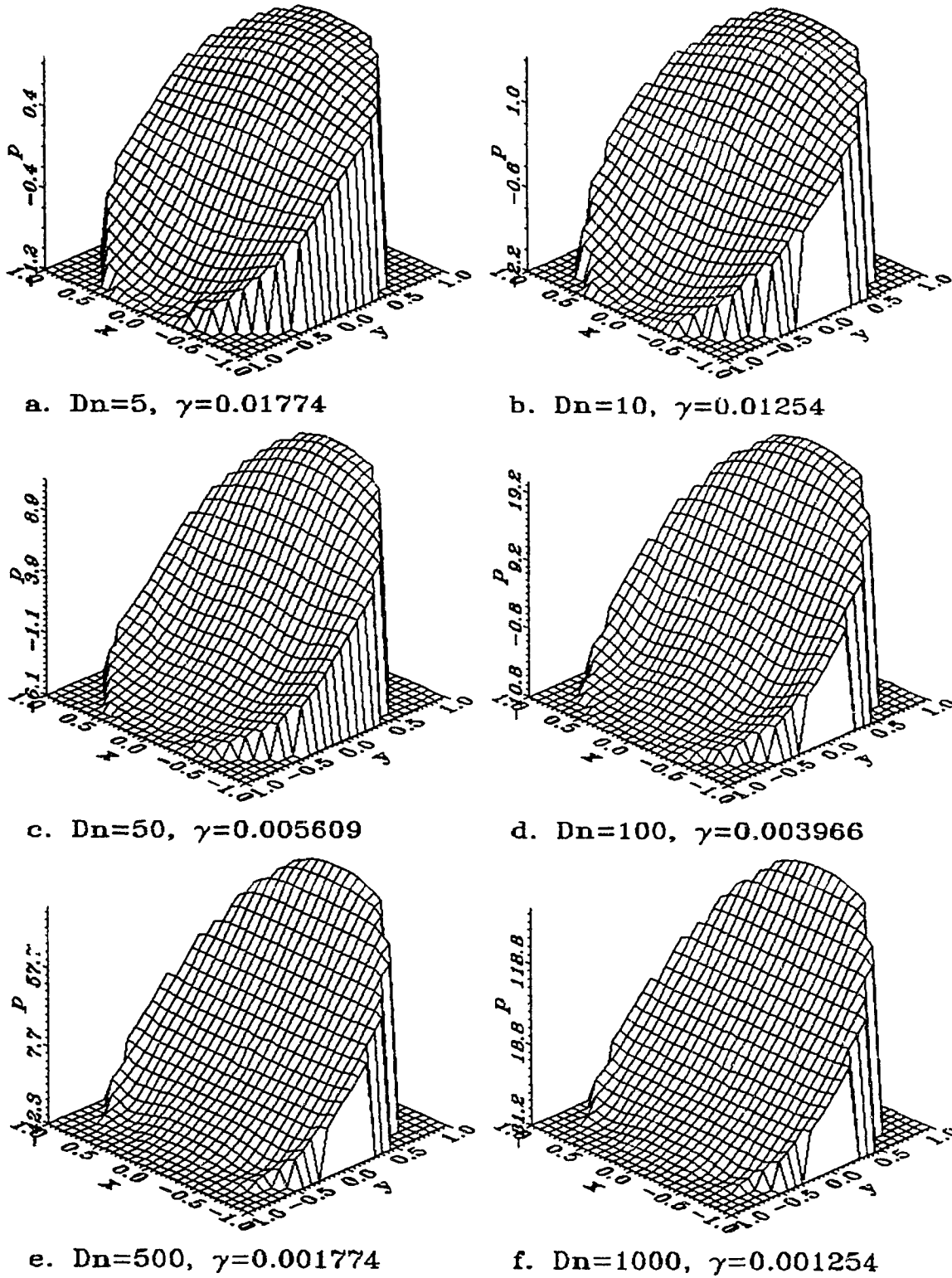
Fig. 3.13. Dn effect on cross—sectional pressure distribution for fixed helical pipe geometry of Rc = 4, H = 2.

$\gamma^* = 0.03606$ and one vortex at $\gamma^* = 0.0415$. The critical value is found to be $\gamma^* = 0.039$. Notice that Wang (1981) also found the same group ($\eta/\lambda Re = 1/24 = 0.0417$) from his perturbation series. Our value of γ^* differs slightly (smaller) from Wang's by about 7%.

Figures 3.9–3.13 show the effect of the Dean number on the helical flow behavior for the same geometry as that of Figure 3.7, Rc = 4 and H = 2, but with Dean numbers higher than 4. As an extension of Figure 3.7, Figure 3.9 shows that the lower vortex expands until it is equivalent to the upper vortex, at which the flow becomes torus–like type with two vortices of equal size and strength but opposite in rotating directions. The centers of the secondary flow vortices are pushed closer to the upper and the lower walls as the Dean number increases. With Dn increasing, the secondary flow streamlines (tubes) become denser near the wall and sparser in the center region. The two vortices always appear to be up–and–down. The maximum of the axial velocity shown in Figures 3.10 and 3.12 moves away from the center of the pipe toward the outer wall as the Dean number increases. Furthermore, the center region is flat as shown in Figure 3.12. As Dn increases, the flat area expands to form a larger "plateau". The "plateau" is inclined with the outer region having a higher value than the inner region. The edge of the plateau becomes more stiff indicating that the axial velocity changes more sharply near the wall as Dn increases. The value of the pressure away from the center, where zero is set, increases as the Dean number becomes larger. The surface plot of the pressure in Figure 3.13 shows that the pressure profile is relatively flat.

3.4.3 Pitch effect on helical flows for a fixed Dn and Rc.

To investigate the Germano number effect on the flow in a helical pipe, we computed the solutions for a family of helical pipes with the same radius of coil Rc = 9. Here, the coil is stretched by varying the pitch H. The pipe radius is taken to be one unit, i.e., a = 1. Table 3.3 shows the results for Dean number of 200 and Rc = 9. For given values of H, Rc and Dn, the values of λ, η and γ become fixed. Table 3.3 indicates that as H increases, the values of fRe and u_{max} becomes invariant to H. Also Re Δp_{max} (or $\lambda^{-\frac{1}{2}} \Delta p_{max}$), Re ψ_{max} and Re ψ_{min} (or $\lambda^{-\frac{1}{2}} \psi_{max}$ and $\lambda^{-\frac{1}{2}} \psi_{min}$) becomes independent of H. The reason for such a behavior can be explained as shown below.

The limit of large H corresponds to the range where Gn becomes constant. When the pitch is large, the torsion and the curvature ratio satisfy the relationship

$$\lambda = (Rc/a)\,\eta^2 \qquad\qquad (3\text{--}46)$$

Hence

$$\gamma = \sqrt{(a/Rc)}/Dn \qquad\qquad (3\text{--}47)$$

for large H and fixed Rc. Consequently,

$$Gn = \sqrt{a/Rc}\; Dn \qquad\qquad (3\text{--}48)$$

The above relationships indicate that in the limit of large H, $\lambda \to 0$ as $\eta \to 0$ and Gn becomes a constant for given a/Rc and Dn. As for loose coiling, the flow is dependent only on Dn and Gn, one would then expect that the flow behavior be the same as H $\to \infty$. Indeed, the last four rows of Table 3.3 show that fRe and u_{max} become identical.

Figure 3.14 shows the flow field of Dn = 200, Rc = 9, H = 0 $\sim$ 10^6. It is seen

a. H=0, γ=0

b. H=20, γ=0.00786

c. H=18π, γ=0.0167

d. H=100, γ=0.0205

e. H=10000, γ=0.0236

f. H=1000000, γ=0.0236
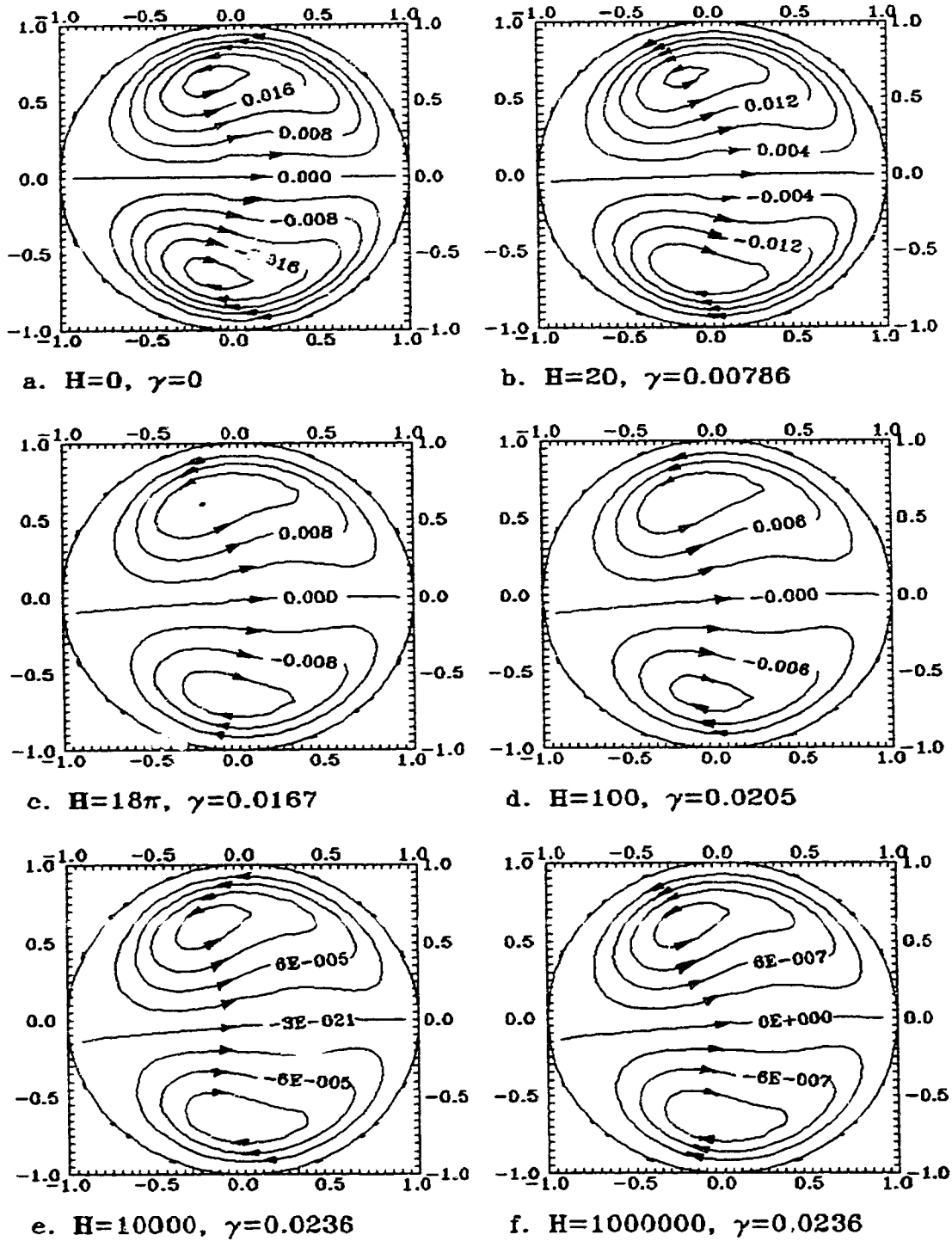
Fig. 3.14. Secondary flow patterns for Dn=200, Rc=9. (λ, η, Re) = a. (.1111, 0, 600); b. (.09876, .03493, 636.4); c. (.05556, .05556, 848.5), d. (.02692, .0476, 1219); e. (3.55 10^{-6}, 6.28 10^{-3}, 106104); f. (3.55 10^{-10}, 6.28 10^{-6}, 10610416)

Table 3.3. Torsion effect on helical flows with Rc = 9, Dn = 200.

H	10^{-4}Re	λ	η	γ	fRe	u_{max}	Δp_{max}	ψ_{max}	$-\psi_{min}$
0	.06	.11111	0	0	31.24	.8341	42.42	.02152	.02152
10	.06093	.10774	.01905	.0041	31.21	.8351	41.87	.02135	.02092
20	.06364	.09876	.03493	.0079	31.14	.8380	40.30	.02062	.01981
40	.07349	.07406	.05238	.0136	30.93	.8452	35.48	.01826	.01689
18π	.08485	.05556	.05556	.0167	30.76	.8508	31.12	.01605	.01454
80	.1039	.03702	.05237	.0192	30.57	.8564	25.75	.01330	.01180
100	.1219	.02692	.04761	.0205	30.46	.8595	22.13	.01143	.01004
200	.2205	.008225	.02909	.0227	30.25	.8654	12.41	.006403	.005521
900	.9568	4.369E–4	6.954E–3	.0235	30.16	.8679	2.879	.001484	.001270
1E4	10.6104	3.553E–6	6.283E–4	.0236	30.15	.8680	.2597	1.34E–4	1.14E–4
1E5	106.104	3.553E–8	6.283E–5	.0236	30.15	.8680	.0259	1.34E–5	1.14E–5
1E6	1061.04	3.55E–10	6.283E–6	.0236	30.15	.8680	.0026	1.34E–6	1.14E–6

that the flow field is distorted torus–like type as H → ∞, even though η is extremely small. On the other hand, the flow does not correspond to the swirl–like type, even though the pitch is extremely large due to the strong and fixed secondary flow specification of large Dn. It is clear that as H → ∞, the flow patterns become independent of H.

3.4.4. Effect of Rc on helical flows at a fixed Dn and large H.

In the last subsection, we have examined the pitch effect and the loose coiling limit by varying the pitch. In this subsection, we examine the loose coiling limit by varying the radius of the coil. Once again, a = 1 is assumed. As we expected in the loose coiling analysis section, the flow behavior should become the loose coiling of negligible effect of torsion (γ is very small), i.e., Dean flow, as the radius of coil increases to be very large for a fixed H. Table 3.4 shows the results for

a. Rc=1, γ=0.05

b. Rc=2, γ=0.0354

c. Rc=5, γ=0.0224

d. Rc=10, γ=0.0158

e. Rc=100, γ=0.005

f. Rc=1000, γ=0.0016
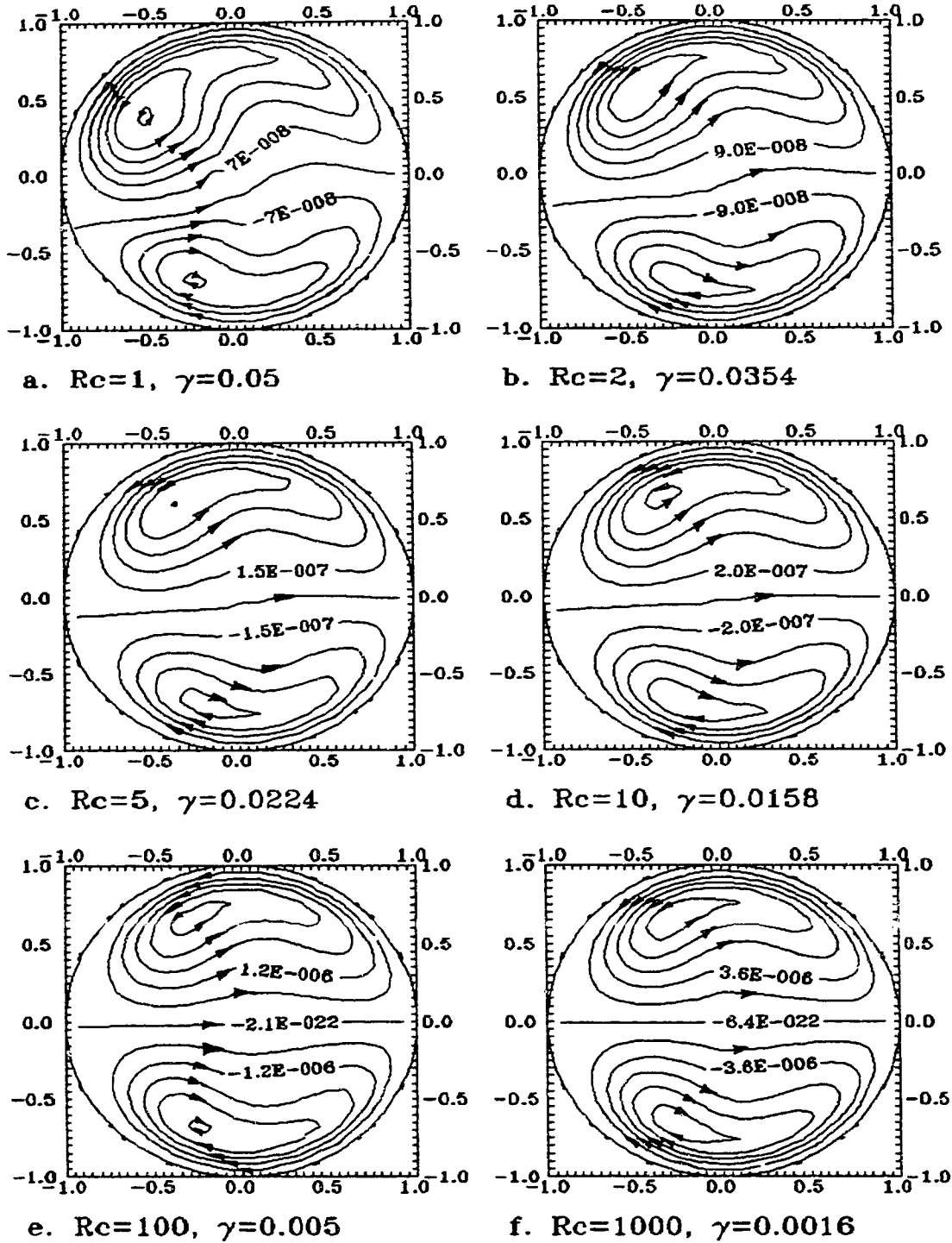
Fig. 3.15.   Secondary flow patterns for   Dn = 400, H = 10^6, η = 6.28 10^{-6}. (λ, Re) = a. (3.95 10^{-11}, 6.366 10^7); b. (7.90 10^{-11}, 4.501 10^7); c. (1.97 10^{-10}, 2.847 10^7); d. (3.95 10^{-10}, 2.013 10^7); e. (3.95 10^{-9}, 6.366 10^6); f. (3.95 10^{-8}, 2.013 10^6).

a. Rc=1, γ=0.05

b. Rc=2, γ=0.0354

c. Rc=5, γ=0.0224

d. Rc=10, γ=0.0158

e. Rc=100, γ=0.005

f. Rc=1000, γ=0.0016
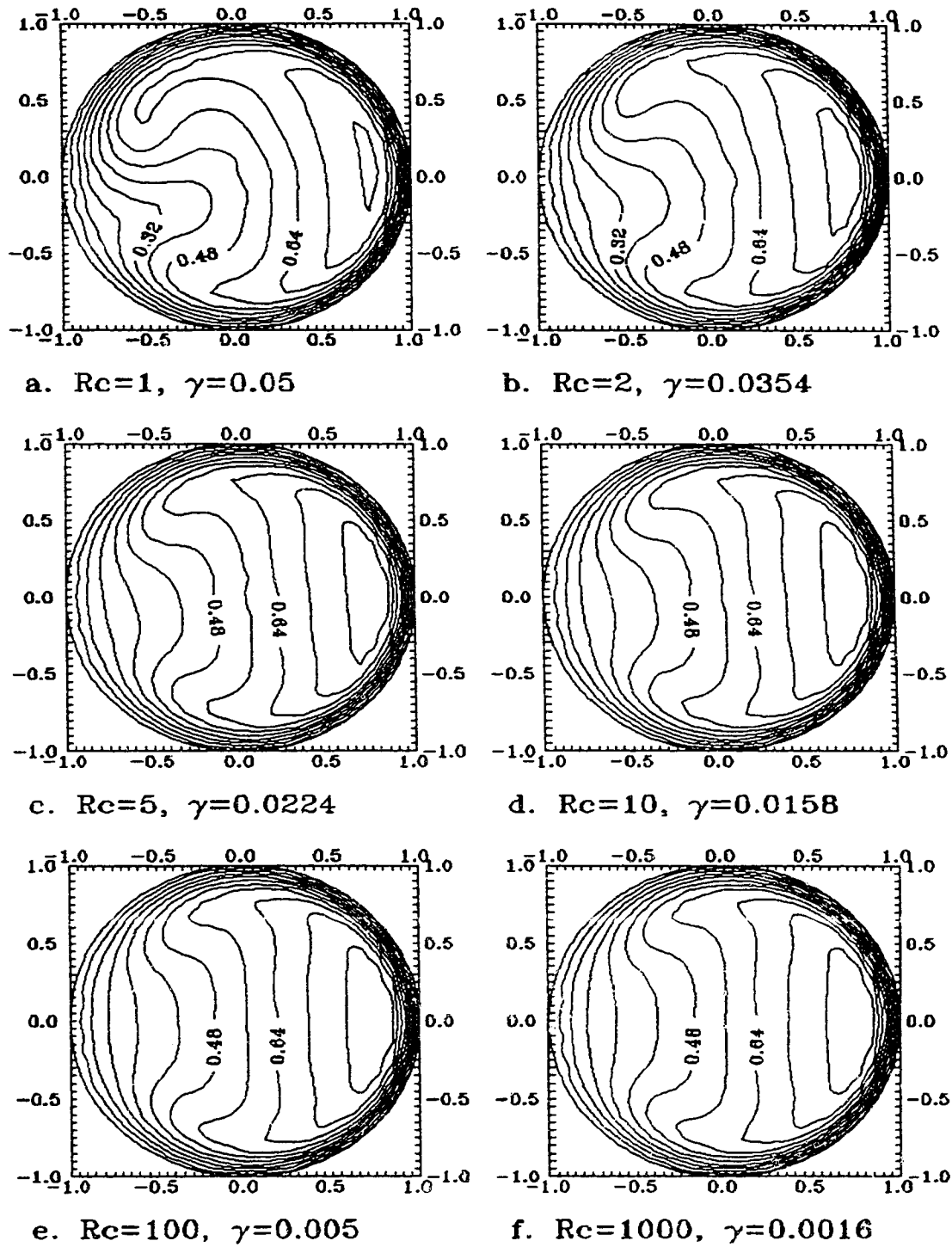
Fig. 3.16. Iso–axial velocity contours for Dn = 400, H = 10^6, η = 6.28 10^{-6}. (λ, Re) = a. (3.95 10^{-11}, 6.366 10^6); b. (7.90 10^{-11}, 4.501 10^6); c. (1.97 10^{-10}, 2.847 10^7); d. (3.95 10^{-10}, 2.013 10^6); e. (3.95 10^{-9}, 6.366 10^5); f. (3.95 10^{-8}, 2.013 10^5).

Table 3.4. Torsion effect on helical flows for $H = 10^6$, $Dn = 400$.

Rc	$10^{-6}Re$	λ	$10^6\eta$	γ	fRe	u_{max}	Δp_{max}	ψ_{max}	$-\psi_{min}$
1	6.366	3.95E–11	6.283	.05	41.44	.4645	.0019	4.521E–7	2.871E–7
2	4.501	7.90E–11	6.283	.0354	40.50	.5122	.0025	5.209E–7	3.995E–7
5	2.847	1.97E–10	6.283	.0224	39.75	.5391	.0038	7.545E–7	6.439E–7
10	2.013	3.95E–10	6.283	.0158	39.50	.5476	.0052	1.041E–6	9.266E–7
40	1.006	1.579E–9	6.283	.0079	39.30	.5537	.0103	2.037E–6	1.922E–6
100	.6366	3.948E–9	6.283	.005	39.25	.5549	.0163	3.203E–6	3.084E–6
1E3	.2013	3.948E–8	6.283	.0016	39.23	.5556	.0515	1.006E–5	9.945E–6
1E4	.06379	3.932E–7	6.258	.0005	39.23	.5557	.1623	3.170E–5	3.159E–5
1E5	.02378	2.830E–6	4.505	.0001	39.23	.5557	.4355	8.501E–5	8.493E–5
1E6	.04050	9.753E–7	.1552	8E–6	39.23	.5557	.2557	4.989E–5	4.989E–5

this case. It can be seen that at small Rc, $|\psi_{max}|$ and $|\psi_{min}|$ are very different. As Rc increases, the difference between $|\psi_{max}|$ and $|\psi_{min}|$ decreases. All the flow characteristics tend to be invariant as Rc tends to be very large. Once again, the scaling of ψ and Δp_{max} has been taken into account to arrive at the above conclusion.

Secondary flow patterns, iso–axial velocity and pressure contours are shown in Figures 3.15 and 3.16 for $Dn = 400$, $H = 10^6$. For the case of $Dn = 400$, it can be seen that although the pitch of the helical coils is very large, $H = 10^6$, the flow behavior is close to the loosely coiled helical flow of negligible torsion effect for $Rc \geq 40$. Hence, it is not necessary to require a coil with its radius greater than the pitch for the flow in the helical pipe to be torus–like.

No solutions other than the two–vortex solution were found in this study. The attempt to obtain a four–vortex solution failed with the full domain formulation, although it has been obtained in our earlier study with a half domain formulation for the toroidal flow (see Chapter 2, or Liu & Masliyah 1992).

3.5. Conclusions

Fully developed laminar Newtonian flows in helical pipes of a constant circular cross–section with a pitch and finite radius of the coil are formulated and numerically studied for the loosely coiled pipes by the Separation Method. The governing equations are constructed from orthogonal helical coordinates and used to obtain the loose coiling approximation with two dominant parameters, Dean number, $Dn = Re \, \lambda^{\frac{1}{2}}$, with Reynolds number Re and curvature ratio λ, and Germano number, $Gn = Re \, \eta$, with η being the torsion. The importance of the Germano number is investigated and a new helical flow group is evolved $\gamma = Gn \cdot Dn^{-3/2} = \eta \cdot (\lambda Dn)^{-\frac{1}{2}}$. For very small Dn flows, the counterpart of γ is defined by $\gamma^* = Gn \cdot Dn^{-2} = \eta/(\lambda Re)$. It is further shown theoretically that under the loose coiling conditions and negligible Germano number: $\lambda \to 0$, $\gamma \to 0$, and $Re > O(\lambda^{-\frac{1}{2}})$, the helical flow problem reduces to the Dean problem. These qualitative theoretical results are further enhanced by numerical simulations.

It is found that the friction factor, the axial velocity profiles are almost invariant with varying λ and η when the conditions: $Dn = $ constant, $Re > O(\lambda^{-\frac{1}{2}})$, $\gamma \leq 0.01$ and most importantly $\lambda \to 0$ are satisfied. As λ changes with the above conditions being held, the cross–plane pressure and the pseudo–secondary flow stream function (as well as the secondary velocities) are proportional to $\lambda^{\frac{1}{2}}$ or Re^{-1} with the contour shapes holding remarkably unchanged. When $\gamma > 0.01$, the flow preserves its pattern and becomes independent of λ and η as long as $\lambda \to 0$ and $\eta \to 0$. For a given helical pipe, i.e., Rc and H are fixed, the flow field consists of swirl–like type for very small Dn as $\gamma^* > 0.039$ and is torus–like for large Dn as $\gamma \leq 0.01$.

The center region on the cross–plane of the pipe has a relatively flat axial velocity profile for large Dn. The flat area become larger as Dn increases. The flow

field changes more sharply near the wall as Dn increases.

For a given Dn and Rc, the helical flow changes from a torus–like flow to a distorted torus–like flow as we increase the pitch. As $H \to \infty$, the flow patterns tend to stay unchanged with respect to H. For a fixed large H and Dn, the helical flow is more distorted at smaller Rc and changes to a torus–like type as Rc increases. For helical flow to behave torus–like, it is not necessary to require Rc being greater than H as long as $\gamma \leq 0.01$ is met for a large Dn flow.

References

Austin L.R. and Seader J.D., "Fully developed viscous flow in coiled circular pipes", *AIChE J.*, 19(1), 85—94(1973).

Berger S.A., "Flow and heat transfer in curved pipes and tubes", AIAA 91—0030, 1991.

Daskopoulos P. and Lenhoff A.M., "Flow in curved ducts: bifurcation structure for stationary ducts", *J. Fluid Mech.*, 203, 125—148(1989).

Dean W.R., "Note on the motion of fluid in a curved pipe", *Phil. Mag. J. Sci.*, 4, 208—223(1927).

Dean W.R., "The stream—line motion of fluid in a curved pipe", *Phil. Mag. J. Sci.*, 5, 673—695(1928).

Dennis S.C.R. and Ng M., "Dual solutions for steady laminar flow through a curved tube", *Q. J. Mech. Appl. Math.*, XXXV, part 3, 305—324(1982).

Germano M., "On the effect of the torsion in a helical pipe flow", *J. Fluid Mech.*, 125, 1—8(1982).

Germano M., "The Dean equations extended to a helical pipe flow", *J. Fluid Mech.*, 203, 289—305(1989).

Kao H.C., "Torsion effect on fully developed flow in a helical pipe", *J. Fluid Mech.*, 184, 335—356(1987).

Liu S. and Masliyah J.H., "A decoupling numerical method for fluid flows", submitted to *Int. J. Num. Meth. Fluid Flows*.

Manlapaz R. and Churchill S.W., "Fully developed laminar flow in a helically coiled tube of finite pitch", *Chem. Eng. Commun.*, 7, 57—58(1980)

Murata S., Miyake Y., Inaba T. and Ogata H., "Laminar flow in a helically coiled pipe", *Bull. JSME*, 24, 355—362(1981).

Chapter 4.

Axially–Invariant Laminar Flow in Helical Pipes with a Finite Pitch

Part 2. Torsion and Curvature Effects

4.0. SUMMARY

Axially—invariant laminar incompressible flows of Newtonian fluids in helical pipes having a circular cross—section are numerically studied. The flow is governed by the generalized Dean number $Dn = Re\sqrt{\lambda}$ and Germano number $Gn = Re\eta$, where Re is the Reynolds number, $\lambda = Rc\ a\ /\ [Rc^2 + (H/2\pi)^2]$ is the curvature ratio, $\eta = (H/2\pi)\ a\ /\ [Rc^2 + (H/2\pi)^2]$ is the torsion, Rc is the radius of coil and H is the pitch. For large Dn flows, the transition of the flow pattern from two— to one—vortex is characterized by $\gamma = \eta\ /\ \sqrt{\lambda Dn} = 0.2$. The orthogonal secondary flow strength of the one vortex flow tends to a fixed non—zero value for a given Dean number as γ increases. The secondary flow structure in the view point of the orthogonal coordinate system tends to a two vortex structure with the vortex—dividing line being vertical, i.e., x—axis, and a strong source in the bottom wall region and a large sink in the upper wall region. For fixed high Dean number and λ flows, increasing the torsion has the effect of changing the relative position of the secondary flow vortices and the eventual formation of a flow having a Poiseuille type axial velocity with a superimposed swirling flow.

The stability of the flow is investigated through the axially parabolized equations. It is found that the four—vortex solution can be observed by a perturbation of the flow field for $\gamma < 0.01$ and $Dn > 130$. However, the four—vortex solution is not stable and it eventually degenerates to the stable two—vortex flow.

The flow friction factor is correlated to account for Dn, λ and γ effects for $Dn \leq 5000$ and $\gamma < 0.1$.

4.1. Introduction

In Chapter 3 (see also Liu & Masliyah 1992b), loose coiling analysis is used to single out the governing flow parameters for flow in a helical pipe with a finite pitch. The parameters are given by the generalized Dean number $Dn = Re \sqrt{\lambda}$, the Germano number $Gn = Re\,\eta$ and a flow parameter $\gamma = \eta/\sqrt{\lambda Dn}$ for large Dn flows or $\gamma^* = \eta/(\lambda Re)$ for small Dn flows. λ and η are the curvature ratio and the torsion, respectively, of the pipe. Re is the Reynolds number of the helical flow. Dn is related to the centrifugal forces and Gn is attributed to the twisting forces. γ is a relative measurement of the strength of the twisting forces versus the centrifugal forces. It is expected that γ or γ^* governs the flow pattern transition in a helical pipe.

The flow parameter γ or γ^* was arrived at from the body–centered azimuthal velocity $\xi = w - \frac{1}{h_1}\,\eta\,r\,u$ coupled with the arguments that $fRe \propto Dn^{\frac{1}{2}}$ for large Dn flows and $fRe \sim$ constant for small Dn flows. u is the axial velocity. w is the circumferential velocity. h_1 is the metrics of the axial direction. f is the Fanning friction factor. γ is proportional to the ratio of the momentum norm of the second term in ξ, i.e., $\eta\,r\,u$, to the momentum norm of the first term, i.e., w. Owing to the nature of the twisting forces, i.e., through the body–centered velocity ξ, the secondary flow is expected to be unidirectional rotating flow when γ or γ^* is large.

In the limit of small Dn, say $Dn < 20$, the flow parameter is γ^*. It was determined in Chapter 3 that the criterion for the flow to be one–vortex type is $\gamma^* > 0.039$. This is in agreement with Wang's finding of a similar group $\frac{\eta}{\lambda Re^*} \geq 0.0417$, where Re^* is the Reynolds number of the corresponding straight pipe flow with the same pressure gradient as the helical flow and Re^* is of order at most 1 (Wang 1982). Since for very small Dn flows, $Re^* \simeq Re$, Wang's group reduces to the same group as our γ^*.

In Chapter 3, we applied the loose coiling approximation to arrive at the conclusion of γ for $Dn \geq 20$ and γ^* for $Dn < 20$ being the flow pattern transition governing parameter. We found the transition criterion of γ^* for small Dn flows to be quite good for $\lambda < 0.25$. However, a criterion is yet to be determined for $Dn \geq 20$. If a similar transition criterion can be found for $Dn \geq 20$ with γ instead of γ^*, then our earlier analysis is confirmed.

The numerical analysis for toroidal flows, i.e., flows in a helical pipe of zero pitch, have been dealt with extensively in the past. A good review of the previous works can be found in Nandakumar & Masliyah (1986) and Berger (1990). Since the toroidal flow is an extreme case of helical flows, one would be willingly to accept the approach of Truesdell & Adler (1970) that the flow in a helical pipe of at least small pitch could be approximated by the toroidal flow. Liu & Masliyah found that the above *ad hoc* assumption is valid for $\gamma < 0.01$.

For the case of flows in a circular toroidal pipe, Yang & Keller (1986) speculated that there may be infinitely many solutions of the type 2n—vortex flows, $n = 1, 2, 3, \cdots$. Hence, the different formulations of the governing equations could lead to different solutions and render a very complicated bifurcation map. However, even the four—vortex solution was found to be unstable by Yanase et al. (1989). The bifurcation of the toroidal flows were studied by a number of investigators. Nandakumar & Masliyah (1982), Dennis & Ng (1982), Yanase et al. (1989) studied the dual (two—vortex and four—vortex) solutions with the symmetrical condition prescribed. Yang & Keller and Daskopoulos & Lenhoff (1989) studied the bifurcation map of possible solutions with extended governing equations and the symmetrical conditions prescribed. Even with the symmetrical condition imposed, the Navier—Stokes equations offer only two— and four— vortex solutions. With different extended governing equations and different mesh sizes, Yang & Keller and Daskopoulos & Lenhoff found different bifurcation maps. Hence, it indicates that

only two—vortex solution could be observed and all the other solutions may be spurious.

The friction factors for helical flows were tabulated for Dn $\leq$ 5000 in Chapter 3 and found to be in agreement with Dennis & Ng and Yang & Keller in the limit of loose coiling and zero pitch. Until now, all the rigorous theoretical analyses stand firmly behind the relationship of fRe $\sim$ Dn$^{\frac{1}{2}}$ with only minor details different. The past experimental results are also overwhelmingly in favor of the above relationship. Ramshankar & Sreenivasan (1988), however, claimed that the above relationship was improper and assumed the validity of Van Dyke's extended Stokes series result of fRe $\sim$ Dn$^{\frac{1}{4}}$ (Van Dyke 1978) "based on" their experimental results. Although their experimental results fell between the two relationships in a limited range of Dn, it seems to us that the functional tendency of their experimental data is still the square root of Dn relation. This as addressed by Jayanti & Hewitt (1991).

In this study, we direct our attention to large curvature and large torsion helical flows. We shall establish that γ governs the flow pattern transition from two vortices to one vortex flow pattern. The representation of the secondary flow will be discussed. The secondary flow structure change in the orthogonal coordinate system will be presented as well to show the difference between different viewpoints when γ varies. Stability of the flow and the convergence of the numerical scheme will be discussed. The friction factors are correlated in the range Dn $\leq$ 5000 for possible design use.

4.2. Governing Equations and Definitions

A coordinate setup of the helical system is shown in Figure 4.1.
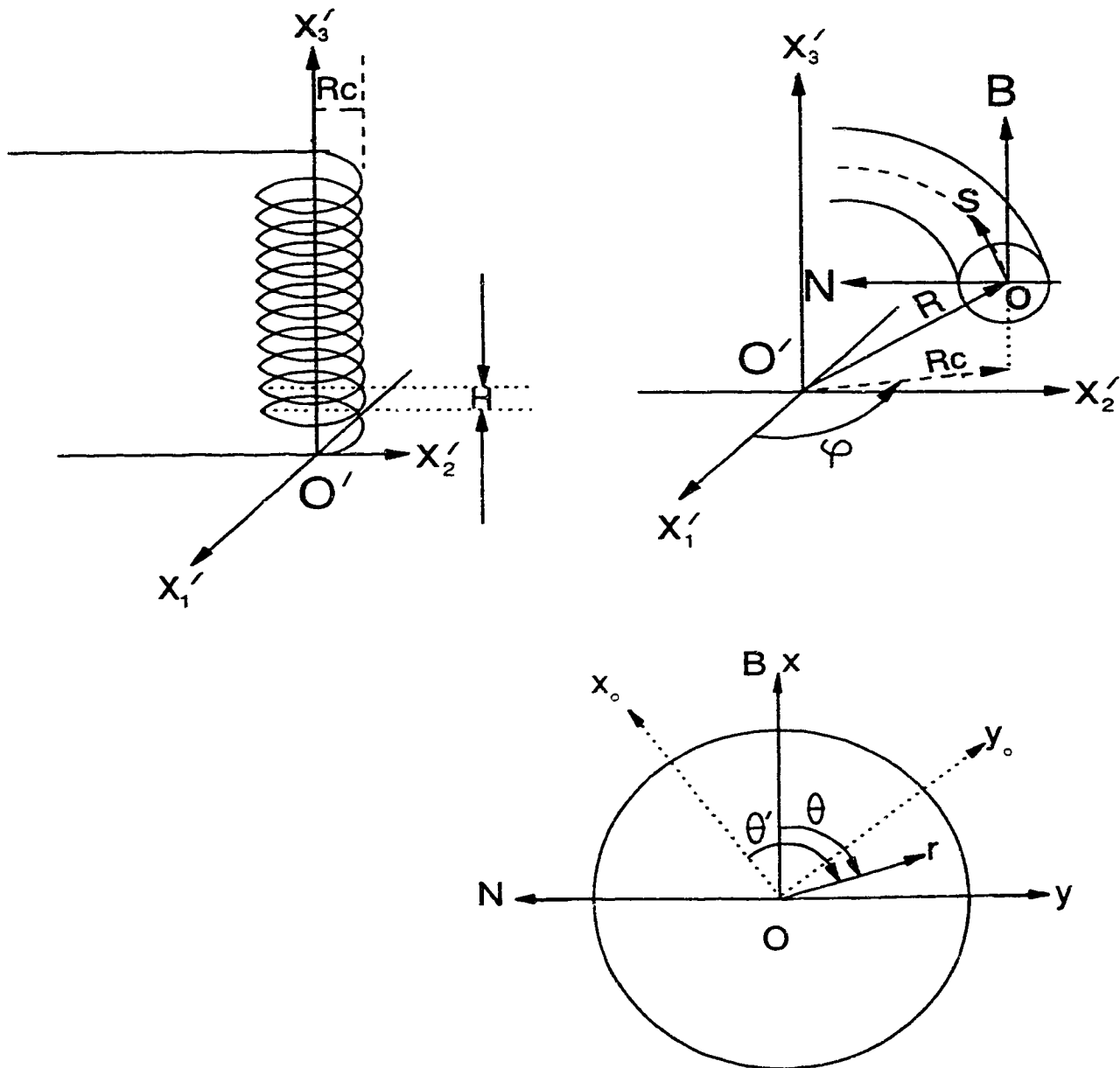
Fig. 4.1 The helical system set up.

$\vec{s}$, $\vec{N}$ and $\vec{B}$ are the tangential, normal and binormal to the generic curve at the point of consideration on the generic curve respectively. s is the curve length parameter along the generic curve. (r, θ', s) is the orthogonal coordinate system. (r, θ, s) is the non—orthogonal coordinate system of use. Rc and H are the radius of coil and the pitch for the helix, respectively. With the radius of the pipe denoted by a, the curvature ratio λ and the torsion η are defined as:

$$\lambda = \frac{a \ Rc}{Rc^2 + (H/2\pi)^2} \tag{4-1}$$

$$\eta = \frac{a \ (H/2\pi)}{Rc^2 + (H/2\pi)^2} \tag{4-2}$$

The metric coefficient in the axial (s—) direction is

$$h_1 = 1 + \lambda r \sin\theta \tag{4-3}$$

The variables and parameters involved are non—dimensionalized in the following manner:

$$s = \frac{s'}{a}, \quad r = \frac{r'}{a}, \quad t = \frac{\nu t'}{a^2}, \quad u = \frac{u'}{2U}, \quad v = \frac{v'}{2U}, \quad w = \frac{w'}{2U}, \quad p = \frac{ReP'}{4\rho U^2}$$

$$\text{and} \quad Re = \frac{2aU}{\nu}, \quad s^+ = \frac{s}{2Re} \tag{4-4}$$

Where U is the average axial velocity, t is time, ν is kinematic viscosity, u is the axial velocity component (orthogonal s—directional component), v is the radial velocity component (r—direction), w is the angular velocity component (orthogonal θ'—directional component), Re is the Reynolds number, p is the

pressure. The primed variables are dimensional quantities.

The final flow governing equations after all the necessary substitution and rearrangement are shown as follows:

The continuity,

$$\frac{1}{h_1}(\frac{\partial u}{\partial s} - \eta\frac{\partial u}{\partial\theta}) + \frac{1}{rh_1}\cdot\frac{\partial(rh_1v)}{\partial r} + \frac{1}{rh_1}\cdot\frac{\partial(h_1w)}{\partial\theta} = 0 \qquad (4-5)$$

The general form of the momentum equations,

$$(M + d_\phi)\phi = S_\phi \qquad (4-6a)$$

$$M\phi = \frac{\partial\phi}{\partial t} + \frac{1}{h_1}\frac{\partial}{\partial s}[(Re\ u - \lambda\ \eta\ r\ \frac{\cos\theta}{h_1^2})\phi - \frac{1}{h_1}\frac{\partial\phi}{\partial s}] + \frac{1}{rh_1}\ \partial_r[rh_1(Re\ v\ \phi - \frac{\partial\phi}{\partial r})] +$$

$$\frac{1}{rh_1}\frac{\partial}{\partial\theta}[Re(h_1w - \eta ru)\phi - \frac{h_1}{r}(1 + \frac{\eta^2r^2}{h_1^2})\frac{\partial\phi}{\partial\theta}] + \frac{2\eta}{h_1^2}\frac{\partial^2\phi}{\partial s\partial\theta} \qquad (4-6b)$$

where ϕ stands for any velocity component, M denotes the momentum operator. The individual momentum equations are obtained by a specification of the velocity component ϕ, extra diagonal term d_ϕ and the source term S_ϕ.

s—momentum

$$\phi = u \qquad (4-7a)$$

$$d_\phi = \frac{v\sin\theta + w\cos\theta}{h_1}\lambda\ Re + \frac{\lambda^2}{h_1^2} \qquad (4-7b)$$

$$S_\phi = -\frac{1}{h_1}(\frac{\partial p}{\partial s} - \eta\frac{\partial p}{\partial\theta}) + \frac{1}{h_1^2}[2\lambda\sin\theta(\frac{\partial v}{\partial s} - \eta\frac{\partial v}{\partial\theta}) + 2\lambda\cos\theta(\frac{\partial w}{\partial s} - \eta\frac{\partial w}{\partial\theta}) +$$

$$\frac{\lambda\eta\cos\theta}{h_1}v - \frac{\lambda r + \sin\theta}{h_1}\lambda\eta w] \qquad (4-7c)$$

r—momentum

$$\phi = v \tag{4-8a}$$

$$d_\phi = \frac{1 + 2h_1\lambda r \sin\theta}{r^2 h_1^2} \tag{4-8b}$$

$$S_\phi = -\frac{\partial p}{\partial r} + Re(\frac{\lambda\sin\theta}{h_1}u^2 + \frac{w^2}{r}) - \frac{2\lambda\sin\theta}{h_1^2}(\frac{\partial u}{\partial s} - \eta\frac{\partial u}{\partial\theta}) + \frac{\lambda\eta\cos\theta}{h_1^3}u -$$

$$\frac{2}{r^2}\frac{\partial w}{\partial\theta} - \frac{2h_1-1}{rh_1^2}\lambda\cos\theta w \tag{4-8c}$$

θ—momentum

$$\phi = w \tag{4-9a}$$

$$d_\phi = Re\frac{v}{r} + \frac{1}{h_1^2}(\lambda^2 + \frac{2h_1-1}{r}) \tag{4-9b}$$

$$S_\phi = -\frac{\partial p}{\partial\theta} + Re\frac{\lambda\cos\theta}{h_1}u^2 - \frac{2\lambda\cos\theta}{h_1^2}(\frac{\partial u}{\partial s} - \eta\frac{\partial u}{\partial\theta}) - \frac{\lambda r + \sin\theta}{h_1^3}\lambda\eta u +$$

$$\frac{3h_1-1}{r^2h_1^2}\frac{\partial v}{\partial\theta} + \frac{1}{rh_1^2}\lambda\cos\theta v \tag{4-9c}$$

The boundary is defined by the pipe wall. Although a numerical scheme with a polar coordinate system would prefer to have a condition set at the center of the pipe, there are no conditions that can fit such a need. We can only say that the properties are continuous at the center. Hence, the center point of the pipe is simply an interior of the computational domain and should not be treated differently. The boundary and necessary conditions are:

$$u = v = w = 0 \qquad \text{at } r = 1;$$

$p = 0$ at one reference point inside the computational domain

and the total flow rate is given by

$$\frac{\displaystyle\int_0^{2\pi} d\theta \int_0^1 r \ u \ dr}{\pi} = \frac{1}{2} \qquad \text{(from the nondimensionalization)} \qquad (4\text{--}10)$$

When the flow reaches the fully–developed (i.e., axially–invariant) stage, the transverse velocity field can be represented by a field scalar quantity, ψ, as follows:

$$rh_1 v = -\frac{\partial \psi}{\partial \theta} \qquad (4\text{--}11)$$

$$h_1 w - \eta r u = \frac{\partial \psi}{\partial r} \qquad (4\text{--}12)$$

To the same extent as ordinary two–dimensional flows, the field scalar quantity ψ can be called the pseudo–secondary flow stream function.

To compute the pseudo–secondary flow stream function, we take equation (4–12) after the velocity field is obtained. To approximate the secondary flow pattern of the developing flow, we take equation (4–12) as well when $\frac{\partial u}{\partial s}$ is small. It is obvious that if u, v and w satisfy the following pseudo–continuity equation

$$\frac{1}{rh_1} \frac{\partial(rh_1 v)}{\partial r} + \frac{1}{h_1} \frac{\partial}{\partial \theta}(h_1 w - \eta \, r \, u) = 0 \qquad (4\text{--}13)$$

which is the continuity equation (4–5) with $\frac{\partial u}{\partial s}$ dropped, then the potential ψ can be defined as it appears in equations (4–11) and (4–12) even if the secondary velocities are not axially–invariant. Hence, it is justified to use ψ when $\frac{\partial u}{\partial s}$ is small. However, this secondary flow pattern is not to be used when the error in the pseudo–continuity equation (4–13), ESN, is greater than 5%. ESN is defined as the conservational domain average measurement of the discrete $\frac{\partial u}{\partial s}$ normalized by the average of the discrete flow strength in and out across the cross–sectional plane. Hence,

$$ESN = \frac{\displaystyle\sum_{i,j} \frac{4 \; |FRI_{ij} + FCI_{ij} - FRO_{ij} - FCO_{ij}|}{|FRI_{ij}| + |FRO_{ij}| + |FCI_{ij}| + |FCO_{ij}|}}{\displaystyle\sum_{i,j} 1} \qquad (4-14)$$

where FRI_{ij}, FRO_{ij}, FCI_{ij}, FCO_{ij} are the fluid flow in and out at the radial direction and flow in and out at the circumferential direction, respectively, for the conservational domain of P_{ij}, i.e., the pressure node ij. To calculate the flow in and out a conservational domain, the body—centered velocity must be used. For instance, $w - \eta \, r \, u \, / \, h_1$ is the body—centered velocity of the azimuthal direction and v is the body—centered velocity of the radial direction.

The Germano number Gn and the Dean number Dn are defined as

$$Gn = Re \; \eta \cdots \text{'.e} \; \frac{a(\frac{H}{2\pi})}{Rc^2 + (\frac{H}{2\pi})^2} \qquad (4-15)$$

$$Dn = Re \sqrt{\lambda} = Re \left[\frac{a \; Rc}{Rc^2 + (\frac{H}{2\pi})^2} \right]^{\frac{1}{2}} \qquad (4-16)$$

γ and γ^* are defined as

$$\gamma = \frac{Gn}{Dn^{3/2}} = \frac{\eta}{\sqrt{\lambda} \; Dn} \qquad (4-17a)$$

$$\gamma^* = \frac{Gn}{Dn^2} = \frac{\eta}{\lambda Re} \qquad (4-17b)$$

The dimensionless group γ is the controlling parameter to determine whether the torsion exerts a significant effect on the helical flows. For very small Dn helical flow, γ^* is used in place of γ. However, γ and γ^* are not equivalent in scale.

For details, the reader is referred to Chapter 3 (or Liu & Masliyah 1992b).

The friction is evaluated in terms of Fanning friction factor f as defined by:

$$fRe = -4\frac{\partial p}{\partial s} = -\frac{aRe}{\rho U^2}\frac{\partial p'}{\partial s'} \qquad (4\text{--}18)$$

The secondary flow strength is defined as the norm of the orthogonal secondary velocity, $\|v\|_{r\theta}$.

$$\|v\|_{r\theta} = \int_0^1 r\,dr \int_0^{2\pi} (1 + \lambda \sin\theta)\,(v^2 + w^2)^{\frac{1}{2}}\,d\theta \qquad (4\text{--}19)$$

The Separation Method (Chapter 2 or Liu & Masliyah 1992a) is used to solve the flow problem. The advantage of this numerical method is that at each step, the complicated problem is subdivided into multi–simple problems. The numerical stability is achieved by the careful interpolation in discretization. The spurious pressure modes are eliminated by the careful velocity–pressure nodal and interpolate coupling. The stability ensured method renders a smooth solution that has small round–off error remaining local. Details can be found in Chapters 2 and 3 (see also Liu & Masliyah 1992a and 1992b).

The grid used is n25x32fu, i.e., 25 grid points non–uniformly placed in r direction and 32 grid points uniformly in θ direction with full domain formulation. At the center of the pipe, the node for v velocity component was arranged in the fully staggered grid and removed when discretizing the governing equations. That the center point is an interior point of the computational domain is achieved by considering the diametrical line in place of the radial line when discretizing the governing equations. Special care is then given to the variables: r, v and w. When r, v and w are referred from a node across the center to the other quadrant, they are assigned their opposite signs. Since no node is present at the center of the pipe, the singularity associated with the polar coordinates is eliminated.

4.3. Torsion effect

In this section, we focus on the large Re flows. The results are discussed in two subsections. The first section deals with fixed Dn and λ. It is aimed at determining the flow pattern transition. The second section deals with fixed Re and Rc. This is of the interest for viewing the flow characteristics change with the variation of the pitch alone.

4.3.1 Torsion effect under fixed Dn and λ

From the definition of γ as given by equation (4–17), by keeping Dn and λ constant, γ can only change through the variation of the torsion η. Here γ and η become linearly related to each other. Hence one can refer to either γ or η interchangeably. When Dn is fixed, the centrifugal forces are kept constant. As the torsion increases, the "twisting" forces increase and result in an increase in the secondary flow strength as well. Hence, although Dn and λ are kept constant, the secondary flow strength is still expected to rise as γ (or η) increases. When η (or γ) is large, the body–centered circumferential velocity $\xi = w - \eta \, r \, u \, / \, h_1$ (see Chapter 3) is dominated by the twisting component $\eta \, r \, u \, / \, h_1$. Since the axial velocity u is expected to be sign–conservative (irrespective to the change of θ), it follows that the secondary flow is expected to be uni–directional, i.e., one–vortex or swirl–like at large η values. Apart from the axial flow, the projection of such a flow on the cross–section of the pipe is a one–vortex rotating flow.

Table 4.1 gives a summary of the numerical simulations for small to moderate Dn flows for selected cases. In each case, Dn and λ are fixed and only γ, or η, varies.

$u_{0,0}$, u_{max}, p_{max}, p_{min}, ψ_{max} and ψ_{min} are the axial velocity at the center of the pipe, the maximum axial velocity, the maximum and the minimum pressure

Table 4.1. Torsion effect on helical flows.

$Dn = 20$, $Re = 80$, $\lambda = 0.0625$

R_c	H	η	γ	fRe	$u_{0,0}$	u_{max}	P_{max}	$-P_{min}$	ψ_{max}	$-\psi_{min}$
16	0	0	0	16.80	.9300	.9835	2.565	1.506	.0166	.0166
12.8	12.8π	.03125	.0280	16.80	.9301	.9824	2.565	1.510	.02038	.01276
8	16π	.0625	.0559	16.80	.9309	.9839	2.559	1.519	.02488	.009202
4.494	45.18	.1	.0894	16.80	.9321	.9850	2.546	1.537	.03026	.005519
3.2	12.8π	.125	.1118	16.79	.9334	.9853	2.525	1.554	.03421	.00342
2.659	37.42	.14	.1252	16.78	.9343	.9859	2.514	1.564	.03649	.002406
1.6	9.6π	.1875	.1677	16.76	.9382	.9879	2.460	1.607	.04462	.000315
1	24.33	.242061	.2164	16.72	.9443	.9916	2.366	1.666	.05488	0
.6154	19.33	.3125	.2795	16.65	.9539	.9962	2.202	1.732	.06989	0
.3813	15.33	.4	.3578	16.52	.9677	.9993	1.974	1.776	.09038	0
.2462	12.37	.5	.4472	16.39	.9804	1.002	1.745	1.746	.1163	0
.1584	9.954	.625	.5590	16.28	.9898	1.003	1.534	1.650	.1497	0
.1265	8.905	.7	.6261	16.23	.9930	1.003	1.432	1.574	.1694	0
.0812	7.144	.875	.7826	16.16	.9969	1.003	1.237	1.384	.2144	0
.0623	6.259	1	.8944	16.12	.9985	1.002	1.117	1.248	.2460	0

$Dn = 50$, $Re = 200$, $\lambda = 0.0625$

R_c	H	η	γ	fRe	$u_{0,0}$	u_{max}	P_{max}	$-P_{min}$	ψ_{max}	$-\psi_{min}$
16	0	0	0	20.29	.7324	.9024	6.977	2.465	.02307	.02307
12.12	43.08	.035355	.02	20.31	.7322	.9021	6.959	2.457	.02476	.02133
5.333	47.39	.088388	.05	20.38	.7311	.9010	7.095	2.419	.02737	.01888
2.614	37.17	.14142	.08	20.49	.7294	.8997	7.318	2.343	.03035	.01686
2.139	34.21	.159099	.09	20.54	.7290	.8999	7.402	2.309	.03136	.01630
1.778	31.59	.176778	.1	20.59	.7287	.9003	7.485	2.271	.03254	.01571
1.498	29.29	.194454	.11	20.64	.7286	.8999	7.575	2.229	.03366	.01507
1.102	25.46	.22981	.13	20.72	.7300	.9024	7.718	2.143	.03598	.01380
.9592	23.86	.24749	.14	20.74	.7317	.9066	7.754	2.100	.03715	.01302
.8421	22.45	.265165	.15	20.75	.7349	.9911	7.755	2.061	.03851	.01229
.7449	21.18	.282843	.16	20.72	.7398	.9128	7.702	2.034	.04007	.01119
.6633	20.04	.30052	.17	20.64	.7478	.9235	7.558	2.028	.04155	.00967
.5944	19.01	.318198	.18	20.46	.7599	.9337	7.283	2.060	.04332	.00751
.4848	17.23	.35355	.2	19.75	.7995	.9601	6.266	2.344	.04978	.00193

Table 4.1. Torsion effect on helical flows, contd.

Rc	H	η	γ	fRe	$u_{0,0}$	u_{max}	p_{max}	$-P_{min}$	ψ_{max}	$-\psi_{min}$
.3137	13.94	.44194	.25	17.96	.9206	1.001	4.103	3.283	.08332	0
.2192	11.68	.53033	.3	17.25	.9666	1.005	3.389	3.433	.1138	0
.1616	10.05	.61872	.35	16.90	.9832	1.003	3.025	3.310	.1417	0
.1240	8.817	.707107	.4	16.68	.9904	1.003	2.767	3.109	.1669	0
.0982	7.850	.795495	.45	16.54	.9935	1.002	2.552	2.892	.1908	0
.0796	7.073	.88388	.5	16.44	.9954	1.002	2.360	2.677	.2138	0
.0554	5.903	1.0607	.6	16.31	.9971	1.001	2.017	2.281	.2590	0
.0407	5.065	1.2374	.7	16.22	.9981	1.001	1.723	1.931	.3036	0
.0312	4.434	1.4142	.8	16.17	.9986	1.000	1.471	1.635	.3484	0

$$Dn = 100, \ Re = 2000, \ \lambda = 0.0025$$

Rc	H	η	γ	fRe	$u_{0,0}$	u_{max}	p_{max}	$-P_{min}$	ψ_{max}	$-\psi_{min}$
400	0	0	0	⌐3.80	.6313	.8779	2.697	.821	.004133	.004133
23.53	591.4	.01	.02	23.82	.6296	.8736	2.729	.813	.004399	.003837
3.960	248.8	.025	.05	23.92	.6207	.8661	2.874	.769	.004893	.003492
2.030	173.6	.035	.07	23.99	.6116	.8556	3.024	.718	.005374	.003346
1.556	156.5	.04	.08	24.01	.6065	.8479	3.103	.686	.005588	.003285
1.231	139.2	.045	.09	24.02	.6018	.8404	3.184	.649	.005583	.003233
.9975	125.4	.05	.1	24.02	.5980	.8317	3.257	.608	.006179	.003176
.6932	104.5	.06	.12	23.89	.5982	.8377	3.339	.520	.006959	.003112
.4440	83.68	.075	.15	23.07	.6675	.9029	3.049	.429	.008871	.002903
.3084	69.76	.09	.18	19.73	.8706	.9747	1.874	.759	.01289	.00011
.2065	57.09	.11	.22	17.89	.9499	.9802	1.429	1.076	.02118	0
.1479	48.31	.13	.26	17.15	.9680	.9814	1.280	1.149	.02810	0
.1111	41.88	.15	.3	16.77	.9762	.9841	1.204	1.153	.03413	0
.0816	35.90	.175	.35	16.52	.9823	.0872	1.143	1.131	.04105	0
.0625	31.41	.2	.4	16.37	.9861	.9892	1.099	1.100	.04764	0
.0400	25.13	.25	.5	16.21	.9904	.9920	1.030	1.038	.06038	0
.0278	20.94	.3	.6	16.15	.9922	.9931	.9746	.9781	.07280	0
.0204	17.95	.35	.7	16.13	.9920	.9925	.9270	.9226	.08505	0
.0156	15.71	.4	.8	16.14	.9903	.9906	.8859	.8696	.09718	0
.0123	13.96	.45	.9	16.15	.9887	.9889	.8467	.8215	.1094	0
.0100	12.57	.5	1	16.08	.9944	.9946	.7928	.7899	.1224	0

Table 4.1. Torsion effect on helical flows, contd.

Rc	H	η	γ	fRe	$u_{0,0}$	u_{max}	P_{max}	$-P_{min}$	ψ_{max}	$-\psi_{min}$
				$Dn = 100, Re = 1000, \lambda = 0.01$						
20	40π	.02	.02	23.94	.6288	.8733	5.406	1.648	.008771	.007658
5.882	147.8	.04	.04	24.00	.6238	.8684	5.571	1.599	.009435	.007183
1.538	77.33	.08	.08	24.13	.6072	.8447	6.132	1.397	.01116	.006572
1	62.52	.0994987	.0995	24.16	.5988	.8289	6.414	1.250	.01232	.006417
.8197	56.65	.11	.11	24.14	.5965	.8272	6.564	1.128	.01303	.006331
.5882	48.05	.13	.13	23.94	.6062	.8558	6.586	.934	.01488	.06299
.4425	41.70	.15	.15	23.28	.6682	.9074	5.994	0.819	.01768	.005867
.3448	36.83	.17	.17	20.95	.8174	.9678	4.278	1.199	.02000	.0007
.2913	33.86	.185	.185	19.54	.8929	.9796	3.476	1.653	.02808	.0002
.2494	31.34	.2	.2	18.7?	.9290	.9812	3.066	1.925	.03461	0
.2062	28.50	.22	.22	18.02	.9517	.9826	2.769	2.155	.04269	0
.1597	25.09	.25	.25	17.41	.9655	.9822	2.536	2.244	.05296	0
.1110	20.92	.3	.3	16.87	.9765	.9847	2.311	2.247	.06824	0
.0625	15.70	.4	.4	16.44	.9860	.9895	2.052	2.090	.09525	0
.0278	10.47	.6	.6	16.23	.9882	.9892	1.704	1.728	.1455	0
.0156	7.853	.8	.8	16.13	.9834	.9838	1.417	1.405	.1947	0
.0100	6.283	1	1	16.07	.9975	.9977	1.127	1.154	.2463	0
				$Dn = 100, Re = 400, \lambda = 0.0625$						
16	0	0	0	24.26	.6343	.8571	12.67	4.40	.02045	.02045
12.8	12.8π	.03125	.0125	24.29	.6338	.8557	12.73	4.38	.02117	.01962
8	16π	.0625	.025	24.34	.6320	.8520	12.89	4.33	.02191	.01889
4.494	45.18	.1	.04	24.45	.6283	.8488	13.21	4.21	.02300	.01811
3.2	12.8π	.125	.05	24.55	.6249	.8444	13.50	4.10	.02379	.01774
1.6	9.6π	.1875	.075	24.86	.6142	.8284	14.39	3.70	.02635	.01716
1	24.33	.242061	.0968	25.14	.6043	.8155	15.20	3.18	.02910	.01683
.6154	19.33	.3125	.125	25.30	.6043	.8512	15.58	2.35	.03437	.01681
.4681	16.81	.36	.144	24.94	.6337	.9011	14.52	1.84	.04053	.01644
.3813	15.33	.4	.16	23.48	.7743	.9760	11.24	2.54	.04902	.01051
.3028	13.70	.45	.18	20.98	.8937	.9968	8.077	3.812	.06109	.0005
.2462	12.37	.5	.2	19.52	.9413	.9985	6.654	4.675	.08823	0
.1584	9.954	.625	.25	18.18	.9715	.9920	5.238	5.036	.1327	0

Table 4.1. Torsion effect on helical flows, contd

Rc	H	η	γ	fRe	$u_{0,0}$	u_{max}	P_{max}	$-P_{min}$	ψ_{max}	$-\psi_{min}$
.1265	8.905	.7	.28	17.71	.9773	.9913	4.750	4.915	.1566	0
.0971	7.806	3	.32	17.32	.9813	.9906	4.241	4.657	.1868	0
.0768	6.948	.9	.36	17.04	.9843	.9909	3.851	4.264	.2137	0
.0623	6.259	1	.4	16.86	.9855	.9903	3.525	3.845	.2383	0

$$\text{Dn} = 100, \text{Re} = 250, \lambda = 0.16$$

Rc	H	η	γ	fRe	$u_{0,0}$	u_{max}	P_{max}	$-P_{min}$	ψ_{max}	$-\psi_{min}$
6.25	0	0	0	24.95	.6374	.8260	18.40	7.88	.03210	.03210
5.694	11.18	.05	.0125	24.99	.6371	.8251	18.49	7.83	.03304	.03104
4.494	17.65	.1	.025	25.10	.6360	.8224	18.74	7.73	.03396	.03018
3.125	6.25π	.16	.04	25.33	.6336	.8168	19.22	7.49	.03548	.02926
2.439	19.16	.2	.05	25.54	.6317	.8125	19.67	7.25	.03640	.02899
1.816	17.83	.25	.0625	25.85	.6281	.8060	20.31	6.90	.03810	.02862
1.384	16.31	.3	.075	26.21	.6239	.7970	21.03	6.43	.04000	.02844
1.080	14.85	.35	.0875	26.59	.6194	.7977	21.76	5.85	.04197	.02840
.8621	13.54	.4	.1	26.99	.6151	.8071	22.42	5.13	.04468	.02868
.7014	12.40	.45	.1125	27.31	.6125	.8223	22.80	4.31	.04753	.02909
.5806	11.40	.5	.125	27.51	.6160	.8554	22.66	3.37	.05208	.02908
.5405	11.04	.52	.13	27.52	.6209	.8786	22.38	2.91	.05413	.02923
.5044	10.70	.54	.135	27.48	.6301	.8897	21.82	2.62	.05682	.02905
.4717	10.37	.56	.14	27.33	.6461	.9224	20.96	2.40	.06003	.02892
.4149	9.777	.6	.15	26.49	.7181	.9784	17.78	2.88	.06957	.02475
.3571	9.114	.65	.1625	24.38	.8374	1.017	13.34	4.63	.08477	.00722
.3103	8.530	.7	.175	22.93	.9045	1.029	10.90	5.88	.1064	.00178
.2721	8.013	.75	.1875	21.92	.9407	1.026	9.479	6.626	.1268	.00097
.2404	7.552	.8	.2	21.13	.9589	1.022	8.441	7.016	.1470	.0001
.1915	6.767	.9	.225	19.99	.9742	1.011	7.134	7.110	.1826	0
.1560	6.126	1	.25	19.20	.9792	1.002	6.262	6.835	.2164	0
.1092	5.145	1.2	.3	18.22	.9818	.9954	5.026	5.995	.2784	0

$$\text{Dn} = 200, \text{Re} = 800, \lambda = 0.0625$$

Rc	H	η	γ	fRe	$u_{0,0}$	u_{max}	P_{max}	$-P_{min}$	ψ_{max}	$-\psi_{min}$
16	0	0	0	30.64	.5791	.8511	24.70	7.83	.01632	.01632
7.018	49.89	.07071	.02	30.80	.5744	.8459	25.34	7.63	.01738	.01541
1.778	31.59	.1768	.05	31.53	.5487	.8213	28.19	6.669	.02031	.01496
.7449	21.18	.2828	.08	32.02	.5094	.7724	31.08	4.99	.02581	.01513

Table 4.1. Torsion effect on helical flows, contd

Rc	H	η	γ	fRe	$u_{0,0}$	u_{max}	P_{max}	$-P_{min}$	ψ_{max}	$-\psi_{min}$
.'.··	17.23	.35355	.1	31.01	.5448	.8769	29.00	5.17	.03433	.01553
.3398	14.50	.4243	.12	No solution found with the grid used.						

$$Dn = 500, \quad Re = 2000, \quad \lambda = 0.0625$$

Rc	H	η	γ	fRe	$u_{0,0}$	u_{max}	P_{max}	$-P_{min}$	ψ_{max}	$-\psi_{min}$
16	0	0	0	44.01	.5623	.8285	59.51	17.37	.01110	.01110
12.8	12.8π	.03125	.0056	44.08	.5612	.8276	59.86	17.27	.01113	.01081
3.2	12.8π	.125	.0224	45.20	.5446	.8155	64.72	15.88	.01185	.01027
1.6	9.6π	.1875	.0335	46.67	.5185	.8009	70.64	13.69	.01289	.01023
1	24.33	.242061	.0433	48.32	.4784	.7837	76.51	11.21	.01416	.01044
.6154	19.33	.3125	.0559	49.90	.4372	.7471	80.91	11.56	.01912	.01145*
.3813	15.33	.4	.0716	No solution found with the grid used.						

*Note: the convergence is not very good, $RSD = 3.863 \times 10^{-5}$.

difference from that at the pipe center, and the maximum and the minimum values of the pseudo—secondary flow stream function, respectively.

From Table 4.1, we observe that the pressure decreases as γ increases. The cross—plane pressure difference decrease suggests that the secondary flow strength due to the centrifugal forces decreases and reduces to a certain constant limit of negligible effect on the main flow as γ increases. The constant limit (of non—zero) is expected due to the fixed centrifugal forces, for the flow Dean number and curvature ratio are fixed. It is then expected that the center and the maximum axial velocities increase and the main flow becomes close to a straight pipe Poiseuille—like flow as the centrifugal force effects become insignificant. On the other hand, the secondary flow strength in the non -orthogonal coordinate system, $\psi_{max} - \psi_{min}$, which includes the effect of the rotation of the pipe geometry increases proportionally with γ. Hence, the overall non—orthogonal secondary flow strength, $\psi_{max} - \psi_{min}$, due to the twisting forces increases more rapidly than its decrease due to the centrifugal forces.

When $\gamma > 0.2$, the minimum pseudo–secondary flow stream function value increases to zero. This marks the elimination of one vortex which is represented by the negative value of the pseudo–secondary flow stream function. Although Dn and λ vary over a wide range as shown in Table 4.1, the transition point is given by $\gamma \simeq 0.02$. Hence, the transition from two–vortex flow to one–vortex flow for large Dn systems is characterized by γ.

To show the flow transitions and other characteristics, some contour plots are shown in Figures 4.3 − 4.9 for Dn = 100, λ = 0.01 and 0.0625 and Dn = 20, λ = 0.0625.

Figure 4.2 shows that the secondary flow pattern varies from an almost symmetric two–vortex pattern torus–like to a single vortex swirl–like pattern as γ is increased. By increasing γ, the upper vortex increases both in strength and in size while the lower vortex becomes weaker. The bending of the dividing line between the two vortices can be seen as γ increases and it is viewed as the distortion generated by the torsion of the helical pipe. The distortion is more evident at larger Dn. The picture becomes that of two vortices turning anti–clockwise   ower vortex (negatively ψ–valued vortex) looses both its strength and its si.   .ver, towards the disappearance of the negatively ψ–valued vortex, its size reduces rather slowly while its strength reduces much faster. The scale of the contours for the outer vortex in Figure 4.2e are one order of magnitude lower than the rest of the contours in Figure 4.2. For large Dn flow, as shown in Figure 4.2, two vortices appear to be left–and–right, or inner–and–outer. For small Dn, as shown in Figure 4.7, the two vortices always stay up–and–down. The lower or left (outer) vortex eventually disappears as $\gamma > 0.2$.

The axial velocity isoplethes, as shown in Figure 4.3, rotate anti–clockwise with the maximum axial velocity location moving slowly towards the center of the pipe as the torsion increases. For clarity, surface plots of the axial velocity profiles

a. $\gamma=0.02$, $\eta=0.02$

b. $\gamma=0.08$, $\eta=0.08$

c. $\gamma=0.0995$, $\eta=0.0995$

d. $\gamma=0.15$, $\eta=0.15$

e. $\gamma=0.17$, $\eta=0.17$

f. $\gamma=0.22$, $\eta=0.22$
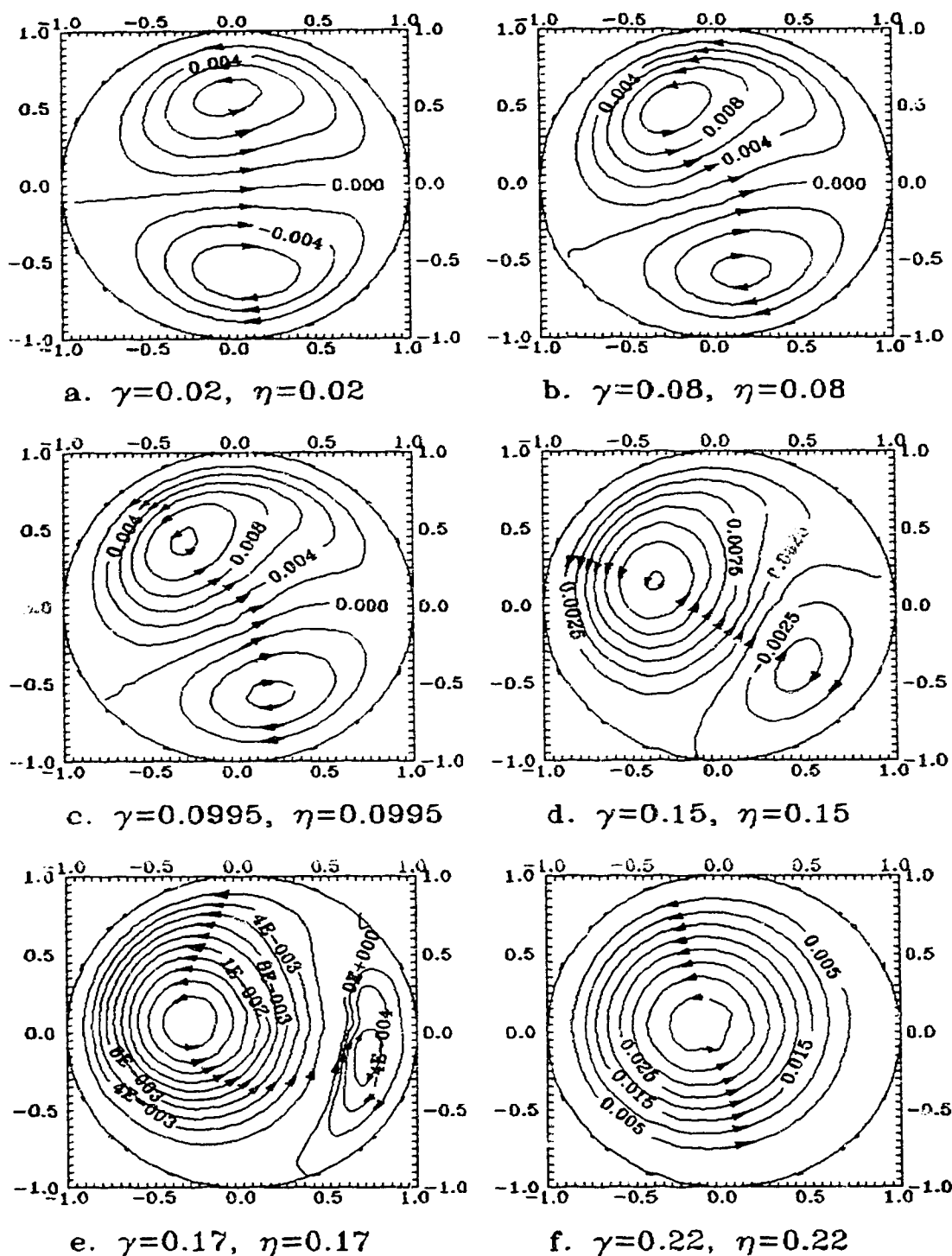
Fig. 4.2. Secondary flow patterns for Re=1000, Dn=100, λ=0.01, $\gamma > 0.01$. All the contour lines are equally spaced except in e), where the smaller vortex on the left is exactly one order of magnitude smaller in scaling.

a. $\gamma=0.02$, $\eta=0.02$

b. $\gamma=0.08$, $\eta=0.08$

c. $\gamma=0.0995$, $\eta=0.0995$

d. $\gamma=0.15$, $\eta=0.15$

e. $\gamma=0.17$, $\eta=0.17$

f. $\gamma=0.22$, $\eta=0.22$
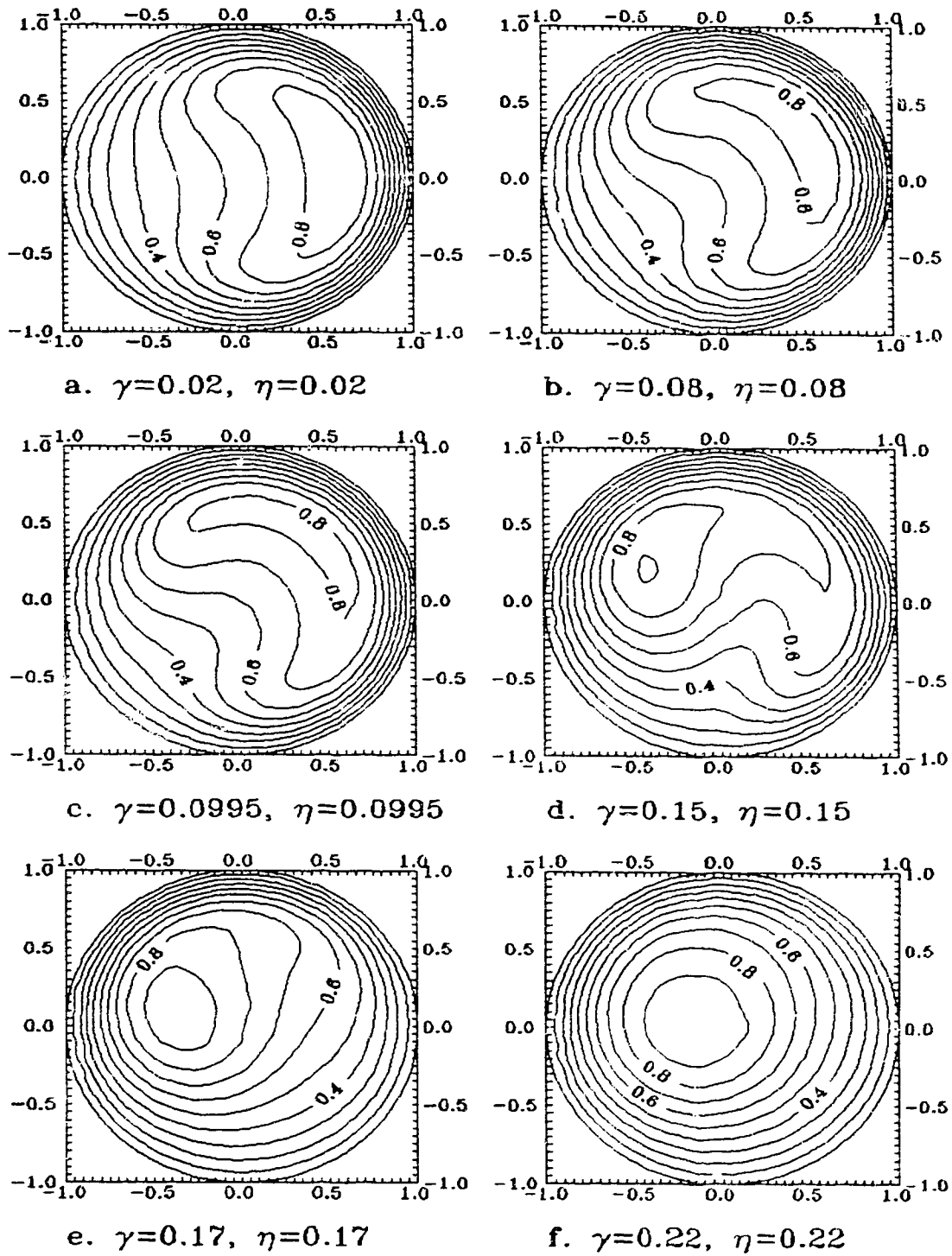
Fig. 4.3. Iso–axial velocity contours for Re=1000, Dn=100, $\lambda=0.01$, $\gamma > 0.01$.

a. $\gamma=0.02$, $\eta=0.02$

b. $\gamma=0.08$, $\eta=0.08$

c. $\gamma=0.0995$, $\eta=0.0995$

d. $\gamma=0.15$, $\eta=0.15$

e. $\gamma=0.17$, $\eta=0.17$

f. $\gamma=0.22$, $\eta=0.22$

Fig. 4.4. Pressure contours for Re=1000, Dn=100, $\lambda=0.01$, $\gamma > 0.01$.

a. $\gamma=0.02$, $\eta=.02$

b. $\gamma=0.08$, $\eta=.08$

c. $\gamma=0.0995$, $\eta=0.0995$

d. $\gamma=0.15$, $\eta=0.15$

e. $\gamma=0.17$, $\eta=0.17$

f. $\gamma=0.22$, $\eta=0.22$
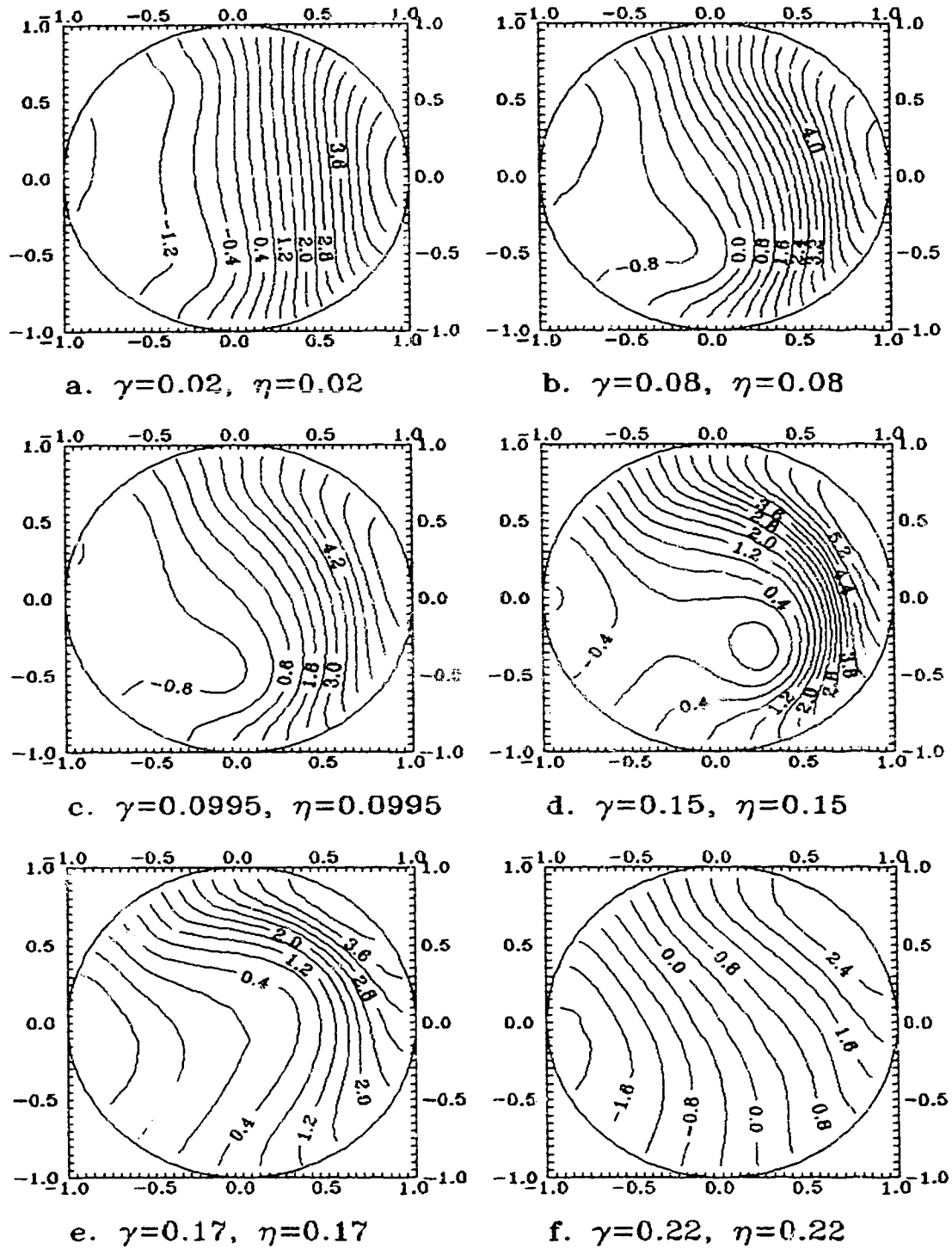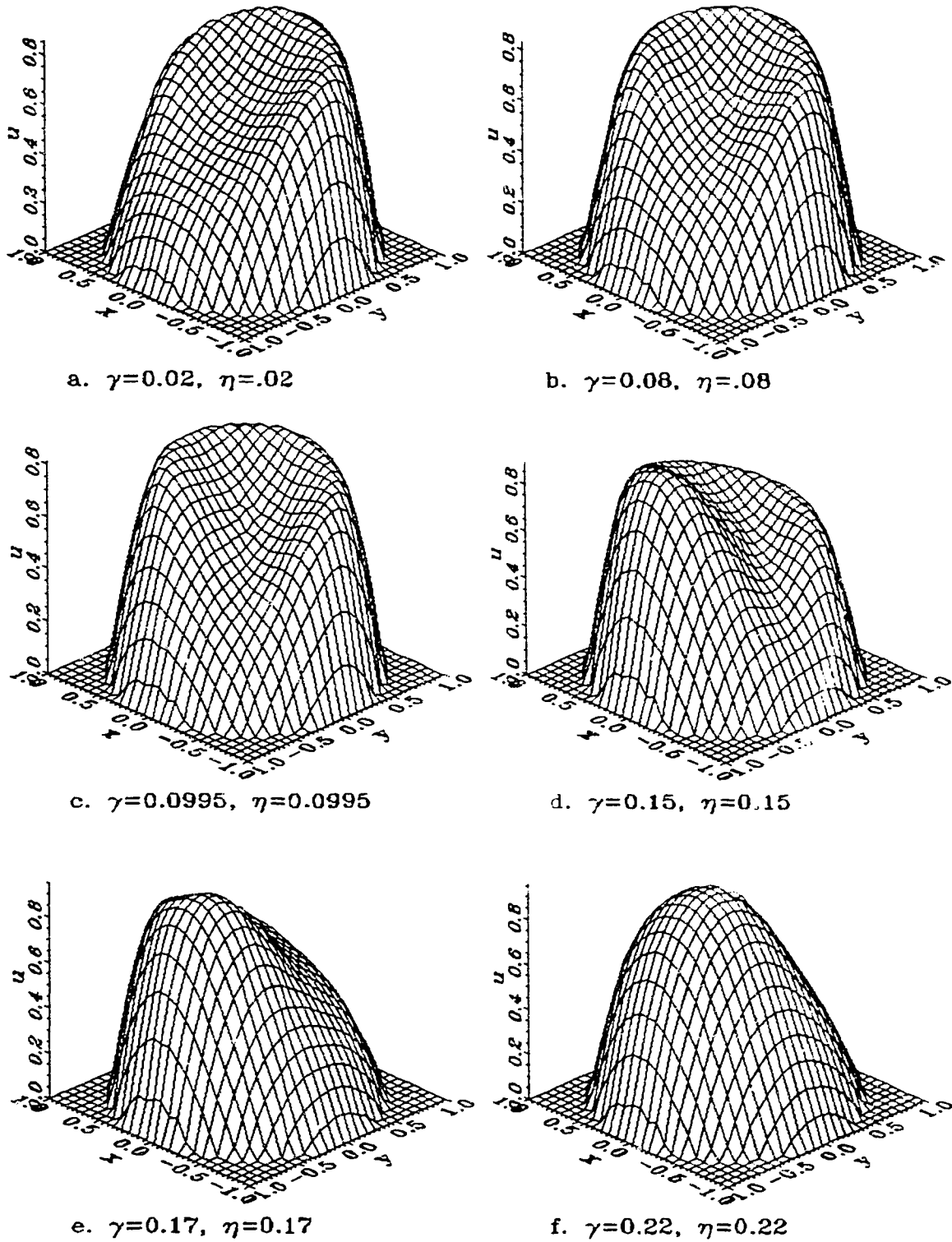
Fig. 4.5.   Axial velocity profiles for $Re=1000$, $Dn=100$, $\lambda=0.01$, $\gamma > 0.01$.

a. $\gamma=0.02$, $\eta=0.02$

b. $\gamma=0.08$, $\eta=0.08$

c. $\gamma=0.0995$, $\eta=0.0995$

d. $\gamma=0.15$, $\eta=0.15$

e. $\gamma=0.17$, $\eta=0.17$

f. $\gamma=0.22$, $\eta=0.22$
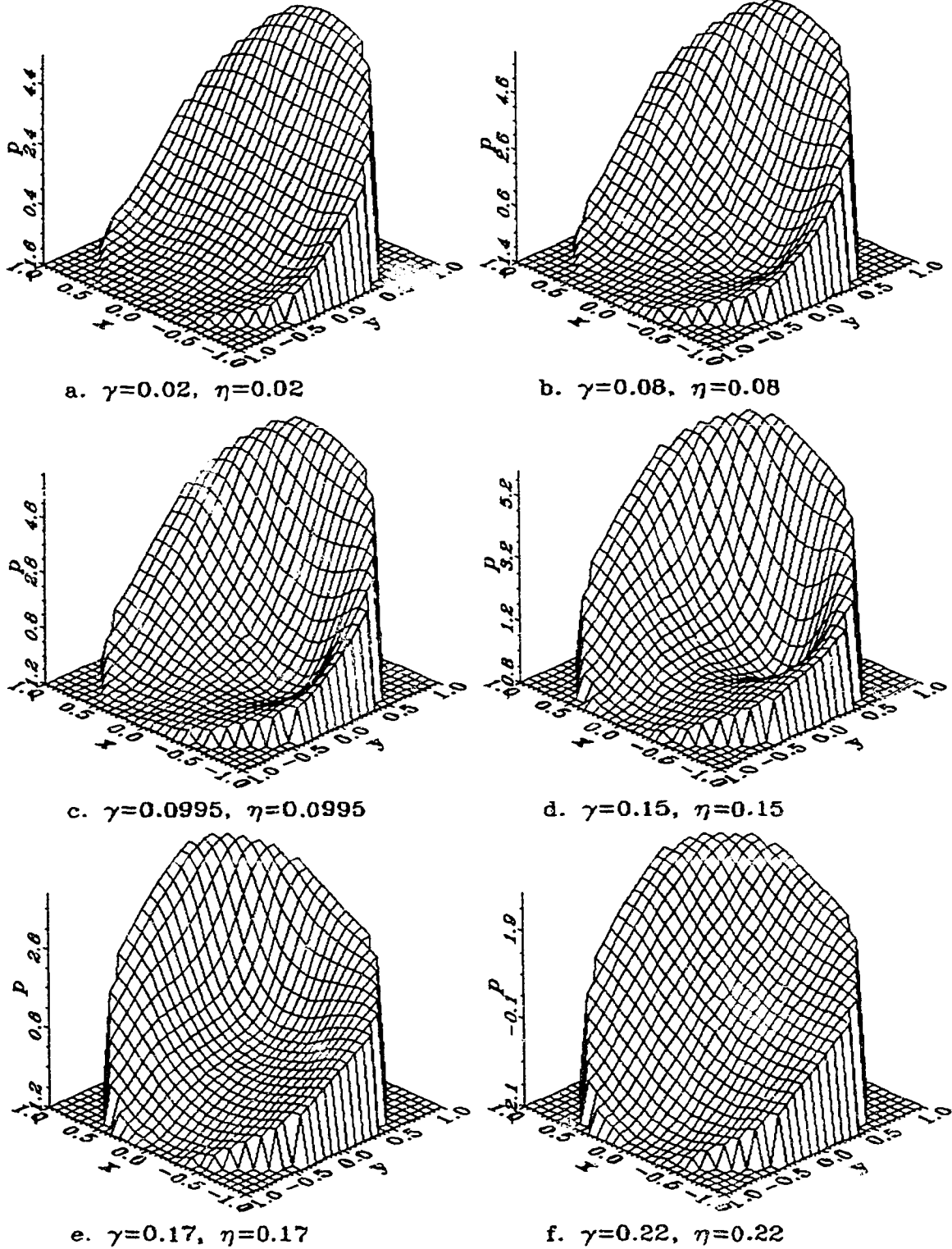
Fig. 13 Pressure profiles for Re=1000, Dn=100, $\lambda=0.01$, $\gamma>0.01$.

a. $\gamma=0,\ \eta=0$

$\gamma=0.02795,\ \eta=0.03125$

c. $\gamma=0.08944,\ \eta=0.1$

d. $\gamma=0.1252,\ \eta=0.14$

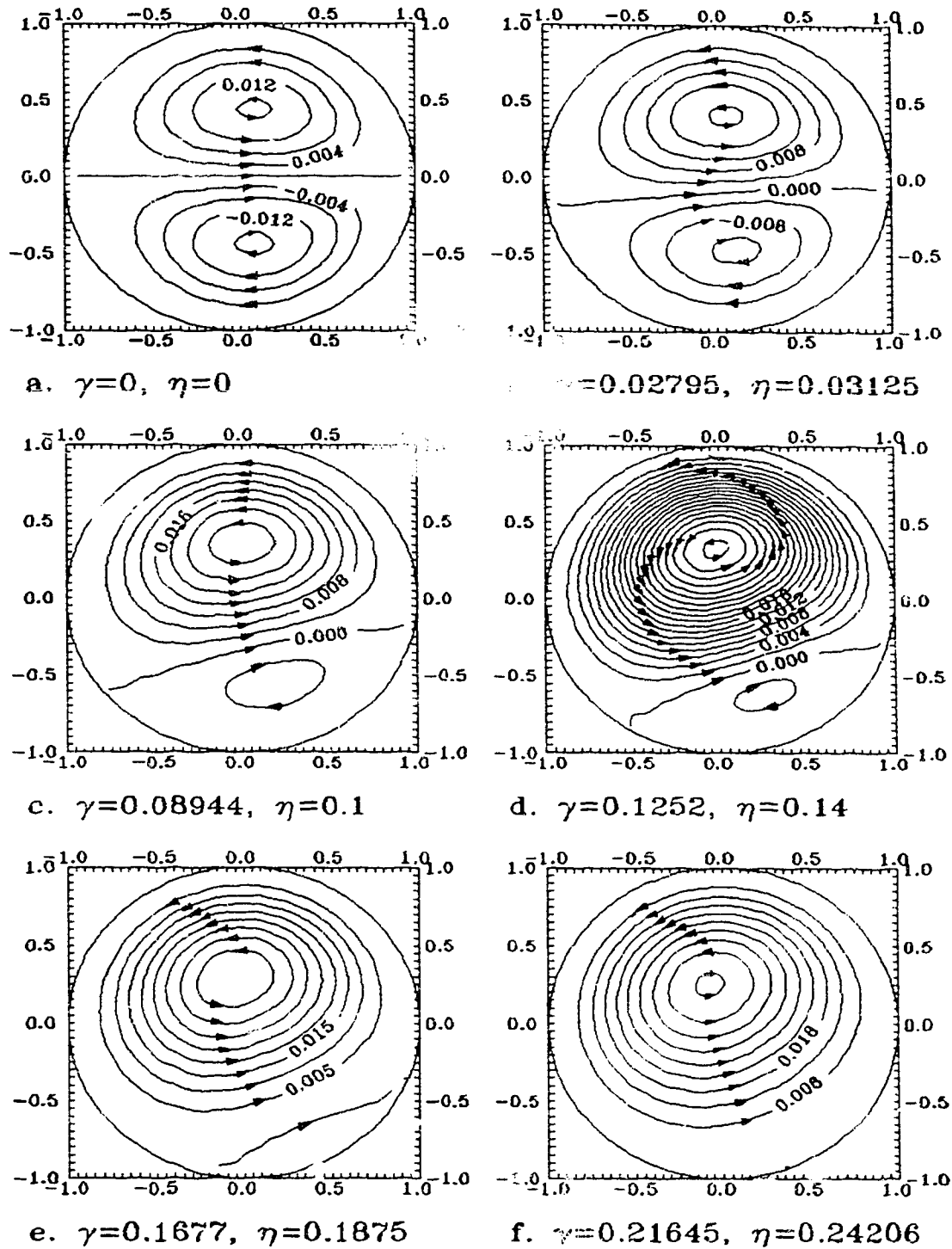e. $\gamma=0.1677,\ \eta=0.1875$

f. $\gamma=0.21645,\ \eta=0.24206$

Fig. 4.7. Secondary flow patterns for $Dn = 20$, $\lambda = 0.0625$.

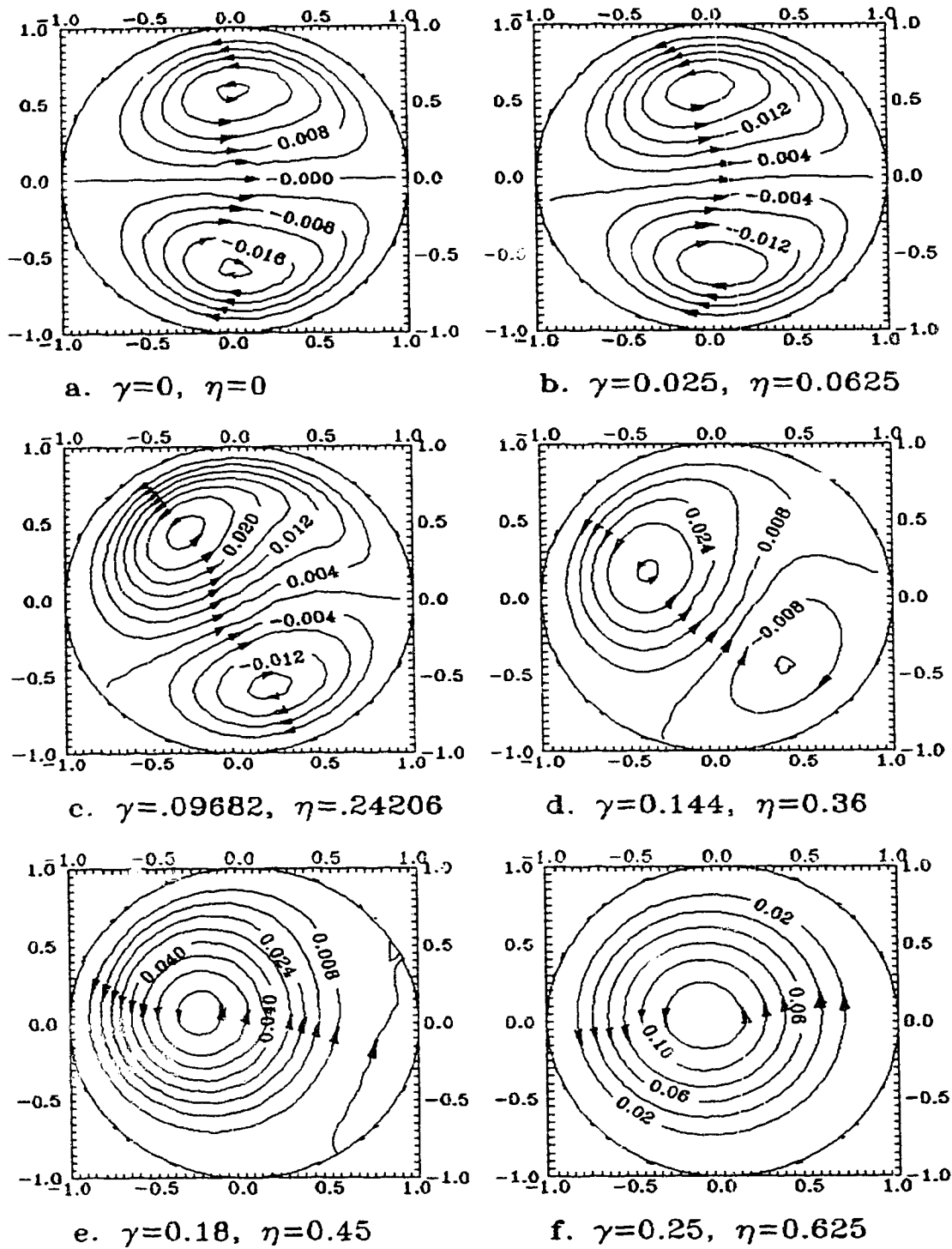Fig. 4.8. Secondary flow patterns for Dn = 100, $\lambda = 0.0625$.

are shown in Figure 4.5. At large γ, the axial velocity profile reduces to the neighborhood of the axi–symmetrical straight pipe Poiseuille–like profile. It can be seen that the maximum axial velocity moves from the outer y axis at $\eta = 0$ toward the center of the pipe spirally. The maps of the maximum axial velocity for Dn $= 100$, $\lambda = 0.01$ and Dn $= 20$, $\lambda = 0.0625$ are shown in Figures 4.9 and 4.10.

The vertical pressure isobar lines become distorted with a locally low pressure zone (cone) forming in helical pipes of large torsion near the lower wall as γ increases. To clearly show the low pressure cone, surface plots of the pressure are presented in Figure 4.6. It can be seen clearly that at $\gamma = 0.15$, a hole (minimum pressure zone) is located near the lower wall. This pressure cone is again attributed to the distortion effect of the torsion.

Figures 4.7 and 4.8 show the secondary flow pattern for $\lambda = 0.0625$ with Dn $= 20$ and 100, respectively. Comparison of Figure 4.8 with Figure 4.2 for Dn $= 100$ and $\lambda = 0.01$ indicates that the secondary flow pattern is governed by the value of γ alone. For example, compare Figure 4.2d ($\gamma = 0.15$, $\eta = 0.15$) with Figure 4.8d ($\gamma = 0.144$, $\eta = 0.36$). Figures 4.2, 4.7 and 4.8 indicate that the flow pattern transition from a two– to one– vortex pattern occurs at $\gamma \simeq 0.2$.

At large Dn and large γ, $\gamma > 0.2$, the flow in a helical pipe can be characterized by a Poiseuille–like main flow superimposed with a rotating secondary flow. Both the axial and the secondary flows are unidirectional. The friction factor is very close to that of the Poiseuille flow.
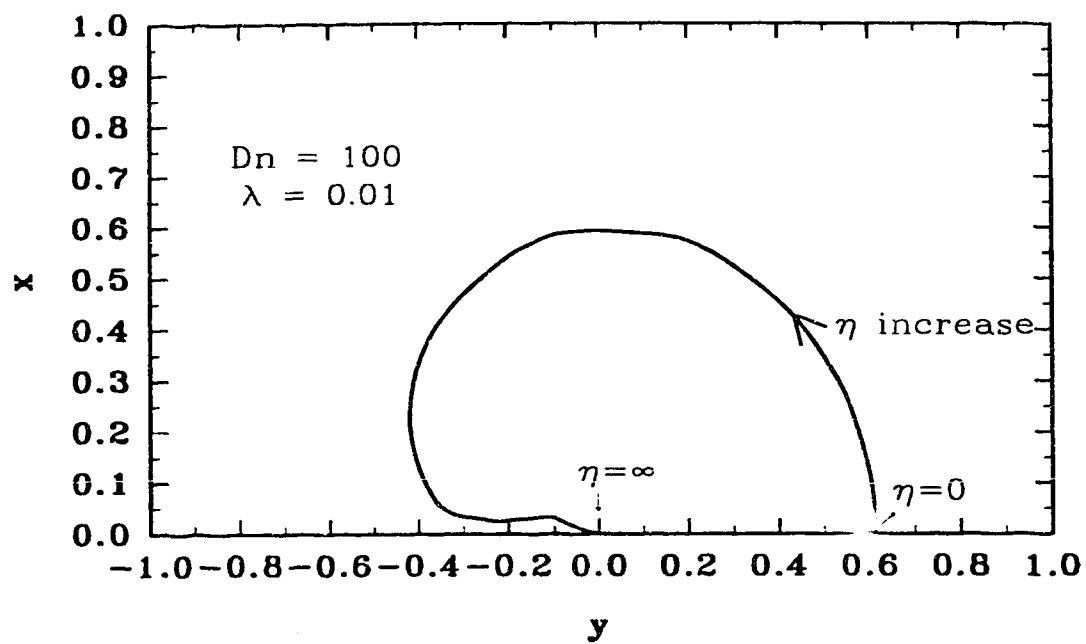
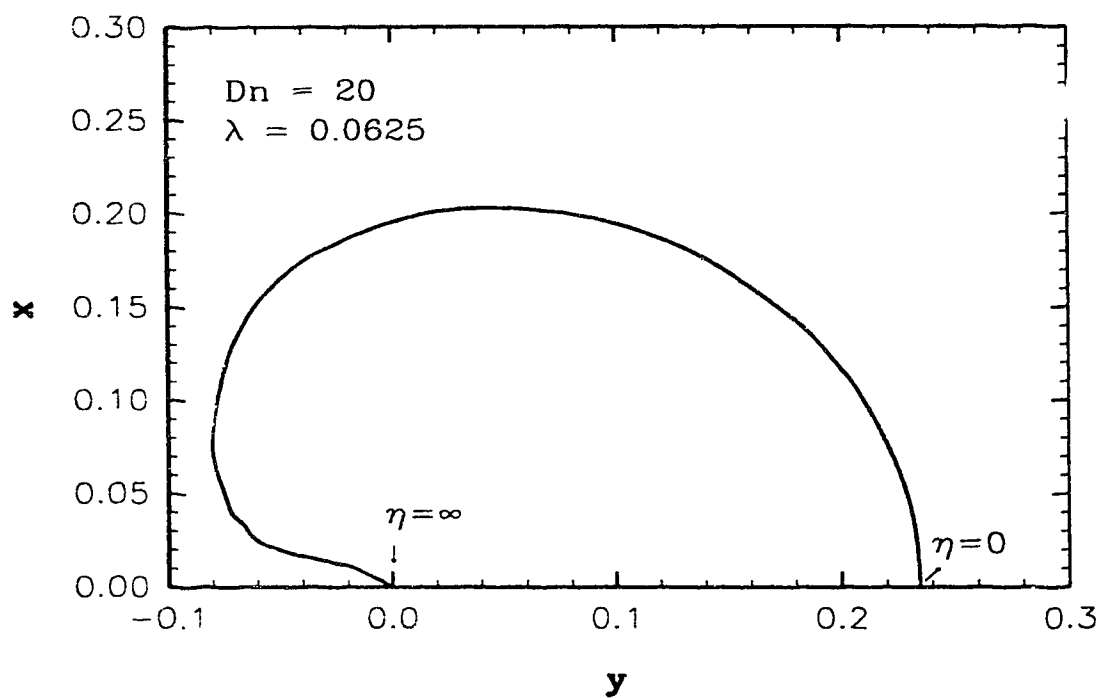Fig. 4.9. Maximum axial velocity location map for Dn = 100, λ = 0.01.

Fig. 4.10. Maximum axial velocity location map for Dn = 20, λ = 0.0625.

4.3.2 Helical flows of varying H for fixed Re and Rc.

Another configuration of interest is that the radius of coil remains constant but its pitch increases. Under this configuration, $\eta = O(\lambda^{\frac{1}{2}}) \to 0$ as $H \to \infty$. The radius of the pipe is set to be unit, i.e., $a = 1$. Instead of having constant centrifugal forces, i.e., constant Dean number, we keep Re and Rc constant. The computed flow characteristics are shown in Table 4.2. The secondary flow patterns are shown in Figure 4.11. It can be seen that the flow field changes from a torus—like flow at $H = 0$ to a Poiseuille—like flow superimposed with very weak swirl—like secondary flow at $H \to \infty$.

For very small Dn, Dn < 20, the counterpart of γ is γ^* in controlling the flow pattern transition. For $\gamma^* > 0.039$, the flow is swirl—like as is found in Chapter 3. In Figure 4.11e, the flow is swirl—like although $\gamma = 0.1401 < 0.2$. By calculating γ^*, we find that $\gamma^* = 0.05893 > 0.039$ for this case. Since Dn = 5.654, which is very small, the flow must be swirl—like as that established in Chapter 3 (see also Liu & Masliyah 1992b).

Figure 4.12 shows the variation of fRe with H for Rc/a = 9 and Re = 1200. fRe decreases monotonically as H increases. The decrease in fRe is not due to the change from two to one vortex pattern. Rather, the decrease in fRe with H is due to the decrease in the intensity of the secondary flow. For H < 10, the friction factor remains relatively constant, and it decreases sharply as H > 20.

a. H=0, Dn=400, γ=0

b. H=18π, Dn=282.6, γ=.01402

c. H=100, Dn=196.9, γ=.02068

d. H=2000, Dn=11.30, γ=.09906

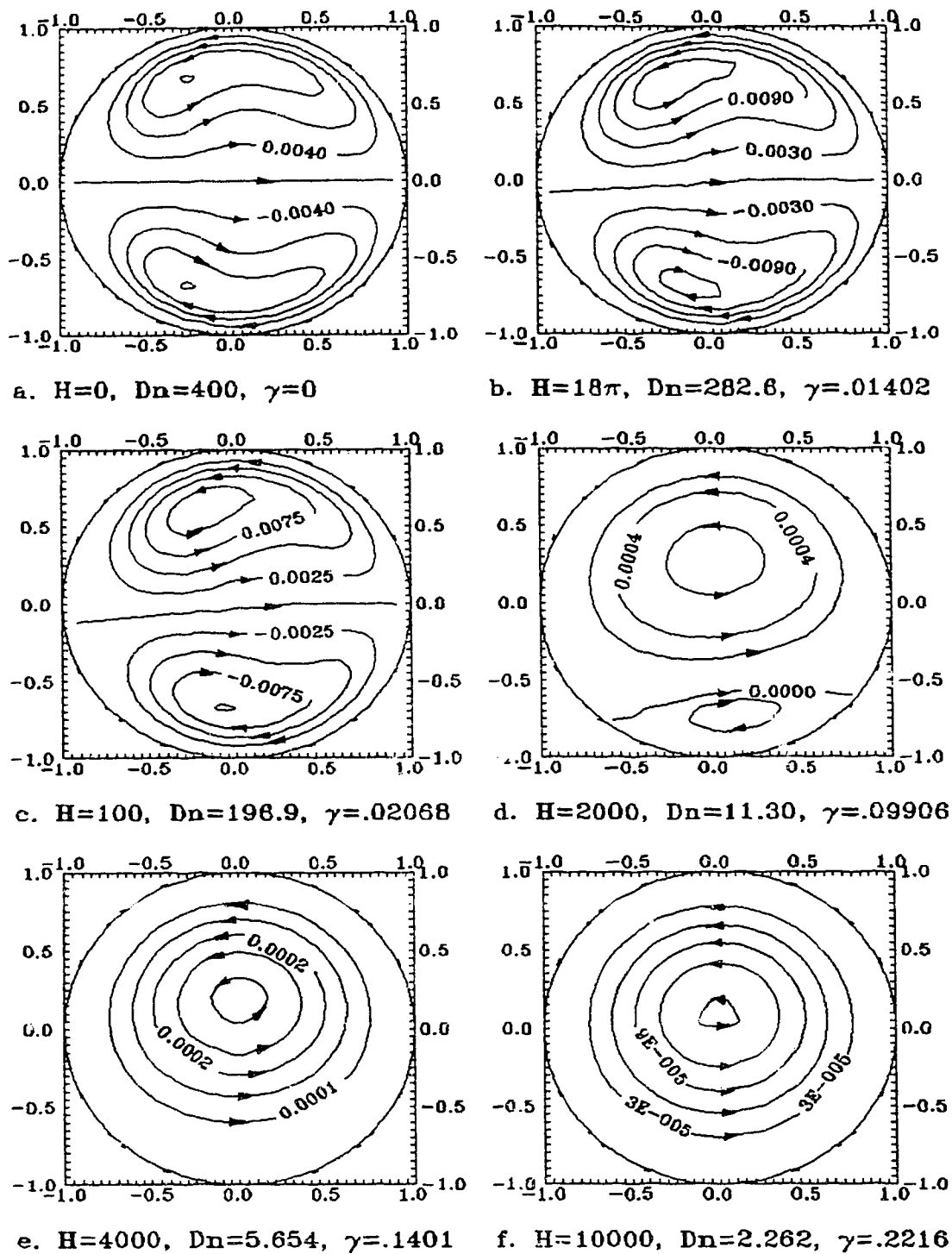e. H=4000, Dn=5.654, γ=.1401

f. H=10000, Dn=2.262, γ=.2216

Fig. 4.11. Secondary flow patterns for Re = 1200, Rc = 9. All the contours are equally–spaced except in d) the lower vortex is one order of magnitude smaller than the upper vortex.
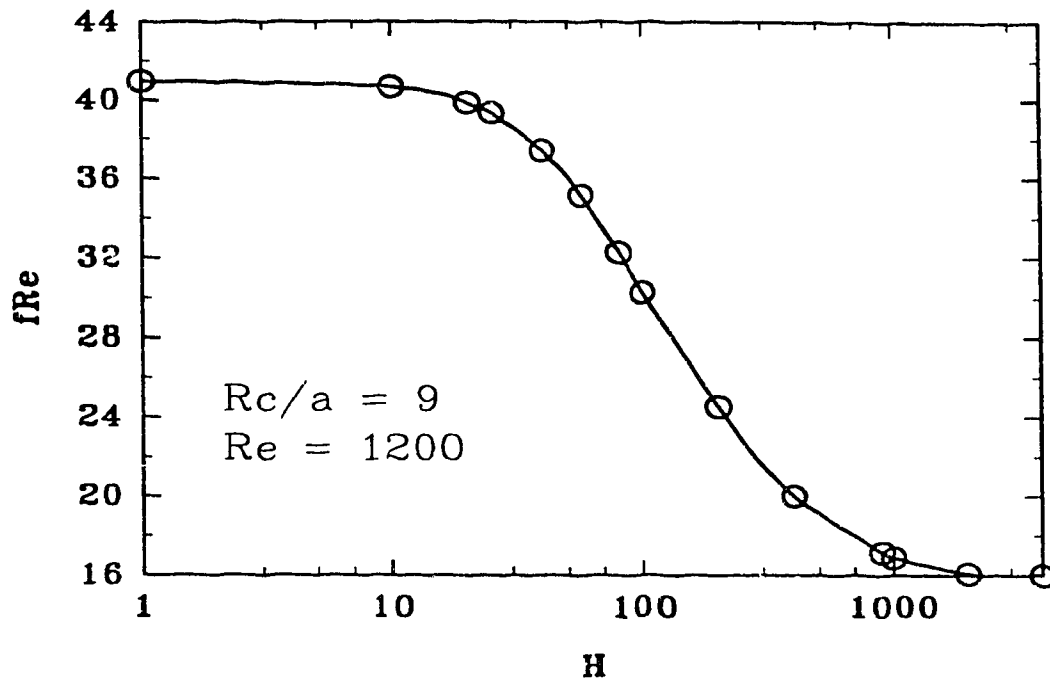
Fig. 4.12. Friction factor variation with H for Rc = 9 and Re = 1200.

Table 4.2. Torsion effect under Re = 1200 and Rc = 9

H	λ	η	γ	Dn	fRe	$u_{0,0}$	u_{max}	p_{max}	$-p_{min}$
0	.11111	0	0	400	40.96	.5674	.8153	60.99	19.99
10	.10774	.01905	.002924	393.9	40.67	.5670	.8168	59.46	19.32
20	.09876	.03493	.005721	377.1	39.88	.5658	.8210	55.30	17.57
40	.07406	.05238	.01065	326.6	37.41	.5632	.8338	43.19	12.96
18π	.05556	.05556	.014016	̇82.8	35.14	.5628	.8439	33.44	9.66
80	.03702	.05237	.0179	̇30.9	32.28	.5664	.8547	23.01	6.48
100	.02692	.04761	.0206	̇ 96.9	30.29	.5726	.8596	17.04	4.77
200	.008225	.02909	.0307 ̇	108.8	24.52	.6180	.8684	5.416	1.569
900	4.369E–4	.006954	.066 ̇	25.08	17.15	.8820	.9867	.3030	.1315
1000	3.542E–4	.006263	.0 ̇00 ̇	22.58	16.87	.9042	.9899	.2359	.1121
2000	8.876E–5	.003139	̇ ̇ ̇6	11.30	16.08	.9879	.9988	.0489	.0380
4000	2.220E–5	.001570	.14013	5.654	16.01	.9985	.9996	.0113	.0105
8000	5.551E–6	7.854E–4	.19823	2.827	16.00	.9998	.9999	.0028	.0027
10000	3.553E–6	6.283E–4	.22161	2.262	16.00	.9999	.9999	.0018	.0017

4.4. Curvature ratio effect

The curvature ratio λ effect on the helical flow has not been investigated in great detail in the past. In this study, we separate the curvature ratio from all the other parameters. Some results are listed in Table 4.3.

The contours showing the secondary flow pattern under various λ for Dn = 100 and Dn = 500 are presented in Figures 4.13 − 4.16. For the case of $\eta = 0$, i.e., a torus, Figure 4.13 shows that for the smaller Dn of 100, the secondary flow patterns look remarkably similar, even though λ changes from 0.04 to an extremely tight torus. For the larger Dn of 500, there is much distortion to the kidney shaped vortices. For λ approaching unity, the vortices are separated from each other near the inner wall where the secondary flow near the inner wall is weaker than that at the outer wall. Figures 4.15 and 4.16 show the secondary flow patterns at $\eta = 0.5\lambda$ for Dn = 100 and 500, respectively. The vortex dividing line becomes much distorted when λ is increased. This is very much evident especially for the case of Dn = 500. Here, the effect of the terms $\lambda\eta$ and $\lambda^2\eta$ which appear in the governing equations (4.5–4.9) becomes significant. It should be recalled that these terms are dropped out for a loose coiling approximation.

The axial velocity isolines are shown in Figures 4.17 and 4.18 for a very wide range of curvature ratio. A low value of λ, i.e., when loose coiling approximation holds, the axial velocity is characterized by a single maximum velocity value located along the line of symmetry. Its location is close to the outer wall. However, as λ is increased beyond 0.5, a case not as yet reported in the literature, the maximum velocity occurs at two locations in the upper and lower section of the torus. In fact, their locations shift towards the inner wall as λ is increased.

Table 4.3. Curvature ratio effect under small torsion

Rc	H	λ	η	Gn	γ	fRe	$u_{0,0}$	u_{max}	p_{max}	$-p_{min}$
				Dn = 20						
10000	0	.0001	0	0	0	16.61	.9291	.9953	.1091	.0564
100	0	.01	0	0	0	16.65	.9290	.9937	1.083	.568
16	0	.0625	0	0	0	16.80	.9299	.9835	2.567	1.505
10	0	.1	0	0	0	16.91	.9303	.9767	3.129	1.983
5	0	.2	0	0	0	17.17	.9293	.9598	4.019	3.120
3.333	0	.3	0	0	0	17.42	.9252	.9421	4.478	4.257
2.5	0	.4	0	0	0	17.65	.9186	.9271	4.711	5.488
2	0	.5	0	0	0	17.86	.9094	.9126	4.802	6.885
1.667	0	.6	0	0	0	18.06	.8975	.8975	4.793	8.537
1.429	0	.7	0	0	0	18.26	.8829	.8832	4.713	8.537
1.25	0	.8	0	0	0	18.46	.8657	.8691	4.581	13.30
1.111	0	.9	0	0	0	18.72	.8466	.8542	4.419	17.33
				Dn = 40						
10000	0	.0001	0	0	0	18.94	.7726	.9475	.2412	.0782
100	0	.01	0	0	0	18.99	.7734	.9444	2.387	.7914
16	0	.0625	0	0	0	19.25	.7760	.9274	5.645	2.116
10	0	.1	0	0	0	19.44	.7774	.9159	6.869	2.805
5	0	.2	0	0	0	19.88	.7794	.8871	8.783	4.491
3.333	0	.3	0	0	0	20.28	.7787	.8606	9.755	6.222
2.5	0	.4	0	0	0	20.64	.7757	.8366	10.24	8.14
2	0	.5	0	0	0	20.95	.7701	.8140	10.41	10.36
1.667	0	.6	0	0	0	21.23	.7623	.7967	10.37	13.02
1.429	0	.7	0	0	0	21.48	.7522	.7831	10.19	16.38
1.25	0	.8	0	0	0	21.70	.7400	.7711	9.89	20.93
1.111	0	.9	0	0	0	21.93	.7262	.7646	9.53	27.90
1	0	1	0	0	0	22.25	.7145	.7586	9.21	41.10
				Dn = 100						
25	0	.04	0	0	0	24.12	.6321	.8649	10.35	3.45
20	20π	.04	.02	10	.01	24.13	.6317	.8642	10.38	3.44

Table 4.3. Curvature ratio effect under small torsion, contd.

Rc	H	λ	η	Gn	γ	fRe	$u_{0,0}$	u_{max}	p_{max}	$-p_{min}$
12.5	25π	.04	.04	20	.02	24.14	.6318	.8608	10.49	3.40
10	0	.1	0	0	0	24.56	.6346	.8450	15.40	5.84
8	8π	.1	.05	15.81	.0158	24.60	.6338	.8435	15.51	5.80
5	10π	.1	.1	31.62	.0316	24.70	.6327	.8383	15.86	5.65
5	0	.2	0	0	0	25.21	.6383	.8144	19.81	9.22
4	4π	.2	.1	22.36	.0224	25.36	.6374	.8120	20.11	9.07
2.5	5π	.2	.2	44.72	.0447	25.78	.6349	.8045	20.94	8.61
4	0	.25	0	0	0	25.55	.6380	.8006	21.08	10.95
3.2	3.2π	.25	.125	25	.025	25 77	.6377	.7981	21.50	10.73
2	4π	.25	.25	50	.05	26.40	.6371	.7896	22.72	9.96
3.333	0	.3	0	0	0	25.82	.6393	.7870	22.12	12.66
2.667	8.376	.3	.15	27.39	.0274	26.14	.6397	.7846	22.68	12.32
1.667	10.47	.3	.3	54.77	.0548	27.07	.6405	.7780	24.24	11.23
2.5	0	.4	0	0	0	26.37	.6387	.7620	23.37	16.44
2	2π	.4	.2	31.62	.0316	26.95	.6425	.7655	24.29	15.75
1.25	2.5π	.4	.4	63.25	.0632	28.59	.6511	.7674	26.80	13.60
2	0	.5	0	0	0	26.89	.6363	.7484	23.90	20.84
1.6	1.6π	.5	.25	35.36	.0354	27.83	.6464	.7611	25.32	19.61
1	2π	.5	.5	70.71	.0707	30.40	.6680	.7692	29.13	15.58
1.667	0	.6	0	0	0	27.28	.6339	.7432	24.10	26.03
1.333	4.189	.6	.3	38.73	.0387	28.76	.6537	.7623	26.24	23.77
.8333	5.236	.6	.6	77.46	.0775	32.51	.6914	.7859	31.44	16.87
1.429	0	.7	0	0	0	27.65	.6302	.7364	23.93	32.71
1.143	3.590	.7	.35	41.83	.0418	29.89	.6646	.7722	27.03	28.60
.7143	4.488	.7	.7	83.67	.0837	34.80	.7197	.8012	33.72	16.89
1.25	0	.8	0	0	0	27.91	.6258	.7358	23.37	41.75
1	π	.8	.4	44.72	.0447	31.27	.6808	.7811	27.95	33.93
1.111	0	.9	0	0	0	28.24	.6199	.7339	22.85	56.71
1	0	1	0	0	0	28.67	.6154	.7325	22.13	89.30

Dn = 150

10000	0	.0001	0	0	0	27.08	.5936	.8767	.7968	.2309
100	0	.01	0	0	0	27.18	.5943	.8730	7.885	2.334
16	0	.0625	0	0	0	27.68	.5975	.8538	18.67	6.185

Table 4.3. Curvature ratio effect under small torsion, contd.

Rc	H	λ	η	Gn	γ	fRe	$u_{0,0}$	u_{max}	P_{max}	$-P_{min}$
10	0	.1	0	0	0	28.02	.5996	.8410	22.74	8.155
5	0	.2	0	0	0	28.87	.6041	.8094	29.21	12.87
3.333	0	.3	0	0	0	29.63	.6074	.7810	32.66	17.62
2.5	0	.4	0	0	0	30.32	.6099	.7548	34.55	22.82
2	0	.5	0	0	0	30.92	.6115	.7303	35.48	28.82
1.667	0	.6	0	0	0	31.45	.6125	.7154	35.75	36.07
1.429	0	.7	0	0	0	31.88	.6127	.7169	35.52	45.36
1.25	0	.8	0	0	0	32.22	.6116	.7178	31.88	58.31
1.111	0	.9	0	0	0	32.47	.6084	.7237	33.88	79.35
1	0	1	0	0	0	32.79	.6024	.7182	32.74	128.6

Dn = 250

Rc	H	λ	η	Gn	γ	fRe	$u_{0,0}$	u_{max}	P_{max}	$-P_{min}$
10000	0	.0001	0	0	0	32.65	.5650	.8725	1.311	.354
100	0	.01	0	0	0	32.78	.5660	.8684	12.97	3.578
16	0	.0625	0	0	0	33.44	.5705	.8477	30.68	9.469
10	0	.1	0	0	0	33.89	.5736	.8337	37.36	12.47
5	0	.2	0	0	0	35.01	.5812	.7990	47.93	19.65
3.333	0	.3	0	0	0	36.02	.5879	.7676	53.57	26.89
2.5	0	.4	0	0	0	36.91	.5938	.7390	56.64	34.84
2	0	.5	0	0	0	37.68	.5987	.7123	58.13	44.05
1.667	0	.6	0	0	0	38.31	.6023	.6872	58.51	55.25
1.429	0	.7	0	0	0	38.81	.6038	.6919	58.05	69.65
1.25	0	.8	0	0	0	39.15	.6024	.6999	56.90	89.84
1.111	0	.9	0	0	0	39.33	.5970	.6964	55.15	123.0
1	0	1	0	0	0	39.46	.5975	.7059	53.11	205.9

Dn = 500

Rc	H	λ	η	Gn	γ	fRe	$u_{0,0}$	u_{max}	P_{max}	$-P_{min}$
10000	0	.0001	0	0	0	42.90	.5553	.8554	2.547	.649
400	0	.0025	0	0	0	42.94	.5555	.8543	12.70	3.25
100	0	.01	0	0	0	43.08	.5564	.8510	25.19	6.56
80	80π	.01	.005	25	.0022	43.08	.5562	.8509	25.22	6.55
50	100π	.01	.01	50	.0045	43.11	.5556	.8505	25.29	6.53
25	0	.04	0	0	0	43.61	.5598	.8377	48.76	13.56
20	20π	.04	.02	50	.0045	43.66	.5591	.8371	48.95	13.50

Table 4.3. Curvature ratio effect under small torsion, contd.

Rc	H	λ	η	Gn	γ	fRe	$u_{0,0}$	u_{max}	P_{max}	$-P_{min}$
12.5	25π	.04	.04	100	.0089	43.78	.5569	.8355	49.49	13.39
16	0	.0625	0	0	0	44.01	.5623	.8284	59.51	17.37
10	0	.1	0	0	0	44.64	.5662	.8138	72.39	22.89
8	8π	.1	.05	79.06	.0077	44.78	.5647	.8124	73.06	22.70
5	10π	.1	.1	158.1	.0144	45.20	.5603	.8082	74.96	22.16
5	0	.2	0	111.8	0	46.20	.5756	.7775	92.72	36.12
4	4π	.2	.1	111.8	.01	46.60	.5739	.7748	94.39	35.54
2.5	5π	.2	.2	223.6	.02	47.80	.5683	.7672	99.19	33.59
4	0	.25	0	0	0	46.92	.5797	.7611	98.88	42.69
3.333	0	.3	0	0	0	47.58	.5833	.7456	103.4	49.5
2.667	8.378	.3	.15	136.9	.0123	48.39	.5828	.7425	106.4	48.2
1.667	10.47	.3	.3	273.9	.0245	50.79	.5796	.7333	110.1	37.0
2.5	0	.4	0	0	0	48.79	.5891	.7165	109.2	64.2
2	2π	.4	.2	158.1	.0141	50.19	.5914	.7143	113.8	61.6
1.25	2.5π	.4	.4	316.2	.0283	54.34	.5941	.7072	127.0	52.4
2	0	.5	0	0	0	49.82	.5926	.6900	112.0	81.2
1.6	1.6π	.5	.25	176.8	.0158	52.07	.5997	.6907	118.8	76.2
1	2π	.5	.5	353.6	.0316	58.65	.6111	.6909	138.2	59.1
1.667	0	.6	0	0	0	50.65	.5936	.6652	112.7	101.9
1.333	4.189	.6	.3	193.7	.0173	54.20	.6077	.6717	122.7	92.3
.8333	5.236	.6	.6	387.3	.0346	63.87	.6287	.6864	149.7	62.2
1.429	0	.7	0	0	0	51.?8	.5917	.6499	111.8	128.5
1.143	3.590	.7	.35	209.?	.0187	56.76	.6159	.7546	126.4	109.6
1.25	0	.8	0	0	0	51.67	.5865	.6557	109.6	165.8
1.111	0	.9	0	0	0	51.75	.5780	.6801	106.3	227.5
1	0	1	0	0	0	51.77	.5670	.6968	102.3	394.1

a. $\lambda = 0.04$

b. $\lambda = 0.2$

c. $\lambda = 0.4$

d. $\lambda = 0.6$

e. $\lambda = 0.8$

f. $\lambda = 1$
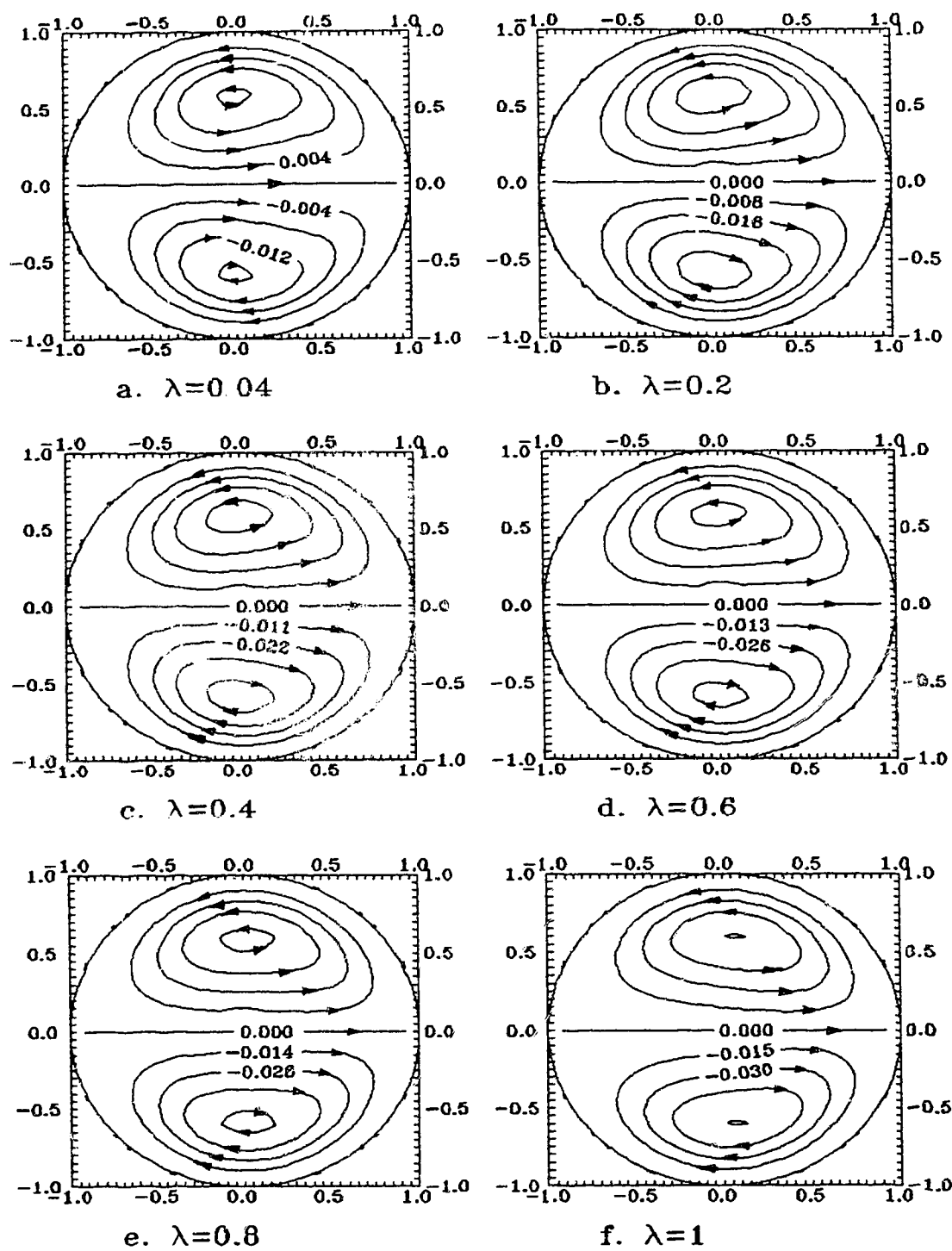
Fig. 4.13. Secondary flow patterns for $Dn = 100$, $\eta = 0$.
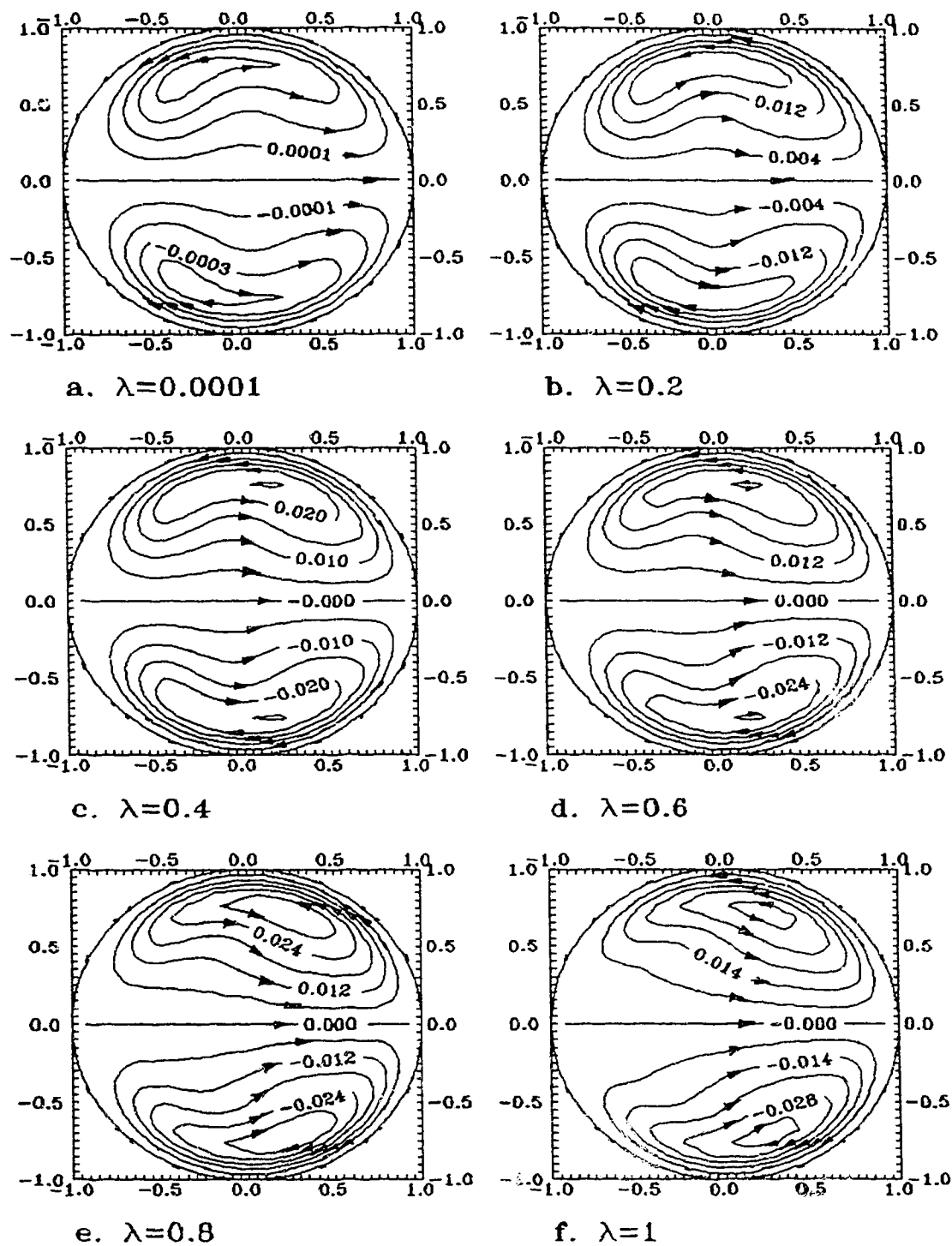
a. $\lambda = 0.0001$

b. $\lambda = 0.2$

c. $\lambda = 0.4$

d. $\lambda = 0.6$

e. $\lambda = 0.8$

f. $\lambda = 1$

Fig. 4.14. Secondary flow patterns for $Dn = 500$, $\eta = 0$.

a. $\lambda{=}.04$, $\eta{=}.02$, $\gamma{=}.01$

b. $\lambda{=}.2$, $\eta{=}.1$, $\gamma{=}.0224$

c. $\lambda{=}.4$, $\eta{=}.2$, $\gamma{=}.0316$

d. $\lambda{=}.6$, $\eta{=}.3$, $\gamma{=}.0387$

e. $\lambda{=}.7$, $\eta{=}.35$, $\gamma{=}.0418$

f. $\lambda{=}.8$, $\eta{=}.4$, $\gamma{=}.0447$

Fig. 4.15. Secondary flow patterns for $Dn = 100$, $\eta = 0.5\lambda$.

a. $\lambda=.04$, $\eta=.02$, $\gamma=.0045$

b. $\lambda=.2$, $\eta=.1$, $\gamma=.01$

c. $\lambda=.4$, $\eta=.2$, $\gamma=.0141$

d. $\lambda=.5$, $\eta=.25$, $\gamma=.0158$

e. $\lambda=.6$, $\eta=.3$, $\gamma=.0173$

f. $\lambda=.7$, $\eta=.35$, $\gamma=.0187$
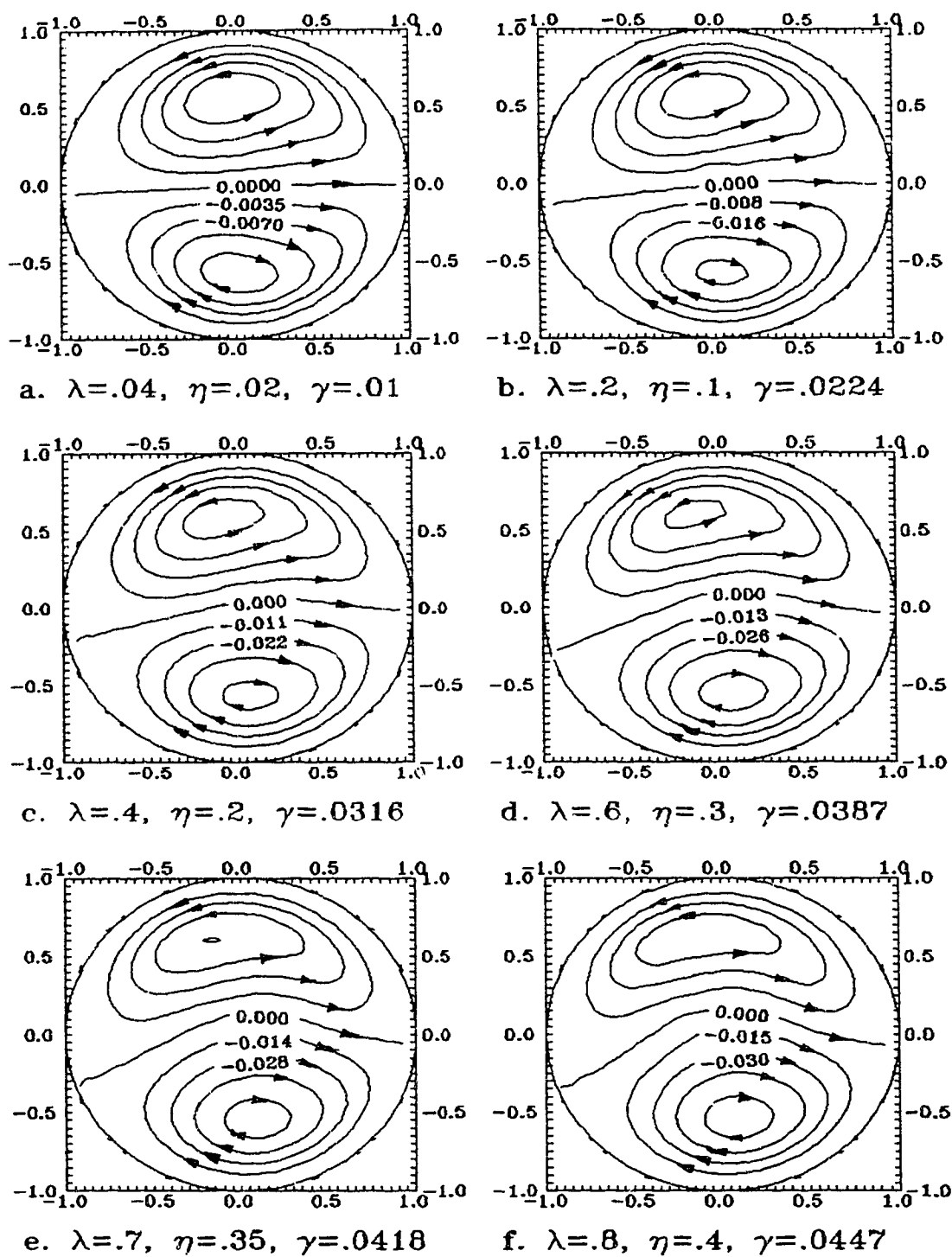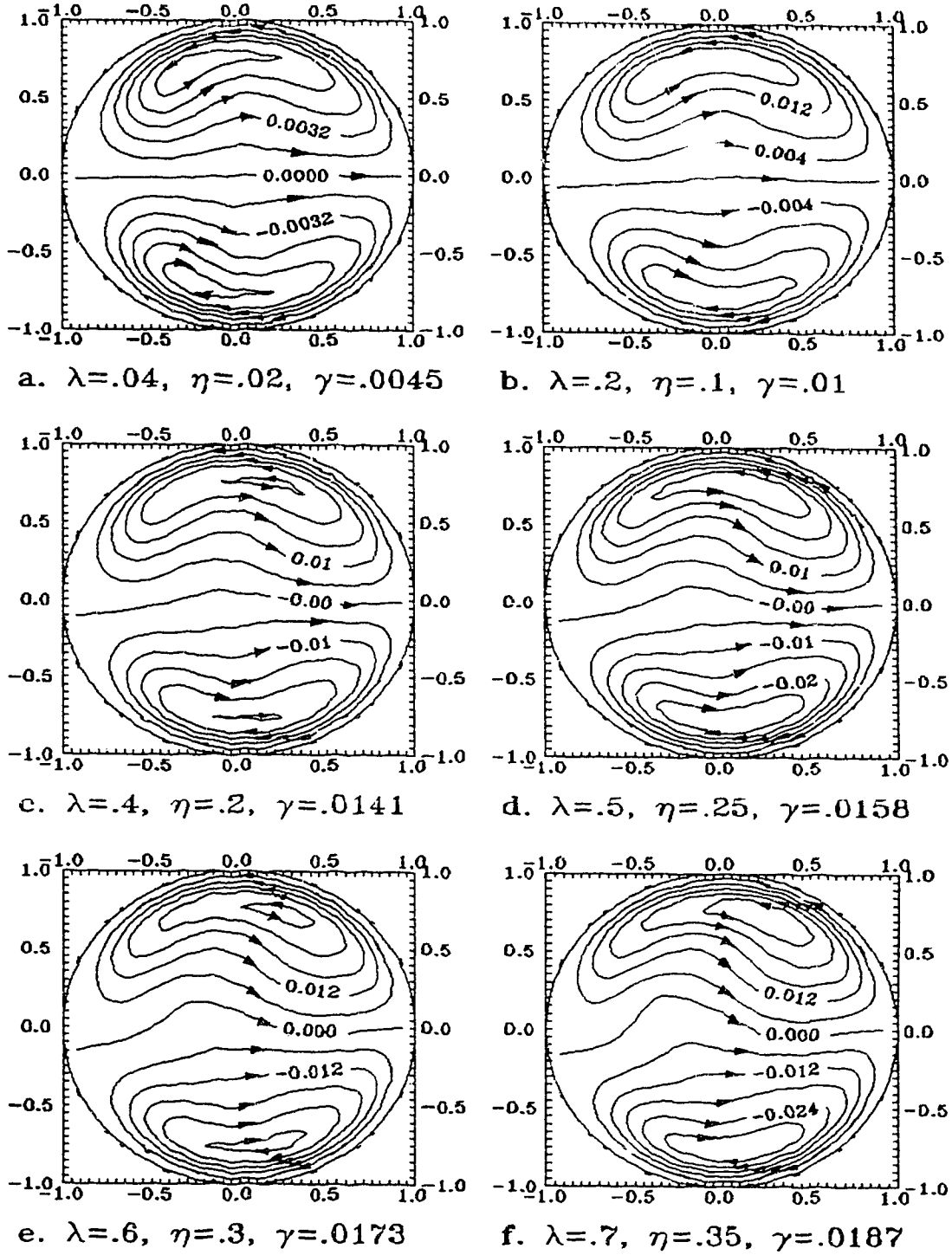
Fig. 4.16. Secondary flow patterns for $Dn = 500$, $\eta = 0.5\lambda$.
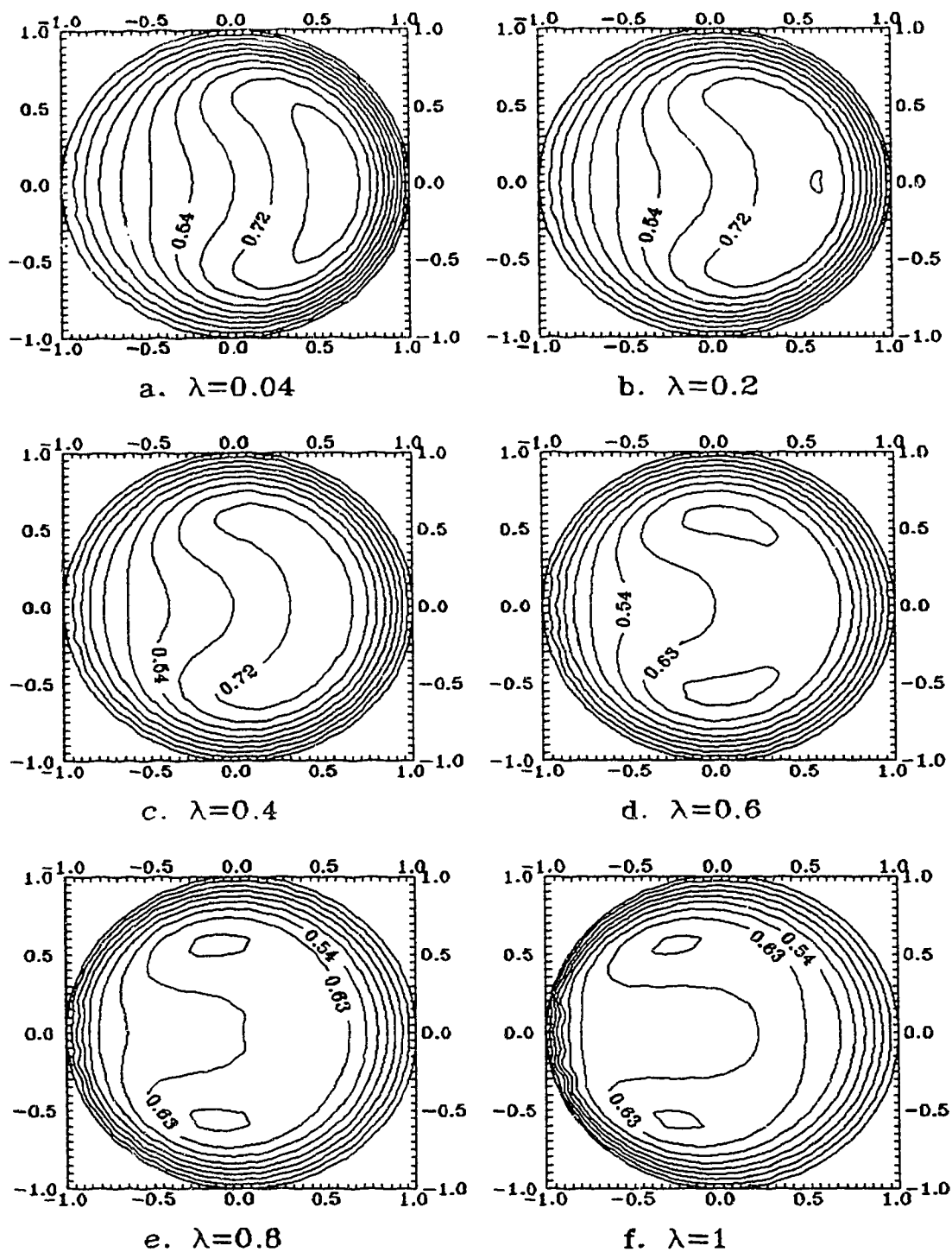
Fig. 4.17. Iso–axial velocity contours for Dn = 100, η = 0.

a. $\lambda=.04$, $\eta=.02$, $\gamma=.01$

b. $\lambda=.2$, $\eta=.1$, $\gamma=.0224$

c. $\lambda=.4$, $\eta=.2$, $\gamma=.0316$

d. $\lambda=.6$, $\eta=.3$, $\gamma=.0387$

e. $\lambda=.7$, $\eta=.35$, $\gamma=.0418$

f. $\lambda=.8$, $\eta=.4$, $\gamma=.0447$
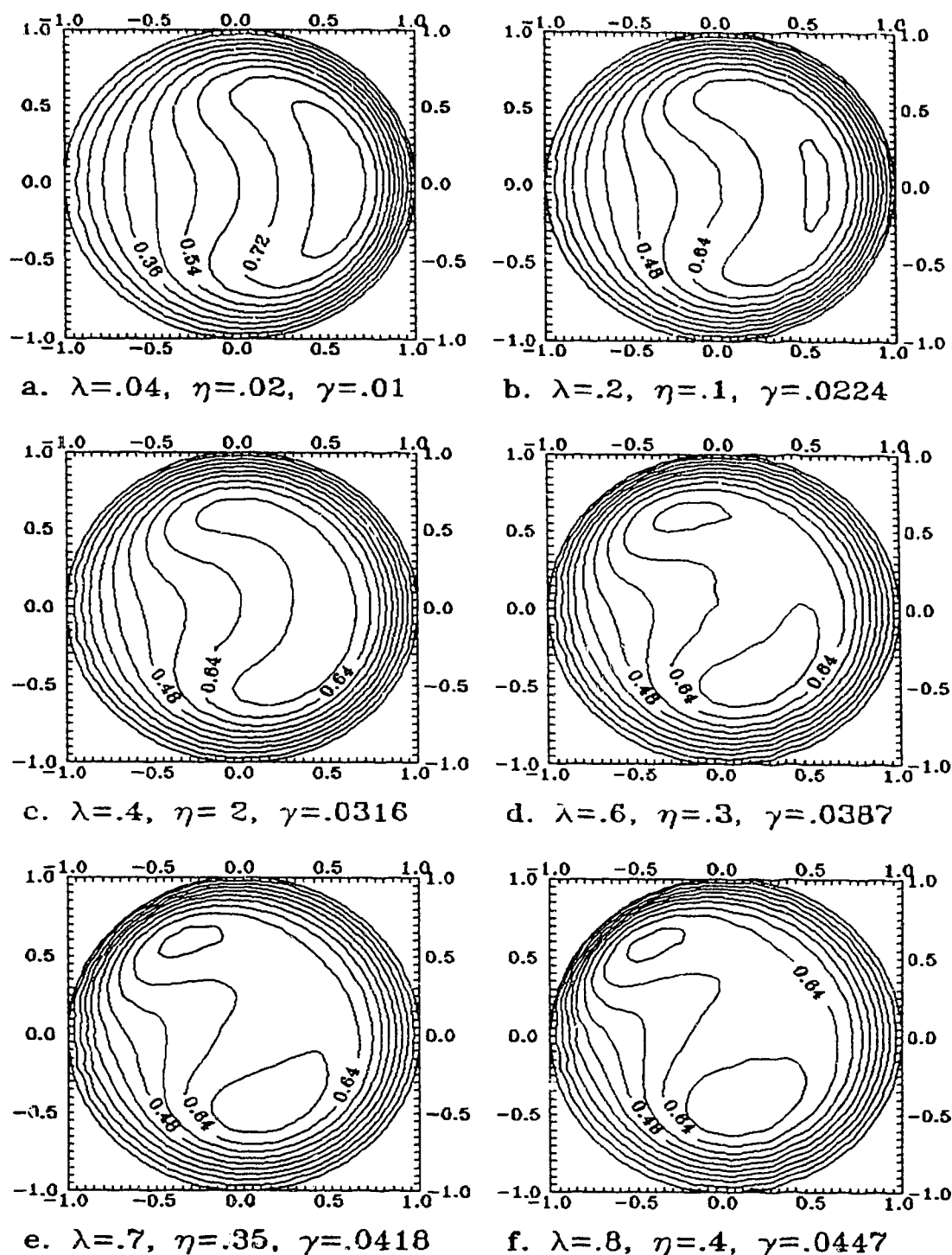
Fig. 4.18. Iso—axial velocity contours for $Dn = 100$, $\eta = \dfrac{\lambda}{2}$.

4.5. Stability of helical flows

If the time—dependent or the parabolized axial—depende[n]
retained, the momentum equations take the form:

$$b\frac{\partial \phi}{\partial \zeta} = (M + d_\phi)\,\phi - S_\phi$$

Where M is defined by equation (4—6b) with $\frac{\partial}{\partial t}$ and $\frac{\partial}{\partial s}$ terms [c]
parameter, for $\zeta = t$, $b = -1$, and for $\zeta = s$, $b = -h_i^{-1}\,\text{Re}\,u\,+$
Correspondingly, the discrete equations can be written as

$$\frac{\partial X}{\partial \zeta} = K(X,\ \text{Re},\ \lambda,\ \eta)$$

If X^0 denotes a steady—state axially—invariant solution and
small disturbance, equation (4—21) becomes, after quasi—linearizati[on]
the steady—state axially invariant solution,

$$\frac{\partial d}{\partial \zeta} = \frac{\partial X}{\partial \zeta} = \frac{\partial K}{\partial X}(X^0,\ \text{Re},\ \lambda,\ \eta)\cdot d$$

Owing to the non—linearity of the problem, it is natural in ou[r]
procedure to use equation (4—22) to arrive at a solution either in
unintentionally. If the solution X^0 is stable and $d^0 = X(\zeta = 0) - X$
enough to cause $X^0 + d^0$ to be more close to another stable solution
will eventually degenerate to zero as $\zeta \to \infty$. This physical explanation [c]
can be represented mathematically as all the real parts of the eige[n]
Jacobian matrix $\frac{\partial K}{\partial X}(X^0,\ \text{Re},\ \lambda,\ \eta)$ must be negative if X^0 is a stable s[o]
also called the first Liapunov method for determining the stability [c]

a. $s^* = 0.00196$, ESN=0.019   b. $s^* = 0.00999$, ESN=0.0081

c. $s^* = 0.0140$ ESN=0.0030   d. $s^* = 0.01999$, ESN=0.0042

e. $s^* = 0.02503$, ESN=0.011   f. $s^* = 0.06833$, ESN=3.5E−5
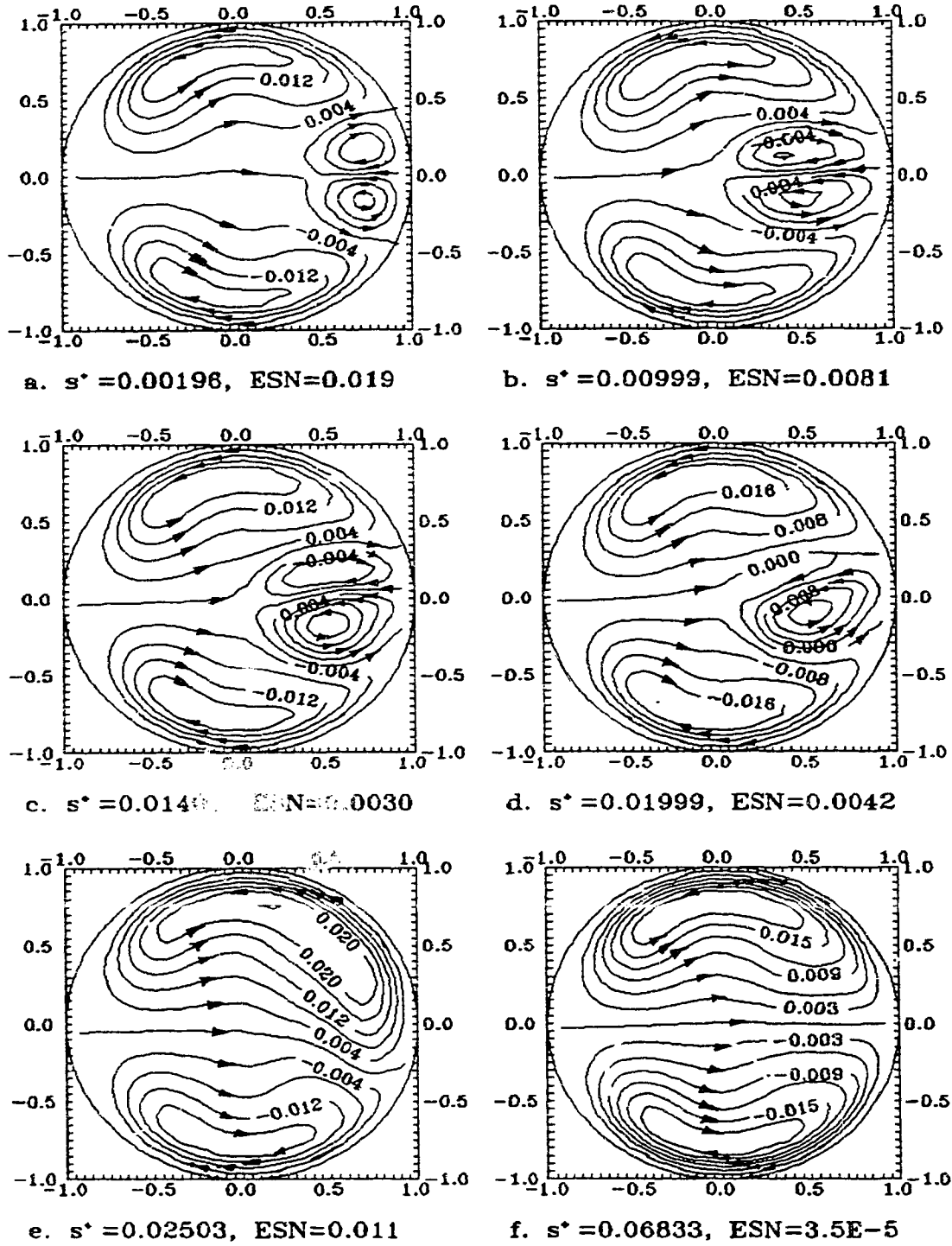
Fig. 4.19.   Secondary flow pattern evolvement after disturbing the two—vortex flow at $s^* = 0$, $\theta = \frac{\pi}{2}$ with a fine grid of n40x48fn for Dn = 500, $\lambda = 0.25$, $\gamma = 0.0032$.

Secondary flow patterns

Iso–axial velocity contours

The pressure contours
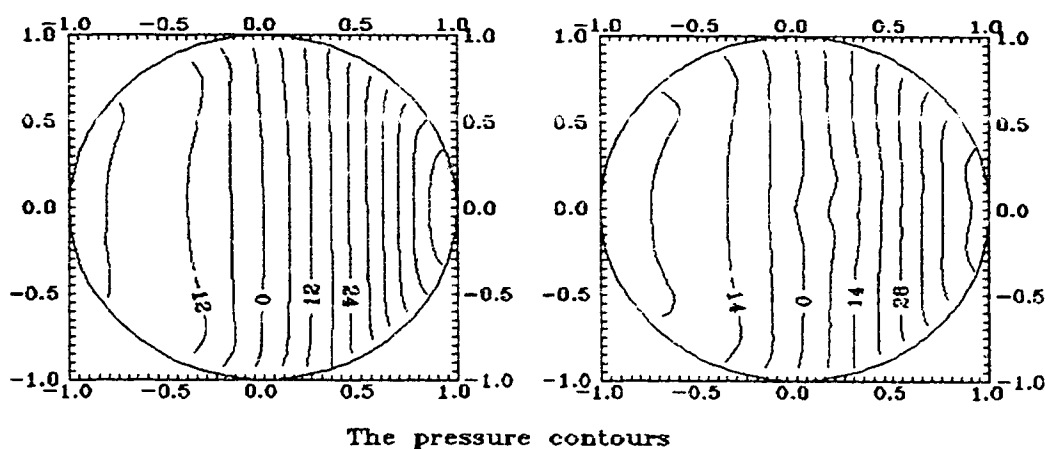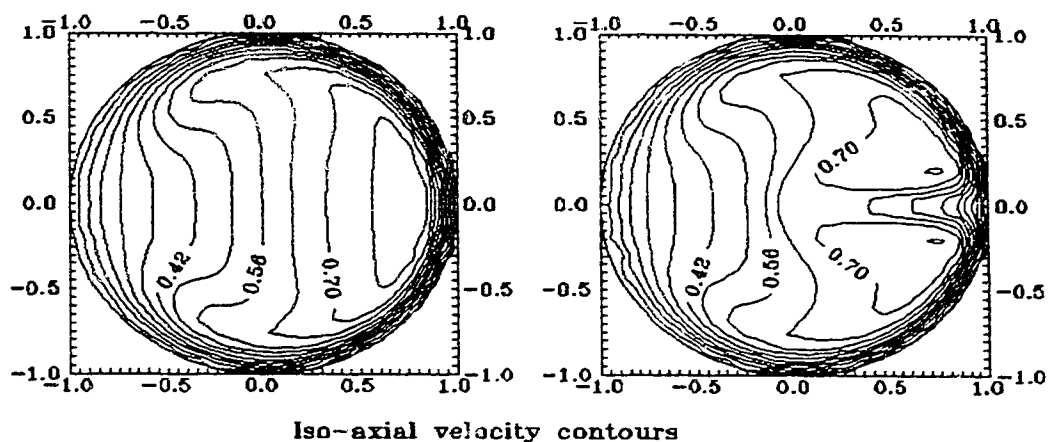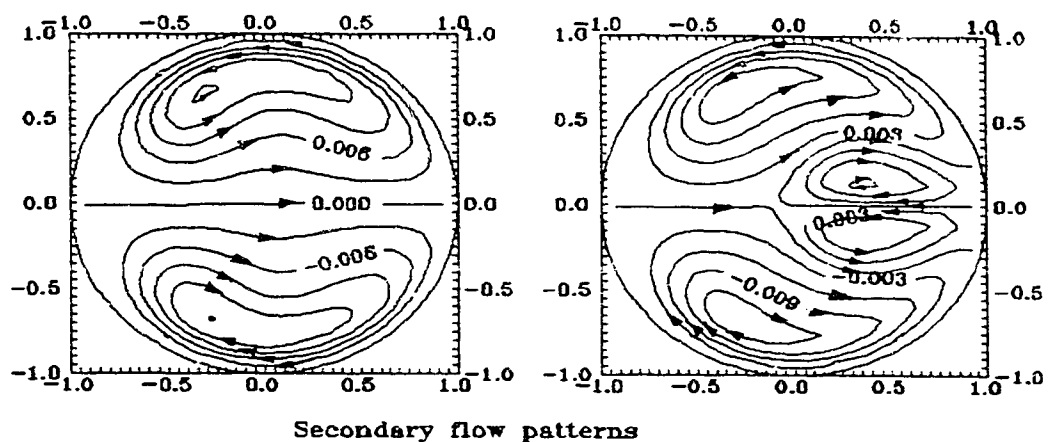
a. Non–perturbed flow   b. Needle–perturbed flow

Fig. 4.20.   Four—vortex flow b) (fRe = 43.67) obtained from a needle–like disturbance on fully developed two—vortex flow a) for Dn = 404.4, Rc = 10, H = 10 with a coarse grid of u25×32fn.

a. s* =0.00205, ESN=0.036

b. s* =0.00598, ESN=0.0097

c. s* =0.01008, ESN=0.0058

d. s* =0.01999, ESN=0.00027

e. s* =0.03006, ESN=0.000031

f. s* =0.09993, ESN=7.2E−6
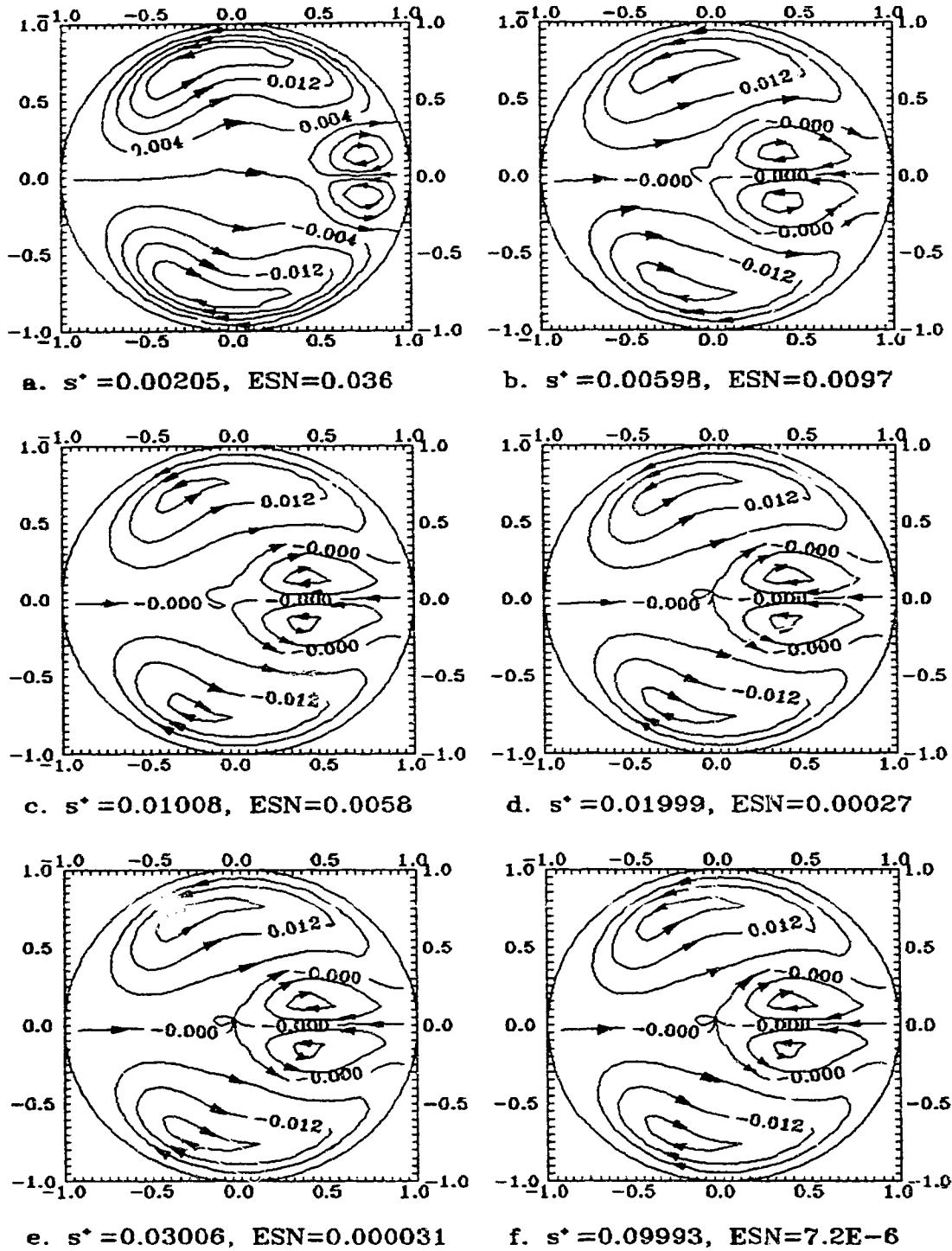
Fig. 4.21. Secondary flow pattern evolvement after disturbing the two—vortex flow at $s^+ = 0$, $\theta = \frac{\pi}{2}$ with a coarse grid of n25x32fn for $Dn = 500$, $\lambda = 0.25$, $\gamma = 0.0032$.

stress jump ($\frac{\partial u}{\partial \theta}$ has a finite jump at $\theta = -\frac{\pi}{2}$) between them. As long as the asymmetrical appearance occurs, the two small vortices are encapsulated by the two main vortices. The two—vortex pattern stays. Hence, the four—vortex flows are not stable. The forming of the four—vortex pattern lengthens the axial distance required for the flow to reach fully—developed. To obtain the axially—invariant four—vortex solution, one must force the discontinuity to be formed and ensure the symmetry about the y—axis not to be disturbed.

When the grid is not fine enough for a large Dean number flow problem, a four—vortex solution is seemingly stable as it appears not to degenerate to a two—vortex solution as the flow develops down the pipe. Actually, an axially—invariant four—vortex flow solution can be obtained for large Dean number flow problems with a coarse mesh. One such example is shown in Figure 4.20. To be complete, the flow evolvement after disturbance for the case of Dn=500, Rc=3.846, H=4.833 is provided in Figure 4.21, where the grid of n25×32fu is used to show the formation of the four—vortex type solutions.

Although the four—vortex solution is not stable as we find, experimental observations of four—vortex solution have been made by Cheng & Mok (1986) and Cheng & Yuen (1987). However, this is not surprising. Owing to the long length required for the disappearing of the four vortices, $s^{+} \simeq 0.02$ for Dn = 500 and $\gamma = 0.0032$, one has enough opportunity to observe the four vortices. In the experimental studies of Cheng & Mok and Cheng & Yuen, a short pipe was used to obtain the four—vortex flow patterns in a torus.

4.6. Some discussions on the representation of secondary flow

The flow structure is independent of reference frame. Using a different reference frame, one may observe different patterns. Hence, there is no right or wrong in presenting the flow in different reference frames.

The secondary flow is an important aspect of the helical flow behavior. It determines the fluid movement and the momentum and energy / mass transport in the cross plane normal to the axial direction. The rotating secondary flow can also stabilize the helical flow up to a certain extent. Hence turbulence in the helical flow is delayed compared to the Poiseuille flow where the secondary flow is absent. The stabilizing effect was first observed by Taylor (1929).

As Tuttle (1990) noted that the stream tube is a correct observation in the rotating Frenet frame where the axially–invariant (fully–developed) flow is extracted. The advantage of the pseudo–secondary flow stream function approach is that the pseudo–secondary stream tubes (or secondary flow pattern) show a complete picture of the fluid element movement across the pipe when the geometry of the pipe is fixed. In the limit of small γ, the strength of the true secondary flow may be deduced from the pseudo–secondary flow stream function. Owing to the full circular pipe geometry, no pure torsion effect can be observed (Germano 1989). Hence, the secondary flow strength may not be deduced from the pseudo–secondary flow stream function (Chapter 3) when γ is large or Gn is dominant. Since the secondary flow strength is important in the large Dn flows, it is necessary to indicate the secondary flow strength for large Dn flows when Gn is increased.

Figure 4.22 shows the secondary flow strength $\|v\|_{r\theta}$ variation with γ for the case of Dn = 100 and $\lambda = 0.01$. From Figure 4.22, we observe that the secondary flow strength increases with γ when $\gamma < 0.15$ and decreases rapidly with γ when $0.15 < \gamma < 0.4$. When $\gamma > 0.4$, the secondary flow strength is relatively invariant
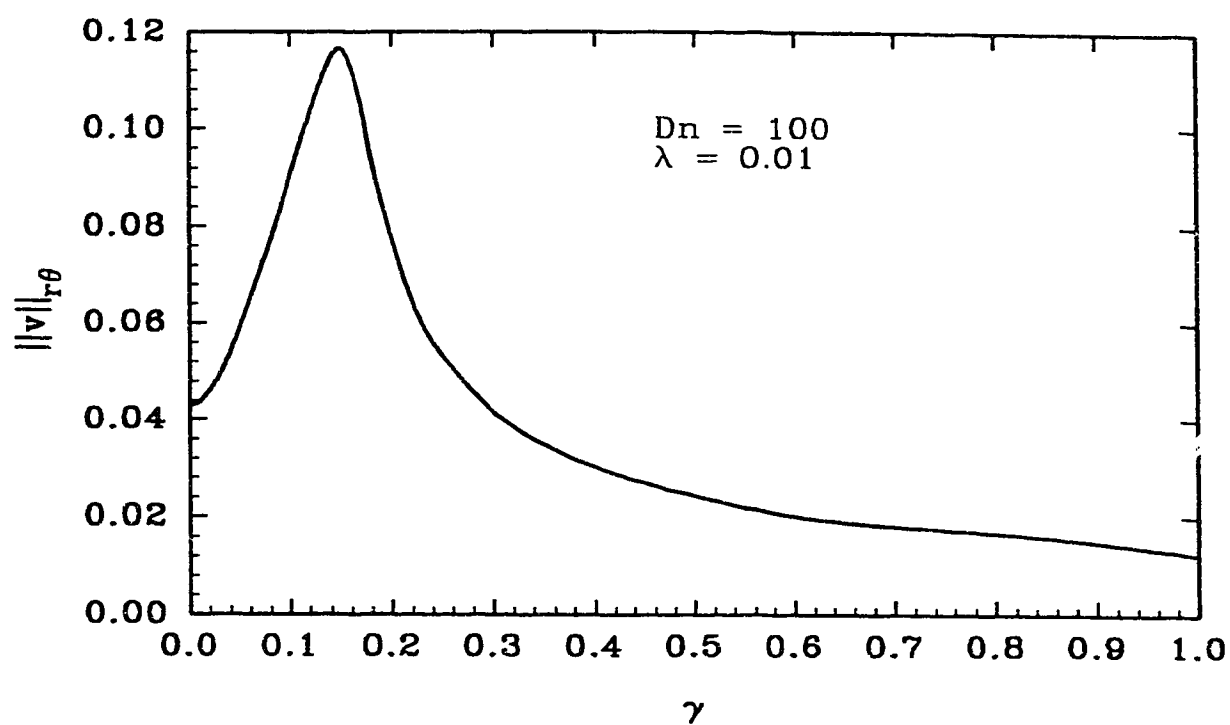
Fig. 4.22.   Orthogonal secondary flow strength variation with γ for Dn $= 100$ and $\lambda = 0.01$.
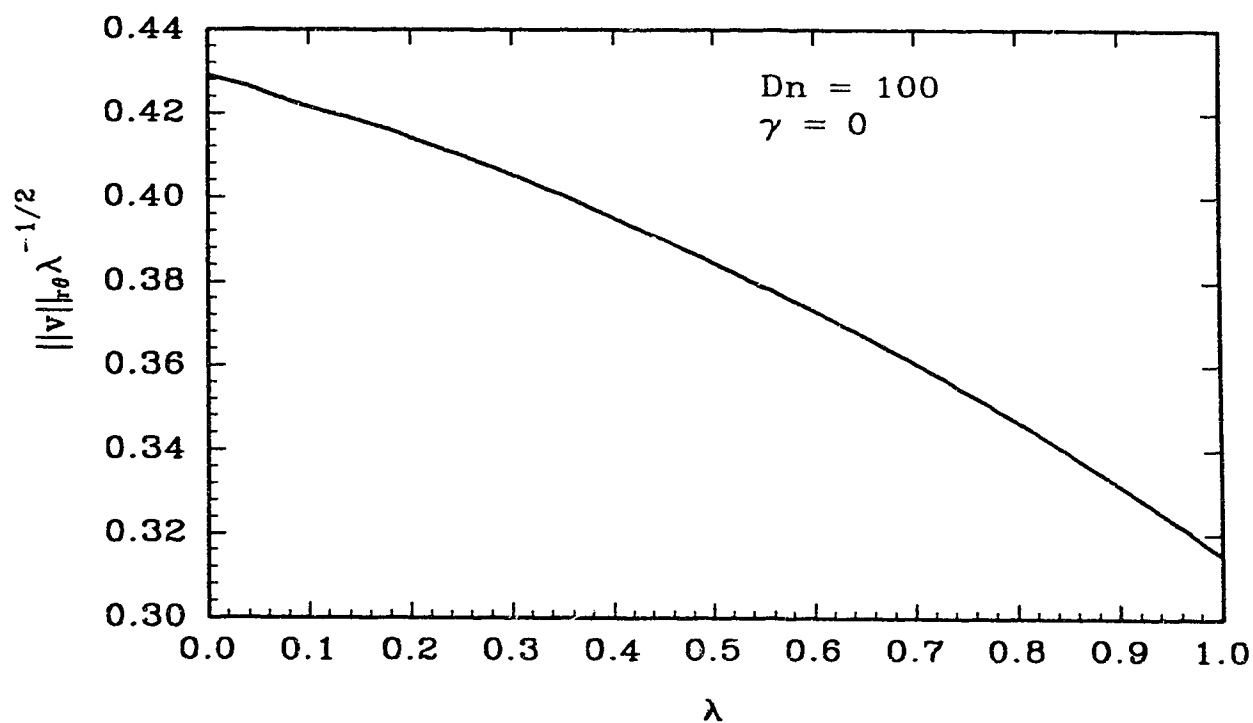
Fig. 4.23.   Orthogonal secondary flow strength variation with λ for Dn $= 100$ and $\gamma = 0$

with varying γ. Although all other properties tend to the limit of the Poiseuille flow, the secondary flow strength tends to a fixed non—zero value due to the fixed Dn. However, a swirling secondary flow does not change the transport property.

Combining with the secondary flow pattern and the secondary flow strength $\|v\|_{r\theta}$, the full picture of the secondary flow may be drawn. The secondary flow pattern shows a fluid element moving direction in the Frenet frame. It is also the momentum and energy / mass transport direction. The secondary flow strength $\|v\|_{r\theta}$ is a measure of the magnitude of the secondary flow in the orthogonal coordinate system (Germano's observer).

To be complete, Figure 4.23 shows the secondary flow strength variation with the curvature ratio λ for the case of Dn = 100 and $\gamma = 0$. It can be seen that $\|v\|_{r\theta}/\sqrt{\lambda}$ decreases slightly with increasing λ.

The introduction of $\|v\|_{r\theta}$ resolved the argument in the controversy over the use of pseudo—secondary flow stream function. However, the secondary flow structure can be different with respect to different inertial frame. To present the other side of the story, the orthogonal secondary velocity vector plots should be introduced to complete the representation.

Figures 4.24a and 4.24b present the secondary flow in the same form as that used by Murata et al. (1981), Kao (1987) and Germano (1989). The arrow plots in Figure 4.24a and 4.24b are the orthogonal secondary velocity vectors on the non—orthogonal r—θ plane. r—θ plane is used to avoid the complication due to the (orthogonal s—) axially variant nature of the helical flow. When the torsion is increased, the secondary flow structure presented in Figures 4.24a and 4.24b is more complicated than that presented in Figure 4.2 for the same flow system.

Figure 4.24a shows that the secondary flow consists of two vortices for small γ. When γ increases, the vortex appearance change in the orthogonal coordinate system is the opposite of that in the non—orthogonal coordinate system. An increase

a). $\gamma = 0$, $\eta = 0$

b). $\gamma = 0.01$, $\eta = 0.01$

c). $\gamma = 0.02$, $\eta = 0.02$

d). $\gamma = 0.04$, $\eta = 0.04$

e). $\gamma = 0.08$, $\eta = 0.08$

f). $\gamma = 0.10$, $\eta = 0.10$
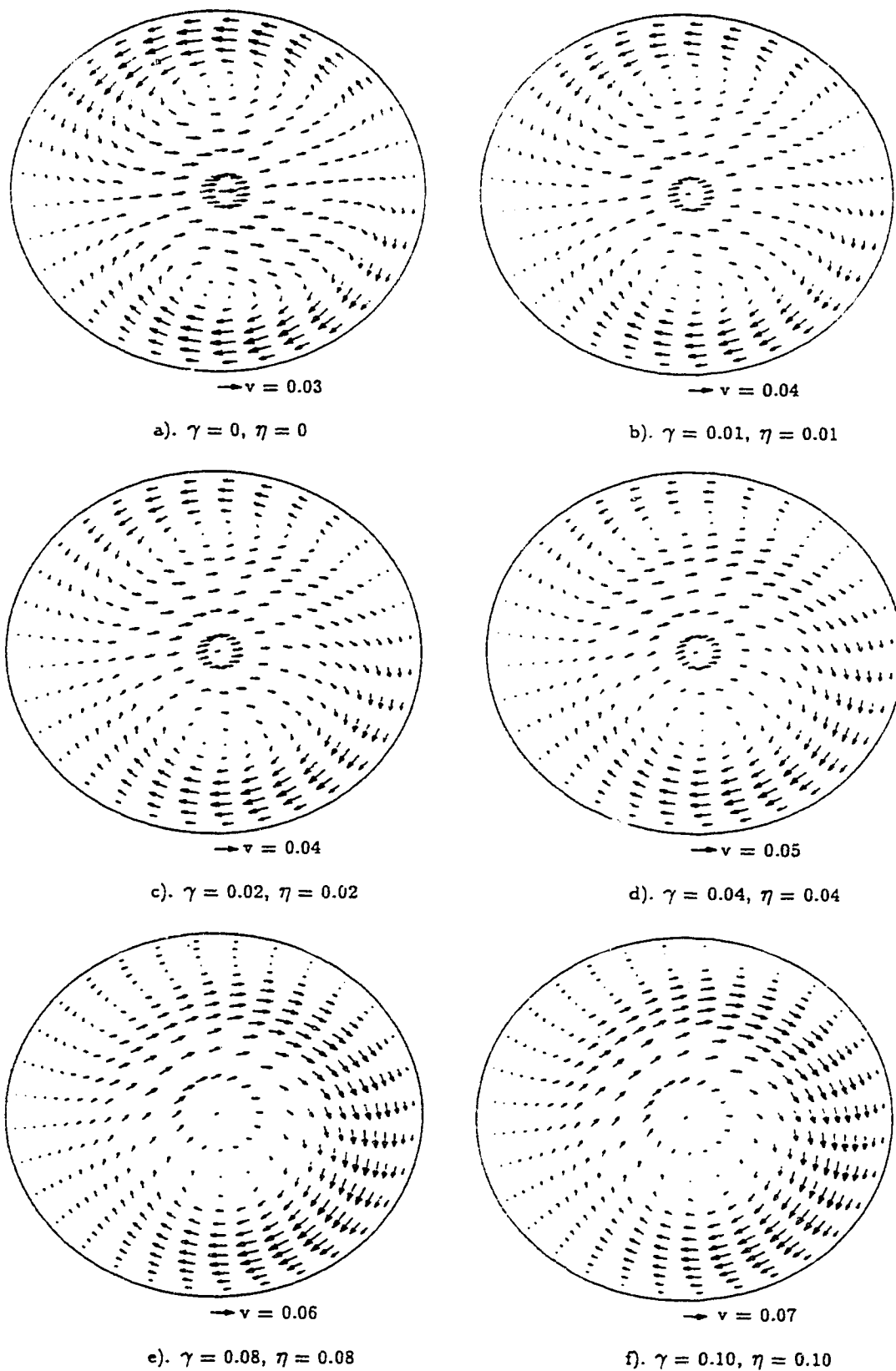
Figure 4.24a.   Orthogonal secondary flow structure variation with γ for $Dn = 100$, $\lambda = 0.01$ and $0 \leq \gamma \leq 0.1$.

a). $\gamma = 0.13$, $\eta = 0.13$ b). $\gamma = 0.18$, $\eta = 0.18$

c). $\gamma = 0.22$, $\eta = 0.22$ d). $\gamma = 0.30$, $\eta = 0.30$

e). $\gamma = 0.60$, $\eta = 0.60$ f). $\gamma = 1$, $\eta = 1$
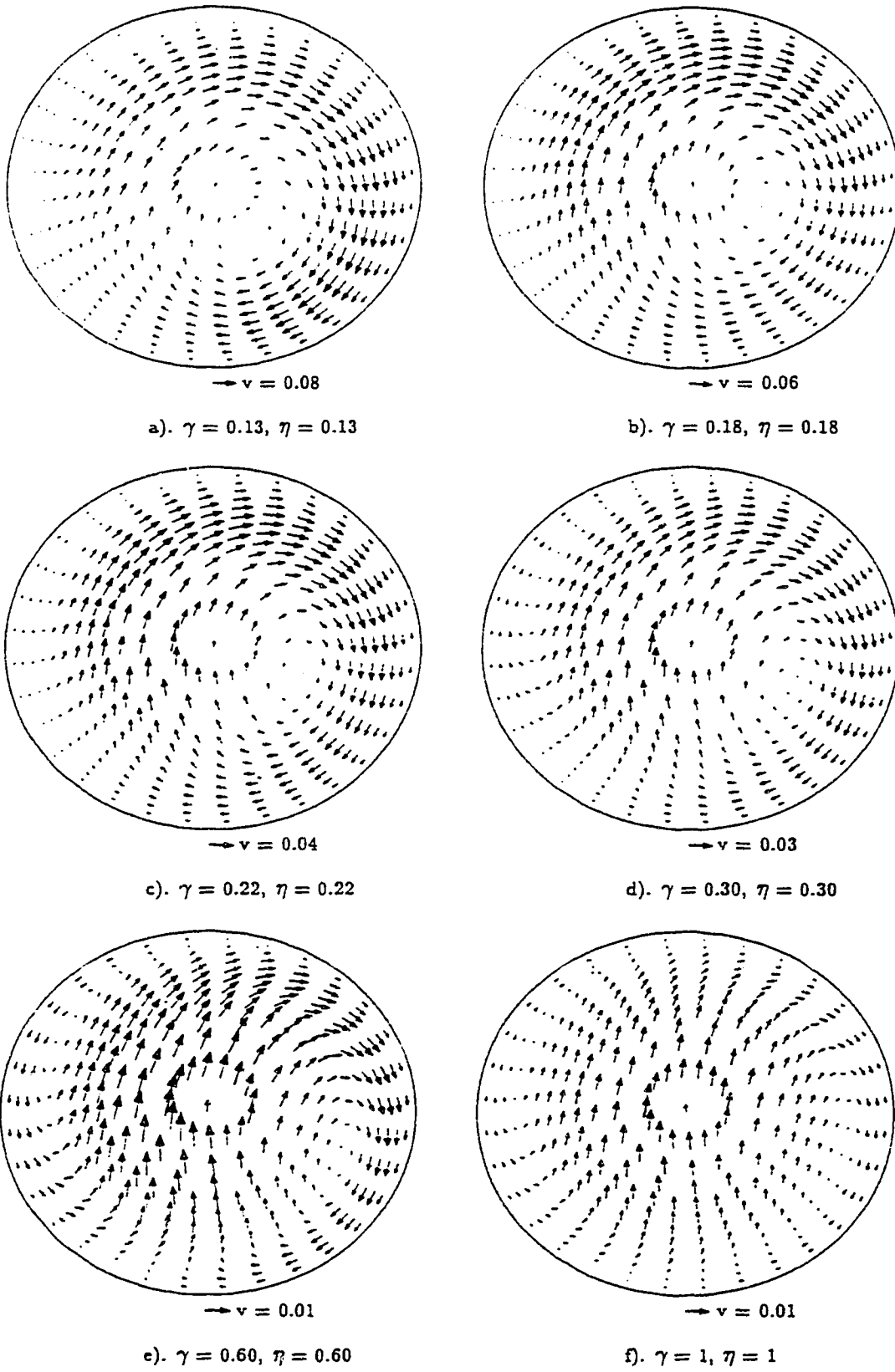
Figure 4.24b.   Orthogonal secondary flow structure variation with γ for $Dn = 100$, $\lambda = 0.01$ and $\gamma > 0.1$.

in γ for $\gamma < 0.1$ results in the lower vortex gaining in both size and strength, while Figure 4.2. shows the upper vortex gaining in size and strength. The change in the vortex structure is relatively abrupt when $\gamma \geq 0.04$ as shown in Figure 4.24a.

Figure 4.24b is a continuation Figure 4.24a. The upper vortex becomes very small in Figure 4.24b.b) where $\gamma = 0.18$. For further increase in γ, the upper vortex starts to gain back in size and in strength. The vortex dividing line rotates anti—clockwise as γ is increased. When $\gamma = 1$, the two vortices become left—and—right. The two vortices are nearly of the same size and strength. The orthogonal secondary flow is strong in the center region and is in the upward direction. In the inner and outer wall region, the secondary flow is very weak and downward. Hence, there is a strong source (coming from the axial flow) located near the lower wall region. A large sink (to the axial flow) appears near the upper wall.

The orthogonal secondary velocity vector plots represent the time—instantaneous secondary flow structure on the $r-\theta$ plane. They indicate the direction of the flow and hence are directly measurable. The time—instantaneous direction does not indicate the momentum / energy transport direction on the $r-\theta$ plane owing to the geometrical change of the pipe. Hence, the orthogonal secondary flow structure cannot be used to interpret the helical flow behavior such as the friction factor variation without resorting to the secondary flow pattern (non—orthogonal secondary flow structure).

The secondary flow patterns (pseudo—secondary flow stream function contour plots) represent the s—axis—instantaneous secondary flow structure on the $r-\theta$ plane. They are the overlapped exposures of secondary flow at various s—distance with the outer wall fixed at the right. The secondary flow pattern indicates the momentum / energy transport direction on the $r-\theta$ plane. Hence, the secondary flow pattern is the property useful in characterizing the helical flow. The secondary flow pattern is a preferred representation when transport phenomena are to be concerned.

4.7. Correlation of fRe with respect to Dn, λ and η

Numerous correlations of the friction factor for the toroidal flow and/or the helical flow under small pitch limit can be found in the literature (see Nandakumar & Masliyah 1986). However, none of them dealt with a reasonably large pitched helical flow. Even the effect of curvature ratio has not been examined in a wide range as it should be. To establish formally a suitable correlation, we need to consider the effects of λ and η, separately to bring about a correlation equation for the combined effect.

The curvature ratio effect on the friction factor is very complicated. Since only the form of the correlation equation is needed for the separate effect of the curvature ratio, we restrict to $\eta = 0$. Some results are shown in Figures 4.25 and 4.26. It is obvious that the linear relationship suggested in the literature is not adequate. The regression equation $fRe = A_1 + A_2\lambda^{A_3}$ is attempted. We found that $A_3 \simeq 1$ for very small Dn flows and $A_3 \simeq 0.5$ for large Dn flows. Hence, when Dn number is large, the friction factor is proportional to the square root of curvature ratio. When the Dn number is very small, the friction factor exhibits a linear relationship with the curvature ratio.

The torsion effect on the friction factor is negligible for the commonly used helically coiled systems, where the pitch is usually small as compared with the radius of the coil. However, the potential of using large pitch coils can not be discounted since it may actually improve heat/mass transfer characteristics. To account for the torsion effect, we restrict the analysis to $\gamma < 0.1$. Some results are shown in Figures 4.27 and 4.28. Since physically, the flow behaves the same for a positive torsion (right handed pipe) and negative torsion (left handed pipe), it is intuitive to consider the relation of the friction factor with respect to the torsion to be $fRe \sim A_1 + A_2\gamma^2$ for small γ. This is also true from the perturbation series of
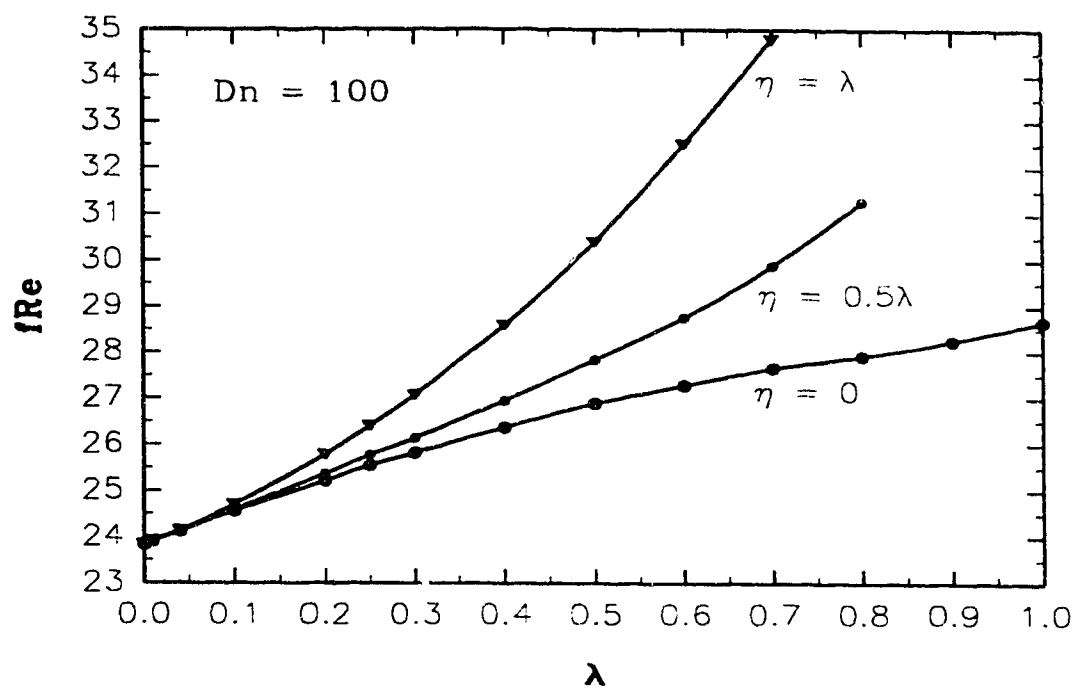
Fig. 4.25. Friction factor changes with λ for Dn = 100.
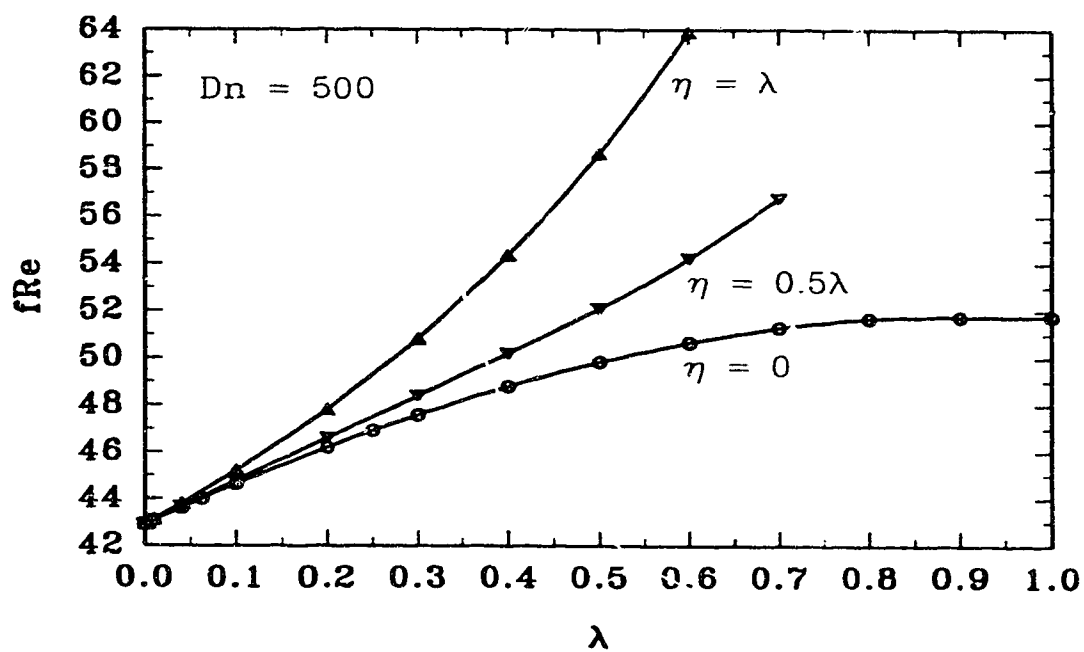
Fig. 4.26. Friction factor changes with λ for Dn = 500.
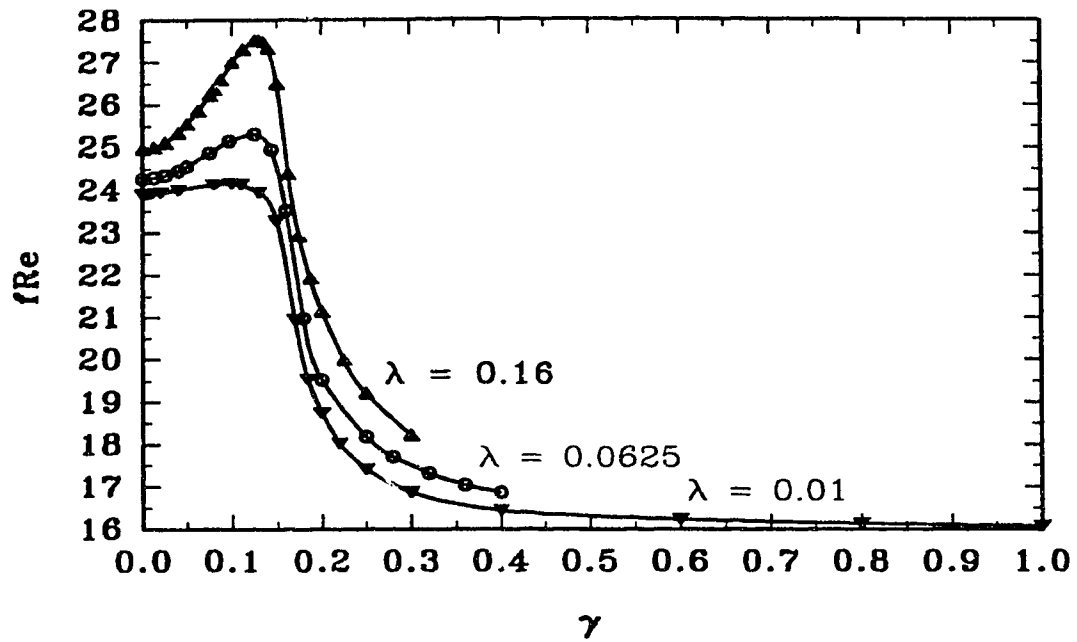
Fig. 4.27. Friction factor dependence on the torsion for Dn = 100.
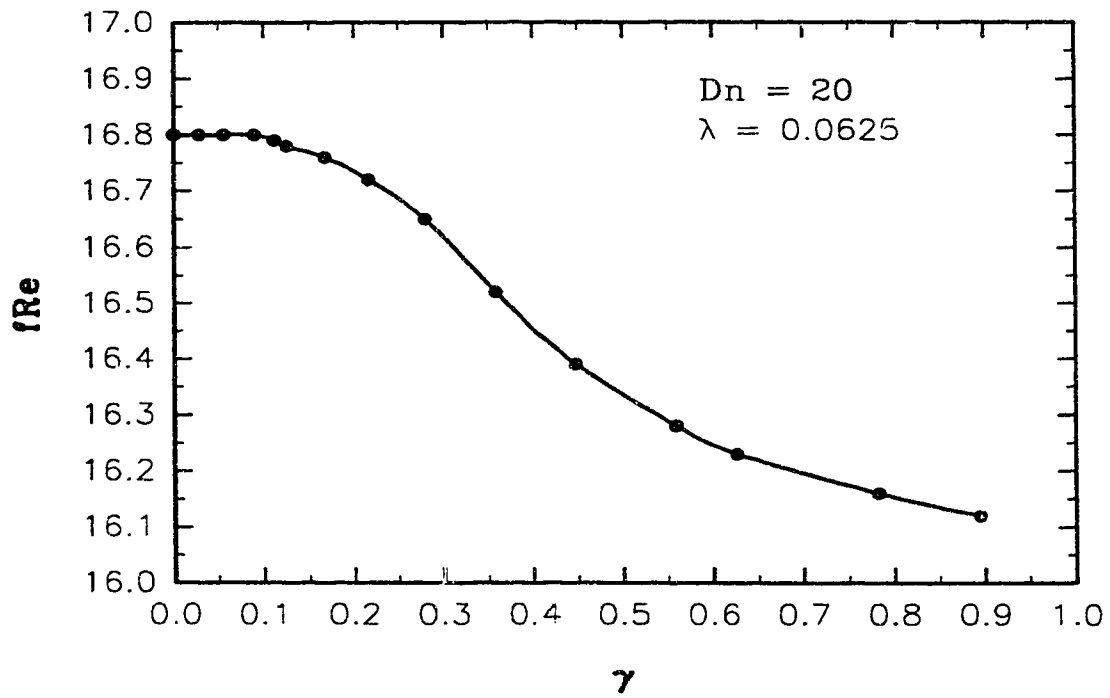
Fig. 4.28. Friction factor dependence on the torsion for Dn = 20.

Table 4.4. Friction factor correlations in the literature in the form of $Dn^{\frac{1}{2}}$.

Equation	Source
$\dfrac{f}{f_s} = 0.1064\, Dn^{\frac{1}{2}}$	Adler (1934)
$\dfrac{f}{f_s} = 0.509 + 0.0918\, Dn^{\frac{1}{2}}$	Barua (1963)
$\dfrac{f}{f_s} = 0.388 + 0.1015\, Dn^{\frac{1}{2}}$	Dennis (1980)
$\dfrac{f}{f_s} = 0.1033\, Dn^{\frac{1}{2}}\left[\sqrt{1 + \dfrac{1.729}{Dn}} - \sqrt{\dfrac{1.729}{Dn}}\,\right]^{-3}$	Ito (1969)
$\dfrac{f}{f_s} = 0.556 + 0.0969\, Dn^{\frac{1}{2}}$	Hasson (1955)
$\dfrac{f}{f_s} = 0.1033\, Dn^{\frac{1}{2}}/\left[1 - \dfrac{3.253}{\sqrt{Dn}}\right]$	Mori & Nakayama (1965)

4.8. Conclusions

Fully developed laminar flows of Newtonian fluids in helical pipes of constant circular cross—section with a finite pitch and finite radius of the coil are numerically studied. The curvature effect on the friction factor is of linear relation for small Dn flows and of $fRe \propto \lambda^{\frac{1}{2}}$ for large Dn flows. For $\lambda > 0.2$, the torsion effect on the helical flow consists of more distortion with increasing λ and/or Dn.

The friction factor increases with increasing torsion when γ is small, especially for large Dean number and large λ systems. When γ is large, the friction factor decreases sharply towards the value of the straight pipe Poiseuille flow as γ increases. The friction factor reaches maximum at $\gamma \simeq 0.1$ for moderate λ and Dn flows. But for small Dn and/or small λ, the increase of the friction factor with γ is not apparent, where the distortion effect of the torsion on the flow field is minimum.

The flow field rotates and distorts as γ increases for large λ and large Dn flows due to the significance of the terms $\lambda\eta$ and $\lambda^2\eta$ in the governing equations. The maximum axial velocity increases as the torsion increases with its location moving along a curve looking like a half heart starting from the outer—half y—axis and a projected end at the center of the pipe. The helical flow changes from a symmetrical two—vortex setting at $\gamma = 0$ to a one vortex setting at $\gamma > 0.2$, with the lower vortex shrinking away from the original inner half y—axis and dragging the upper vortex to expand as γ increases. This is a combination of the rotation and the distortion of the flow field. The size and the strength of the upper vortex increases as the torsion increases. The lower vortex finally disappears at $\gamma \simeq 0.2$ in the case of large Dn flows.

The secondary flow strength behaves in a similar fashion as that of the friction factor when γ increases. In the large γ limit, the secondary flow strength tends to a fixed value for a given Dean number.

The secondary flow structure undergoes a complicated change as viewed in the orthogonal coordinate system when γ is increased. The orthogonal secondary flow is of two upper—and—lower vortices at small γ. Increase in γ results in a reduction of the upper vortex. It is of almost one vortex when $\gamma \simeq 0.18$. Further increase in γ results a retract of lower vortex and rotation of the flow field. When γ is large, the orthogonal secondary flow tends to be of two left—and—right vortices.

For a given main flow strength, i.e., fixed Re, the helical flow changes from a toroidal flow at zero pitch to a Poiseuille—like flow as $H \rightarrow \infty$.

The stability of the flow downstream in the pipe is studied with the governing equations of the axially parabolized three—dimensional Navier—Stokes equations written in the orthogonal helical coordinates. Four—vortex solutions have been found from the numerical experimentation on the flow stability. When $\gamma < 0.01$ and Dn > 130, the four— vortex solution can be observed by disturbing the flow field at the outer half y—axis. The four—vortex solutions are not stable when a fine enough mesh is used.

A new correlation for the friction factor is built up by a series of non—linear regressions based on the numerical solutions of more than 250 cases. Accounted are all the controlling parameters Dn, λ and γ. The friction factors in the limit of negligible torsion and curvature are in good agreement with previous experimental and numerical observations of fRe $\sim$ Dn$^{\frac{1}{2}}$.

References

Adler M., "Strömung in gekrümmten Rohren", *Z. Angew Math. Mech.*, **14**, 257–275(1934).

Barua S.N., "On secondary flow in stationary curved pipes", *Q. J. Mech. Appl. Math.*, **16**, 61–77(1963).

Berger S.A., "Flow and heat transfer in curved pipes and tubes", AIAA 91–0030, 1991.

Cheng K.C. and Mok S.Y., "Flow visualization studies on secondary flow patterns and centrifugal instability phenomena in curved tubes", in: *Fluid Control Measurement*, Vol. 2, ed. M. Harada, p.756–773, Pergamom, Oxford, 1986.

Cheng K.C. and Yuen F.P., "Flow visualization studies on secondary flow patterns in straight tubes downstream of a 180 deg bend and in isothermally heated horizontal tubes", *J. Heat Transfer*, **109**, 49–54(1987).

Daskopoulos P. and Lenhoff A.M., "Flow in curved ducts: bifurcation structure for stationary ducts", *J. Fluid Mech.*, **203**, 125–148(1989).

Dennis S.C.R., "Calculation of the steady flow through a curved tube using a new finite difference method", *J. Fluid Mech.*, **99**, 449–467(1980).

Dennis S.C.R. and Ng M., "Dual solutions for steady laminar flow through a curved tube", *Q. J. Mech. Appl. Math.*, **XXXV**, part 3, 305–324(1982).

Germano M., "On the effect of the torsion in a helical pipe flow", *J. Fluid Mech.*, **125**, 1–8(1982).

Germano M., "The Dean equations extended to a helical pipe flow", *J. Fluid Mech.*, **203**, 289–305(1989).

Hasson D., "Streamline flow resistance in coils", *Res. Correspondence*, **1**, s1(1955).

Ito H., "Laminar flow in curved pipes", *Z. Angew Math. Mech.*, 11, 653–663(1969).

Jayanti S. and Hewitt G.F., "On the paradox concerning friction factor ratio in laminar flow in coils", *Proc. R. Soc. London*, A432, 291–299(1991).

Kao H.C., "Torsion effect on fully–developed flow in helical pipe", *J. Fluid Mech.*, 184, 335–356(1987).

Kubiček M. and Marek M., *Computational Methods in Bifurcation Theory and Dissipative Structures.*, Springer, 1983.

Lin C.C., *Theory of Hydrodynamic Stability*, Cambridge University Press, 1955

Liu S. and Masliyah J.H., "A decoupling numerical method for fluid flows", submitted to *Int. J. Num. Meth. Fluids.*

Liu S. and Masliyah J.H., "Axially–invariant laminar flow in helical pipes with a finite pitch, part 1. theory and loosely coiled pipes", submitted to *J. Fluid Mech.*

Mori Y. and Nakayama W., "Study on forced convective heat transfer in curved pipes", *Int. J. Heat Mass Transfer, Part I.*, 8, 67–82(1965).

Murata S., Miyake Y., Inaba T. and Ogata H., "Laminar flow in a helically coiled pipe", *Bull. JSME*, 24, 355–362(1981).

Nandakumar K. and Masliyah J.H., "Swirling flow and heat transfer in coiled and twisted pipes", in *Advances in Transport Processes*, vol. IV, ed. by Mujumdar A.S. and Mashelkar R.A., Wiley Eastern Ltd., New Delhi, 1986.

Nandakumar K. and Masliyah J.H., "Bifurcation in steady laminar flow through curved tubes", *J. Fluid Mech.*, 119, 475–490(1982).

Ramshankar R. and Sreenivasan K.R., "A paradox concerning the extended Stokes series solution for the pressure drop in coiled pipes", *Physics of Fluids*, 31(6), 1339–1347(1988).

Taylor G.I., "The criterion for turbulence in curved pipes", *Proc. R. Soc. London*, A124, 243–249(1928).

Truesdell L.C. and Adler R.J., "Numerical treatment of fully developed laminar flow in helically coiled tubes", *AIChE J.*, 16, 1010–1015(1970).

Tuttle E.R., "Laminar flow in twisted pipes", *J. Fluid Mech.*, 219, 545–570(1990).

Van Dyke M., "Extended Stokes series: laminar flow through a loosely coiled pipe", *J. Fluid Mech.*, 86, 129–145(1978).

Wang C.Y., "On the low–Reynolds–number flow in a helical pipe", *J. Fluid Mech.*, 108, 185–194(1981).

Yanase S., Goto N. and Yamamoto K., "Dual solutions of the flow through a curved tube", *Fluid Dynamics Research*, 5, 191–201(1989).

Yang Z. and Keller H.B., "Multiple laminar flows through curved pipes", *Appl. Num. Math.*, 2, 257–271(1986).

Chapter 5

Developing Laminar Flow and Heat Transfer in Helical Pipes

5.0. SUMMARY

Simultaneous development of laminar flow and heat transfer of Newtonian fluids in helical pipes of constant circular cross—section are numerically studied. The governing equations were fully parabolized and were written in the orthogonal helical coordinate system. The axial length scale and the parabolic behavior of the developing flow and heat transfer were analyzed through the loose coiling approximation.

The numerical simulations were made without invoking the loose coiling approximation. The results for shear rates, axial velocity and Nusselt number agree well with published data for developing flow in a torus. The axial pressure gradient and Nusselt number in the developing region are found to be oscillatory. The hydrodynamic developing lengths were correlated with the flow Dean number. The Nusselt number for fully—developed flows and the thermal entrance length were correlated with the fluid Prandtl number and the flow Dean number.

When the torsion effect is dominant, the friction factor and the Nusselt number for both thermally and hydrodynamically developed flows decrease with γ. $\gamma = \dfrac{\eta}{\sqrt{\lambda Dn}}$ is the the flow pattern transition parameter for high Dean number flows. When γ is large, the asymptotic friction factor and Nusselt number tend to the limits corresponding to a Poiseuille flow.

5.1. Introduction

Fluid flow and heat transfer in helically coiled pipes of constant circular cross—section are important in many industrial processes. In terms of the space conservation, helically coiled pipes can offer an improved heat transfer efficiency over straight pipes. The majority of studies in the literature deals with the fully developed laminar flows and heat transfer in a torus, where the pitch of the helical pipe is zero. These studies are summarized by Berger et al. (1983), Nandakumar & Masliyah (1986), Ito (1987) and Berger (1990).

The developing flow in toroidal pipes has been numerically treated by, among others, Patankar et al. (1974), Humphrey (1978), Soh & Berger (1984) and Humphrey et al. (1985). Their velocity profiles agree with the experimental results of Austin & Seader (1974) and Agrawal et al. (1978). These investigators used the original three—dimensional Navier—Stokes equations except Patankar et al. (1974) who employed parabolized three—dimensional governing equations. Although the full Navier—Stokes equations are more accurate in predicting developing flows (Humphrey 1978), they are rather difficult to handle when a long pipe is considered. When a stationary axially—invariant solution does not exist, as it is the case for some helical flows of large Dn, see Bara (1991) and Bara et al. (1992), the computation with the full Navier—Stokes equations would be invalid since the flow is "developing" forever without reaching anywhere near any axially stationary flow. On the other hand, it has been shown that the parabolized equations fit the physical problems quite well (Patankar et al. 1974, Sankar et al. 1988 and Bara 1991). However, further studies are needed to remove the doubts concerning the accuracy of the results obtained from parabolized equations.

The hydrodynamic developing length for a torus was correlated by Austin & Seader (1974) for the case of a Poiseuille flow entry. This problem was studied

analytically by Yao & Berger (1975 & 1988) with a boundary layer formulation for a uniform axial velocity entry. They found that the developing length for a curved channel is shorter than that of a straight pipe. Some boundary layer analysis gave a vanishing axial wall shear at a certain location of the torus (Stewartson et al. 1980, Yao & Berger 1988, etc.). However, the vanishing axial wall shear is not a result of numerical studies using full or parabolized equations, nor is it an experimental fact. The maximum axial wall shear rate was found to cross over from the inner bend to the outer bend both analytically by Singh (1974) and experimentally by Choi et al. (1979) and Kluwick & Wohlfahrt (1986). The flow evolvement into a four—vortex flow in a torus having a square cross section was studied by Bara (1991) and Bara et al. (1992). They found that the developing length decreases with increasing flow rate for a four—vortex flow.

Simultaneous developing flow and heat transfer with a heat source in a torus was treated by Patankar et al. (1974). The developing heat transfer from a fully—developed flow in a torus was studied by Tarbell & Samuels (1973) for the uniform wall temperature condition. Akiyama & Cheng (1974 a & b) studied developing laminar forced convection for both boundary conditions. They confirmed, in principle, the experimental findings of the non—monotonic variation in the Nusselt number with the axial distance observed by Dravid et al. (1971), Balejova et al. (1977) and Janssen & Hoogendoorn (1978). Janssen & Hoogendoorn (1978) correlated the thermal entrance length and they found it to be, in general, shorter than that of a straight pipe.

The axially—invariant or fully developed flows in helical pipes of finite pitch was studied in Chapters 3 and 4 (see also Liu & Masliyah 1992 b & c). By employing a loose coiling analysis, there arrived at two controlling parameters, namely, the Dean number Dn and the Germano number Gn. The Dean number is a measure of the ratio of the square root of the product of inertial forces and

centrifugal forces to viscous forces, that is, $Dn = Re \sqrt{\lambda}$. Re is the flow Reynolds number and λ is the normalized curvature ratio: $\lambda = Rc\ a\ /\ [Rc^2 + (\frac{H}{2\pi})^2]$, where Rc is the coil radius, a is the pipe radius and H is the pitch of the coil. The Germano number $Gn = Re\ \eta$ is a measure of the twisting forces over the viscous forces, where η is the normalized torsion, $\eta = (\frac{H}{2\pi})\ a\ /\ [Rc^2 + (\frac{H}{2\pi})^2]$.

The Germano number Gn is always embedded in the body—centered azimuthal velocity, $\xi = u_3 - \frac{Gn}{h_1}ru_1$, as long as $\lambda \to 0$. u_1 and u_3 are the normalized orthogonal axial velocity ($u_1 = u'/2U$) and peripheral velocity ($u_3 = Re\ w'/2U$). U is the average axial velocity. $h_1 = 1 + \lambda \sin\theta$ is the axial coordinate metrics. By taking momentum norm of ξ and using the argument that at high Dn flows the axial pressure gradient for a torus is proportional to the square root of Dn (see Chapter 3) a new flow transition group $\gamma = Gn\ /\ Dn^{3/2} = \eta/\sqrt{\lambda Dn}$ was obtained, where

$$\|M\xi\| = \|Mu_3 - M(\frac{Gn}{h_1}r\ u_1)\| = A_1 Dn^2 - A_2' \ Gn\ G = A_1 Dn^2(1 - A_2\ Gn\ Dn^{-3/2}).$$

Here M is the momentum operator, A's are constants and G is the normalized axial pressure gradient. When $\gamma > 0.2$, the flow is one—vortex type (or swirl—like). When $\gamma < 0.2$, the flow is two—vortex type. When $\gamma \leq 0.01$, the helical flow problem may be approximated by a toroidal flow (Dean) problem, Liu & Masliyah (1992b).

Although the flow structure is independent of reference frame, the flow pattern can be very different when viewing in different coordinate system as that presented in Chapter 4 or by Liu & Masliyah (1992c). When viewing in the orthogonal coordinate system, the secondary flow is of one vortex type at $\gamma \simeq 0.18$. At small γ, the orthogonal secondary flow is of two up—and—down vortices with upper one smaller when γ is not zero. At large γ limit, the secondary flow is of two left—and—right vortices.

In Chapter 4 (see also Liu & Masliyah 1992c), we showed that by making use of a needle—like disturbance for $\gamma \leq 0.01$ the flow develops into a four—vortex type flow and back to the two—vortex flow. It was suggested that only two—vortex type

solution for $\gamma < 0.2$ is present for a circular cross section.

There are no literature data available on the developing flow and/or heat transfer in helical pipes of a finite pitch. Even the simultaneous developing flow and heat transfer with a uniform constant temperature was not numerically treated for the case of a torus.

In this study, the Separation Method (Chapter 2, or Liu & Masliyah 1992a) is used to solve the simultaneous developing laminar flow and forced convective heat transfer problem in helical pipes of a finite pitch. The coordinate system used is of that first introduced by Germano (1982).

5.2. Governing Equations

The coordinate setup of the helical system is shown in Figure
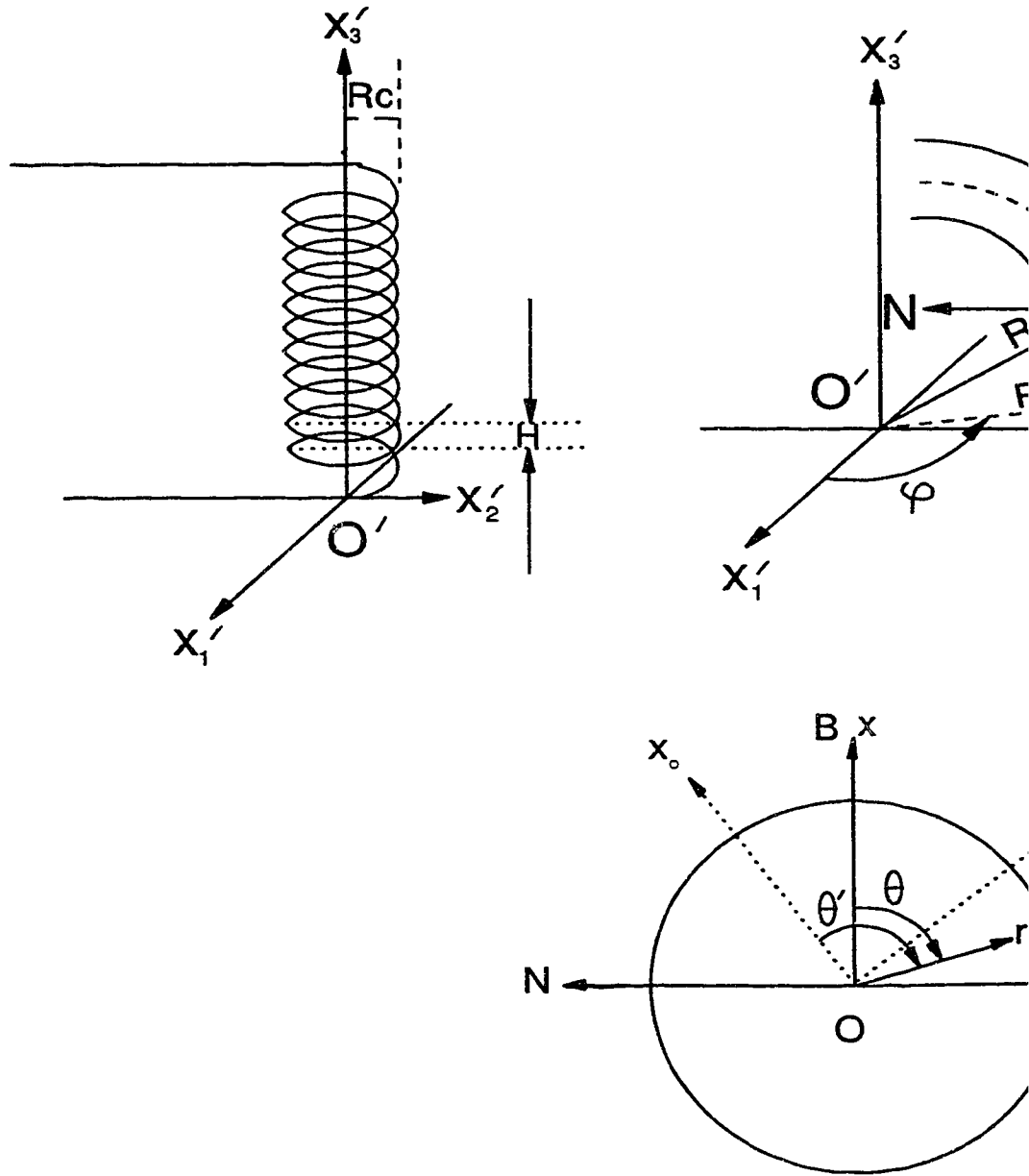
Fig. 5.1 The helical system set up.

The metrics for the transformation are given by

$$g_{ij} = \frac{\partial x'_k}{\partial q_i} \cdot \frac{\partial x'_k}{\partial q_j} \tag{5-7}$$

where $q_1 = s$, $q_2 = r$, $q_3 = \theta'$ and $\theta' = \theta + f(s)$. The basic equations of the curve theory

$$\frac{d\vec{N}}{ds} = \tau\vec{B} - \kappa\vec{T} \tag{5-8}$$

and

$$\frac{d\vec{B}}{ds} = -\tau\vec{N} \tag{5-9}$$

can be applied to derive the metrics of the orthogonal helical system. Where the curvature ratio is defined by:

$$\kappa = \frac{Rc}{Rc^2 + (H/2\pi)^2} \tag{5-10}$$

and the torsion is:

$$\tau = \frac{H/2\pi}{Rc^2 + (H/2\pi)^2} \tag{5-11}$$

By forcing $g_{ij} = 0$, for $i \neq j$, $i,j = 1, 2, 3$, with a suitable choice on the function of $f(s)$, the helical coordinate system (s, r, θ') is set to be orthogonal. The metrics for the coordinate system can be obtained as:

$$\begin{cases} h_1 = g_{11}^{1/2} = 1 + \kappa r \sin\theta \\ h_2 = g_{22}^{1/2} = 1 \\ h_3 = g_{33}^{1/2} = r \end{cases}$$ (5-12)

where $\theta' = \theta + \tau s$, (s, r, θ') and its corresponding rectangular coordinates (s, x_0, y_0) are orthogonal.

The governing equations are first derived in the orthogonal system (s, r, θ') and transformed to the non—orthogonal system (s, r, θ) leaving the velocity components untouched. The transformation is necessary to eliminate the s—dependent coefficients and variable ($\theta' - \tau s$ always appears in place of θ). This would allow an axially—invariant solution to be realizable if exists. It should be noted that the above equations used dimensional quantities. To work with the coordinate system, the variables are non—dimensionalized in the following manner:

$$s = \frac{s'}{a}, \quad r = \frac{r'}{a}, \quad t = \frac{\nu t'}{a^2}, \quad u = \frac{u'}{2U}, \quad v = \frac{v'}{2U}, \quad w = \frac{w'}{2U}, \quad p = \frac{Re P'}{4\rho U^2}$$

and $\lambda = \kappa a$, $\eta = \tau a$, $Re = \frac{2aU}{\nu}$, $Pr = \frac{\mu C_p}{k}$, $T = \frac{T'-T'_w}{T'_i-T'_w}$

Where a is the radius of the pipe, U is the average axial velocity, t is time, ν is the kinematic viscosity, u is the axial velocity component (orthogonal s—directional component), v is the radial velocity component (r—direction), w is the angular velocity component (orthogonal θ'—directional component), λ is the curvature, η is the torsion, Re is the Reynolds number, Pr is the Prandtl number, Cp is the heat capacity, k is the thermal conductivity, p is the pressure and T is the temperature. The subscript w and i denote the pipe wall and the inlet average bulk, respectively. The primed variables are the dimensional quantities. For

simplicity, we will use the non—dimensional variables hereafter.

The final governing flow equations after all necessary substitution and rearrangement are shown as follows:

The continuity,

$$\frac{1}{h_1}\left(\frac{\partial u}{\partial s} - \eta\frac{\partial u}{\partial\theta}\right) + \frac{1}{rh_1}\cdot\frac{\partial(rh_1 v)}{\partial r} + \frac{1}{rh_1}\cdot\frac{\partial(h_1 w)}{\partial\theta} = 0 \tag{5—13}$$

where h_1 is the metric coefficient in the axial direction (s—direction).

$$h_1 = 1 + \lambda\, r\, \sin\theta \tag{5—14}$$

The momentum and energy equations are cast in the following form:

$$(M + d_\phi)\phi = S_\phi \tag{5—15a}$$

where the momentum or energy operator M is defined by,

$$M\phi = \frac{\partial\phi}{\partial t} + \frac{2\eta}{h_1^2}\frac{\partial^2\phi}{\partial s\partial\theta} + \frac{1}{h_1}\frac{\partial}{\partial s}\left[(Re\, u - \lambda\,\eta\, r\, \frac{\cos\theta}{h_1^2})\phi - \frac{1}{h_1}\frac{\partial\phi}{\partial s}\right] +$$

$$\frac{1}{rh_1}\cdot\frac{\partial}{\partial r}[rh_1(Re\, v\, \phi - \frac{\partial\phi}{\partial r})] +$$

$$\frac{1}{rh_1}\frac{\partial}{\partial\theta}[Re(h_1 w - \eta\, r\, u)\phi - \frac{h_1}{r}(1 + \frac{\eta^2 r^2}{h_1^2})\frac{\partial\phi}{\partial\theta}] \tag{5—15b}$$

ϕ stands for any velocity component or the temperature. When $\phi = T$, the Reynolds number Re in equation (5—15b) is replaced by Pr Re. The individual momentum and energy equations are obtained by a specification of the velocity component ϕ, extra diagonal term d_ϕ and the source term S_ϕ.

s—momentum: $\phi = u$

$$d_\phi = \frac{v\sin\theta + w\cos\theta}{h_1}\lambda\,Re + \frac{\lambda^2}{h_1^2} \tag{5-16a}$$

$$S_\phi = -\frac{1}{h_1}(\frac{\partial p}{\partial s} - \eta\frac{\partial p}{\partial\theta}) + \frac{1}{h_1^2}[2\lambda\sin\theta(\frac{\partial v}{\partial s} - \eta\frac{\partial v}{\partial\theta}) + 2\lambda\cos\theta(\frac{\partial w}{\partial s} - \eta\frac{\partial w}{\partial\theta}) +$$

$$\frac{\lambda\eta\cos\theta}{h_1}v - \frac{\lambda r + \sin\theta}{h_1}\lambda\eta w] \tag{5-16b}$$

r—momentum: $\phi = v$

$$d_\phi = \frac{1 + 2h_1\lambda r\sin\theta}{r^2 h_1^2} \tag{5-17a}$$

$$S_\phi = -\frac{\partial p}{\partial r} + Re(\frac{\lambda\sin\theta}{h_1}u^2 + \frac{w^2}{r}) - \frac{2\lambda\sin\theta}{h_1^2}(\frac{\partial u}{\partial s} - \eta\frac{\partial u}{\partial\theta}) + \frac{\lambda\eta\cos\theta}{h_1^3}u -$$

$$\frac{2}{r^2}\frac{\partial w}{\partial\theta} - \frac{2h_1-1}{rh_1^2}\lambda\cos\theta w \tag{5-17b}$$

θ—momentum: $\phi = w$

$$d_\phi = Re\frac{v}{r} + \frac{1}{h_1^2}(\lambda^2 + \frac{2h_1-1}{r}) \tag{5-18a}$$

$$S_\phi = -\frac{\partial p}{\partial\theta} + Re\frac{\lambda\cos\theta}{h_1}u^2 - \frac{2\lambda\cos\theta}{h_1^2}(\frac{\partial u}{\partial s} - \eta\frac{\partial u}{\partial\theta}) - \frac{\lambda r + \sin\theta}{h_1^2}\lambda\eta u +$$

$$\frac{3h_1-1}{r^2 h_1^2}\frac{\partial v}{\partial\theta} + \frac{1}{rh_1^2}\lambda\cos\theta v \tag{5-18b}$$

With the assumption that the viscous dissipation is negligible and the fluid is incompressible with constant physical properties, the energy equation can be written as:

$$\phi = T, \quad d_\phi = 0, \quad S_\phi = 0 \tag{5-19}$$

where Re is replaced by Pr Re in equation (5—15b)

The boundary is defined by the pipe wall. Although a numerical scheme with a polar coordinate system would prefer to have a condition set at the center of the

pipe, there are no conditions that can fit such a need. We can only say that the properties are continuous at the center. Hence, the center point of the pipe is still in the interior of the computational domain and should not be treated differently. The boundary and necessary conditions are:

$$u = v = w = T = 0 \qquad \text{at } r = 1 \text{ for all } s \text{ and } \theta;$$

$p = 0$ at one reference point inside the computational domain and

$$\frac{\int_0^{2\pi} d\theta \int_0^1 r \ u \ dr}{\pi} = \frac{1}{2} \qquad \text{(from the non--dimensionalization)} \qquad (5\text{--}20)$$

The inlet conditions will be given with the numerical results.

When the flow reaches the fully--developed (i.e., axially--invariant) stage, the transverse velocity field can be represented by a field scalar quantity, ψ, as follows:

$$h_1 v = -\frac{\partial \psi}{\partial \theta} \qquad (5\text{--}21a)$$

$$h_1 w - \eta r u = \frac{\partial \psi}{\partial r} \qquad (5\text{--}21b)$$

To the same extent as ordinary two--dimensional flows, the field scalar quantity ψ can be called the pseudo--secondary flow stream function.

To compute the pseudo--secondary flow stream function, we take equation (5--21b) after the velocity field is obtained. To approximate the secondary flow pattern of the developing flow, we take equation (5--21b) as well when $\frac{\partial u}{\partial s}$ is small. It is obvious that if u, v and w satisfy the following pseudo--continuity equation

$$\frac{1}{r h_1} \frac{\partial (r h_1 v)}{\partial r} + \frac{1}{h_1} \frac{\partial}{\partial \theta} (h_1 w - \eta \ r \ u) = 0 \qquad (5\text{--}22)$$

which is the continuity equation (5--13) with $\frac{\partial u}{\partial s}$ dropped, then the field scalar quantity ψ can be defined as it appears in equations (5--21a) and (5--21b) even if

the secondary velocities are not axially—invariant. Hence, it is justified to use ψ when $\frac{\partial u}{\partial s}$ is small. However, this secondary flow pattern is not to be used when the error in the pseudo—continuity equation (5—22) is greater than, say, 5%. An indicative error ESN is measured by the error in the pseudo—continuity equation.

$$ESN = \frac{\displaystyle\sum_{i,j} \frac{4 \ |FRI_{ij} + FCI_{ij} - FRO_{ij} - FCO_{ij}|}{|FRI_{ij}| + |FRO_{ij}| + |FCI_{ij}| + |FCO_{ij}|}}{\displaystyle\sum_{i,j} 1} \qquad (5\text{—}23)$$

where FRI_{ij}, FRO_{ij}, FCI_{ij} and FCO_{ij} are the flow into and out of the conservational domain of P_{ij} in the radial direction, flow in and out of the conservational domain in the θ (non—orthogonal azimuthal) direction, respectively.

If ESN is small, the transverse velocity field can be approximated by the field scalar quantity ψ. If ESN is large, ψ should not be used.

Since the pseudo—secondary flow stream function can only be used to show the secondary flow pattern, the true secondary flow strength may be defined by the norm of the orthogonal secondary flow velocity as

$$\|v\|_{r\theta} = \int_0^1 r \ dr \int_0^{2\pi} (1 + \lambda \ r \ \sin\theta) \ (v^2 + w^2)^{\frac{1}{2}} \ d\theta \qquad (5\text{—}24)$$

The normalized axial length is used to present the flow development. The normalized axial length s^+ is defined as follows:

$$s^+ = \frac{s}{2 \ Re} = \frac{s'}{2 \ a \ Re} \qquad (5\text{—}25)$$

The heat transfer coefficient is estimated by the Nusselt number, Nu, and is defined as follows:

$$Nu = \frac{2a\bar{h}}{k} = \frac{-1}{\pi T_{av}} \int_0^{2\pi} (1 + \lambda \sin\theta) \left(\frac{\partial T}{\partial r}\right)_{r=1} d\theta \qquad (5\text{--}26)$$

where $\bar{h}$ is the peripherally averaged heat transfer coefficient and T_{av} is the axial flow average temperature across a given pipe section. T_{av} is defined as:

$$T_{av} = \frac{2}{\pi} \int_0^1 dr \int_0^{2\pi} r \, u \, T \, d\theta \qquad (5\text{--}27)$$

To show the peripheral distribution of the heat transfer coefficient, a local Nusselt number is defined as follows:

$$Nu(\theta) = \frac{2ah}{k} = -\frac{2}{T_{av}} \left(\frac{\partial T}{\partial r}\right)_{r=1} \qquad (5\text{--}28)$$

where h is the local heat transfer coefficient. It is obvious that

$$\begin{cases} Nu = \frac{1}{2\pi} \int_0^{2\pi} (1 + \lambda \sin\theta) \, Nu(\theta) \, d\theta \\[3mm] \bar{h} = \frac{1}{2\pi} \int_0^{2\pi} (1 + \lambda \sin\theta) \, h \, d\theta \end{cases} \qquad (5\text{--}29)$$

By including the axial metric in the cross sectional averaging, the overall heat transfer rate can be related to the average heat transfer coefficients.

For the convenience of reference, the temperature distribution across a given pipe section is normalized by its average value T_{av}, i.e.

$$T^c = \frac{T}{T_{av}} \qquad (5\text{--}30)$$

When no confusions arises, the superscript c may be dropped hereafter.

5.3. Loose Coiling and Parabolization in Axial Direction

There are four dimensionless parameters involved in the helical flow and heat transfer, namely, λ, η, Re and Pr. It is known that the flow problem can be simplified by applying the loose coiling approximation. In this analysis, we do not intend to make the loose coiling assumption, but we will use it to derive some important properties concerning the computation. Loose coiling refers to the following double limit:

$$\lambda \to 0, \quad \text{while} \quad \text{Re} \to +\infty \quad \text{and} \quad \lambda \neq 0$$

Since the helical pipe reduces to a straight pipe when $\lambda = 0$, the above conditions hold when $\lambda \neq 0$. This can be maintained by having either a large but finite radius of coil Rc or a large pitch H. Under this condition, it has been found that only the Dean number Dn and the Germano number Gn or the γ number are important to the flow field since the terms involving λ and η can be dropped (see Chapter 3, or Liu & Masliyah 1992b). To show this property, let's introduce the following rescaled velocity field, pressure and axial distance:

$$u_1 = u, \quad u_2 = \lambda^{-\frac{1}{2}}v, \quad u_3 = \lambda^{-\frac{1}{2}}w, \quad z = \lambda^{3/4}\text{Re}^{\frac{1}{2}}s, \quad P = \lambda^{\frac{1}{2}}p \qquad (5\text{--}31)$$

The Dean number Dn is defined as

$$\text{Dn} = \text{Re}\,\sqrt{\lambda} = \text{Re}\left[\frac{a\ \text{Rc}}{\text{Rc}^2 + (\frac{H}{2\,\pi})^2}\right]^{1/2} \qquad (5\text{--}32)$$

and the Germano number Gn is

$$\text{Gn} = \text{Re}\,\eta = \text{Re}\,\frac{a\ (\frac{H}{2\,\pi})}{\text{Rc}^2 + (\frac{H}{2\,\pi})^2} \qquad (5\text{--}33)$$

The flow transition parameter γ is defined by

$$\gamma = \frac{\eta}{\sqrt{\lambda Dn}} \qquad (5\text{--}34)$$

By introducing the new variables into the governing equations, we obtain:

The continuity equation,

$$\frac{\sqrt{Dn}}{h_1}(\frac{\partial u_1}{\partial z} - \gamma \frac{\partial u_1}{\partial \theta}) + \frac{1}{rh_1} \cdot \frac{\partial(rh_1 u_2)}{\partial r} + \frac{1}{rh_1} \cdot \frac{\partial(h_1 u_3)}{\partial \theta} = 0 \qquad (5\text{--}35)$$

The momentum/energy operator,

$$M\phi = \frac{\partial \phi}{\partial t} + \frac{2\gamma}{h_1^2}\lambda Dn\frac{\partial^2 \phi}{\partial z \partial \theta} + \frac{Dn}{h_1}\frac{\partial}{\partial z}[(\sqrt{Dn}\, u_1 - \lambda^2\, \gamma\, r\, \frac{\cos\theta}{h_1^2})\phi - \frac{\lambda}{h_1}\frac{\partial \phi}{\partial z}] +$$

$$\frac{1}{rh_1} \cdot \frac{\partial}{\partial r}[rh_1(Dn\, u_2\, \phi - \frac{\partial \phi}{\partial r})] +$$

$$\frac{1}{rh_1}\frac{\partial}{\partial \theta}[Dn(h_1\, u_3 - \gamma\sqrt{Dn}\, r\, u_1)\phi - \frac{h_1}{r}(1 + \frac{\eta^2 r^2}{h_1^2})\frac{\partial \phi}{\partial \theta}] \qquad (5\text{--}36)$$

s—momentum: $\phi = u_1$

$$d_\phi = \frac{u_2 \sin\theta + u_3 \cos\theta}{h_1}\, \lambda\, Dn + \frac{\lambda^2}{h_1^2} \qquad (5\text{--}37a)$$

$$S_\phi = -\frac{\sqrt{Dn}}{h_1}(\frac{\partial P}{\partial z} - \gamma \frac{\partial P}{\partial \theta}) + \frac{\lambda^2}{h_1^2}\sqrt{Dn}\, [2\sin\theta(\frac{\partial u_2}{\partial z} - \gamma \frac{\partial u_2}{\partial \theta}) +$$

$$2\cos\theta(\frac{\partial u_3}{\partial z} - \gamma \frac{\partial u_3}{\partial \theta}) + (\frac{\cos\theta}{h_1}u_2 - \frac{\lambda r + \sin\theta}{h_1}u_3)\gamma] \qquad (5\text{--}37b)$$

r—momentum: $\phi = u_2$

$$d_\phi = \frac{1 + 2h_1\lambda r\sin\theta}{r^2 h_1^2} \qquad (5\text{--}38a)$$

$$S_\phi = -\lambda^{-1} \frac{\partial P}{\partial r} + Dn(\frac{\sin\theta}{h_1}u_1^2 + \frac{u_3^2}{r}) - \frac{2\lambda\sqrt{Dn}\sin\theta}{h_1^2}(\frac{\partial u_1}{\partial z} - \gamma \frac{\partial u_1}{\partial \theta}) +$$

$$\frac{\lambda\gamma\cos\theta}{h_1^3}\sqrt{Dn}\, u_1 - \frac{2}{r^2}\frac{\partial u_3}{\partial \theta} - \frac{2h_1-1}{rh_1^2}\lambda\cos\theta u_3 \qquad (5\text{--}38b)$$

θ–momentum: $\phi = u_3$

$$d_\phi = Dn\frac{u_2}{r} + \frac{1}{h_1^2}(\lambda^2 + \frac{2h_1-1}{r})$$ (5–39a)

$$S_\phi = -\lambda^{-1}\frac{\partial P}{\partial\theta} + Dn\frac{\cos\theta}{h_1}u_1^2 - \frac{2\lambda\sqrt{Dn}}{h_1^2}\cos\theta(\frac{\partial u_1}{\partial z} - \gamma\frac{\partial u_1}{\partial\theta}) -$$

$$\frac{\lambda r + \sin\theta}{h_1^2}\lambda\gamma\sqrt{Dn}\,u_1 + \frac{3h_1-1}{r^2h_1^2}\frac{\partial u_2}{\partial\theta} + \frac{1}{rh_1^2}\lambda\cos\theta u_2$$ (5–39b)

The energy equation is still in the form of equation (5–19), but u_1, u_2 and u_3 in the energy/momentum operator **M** should be replaced by $Pr\,u_1$, $Pr\,u_2$ and $Pr\,u_3$, respectively.

Note that (5–38b) and (5–39b) are of the following form

$$\lambda^{-1}\frac{\partial P}{\partial r} \le O(\lambda^0) \qquad \lambda^{-1}\frac{\partial P}{\partial\theta} \le O(\lambda^0)$$ (5–40)

Hence, when $\lambda \to 0$,

$$P = P_0(z,\eta) + \lambda\,P_1(r,\theta,z,\eta) + \dots$$ (5–41)

i.e., at least when λ is small, the major contribution to the axial pressure gradient can be separated from the cross–sectional component. This ensures that such a treatment may be used for the parabolization of the governing equations. The axial pressure gradient is directly related to the flow friction factor as:

$$fRe = \frac{4\int_0^1 r\,dr\int_0^{2\pi}(-\frac{\partial p}{\partial s})\,d\theta}{\pi} = -4\frac{dp_m}{ds} = -4\,\lambda^{-1/2}\frac{dP_0}{ds}$$ (5–42)

where f is the Fanning friction factor and p_m is the average pressure across the pipe.

The above equation is used to evaluate fRe at any given axial location. The axial pressure gradient is taken as constant for a given axial location in the parabolized equations.

From equation (5–36), we can see that when λ is small, the axial diffusion term can be dropped from the momentum equation. If the loose coiling approximation is to be applied, the governing equations become parabolic in the axial direction. In other words, the parabolization approximation which neglects the axial diffusion terms and separate the axial pressure gradient from the cross–sectional components is good at least for the case of small curvature ratio λ.

In the limits of $\lambda \to 0$ and $\eta \to 0$, equations (5–19) and (5–35) to (5–41) show that the heat transfer and flow problem are governed by three parameters, Pr, Dn and γ, only. Hence, we have retrieved the loose coiling approximation for the case of the developing flow/heat transfer problem.

For the case of $\lambda \to 0$ and $\eta \to 0$, the loose coiling conditions justify the parabolization of the governing equations. Since a useful range of curvature ratio λ in many practical applications may be that of $0.01 < \lambda < 0.2$, it follows that the parabolization of the governing equations can be deemed to be reliable. When Reynolds number is large, the parabolic approximation becomes more suitable in predicting the developing flow behavior (Patankar et al. 1974, Sankar et al. 1988, Bara 1991 and Bara et al. 1992).

By noting the normalization in the above order of magnitude analysis, equation (5–31), the axial length z can be related to s^+ in the following way:

$$z = \lambda^{3/4}\text{Re}^{1/2}s = 2\,\text{Dn}^{3/2}s^+ \tag{5–43}$$

Hence, s^+ defined by equation (5–24) is a good choice in representing the axial length scale for the developing flow and heat transfer.

5.4. Results and Discussions

Calculations were made for Dean numbers lying in the range of $21.86 \leq Dn \leq 5000$ for the values of $0.1 \leq Pr \leq 500$, $0.01 \leq \lambda \leq 0.25$ and $\gamma \leq 0.25$ for the case of simultaneous developing flow and heat transfer with a constant wall temperature. The grid used in most cases for $Dn < 2000$ is n40×50fu, i.e., 40 non—uniform mesh points in the radial direction and 50 uniform mesh points in the full azimuthal direction. For $Dn = 2000$ and $Dn = 5000$, the corresponding meshes are n60x50fu and n100x60fu. The inlet conditions applied to investigate the flow and heat transfer behavior are:

Uniform axial velocity entry:

$$\begin{cases} u|_{s=0} = 0.5 \\ v|_{s=0} = w|_{s=0} = 0, \quad (\frac{\partial p}{\partial r})|_{s=0} = (\frac{\partial p}{\partial \theta})|_{s=0} = 0 \end{cases} \tag{5--44}$$

and **Parabolic axial velocity entry**:

$$\begin{cases} u|_{s=0} = 1 - r^2 \\ v|_{s=0} = w|_{s=0} = 0, \quad (\frac{\partial p}{\partial r})|_{s=0} = (\frac{\partial p}{\partial \theta})|_{s=0} = 0 \end{cases} \tag{5--45}$$

The uniform axial velocity entry defined by equation (5—44) is valid for a flow entering a helical pipe from a large reservoir. The parabolic axial velocity entry defined by equation (5—44) may correspond to a flow having past through a long straight pipe prior to entering the helical pipe.

The inlet condition of the temperature is that of a uniform temperature field, i.e., $T|_{s=0} = 1$.

Before we present the results of the simultaneous developing flow and heat

a. Dn=20, λ=0.0625, γ=0.1677

b. Dn=20, λ=0.0625, γ=0.21

c. Dn=50, λ=0.0625, γ=0.18

d. Dn=50, λ=0.0625, γ=0.25

e. Dn=100, λ=0.16, γ=0.175

f. Dn=100, λ=0.16, γ=0.225
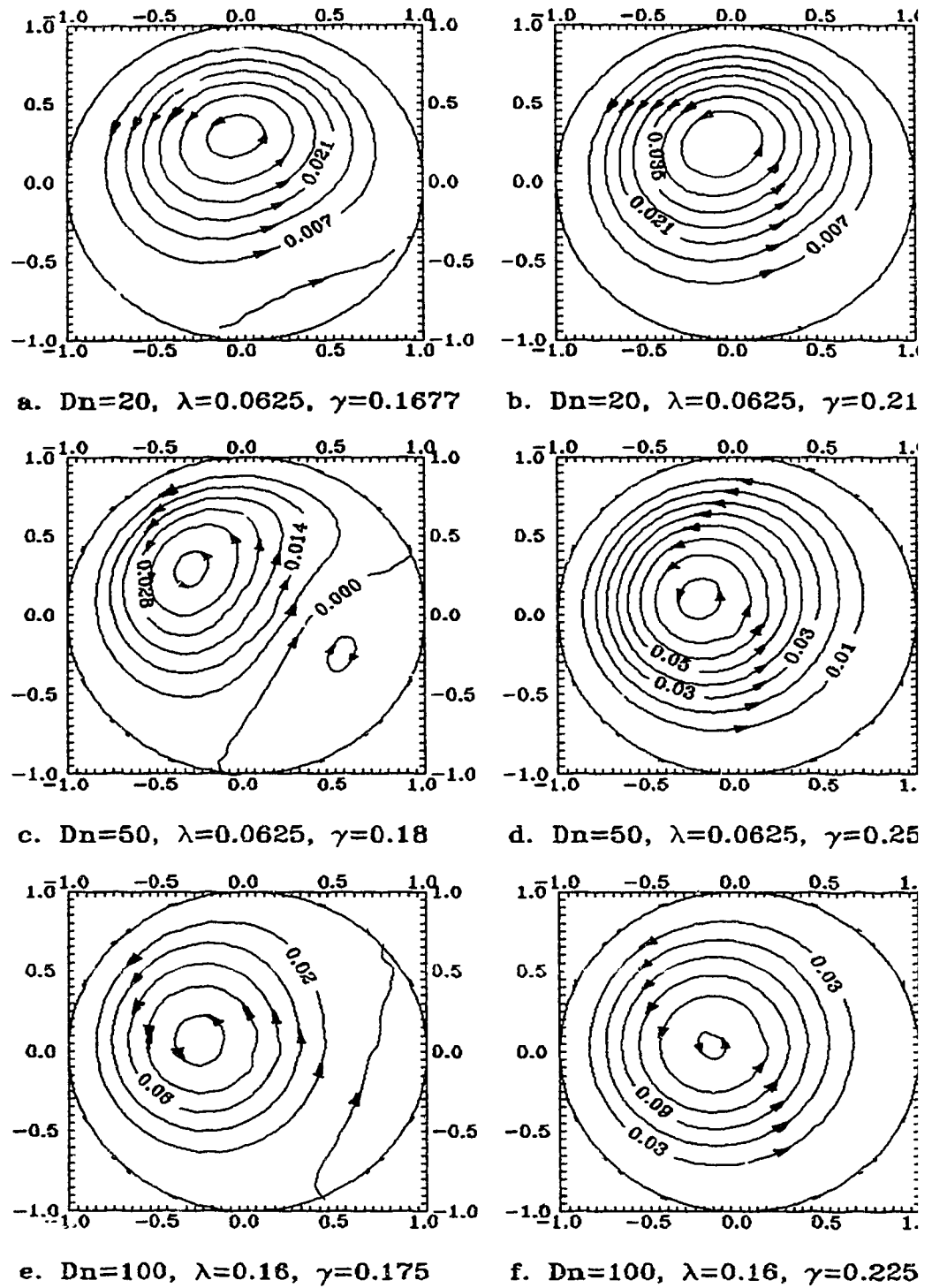
Fig. 5.2a.   Secondary flow vortex transition for various Dn and λ.

transfer, it is necessary to introduce the characterization of the fully—developed laminar helical flows. In Chapters 3 and 4 (see also Liu & Masliyah 1992 b & c), a critical value of $\gamma \simeq 0.2$ was found, where the secondary flow patterns change from two— to one— vortex. Figures 5.2a and 5.2b show that the flow pattern transition occurs at $\gamma \simeq 0.2$ for $20 \leq Dn \leq 100$ and $0.0025 \leq \lambda \leq 0.16$. We observe that the secondary flows have a two—vortex pattern when $\gamma < 0.2$ and a one vortex pattern when $\gamma > 0.2$. The two vortices are positioned left and right near the vortex transition zone. The right (or near outer wall) vortex is small both in size and in strength.

In this study, we shall discuss the developing flow and heat transfer corresponding to both the one— and two— vortex flows.

5.4.1. Secondary flow development

The secondary flow strength developments for various Dn and γ are shown in Figures 5.3a and 5.3b. Figure 5.3a shows the secondary flow strength developments for a typical two—vortex flow of $Dn = 200$, $\lambda = 0.01$ and $\gamma = 0.01$ with both uniform and parabolic axial velocity entries. For a uniform axial velocity entry, the secondary flow strength increases rapidly to a large value shortly after entering the helical pipe and decreases non—monotonically with increasing the axial distance s^+. For a parabolic axial velocity entry, the secondary flow strength increases gradually and reaches the fully—developed value in a non—monotonic fashion.

Figure 5.3b shows the secondary flow strength developments for a typical one—vortex flow of $Dn = 200$, $\lambda = 0.01$ and $\gamma = 0.25$ with both uniform and parabolic axial velocity entries. Similar behaviors to the two—vortex flows are observed except that the oscillation in the case of uniform axial velocity entry is much reduced.

It is traditional to present velocity vector plots for the secondary flow to
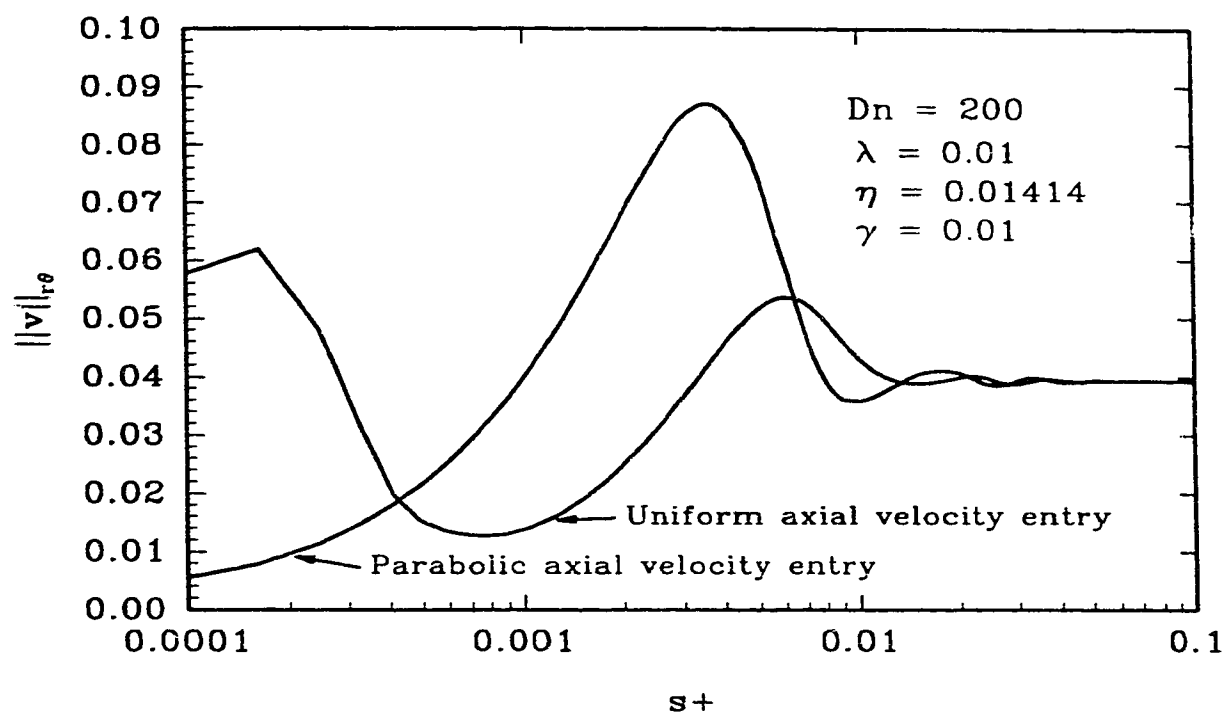
Fig. 5.3a. Orthogonal secondary flow strength developments for Dn = 200, $\lambda = 0.01$ and $\gamma = 0.01$.
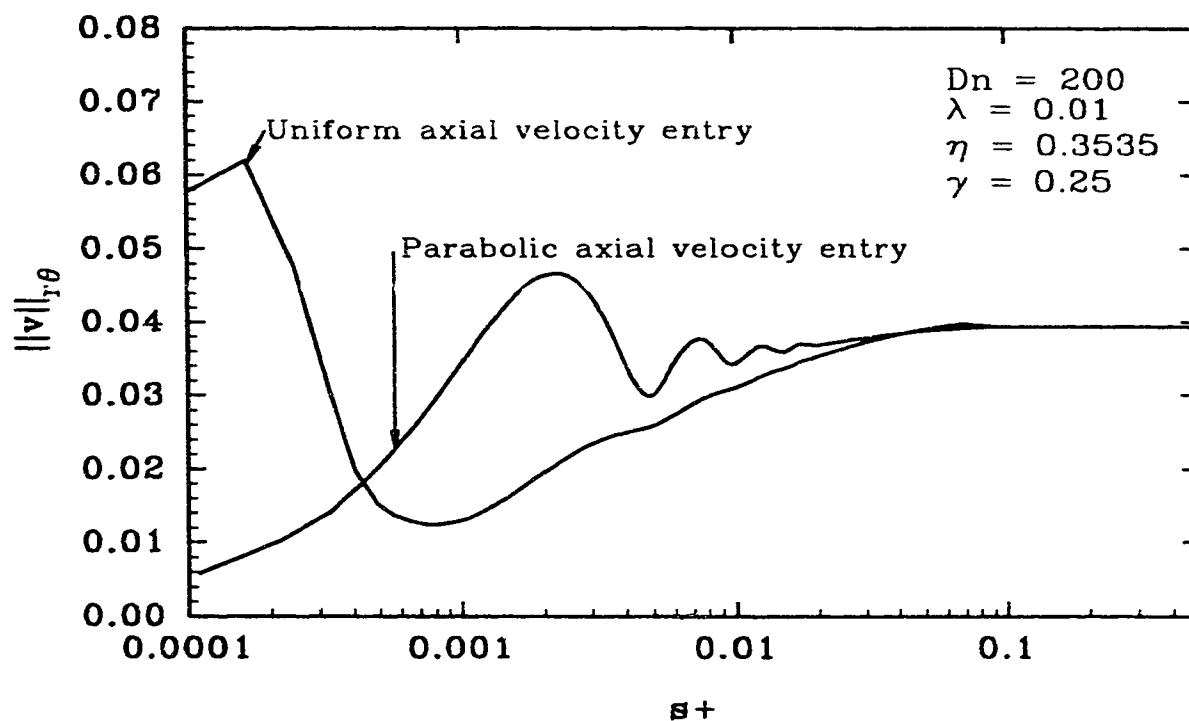
Fig. 5.3b. Orthogonal secondary flow strength developments for Dn = 200, $\lambda = 0.01$ and $\gamma = 0.25$.

a. s* =0.002, ESN=0.047

b. s* =0.006, ESN=0.019

c. s* =0.01, ESN=0.015

d. s* =0.015, ESN=0.0049

e. s* =0.02, ESN=0.0026

f. s* =0.1, ESN=0.00002
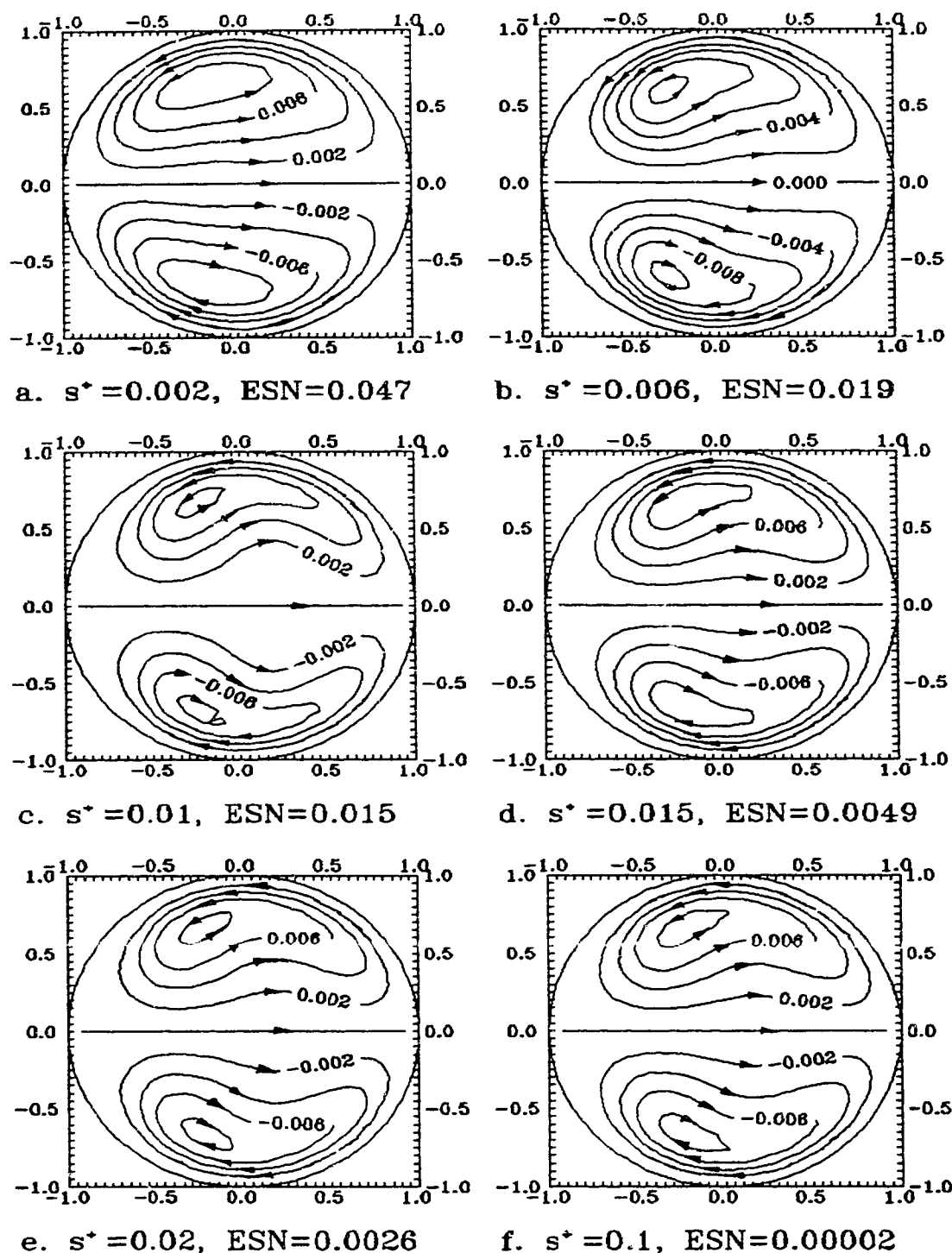
Fig. 5.4a.   Secondary flow pattern development corresponding to a two—vortex flow. $Dn = 312.3$, $\lambda = 0.02439$, $\eta = 0$, $\gamma = 0$. Uniform axial velocity entry.

a. s* =0.000433, ESN=0.058   b. s* =0.00195, ESN=0.010

c. s* =0.00596, ESN=0.0034   d. s* =0.02166, ESN=0.0005

e. s* =0.0395, ESN=0.00016   f. s* =0.4001, ESN=0.0000038
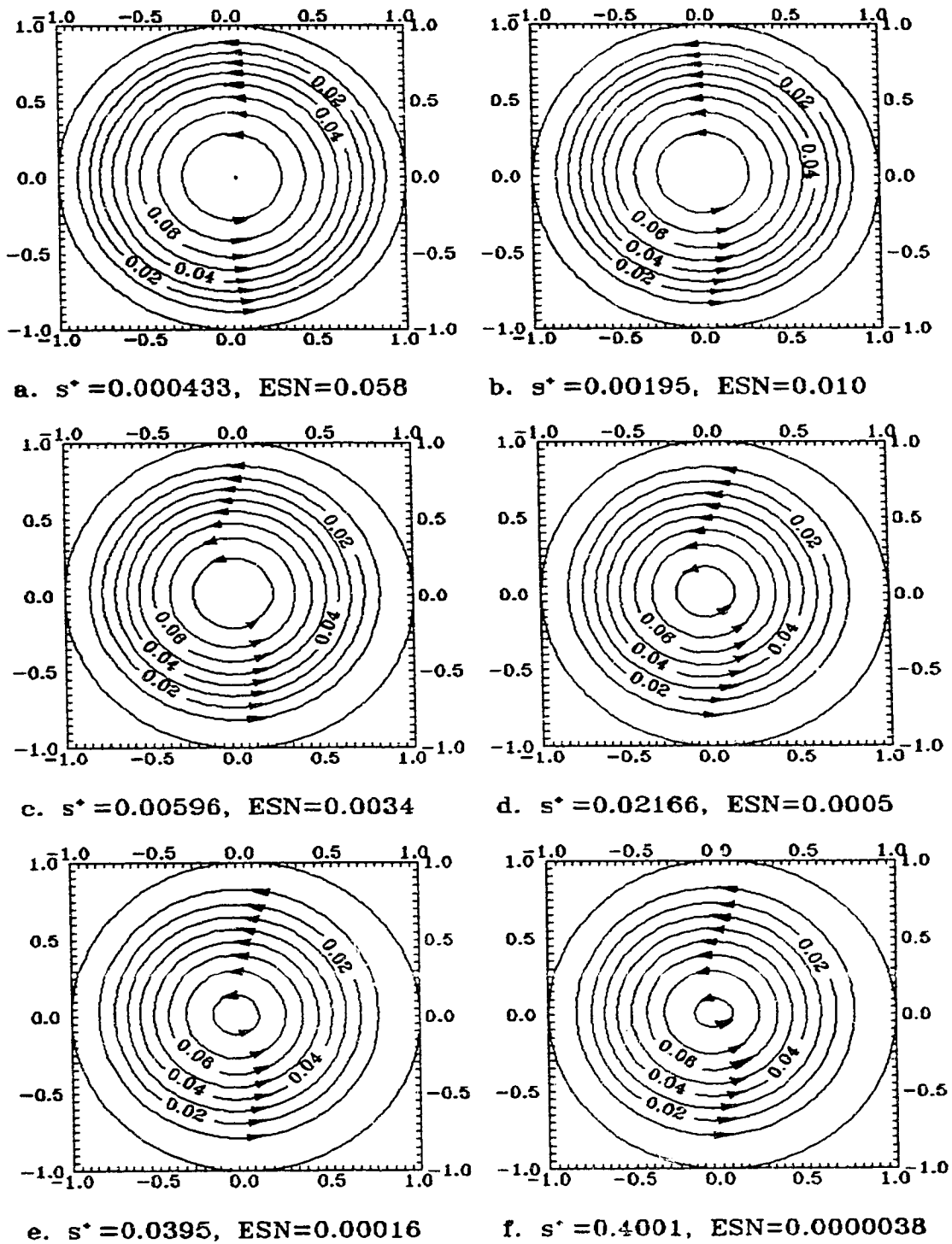
Fig. 5.4b.   Secondary flow pattern development corresponding to a one–vortex flow. Dn = 200, λ = 0.01, γ = 0.25. Uniform axial velocity entry.
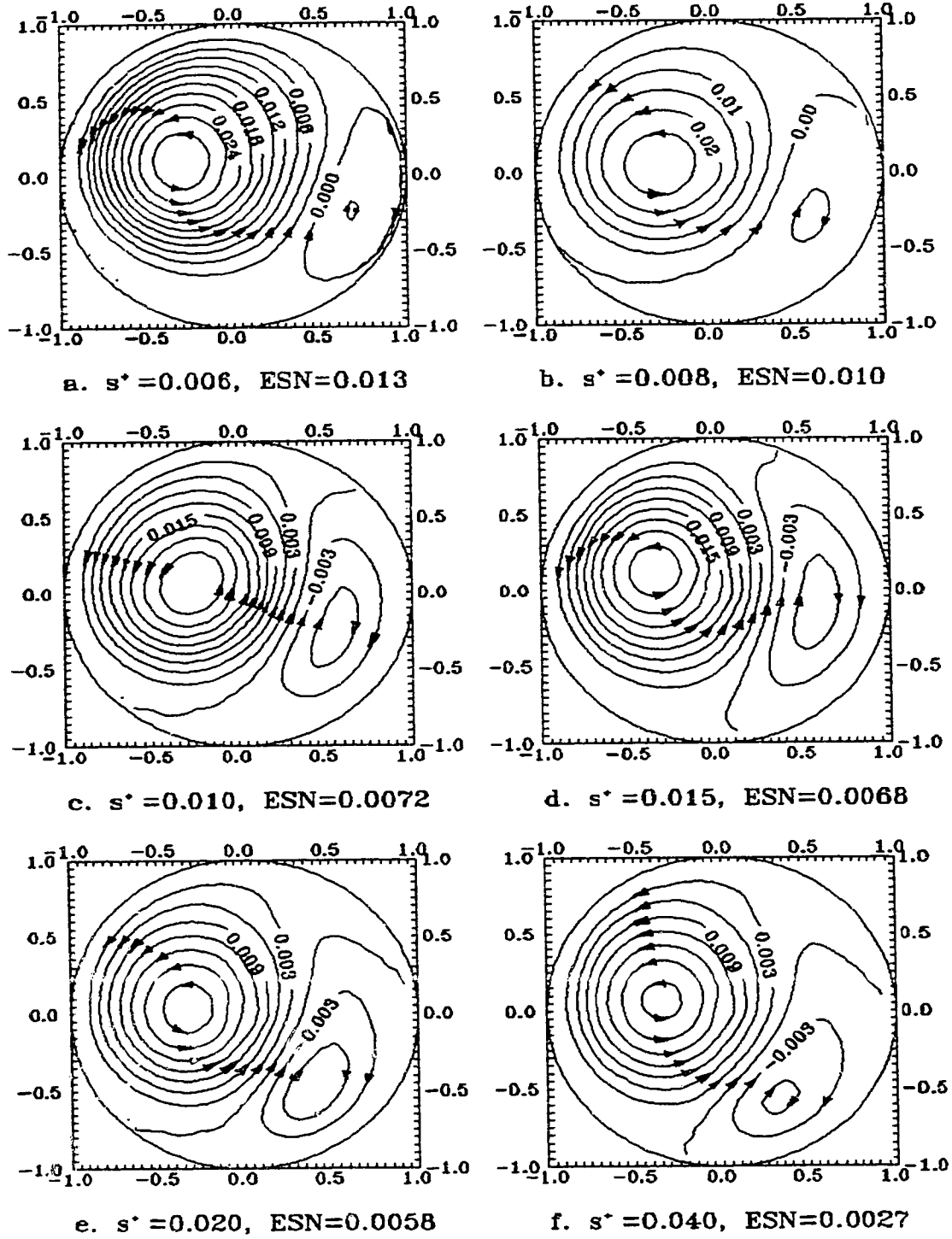
a. s* =0.006, ESN=0.013

b. s* =0.008, ESN=0.010

c. s* =0.010, ESN=0.0072

d. s* =0.015, ESN=0.0068

e. s* =0.020, ESN=0.0058

f. s* =0.040, ESN=0.0027

Fig. 5.5.   Secondary flow pattern evolvement for Dn = 200, $\lambda = 0.01$, $\gamma = 0.12$. Parabolic axial velocity entry.

simulate the same effects, we decided to use the field scalar quantity ψ defined by equation (5–21) when ESN is less than 5%. This was also used in our earlier study (Chapter 4) to show the formation and disappearance of the four–vortex flows, see also Liu & Masliyah (1992c).

Figures 5.4a and 5.4b show the secondary flow developments for typical two– and one– vortex flows. To give a sense of the accuracy of such plots, the error in the pseudo–continuity equation ESN is also shown with the axial distance s^+. We observe that the secondary flow develops very quickly near the wall region. The secondary flow development is controlled by the central region where the centrifugal force is more important than the viscous force.

In Chapter 4, we found that the secondary flow patterns are distinct in the range of Dn > 100 and $0.1 < \gamma < 0.2$. The secondary flow consists of two skewed vortices. Figure 5.5 shows the secondary flow pattern evolvement for Dn = 200, $\gamma = 0.12$ from a Poiseuille flow. It can be seen that for small s^+, the secondary flow pattern is given by a large vortex and a much smaller vortex. The small vortex gains strength and size as the flow develops. We also observe that the secondary vortex rotates slightly in the course of the flow development. We say that the flow field such as that shown in Figure 5.5 consists of distortion since the iso–pseudo– secondary flow stream lines are twisted as compared to those in Figure 5.4a.

To show the orthogonal secondary flow structure, the velocity vector plots have to be introduced (see Chapter 4, or Murata et al. 1981, Kao 1987, Germano 1989 and Liu & Masliyah 1992c). Figures 5.6a and 5.6b show the orthogonal secondary flow developments for the typical (non–orthogonal) two– and one–

a). $s^+ = 4.1 \times 10^{-4}$

b). $s^+ = 9.7 \times 10^{-4}$

c). $s^+ = 2.03 \times 10^{-3}$

d). $s^+ = 9.98 \times 10^{-3}$

e). $s^+ = 0.01996$

f). $s^+ = 0.04$
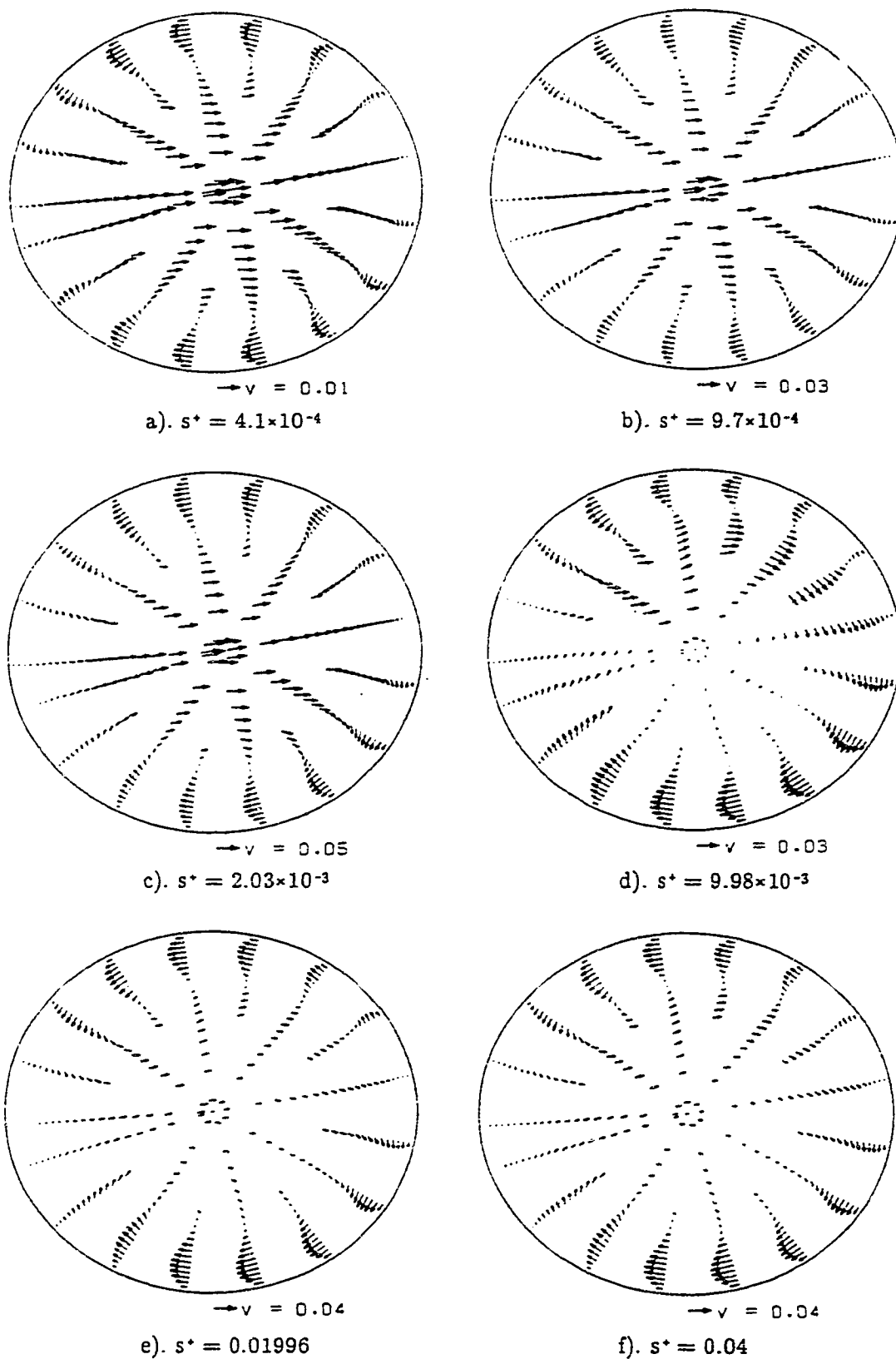
Fig. 5.6a.   Orthogonal secondary velocity vector evolvement for Dn = 200, $\lambda = 0.01$, $\gamma = 0.01$. Parabolic axial velocity entry.

→ v = 0.03

a). s* = 1.6×10⁻⁴

→ v = 0.01

b). s* = 4.1×10⁻⁴

→ v = 0.01

c). s* = 9.7×10⁻⁴

→ v = 0.01

d). s* = 2.03×10⁻³

→ v = 0.02

e). s* = 0.00999

→ v = 0.02

f). s* = 0.07999
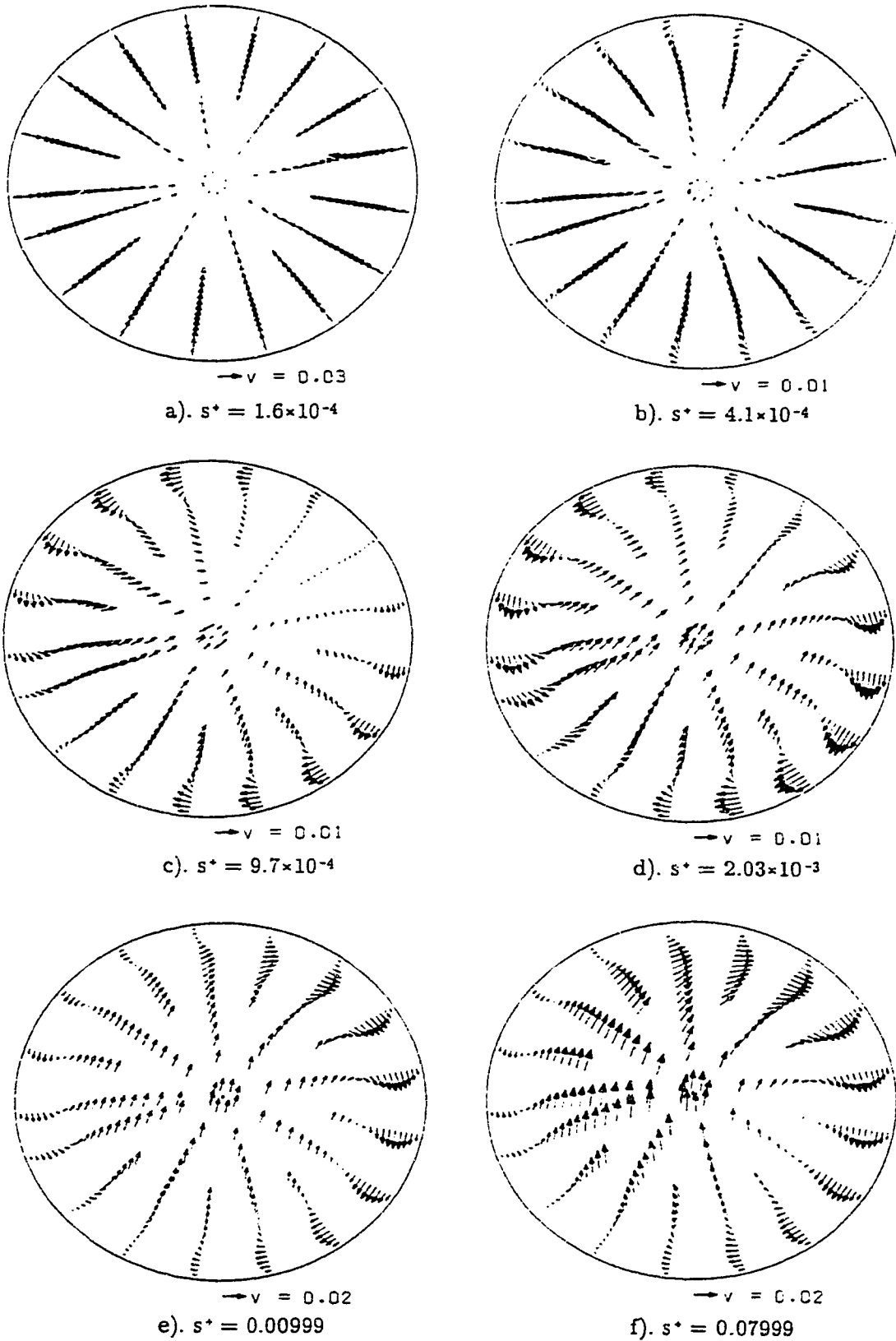
Fig. 5.6b.   Orthogonal secondary velocity vector evolvement for Dn = 200,
λ = 0.01, γ = 0.25. Uniform axial velocity entry.

vortex flows. Figure 5.6a shows the orthogonal secondary flow structure development for $Dn = 200$, $\lambda = 0.01$ and $\gamma = \hat{\ }$ 01 with a parabolic axial velocity entry. We observe that the vortices develop very quickly after entry. Two up—and—down vortices appeared at the early axial distance of $s^+ = 4.1 \times 10^{-4}$. The strength (noting the scale of vectors at the bottom of each plots) grows and there is no orientation change until $s^+ < 0.00998$. When $s^+ = 0.00998$, the strength of the secondary flow is reduced and the lower vortex grows larger in size than the upper vortex. When $s^+ > 0.00998$, the secondary flow strength gains back. The flow reaches fully—developed at $s^+ = 0.04$ and the two vortices are of non—equal size. Figure 5.6b shows the orthogonal secondary flow development for $Dn = 200$, $\lambda = 0.01$ and $\gamma = 0.25$ with uniform axial velocity entry (the same as the flow in Figure 5.4b). Near the entry, the flow is to get axial velocity distributed. The secondary flow velocity vectors are pointing towards the center as shown clearly in Figure 5.6b.a) where $s^+ = 1.6 \times 10^{-4}$. At $s^+ = 4.1 \times 10^{-4}$, vortices start to develop near the inner upper wall and near the outer lower wall. The two vortices grow as the axial distance increases. At $s^+ = 2.03 \times 10^{-3}$, the two inner up and outer down vortices become distinct. When the flow becomes fully—developed, i.e., $s^+ > 0.01$, the inner up vortex is reduced in size and strength. Sources and sinks still exist in the velocity vector plots when the flow is fully—developed because the axial velocity has a transverse component (a rotational component) embedded in it.

The vortices shown in Figure 5.6a.f) are not symmetrical suggesting that the torsion has a noticeable effect. However, our early studies (Chapter 3 and 4) show that the torsion is negligible when $\gamma \leq 0.01$. Hence, as Dn increases, we may expect some more torsion effect.

The vortices in Figure 5.6b.f) agree with those found in Chapter 4. When $\gamma > 0.18$, the orthogonal secondary flow is of two left—and—right vortices with the left one being smaller and upper.

5.4.2. Axial flow development

Figure 5.7 shows the axial velocity development across the pipe at x and y axes. As a comparison, the laser doppler experimental data of Agrawal et al. (1978) is also shown. Figure 5.7 shows a very good agreement between our predictions and Agrawal et al.'s laser anemometer measurements for the case of $\lambda = \frac{1}{7}$ and the relatively small Dn of 183. Such an agreement gives support to the present parabolization procedure.

Figures 5.8 and 5.9 show the center line and maximum axial velocity development for both small and large γ flows. It can be seen that the center line axial velocity is oscillatory as the flow develops. The maximum axial velocity, on the other hand, remains relatively smooth and monotonic. For very large Dn, Dn = 2000 and Dn = 5000 as shown in Figure 5.10, the axial velocity developments do not differ from the lower Dn flows. The developing flow is oscillatory. The magnitude in oscillation remains relatively constant with changing Dn.

Figures 5.11 to 5.14 show the development of the axial velocity field for various γ's correspond to both two— and one— vortex flows. For two—vortex flows, the maximum axial velocity first appears near the top wall and moves towards the outer wall as the flow develops. For a uniform axial velocity entry, the center region of the axial velocity remains flat in the early stage of flow development. The flow distortion (or the twist of axial velocity isoplethes) is more evident in the early stage of the flow development for large γ. The flow distortion is reduced as the flow is fully developed. The flow distortion is present at the first few stations in Figure 5.11 (Dn = 200, $\lambda = 0.01$ and $\gamma = 0.02$). When the flow is fully—developed, Figure 5.11f shows negligible distortion. The distortion in the flow field is present in the fully developed flow of Dn = 200 and $\gamma = 0.12$, see Figure 5.14. The flow field distortion in the fully—developed flow is consistent with our early studies detailed in Chapter 3 & 4 (see also Liu & Masliyah 1992 b & c).
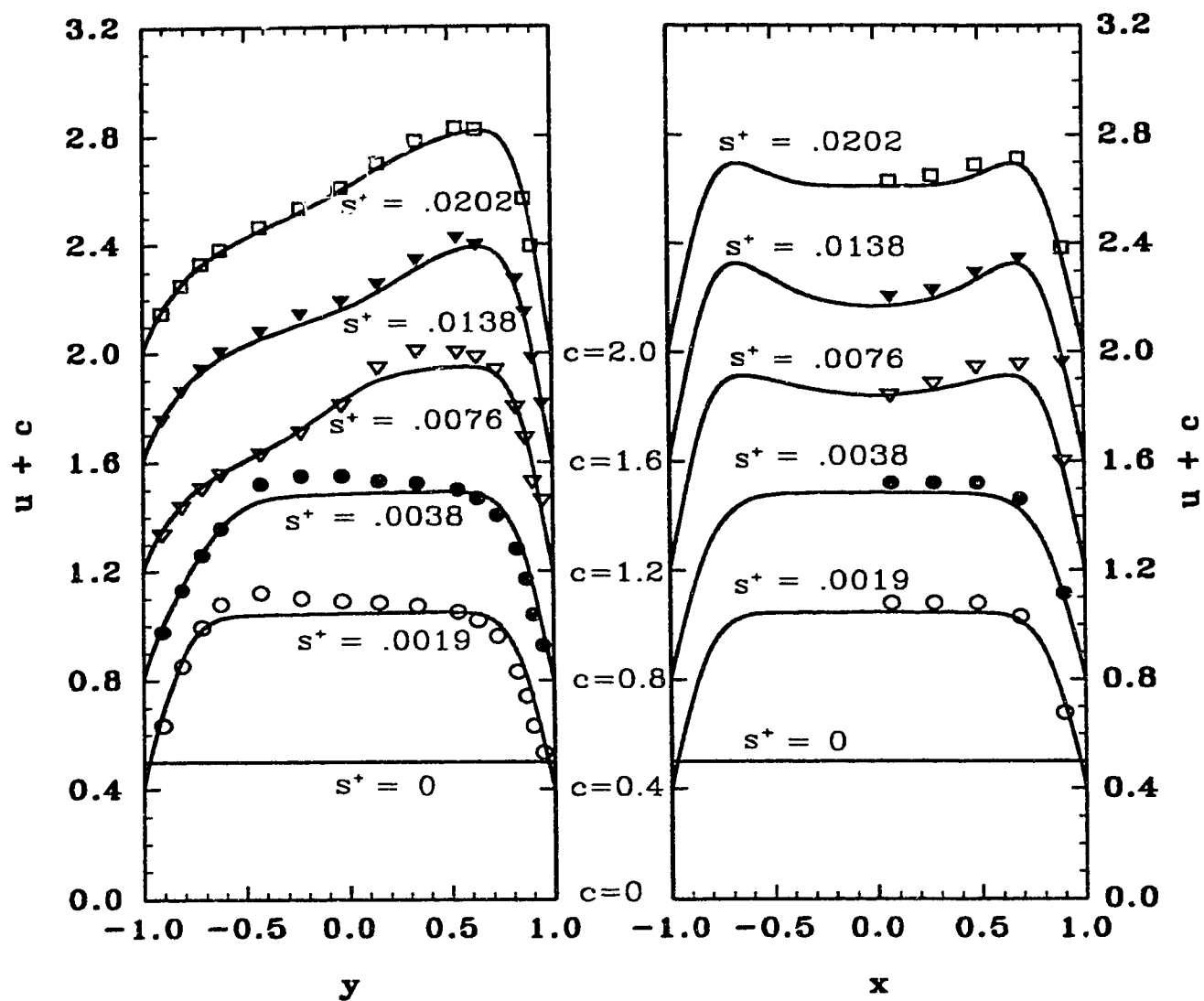
Fig. 5.7.   Axial velocity development for Dn = 183, λ = 1/7 at x = 0 (left) and y = 0 (right) with a uniform axial velocity entry. The solid lines are the present predictions for various axial locations. The symbols are the experimental data of Agrawal et al. (1978). For ease of plotting, each velocity profile is shifted by a value of c as shown in the central part of the figure.
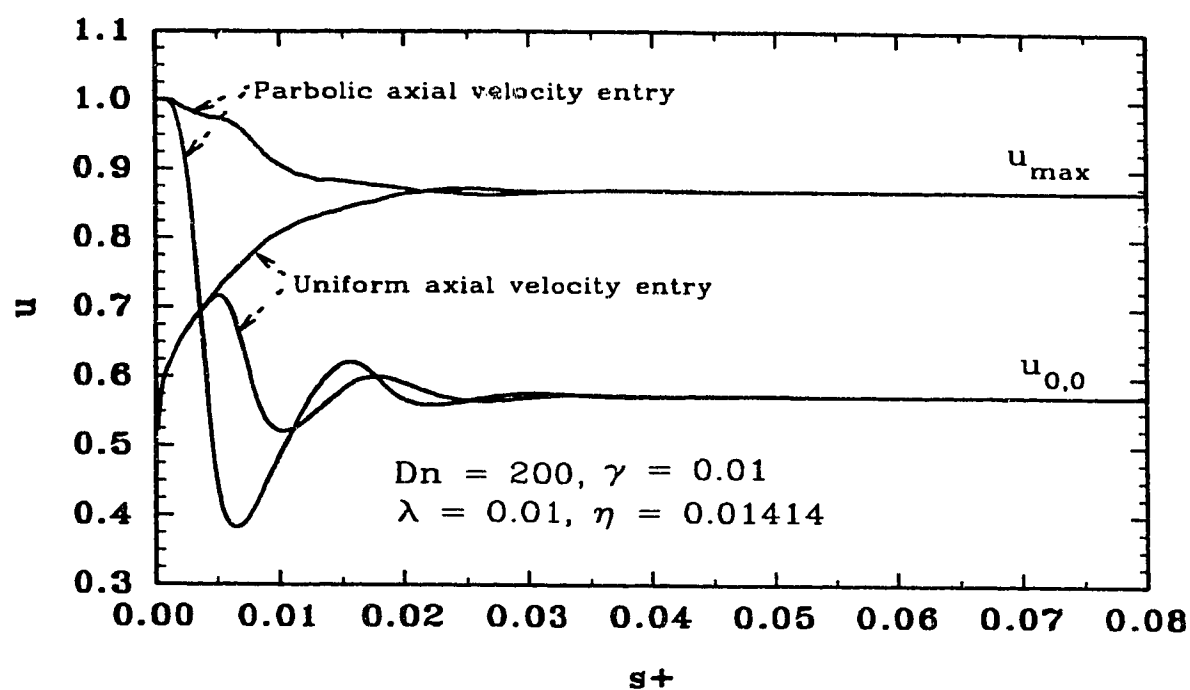
Fig. 5.8.   Center and maximum axial velocity development for small γ flows.
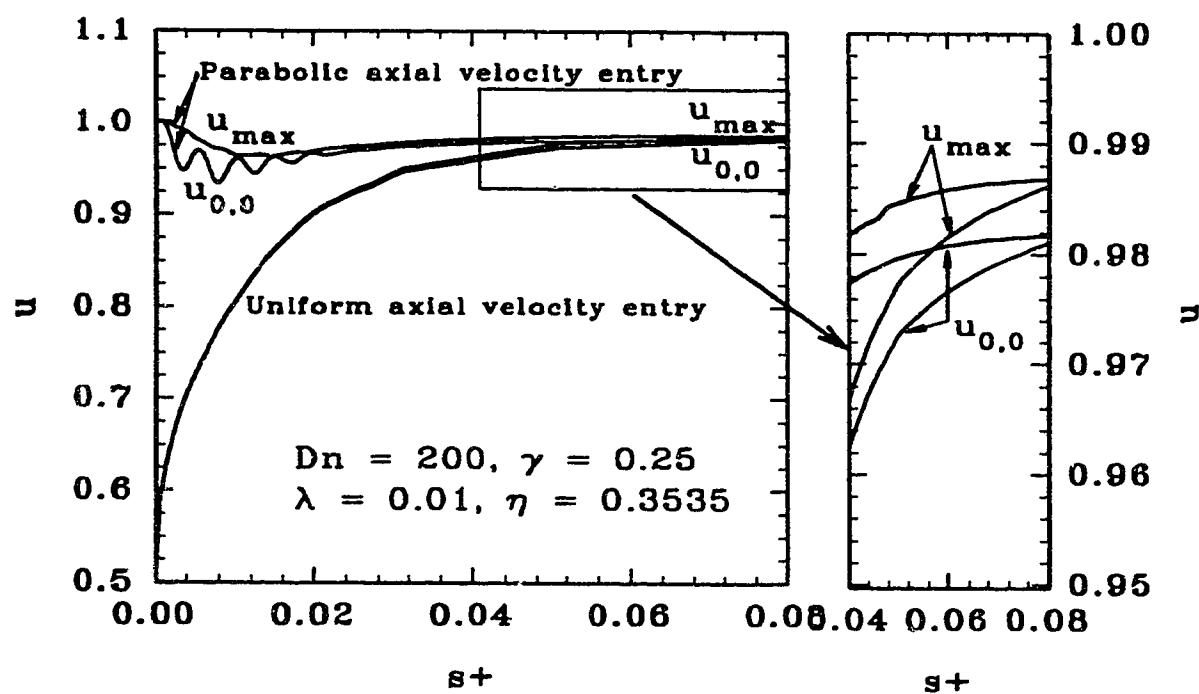
Fig. 5.9.   Center and maximum axial velocity development for large γ flows.
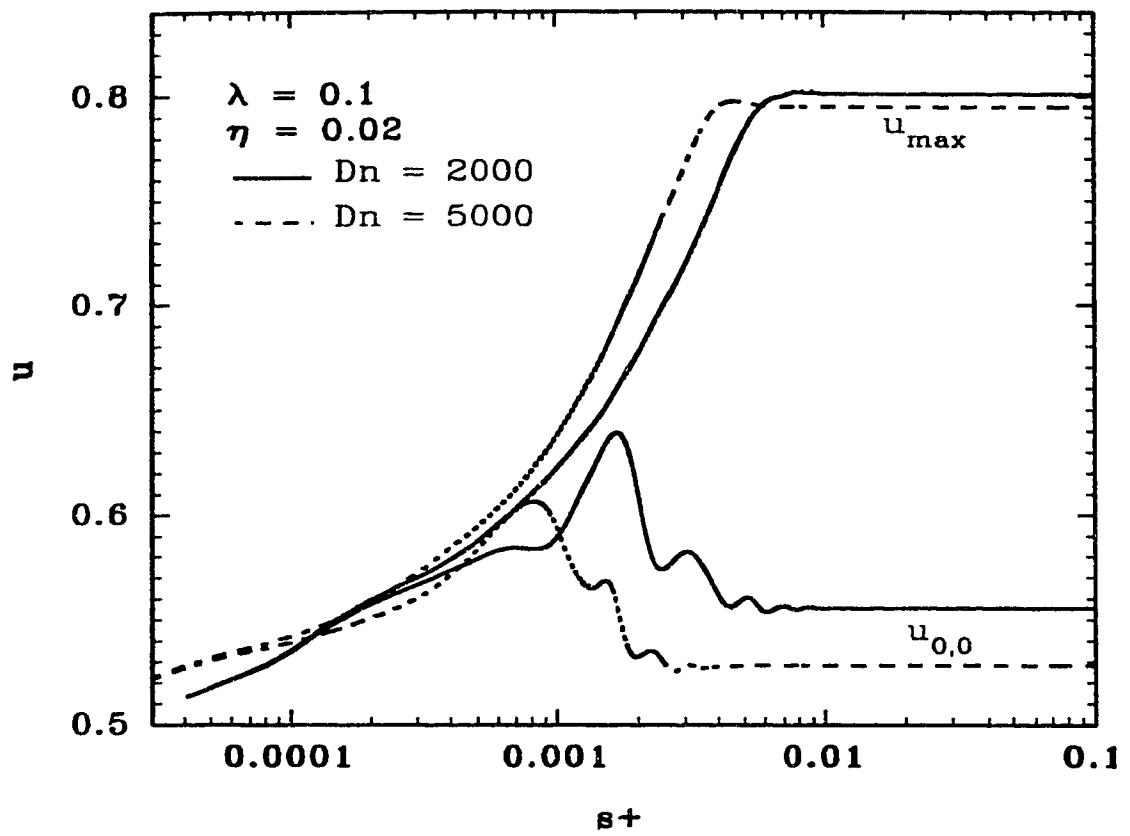
Fig. 5.10.   Center and maximum axial velocity development for very flows. Uniform axial velocity entry.
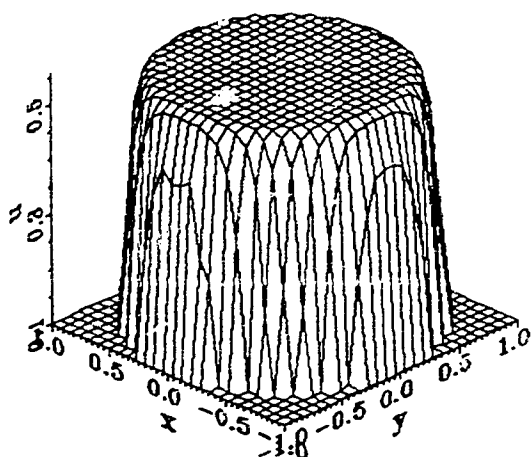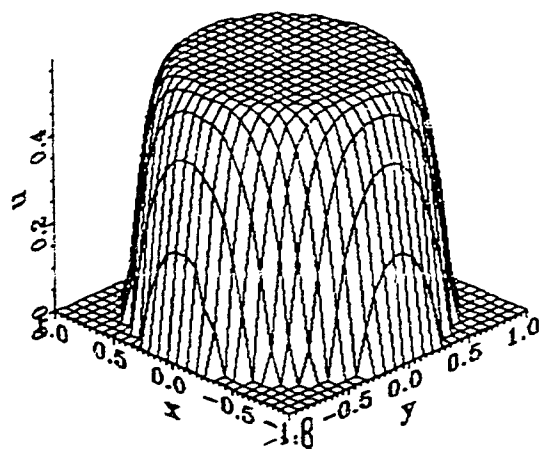
a. s* =0.00021
b. s* =0.000975
c. s* =0.00195
d. s* =0.00596
e. s* =0.02168
f. s* =0.1
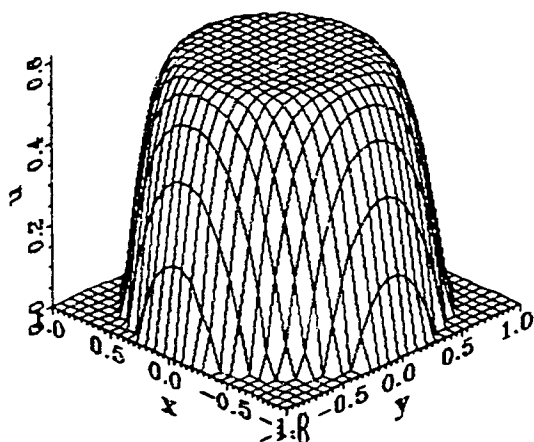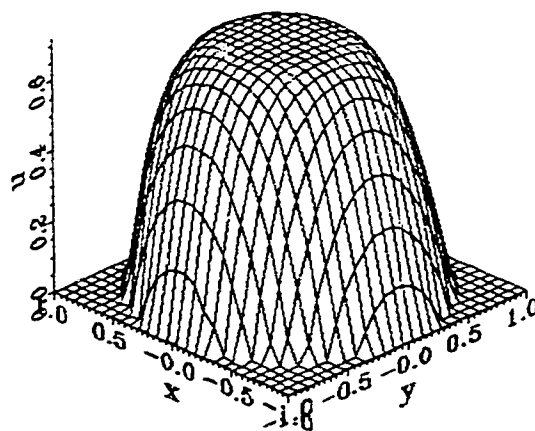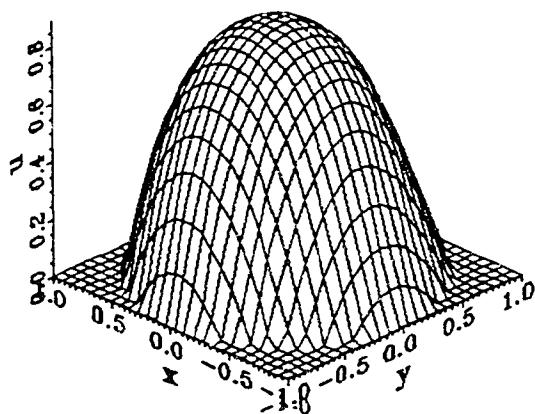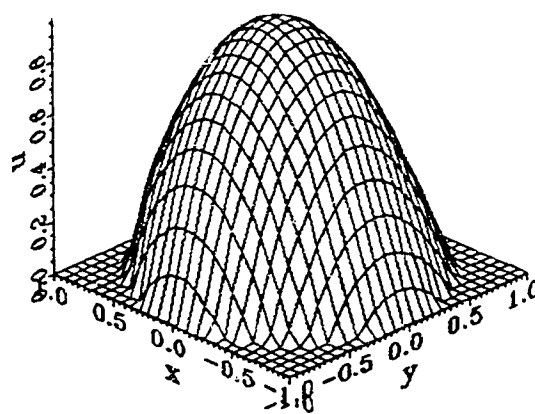
Fig. 5.12. Axial velocity profile development for the one vortex flow. $Dn = 200$, $\lambda = 0.01$, $\gamma = 0.25$. Uniform axial velocity entry.

a. s* =0.002

b. s* =0.006

c. s* =0.010

d. s* =0.015

e. s* =0.02

f. s* =0.1
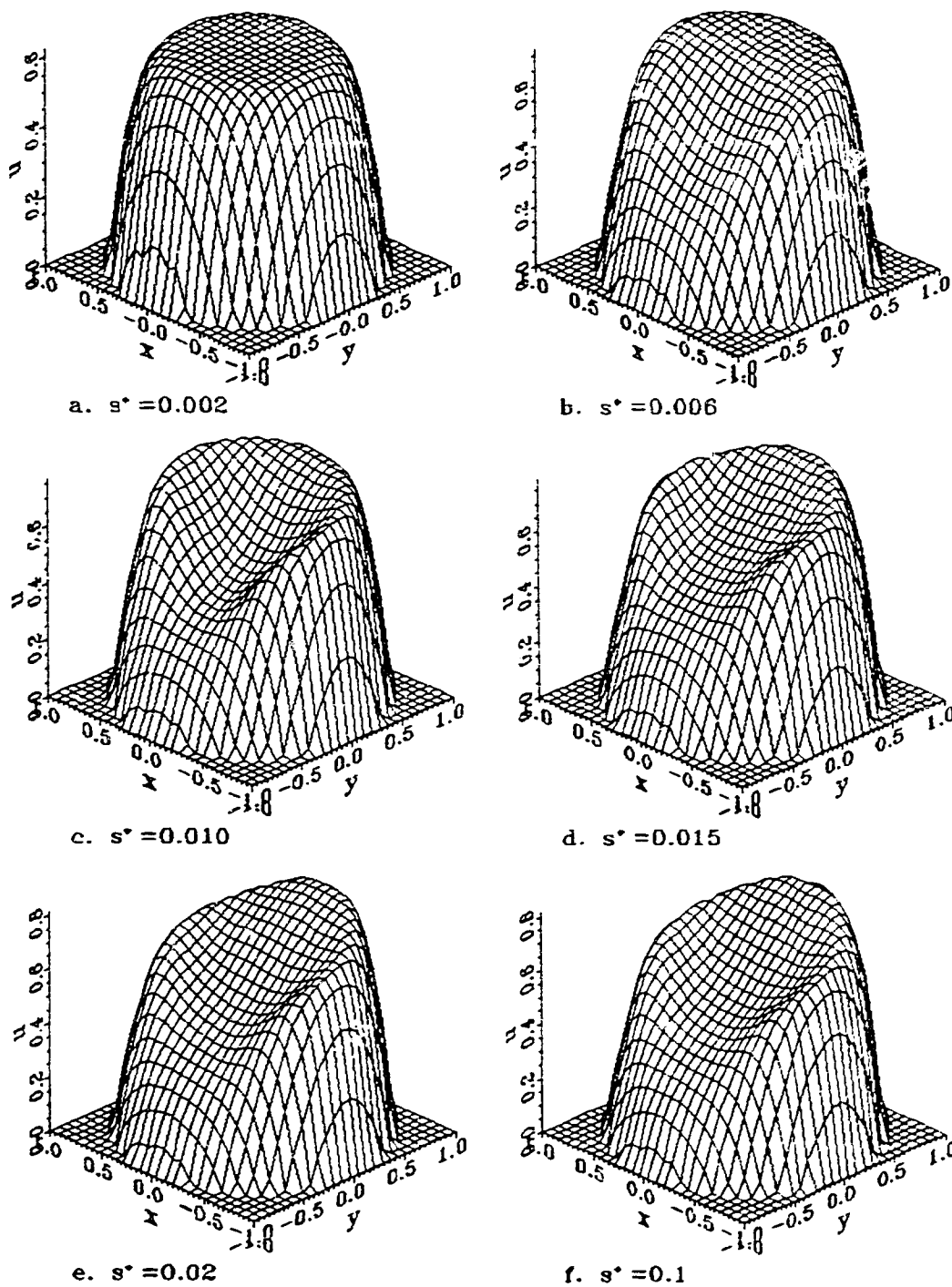
Fig. 5.13. Axial velocity profile development corresponding to a two–vortex flow. Dn = 200, λ = 0.1, η = 0.05 and γ = 0.01118. Uniform axial velocity entry.

a. s* =0.006

b. s* =0.008

c. s* =0.01

d. s* =0.015

e. s* =0.02

f. s* =0.04
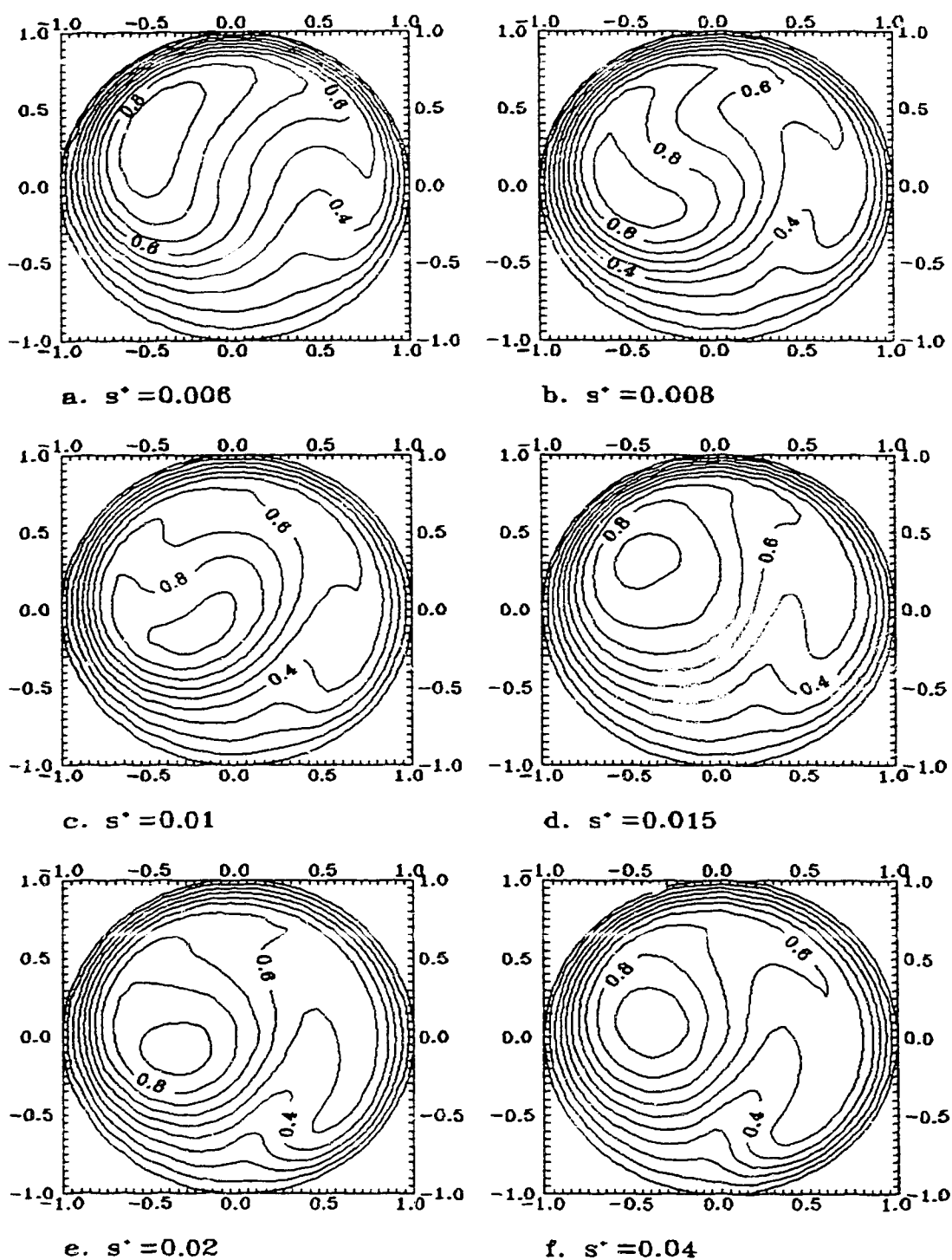
Fig. 5.14. Axial velocity isoplethes evolvement for Dn = 200, $\lambda = 0.01$, $\gamma = 0.12$. Parabolic axial velocity entry.

5.4.3. Pressure and shear stress development

Figures 5.15 to 5.18 show the development (or evolvement) of the axial pressure gradient or fRe. As the flow enters the helical pipe, fRe becomes very large for the case of the flow with a uniform axial velocity entry (the pressure is set to be uniform and the secondary flows are set to be zero). fRe drops sharply as the axial length increases. The decrease in fRe as the axial length increases is not necessarily monotonic. For large Dn flows, fRe development is oscillatory (although not cyclic). When Dn is relatively small, fRe varies with the axial length monotonically.

For the case having a parabolic axial velocity entry, i.e., the flow is a fully developed Poiseuille flow at the entry of the helical pipe, the axial pressure gradient increases non—monotonically until it finally settles down at the fully developed flow, as shown in Figure 5.18.

Attempt was made to compare fRe or total wall shear stress evolvement as the axial length increases with the published experimental data. Since the axial pressure drop is proportional to the local total wall shear stress, the "total shear stress" of Choi et al. (1979) measured via an electrochemical method was used to compare with our computed fRe development. As shown in Figure 5.17, the computed fRe is very different from that deduced from the experimental data of Choi et al. This disagreement is found to be due to the fact that the measured data was not the total shear stress as was claimed by the authors. The electrochemical method used by Choi et al. measures the concentration gradient at the wall. This concentration gradient can only be related to the axial velocity gradient or the axial wall shear component. Only in some special circumstances, such as a straight pipe, i.e., Poiseuille flow, the concentration gradient may be related to the total shear rate. With this fact in mind, we computed the development of the axial shear rate for the case of a torus having $Dn = 643$, $\lambda = 1/7$ and $\eta = 0$. The experimental data of the above mentioned authors and that of Talbot & Wong (1982) for the same
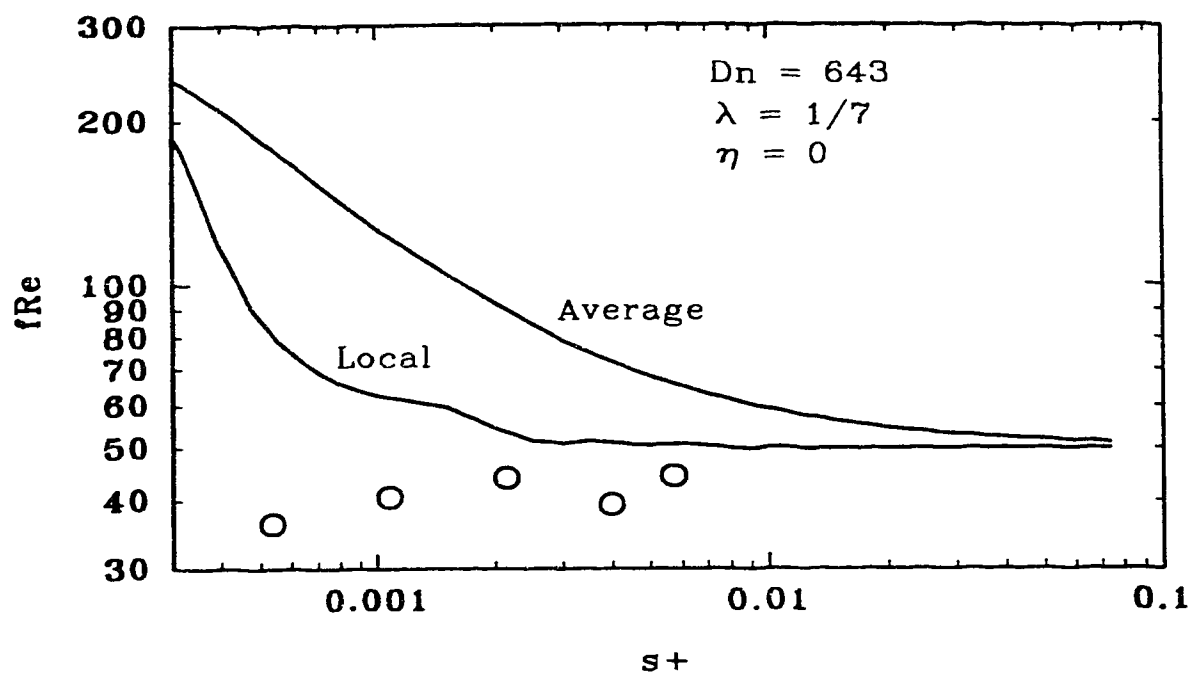
Fig. 5.15. Axial pressure gradient development for Dn = 643 with a uniform axial velocity entry. o represents the experimental data of Choi et al. (1979).
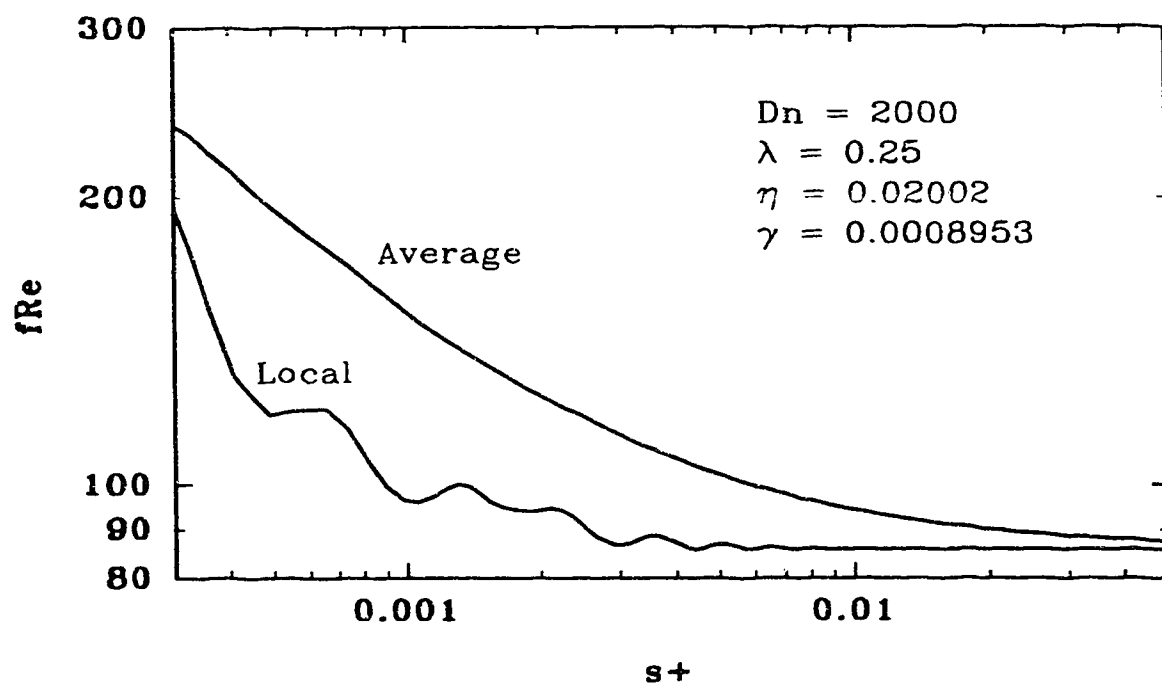
Fig. 5.16. fRe evolvement for large Dn flow in a finite pitch helical pipe with a uniform axial velocity entry.
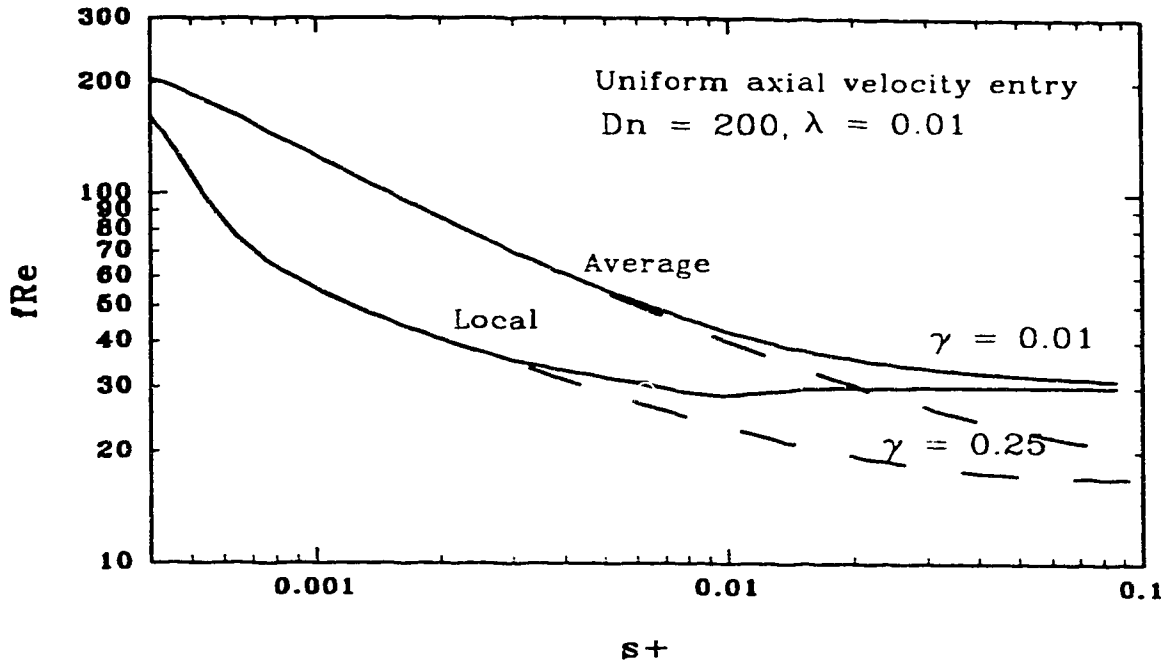
Fig. 5.17. fRe development for both two-vortex and one-vortex flows with a uniform axial velocity entry.
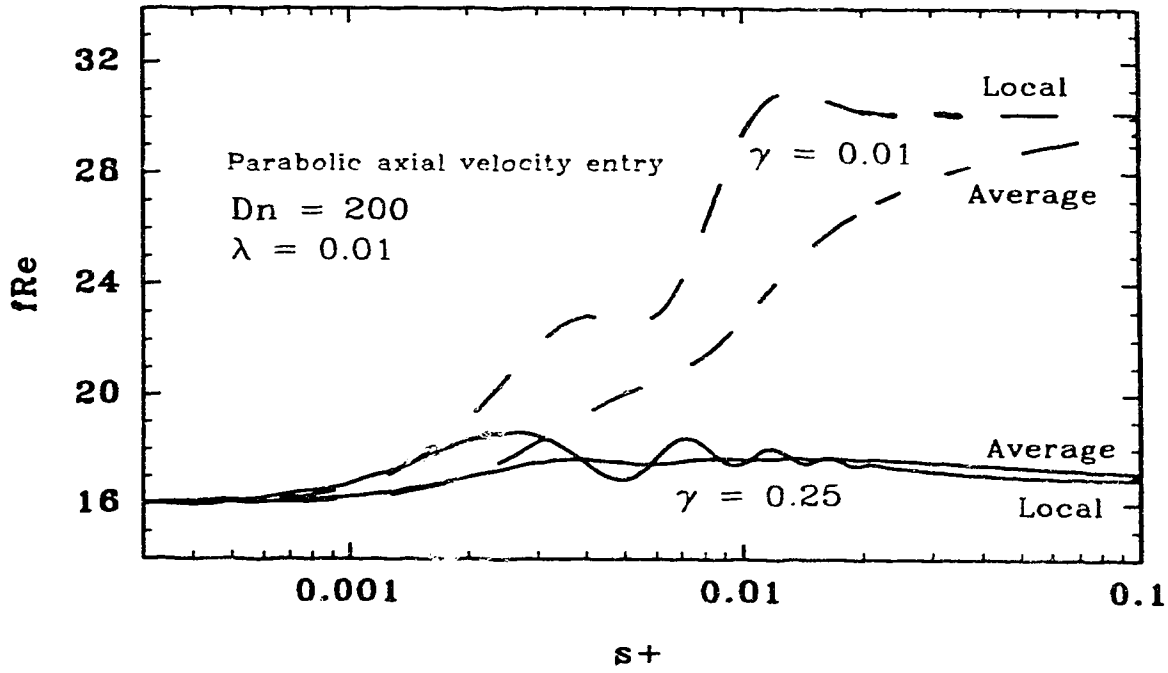
Fig. 5.18. Axial pressure gradient development of Dn = 200 and $\lambda = 0.01$ for both two-vortex and one-vortex flows with the parabolic axial velocity entry.
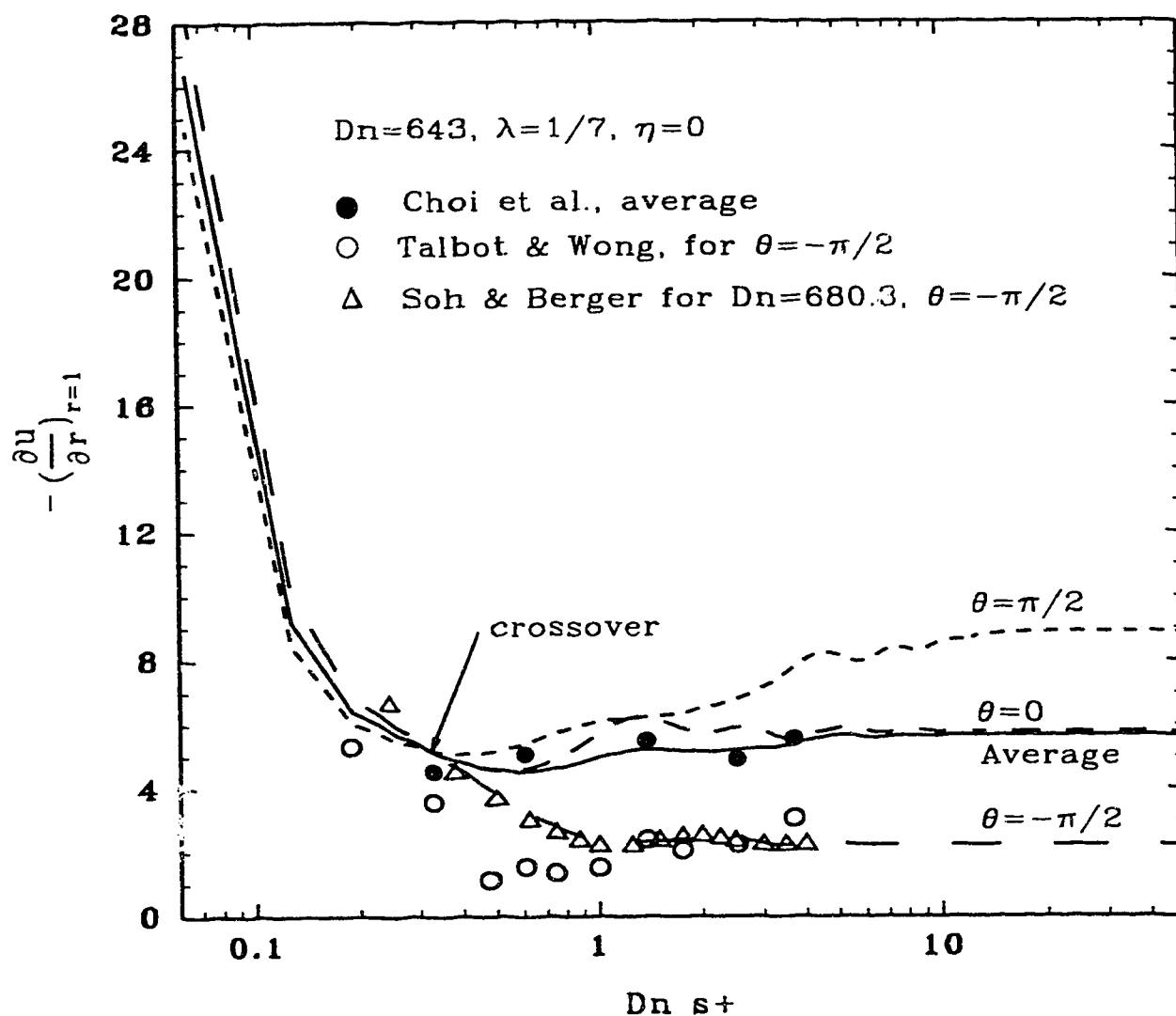
Fig. 5.19. Developments of the peripherally averaged axial shear rate and the axial shear rate at the inner most, outer most and top wall. The experimental data of Choi et al. (1978) for average shear rate, Talbot & Wong (1982) for the axial shear rate measured at the inner wall ($\theta = -\pi/2$) and the numerical solution of Soh & Berger (1984) for the axial shear rate at the inner wall are shown as symbols.

torus and flow conditions are shown in Figure 5.19. It can be seen that the agreement is good. Owing to the large Schmidt number of the media, the experimental data close to the entrance may not be a good representation of the axial shear rate. To verify our findings, the numerical solution of Soh & Berger

(1984) with a slightly higher Dn of 680.3 is also shown in Figure 5.19. Soh & Berger (1984) did not invoke the parabolization and used a slightly different inlet (free—vortex) condition of $u|_{s=0} = \frac{1}{1 + \lambda \sin\theta}$. It can be seen that our computed results are consistent with those of Soh & Berger (1984).

As we note from Figure 5.19, the axial shear rate decreases sharply near the entry. The shear rate at the outer wall is smaller than that at the inner wall. At about Dn $s^+ = 0.328$ or $s = 1.74$, a crossover occurs. The shear rate at the outer wall becomes larger than that at the inner wall. The shear rate becomes gradually varying with the axial distance after the crossover. The crossover point is consistent with the study of Singh (1974) for $s = 1.9$ and Smith (1976) for $s = 1.51$. However, there is no sign of a vanishing shear rate. This is in contrast with the boundary layer analysis which claims a vanishing axial shear rate, see Stewartson et al. (1980). One should bear in mind that the boundary layer analysis attempts to match the sharp decreasing part with the slowly varying part near the fully developed region. In the intermediate region, the flow is more complicated than a simple boundary layer theory can handle. This disagreement with the boundary layer analysis was also reported by Soh & Berger (1984).

To support our findings that there is no vanishing shear rate, we present the axial shear rate developments for very large Dn flows. Figures 5.20a and 5.20b show that a minimum inner wall axial shear rate is present. However, the magnitude of the minimum inner wall axial shear rate is no smaller than that of the fully developed inner wall axial shear rate. Hence, we conclude that the axial wall shear rate does not vanish. The crossover points move closer towards the inlet as the flow Dean number is increased. We observe that the axial wall shear rate crossover occurs at Dn $s^+ = 0.305$ or $s = 1.93$ and Dn $s^+ = 0.234$ or $s = 1.48$ for Dn = 2000 and Dn = 5000, respectively, for a helical pipe of $\lambda = 0.1$, $\eta = 0.02$. As in the case of a torus, this is in agreement with Yao & Berger (1988) who found that the axial
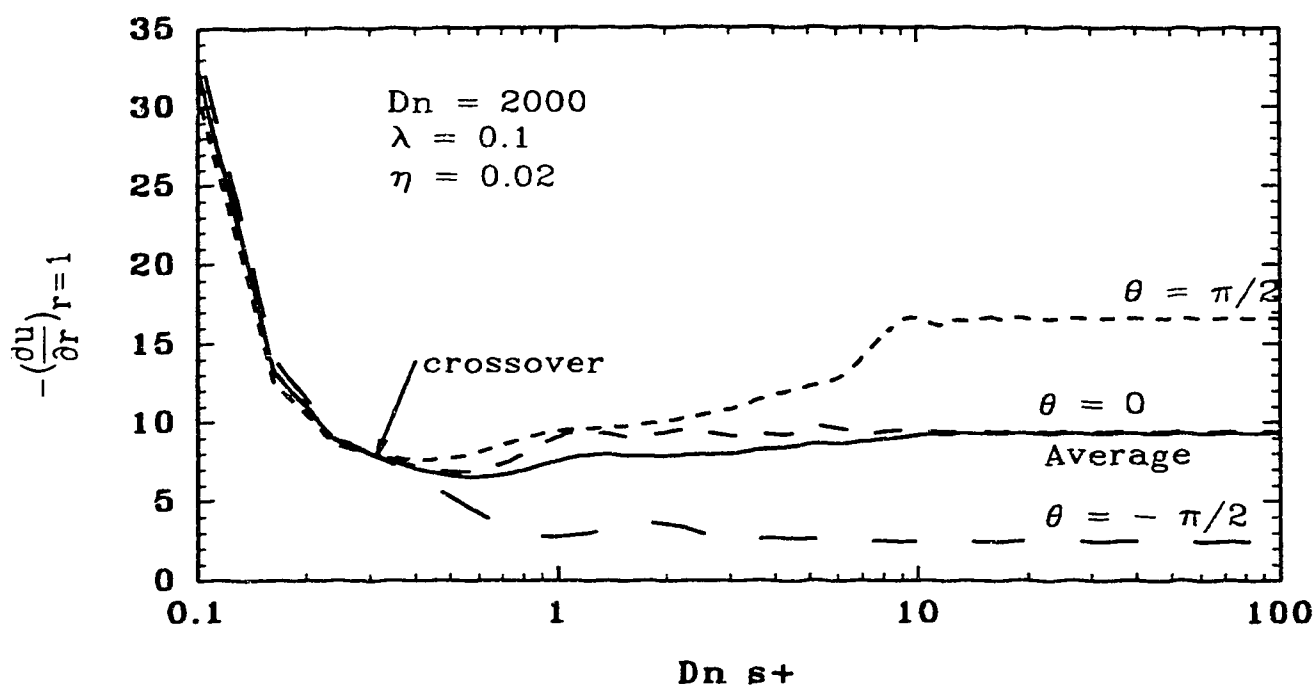
Fig. 5.20a. Axial wall shear rate development for $Dn = 2000$, $\lambda = 0.1$, $\eta = 0.02$ and $\gamma = 0.001414$. Uniform axial velocity entry.
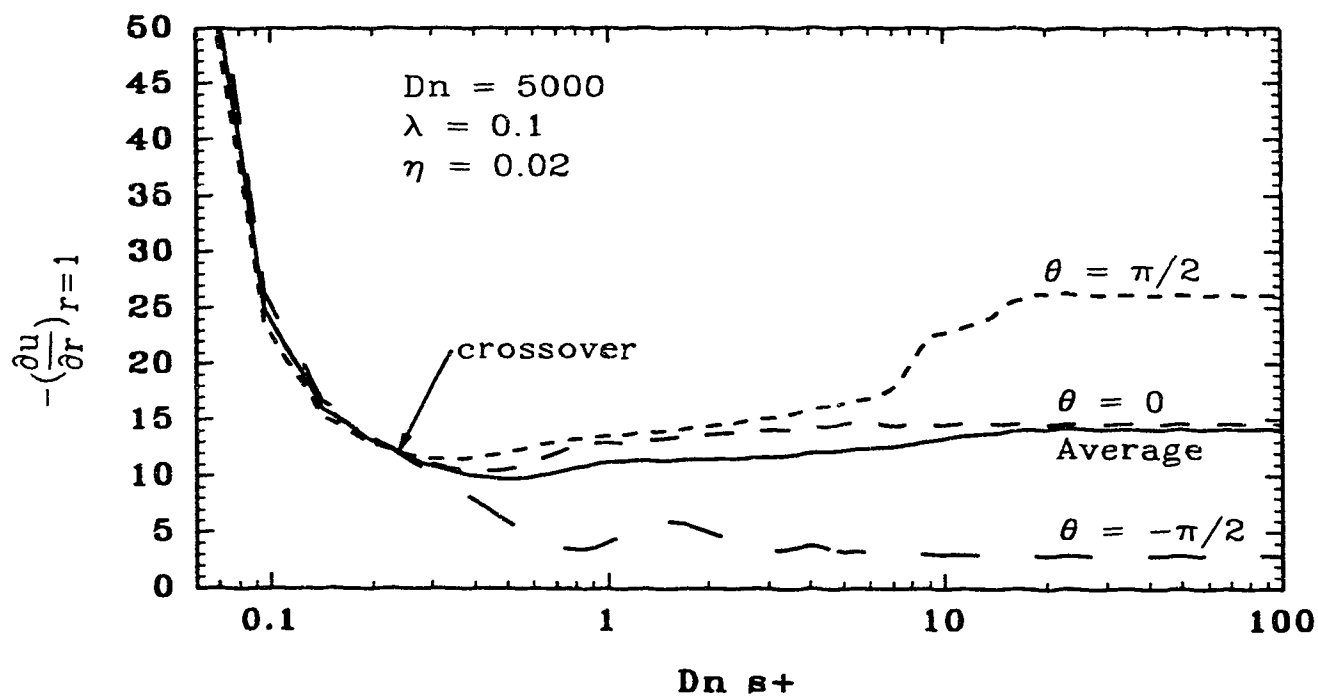

Figure 5.20b. Axial wall shear rate development for $Dn = 5000$, $\lambda = 0.1$, $\eta = 0.02$ and $\gamma = 0.0008944$. Uniform axial velocity entry
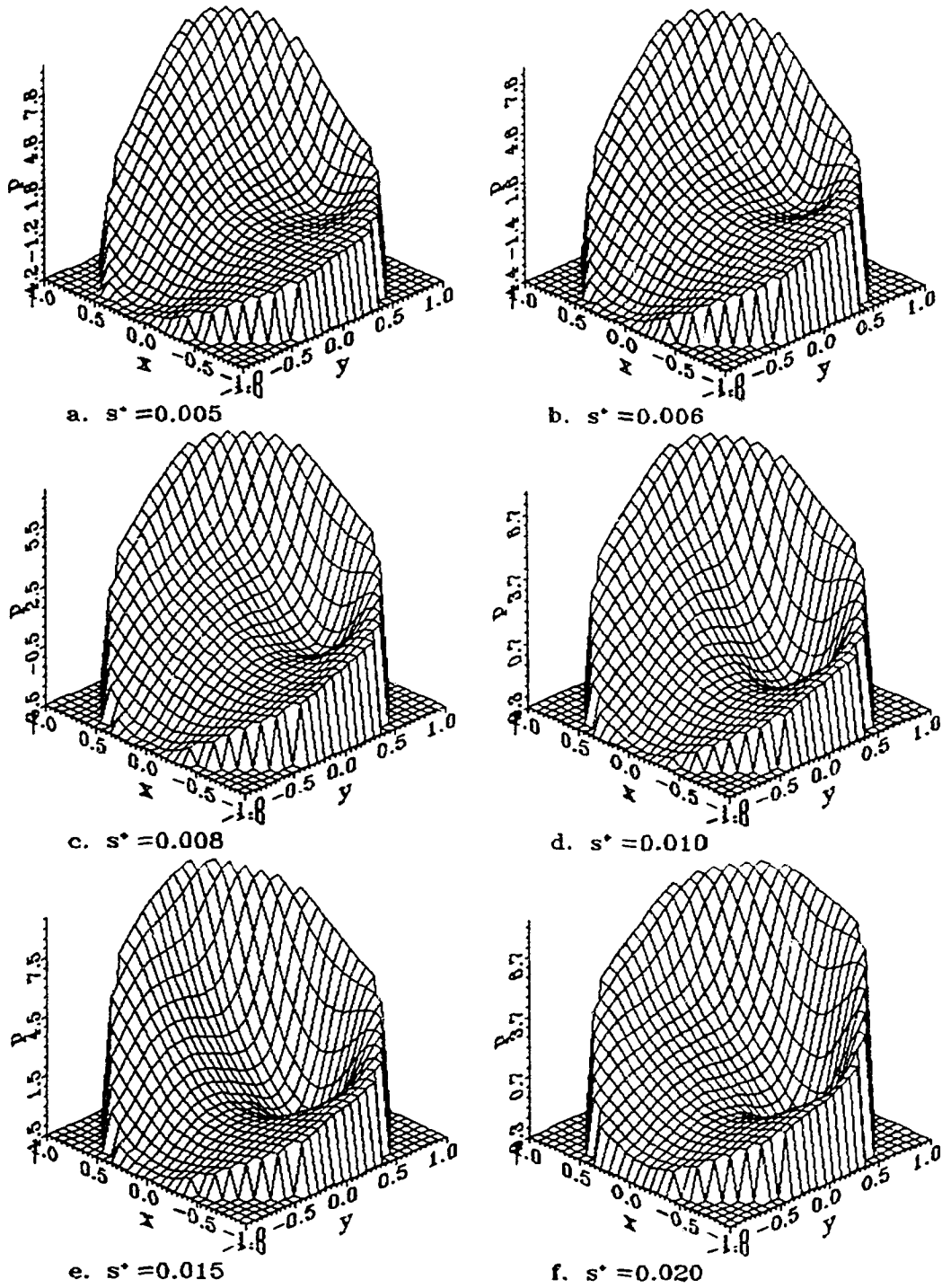
Fig. 5.21. Pressure cone formation for $Dn = 200$, $\lambda = 0.01$ and $\gamma = 0.12$ ($\eta = 0.1697$). Parabolic axial velocity entry.

wall shear rate crossover point moves towards the inlet with increasing Dn and is strongly dependent on the curvature ratio λ.

In Chapter 4, we found a pressure cone (local minimum pressure zone) present for large Dn and $0.1 < \gamma < 0.2$ flows. To show the pressure cone formation, Figure 5.21 shows the pressure profile development for Dn $= 200$, $\lambda = 0.1$, $\gamma = 0.12$ with a parabolic axial velocity entry.

5.4.4. Heat transfer Nusselt number development

Owing to the substantial magnitude of the secondary flow and to its development, the temperature profile and the Nusselt number are expected to be oscillatory (may not be cyclic) in the developing region. This oscillatory behavior was also observed experimentally, see Janssen & Hoogendoorn (1978). However, for a fully developed flow in a torus, periodic oscillation in the Nusselt number was found in the analysis of the developing heat transfer by Tarbell & Samuels (1973). In this study, we set forward to investigate the validity of the parabolization and present some results on the heat transfer behavior in the simultaneous developing region for helical pipes of a finite pitch. Comparison was made with the available data for the case of flow in torus.

Figures 5.22 and 5.23 show the Nusselt number development for a torus having $\lambda = \frac{1}{41}$ for various Prandtl numbers. The oscillation in Nusselt number is evident even for the small Dean number, Dn $= 21.86$, and small Prandtl number, Pr $= 0.707$, a case shown in Figure 5.22. For comparison purposes, the experimental data by Janssen & Hoogendoorn (1978) for the same conditions as those used in computations are also shown in the Figures 5.22 and 5.23. It can be seen that the current predictions are in good agreement with the experimental results of Janssen & Hoogendoorn (1978). It is of interest to note that the agreement is very good even for the case of small Dn flows, as shown in Figure 5.22.
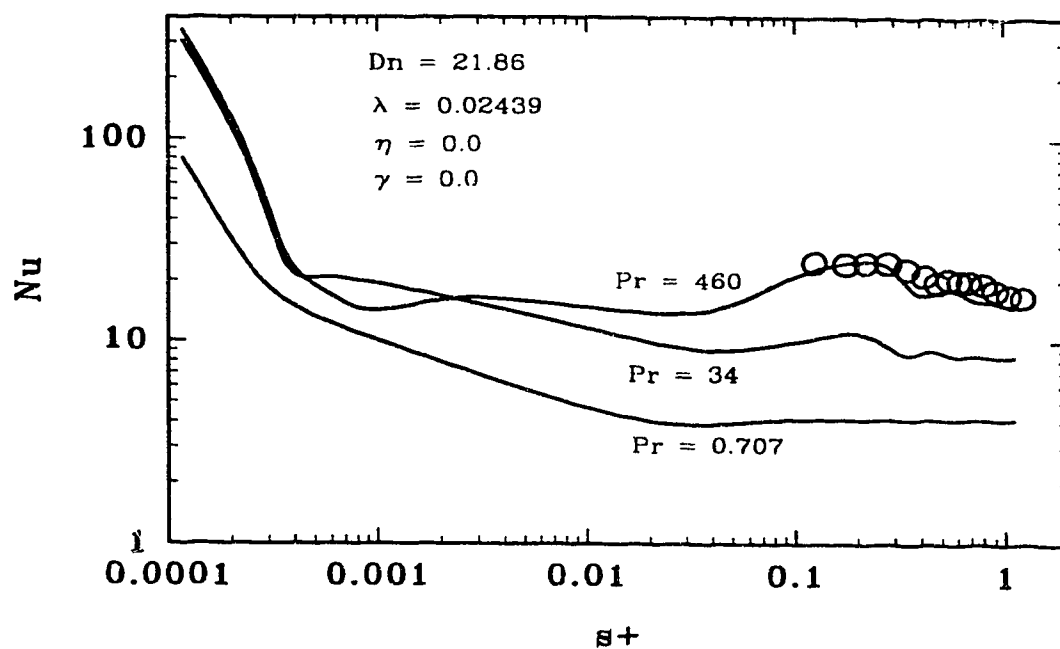
Fig. 5.22.   Nusselt number development for a torus for small Dn flow. The symbol o represents the experimental data of Janssen & Hoogendoorn (1978).
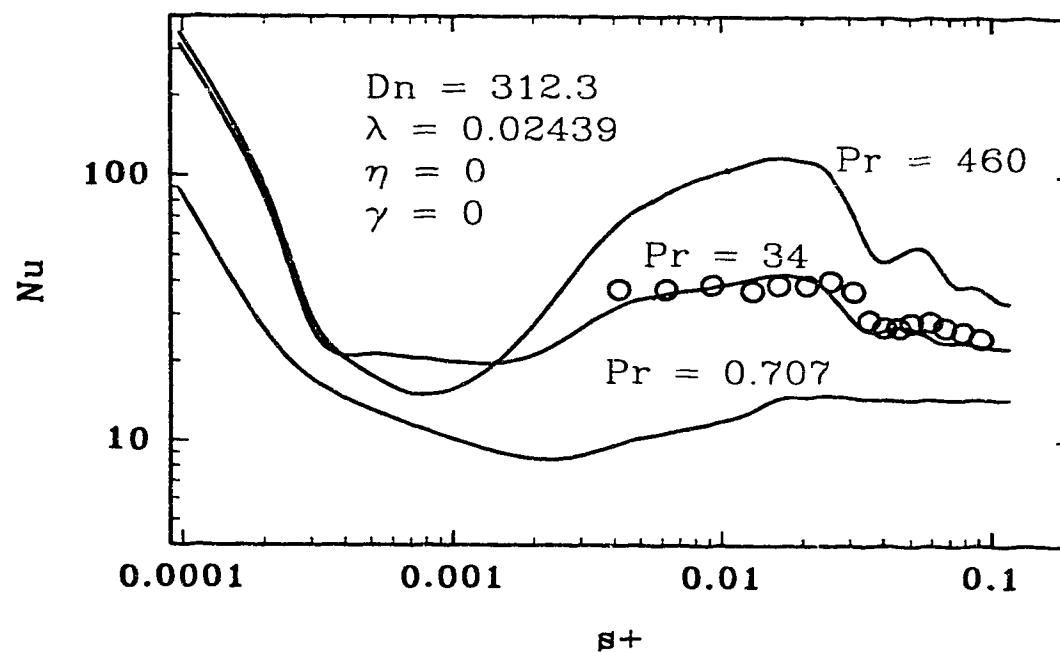

Fig. 5.23.   Nusselt number development for a torus with Dn = 312.3. The symbol o represents the experimental data of Janssen & Hoogendoorn (1978).
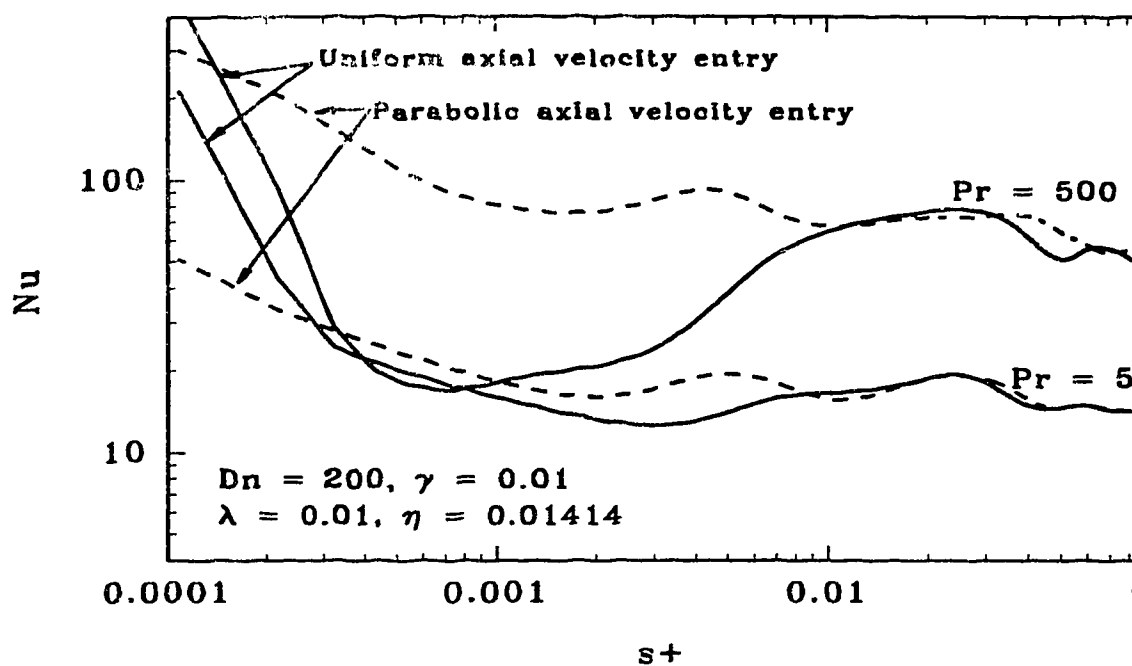
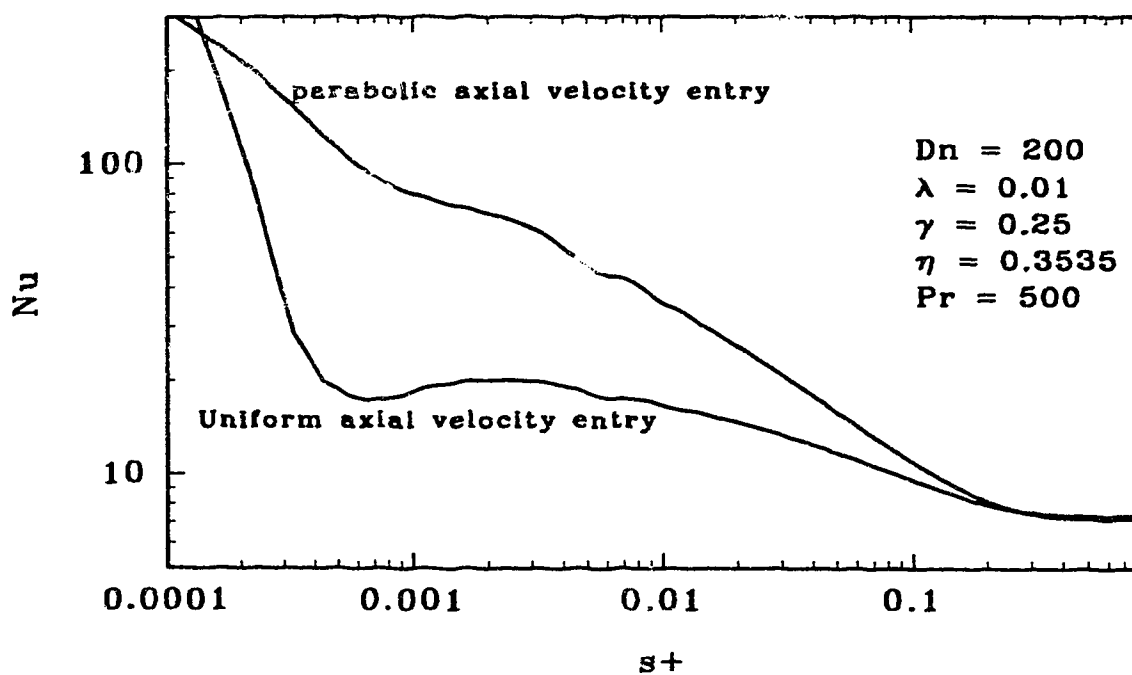Fig. 5.24. Nusselt number development for a two vortex flow of $\lambda = 0.01$ and $\gamma = 0.01$, $\eta = 0.01414$.

Fig. 5.25. Nusselt number development for a one–vortex flow of $\lambda = 0.01$ and $\gamma = 0.25$, $\eta = 0.3535$.

differ qualitatively from those of smaller Dn flow conditions. When Dn is increased, the minima (lowest points of the "valley") move closer to the inlet. The same is true when the fluid Prandtl number is increased.

Figure 5.27. shows the inner wall, the upper wall and the outer wall local Nusselt number variations with axial length for Dn = 2000, $\lambda = 0.1$, $\eta = 0.02$ with Pr = 0.707 and Pr = 500. For the case of a uniform axial velocity entry, we observe that the maximum local Nusselt number crosses over from the inner wall to the outer wall near the inlet. The crossover points are Dn s$^+$ = 0.20 (or s = 0.63) for Pr = 0.707, Dn s$^+$ = 0.19 (or s = 0.60) for Pr = 2 and Dn s$^+$ = 0.10 (or s = 0.32) for Pr = 500. A minimum (valley) value and a maximum (peak) value of the local Nusselt number occur after the crossover. The larger the Prandtl number is, the larger difference in magnitude of the maximum and the minimum inner wall Nusselt number.

Figures 5.25 to 5.27 clearly show that the local Nusselt number, Nu(θ), development is sensitive to θ and to the value of the fluid Prandtl number.

In all cases, the larger the Prandtl number, the deeper the valley and the higher the peak after the valley appear.   avior of the Nusselt number is very much related to the secondary flow str   As shown in Figure 5.3a and 5.3b, "peaks" and "valleys" exist in the course of $\|v\|_{r\theta}$ development. Strong secondary flow is expected to increase the Nusselt number which can be magnified by an increase in fluid Prandtl number. Owing to the similarity between the temperature profile and the concentration profile, the wall concentration gradient with respect to the Schmidt number is expected to behave very similar to the temperature gradient (or Nusselt number) with respect to the Prandtl number. When Pr is very large, the Nusselt number development is very different from the axial wall shear rate development. Hence, by using a very large Schmidt number medium, the measured concentration gradient may not be good in representing the axial wall shear rate in
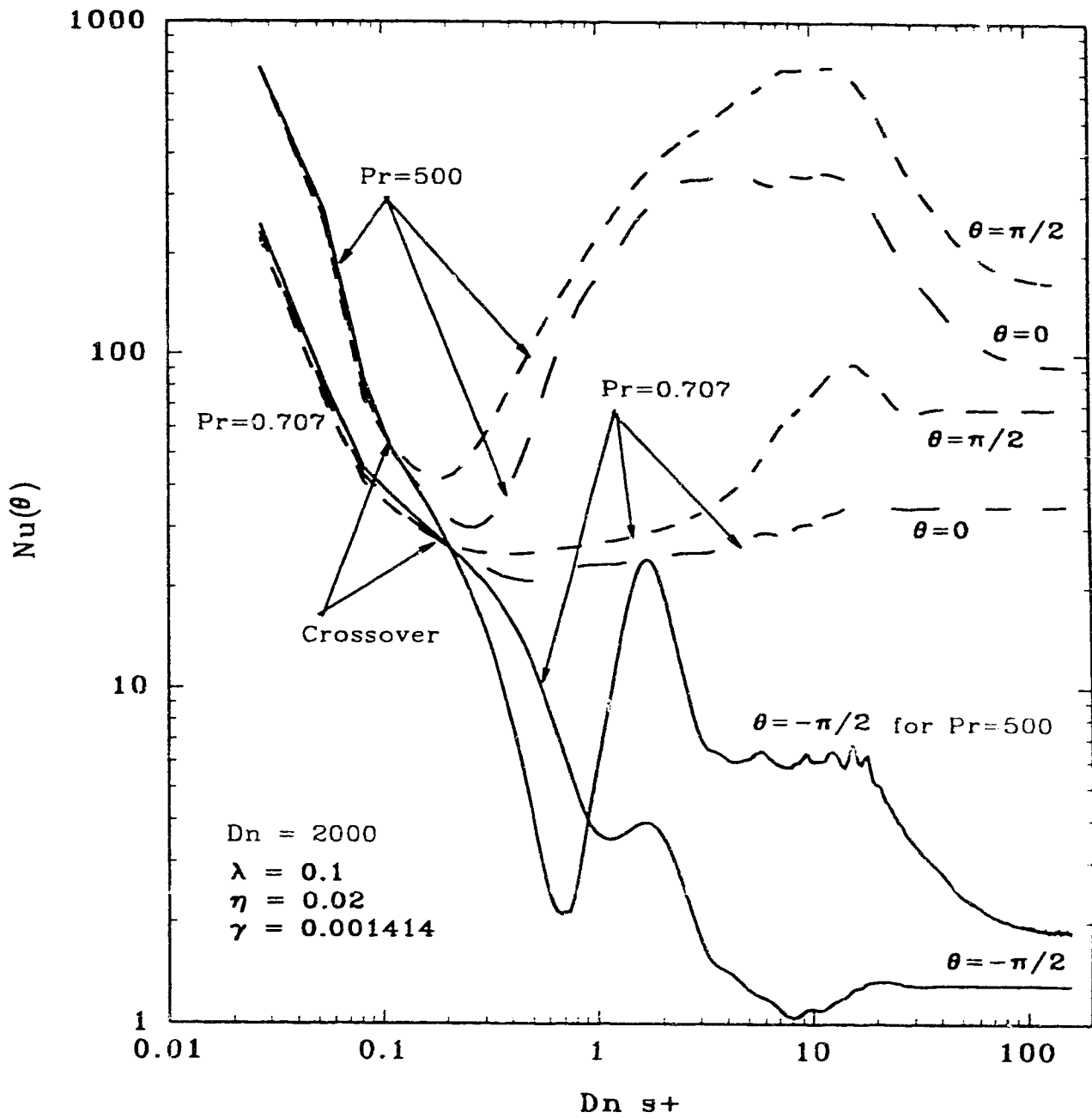
Fig. 5.27. Local Nusselt number evolvement for Dn = 2000, $\lambda = 0.1$, $\eta = 0.02$ with Pr = 0.707 and Pr = 500. Uniform axial velocity entry.
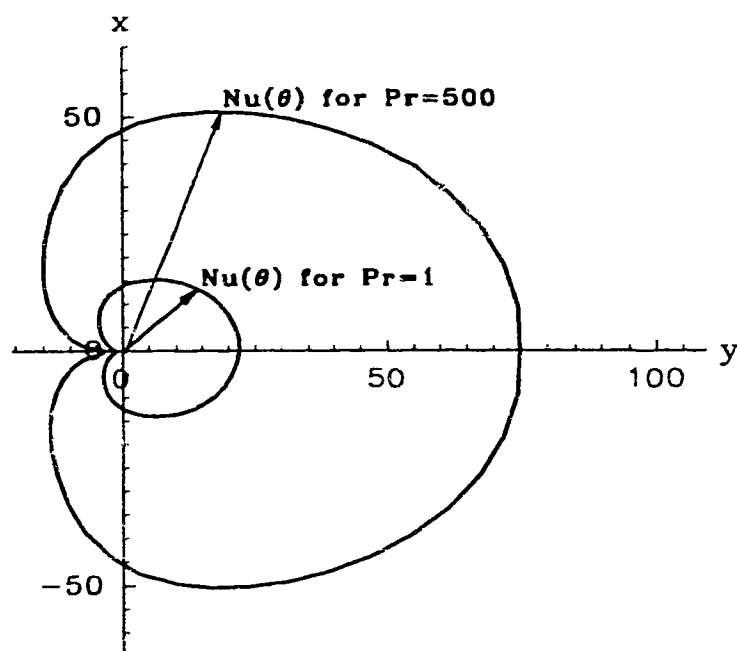
Fig. 5.28.   Fully–developed Nu(θ) variation with θ for a typical two–vortex flow of Dn = 200, λ = 0.01 and γ = 0.01.
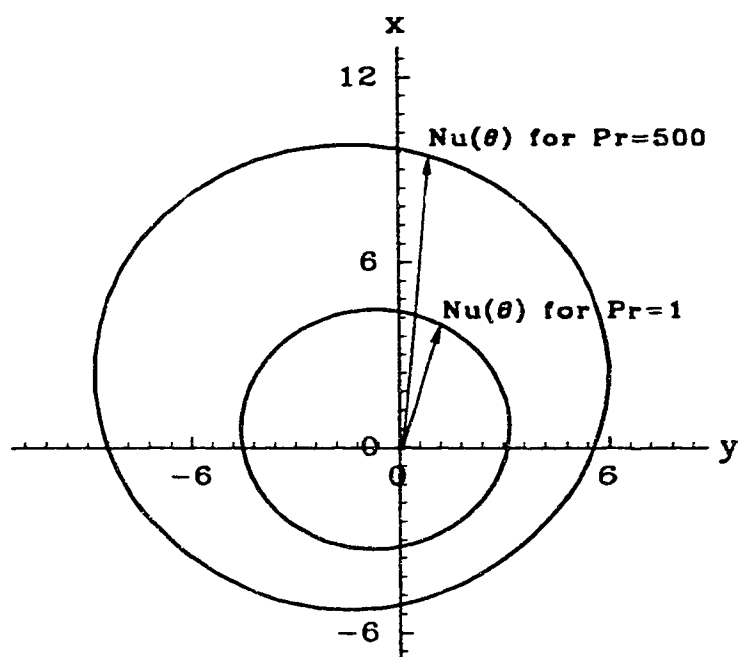

Fig. 5.29.   Fully–developed Nu(θ) variation with θ for a typical one–vortex flow of Dn = 200, λ = 0.01 and γ = 0.25.

the near inlet region.

Figures 5.28 and 5.29 show the asymptotic local Nusselt number distribution with θ for both the two— and one— vortex flows. These two plots are in polar coordinates where the angle θ is defined the same as that on a helical pipe cross section and Nu(θ) is measured by the polar distance. x and y correspond to the x and y axes of the non—orthogonal coordinate system. Figure 5.28 shows the local Nusselt number variation with θ for a typical two—vortex flow of Dn = 200, $\lambda = 0.01$ and $\gamma = 0.01$ with fluid Prandtl numbers of Pr = 1 and Pr = 500. We observe that the Nusselt number reaches maximum at the outer wall ($\theta = \frac{\pi}{2}$) and minimum at the inner wall ($\theta = -\frac{\pi}{2}$). The shape of the curve looks like a heart symmetrical with the y—axis. Nu(θ) increases with increasing Pr, but the qualitative behavior of Nu(θ) does not vary with Pr. Figure 5.29 shows the local Nusselt number variation with θ for a typical fully—developed one—vortex flow of Dn = 200, $\lambda = 0.01$ and $\gamma = 0.25$ with the same fluid Prandtl numbers as the case presented in Figure 5.28. We observe that Nu(θ) is very different from that in Figure 5.28. Nu(θ) is higher in the inner upper wall region and lower in the lower outer wall region. This behavior is consistent with the secondary flow observed in Figure 5.4b.f), where the secondary flow is stronger in the inner upper wall region and weaker in the lower outer wall region. However, the orthogonal secondary flow structure as shown in Figure 5.6b.f) should suggest a higher heat transfer rate in the outer upper wall region. That the heat transfer rate does not follow the orthogonal secondary flow pattern is because the orthogonal secondary velocity does not indicate the momentum and / energy transport direct direction (see Chapter 4). For Nu(θ) with different Pr for the case of the two—vortex flow, a similar behavior is observed. Comparing Figures 5.28 and 5.29, we observe that Nu(θ) is more distributed with θ for two—vortex flow and relatively invariant with θ for one—vortex flow.

5.4.5. Temperature field development

For the case of a torus, Figures 5.30 and 5.31 show the variation of the averaged temperature T_{av} and the local normalized maximum temperature T_{max} with the dimensionless axial distance s^+. T_{av} decreases monotonically and exponentially shortly after the entry into the helical pipe with s^+. The rate of decrease with the distance is fairly large for low values of fluid Prandtl numbers.

Figure 5.32 shows the isothermal lines for a typical two—vortex flow. It can be seen that the temperature profile for $Pr \sim O(1)$ is very similar to that of the axial velocity profile as shown in Figure 5.13. Figure 5.33 shows a typical temperature profile of larger Pr for $Pr = 100$. The flow conditions are identical to the case of those in Figure 5.32, where the two—vortex flow pattern is present. Near the vortex—dividing line, the temperature is much lower as compared to the other regions. At the early stage of development, the temperature profile for large Prandtl number still resembles that of the axial velocity development. Further downstream, the temperature near the vortex dividing line away from the outer wall forms a depression (local low temperature zone). The depression widens as the flow develops. In contrast to the temperature field for the case where a two—vortex pattern is present, Figure 5.34 shows the temperature distribution for the case of a single vortex pattern. Here, the temperature distribution is similar to the corresponding axial velocity, Figure 5.12.

The temperature distribution depends on both the flow Dean number and the fluid Prandtl number. Figure 5.35 shows the temperature distribution for various Dn and Pr flows. We observe that when the fluid Prandtl number is near unity and the flow Dean number is large, the temperature profile looks very much the same as the axial velocity profile. When the flow Dean number and the fluid Prandtl number are small, the temperature profiles are similar to that under the one—vortex flows conditions as shown in Figure 34. When the fluid Prandtl number or the flow Dean
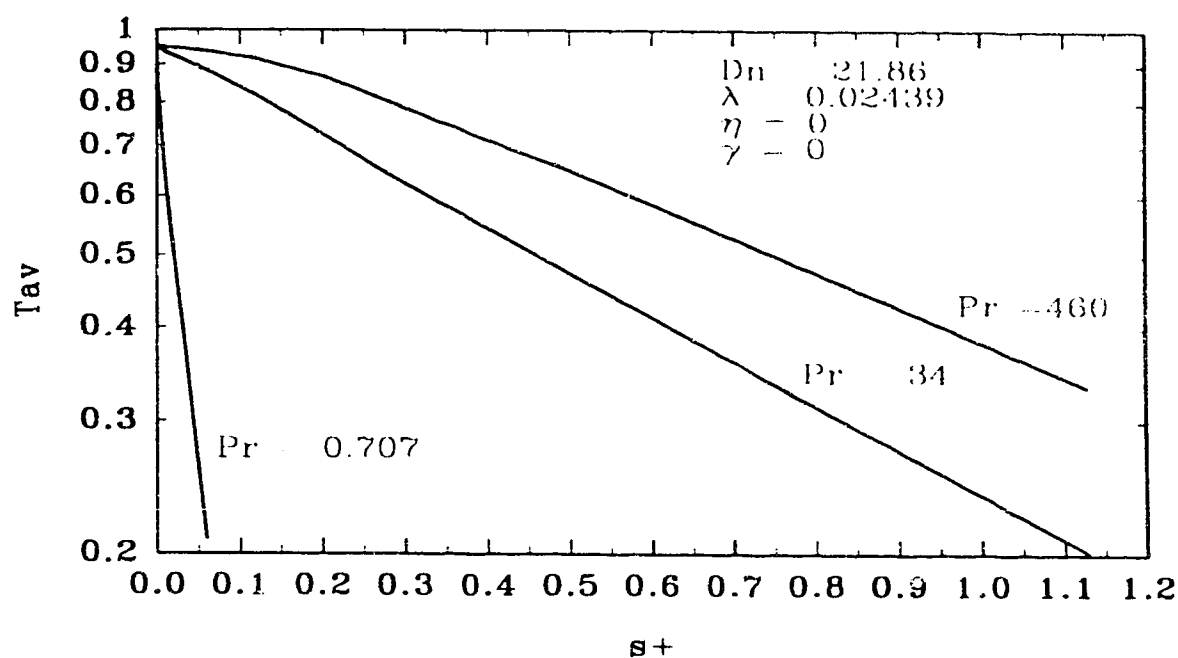
Fig. 5.30. Average temperature across pipe develops with axial length. Uniform axial velocity entry.
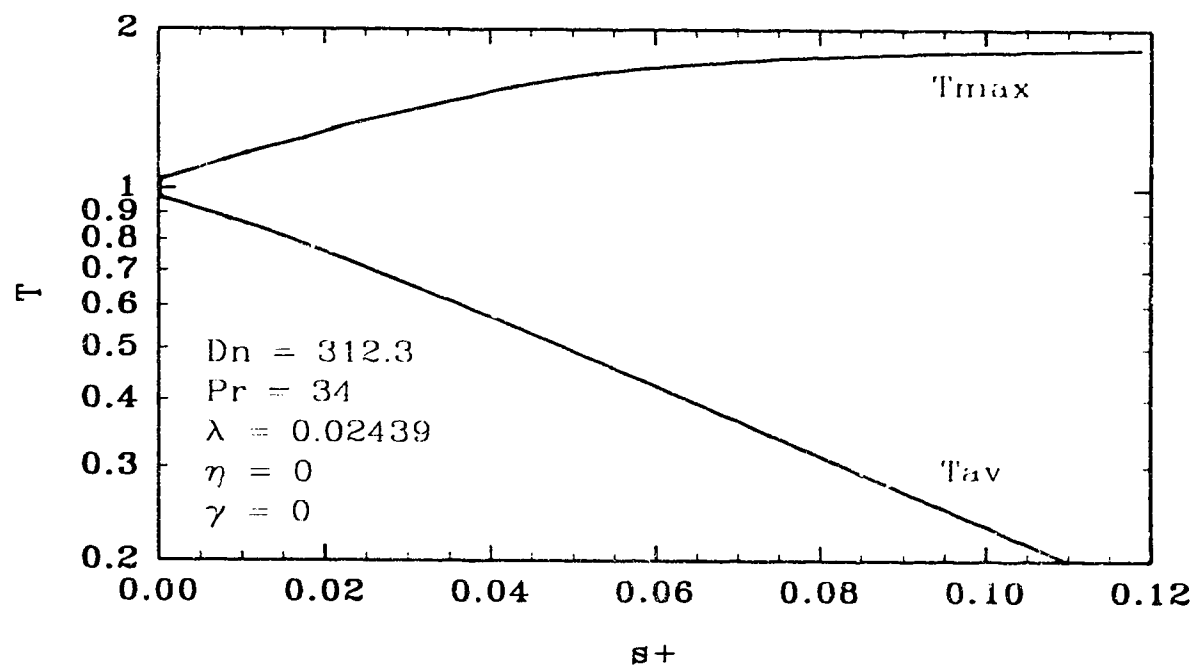

Fig. 5.31. Average temperature and normalized maximum temperature development with uniform axial velocity entry.
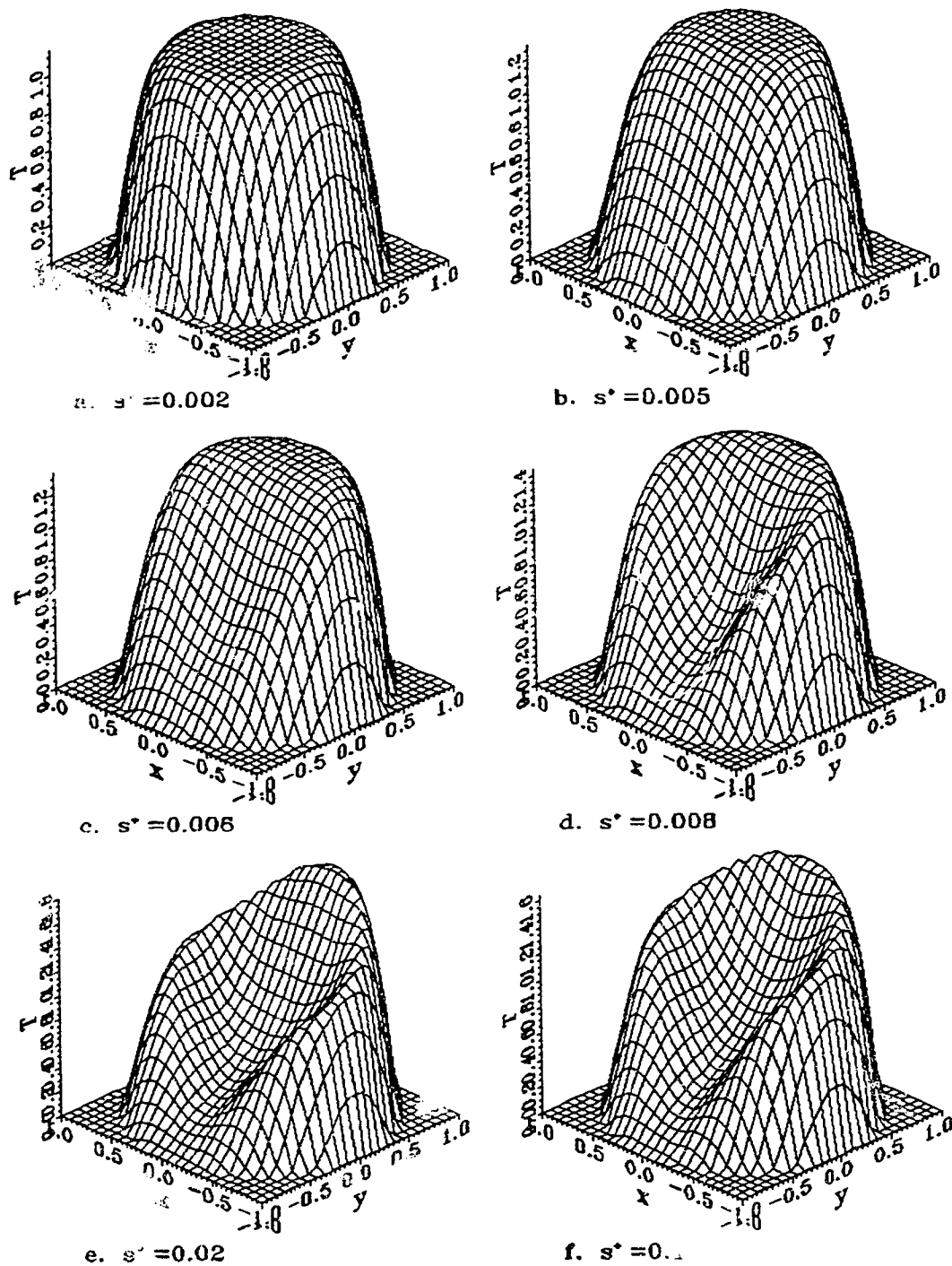
Fig. 5.32. Temperature profile development for Dn $= 200$, $\lambda = 0.1$, $\eta = 0.05$, $\gamma = 0.01118$, Pr $= 1$. Uniform axial velocity entry.
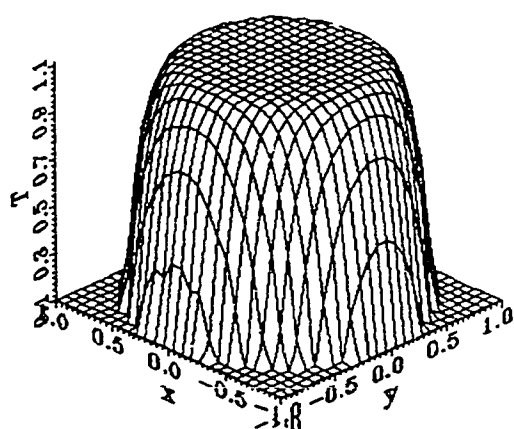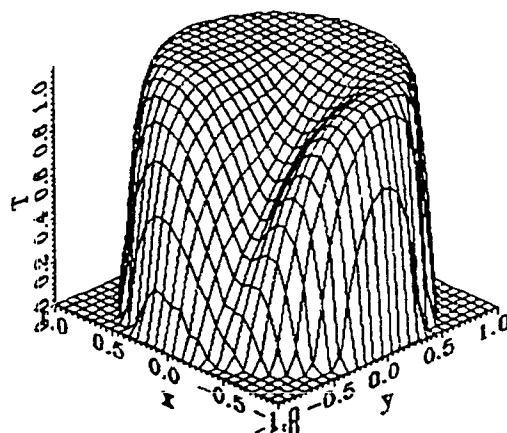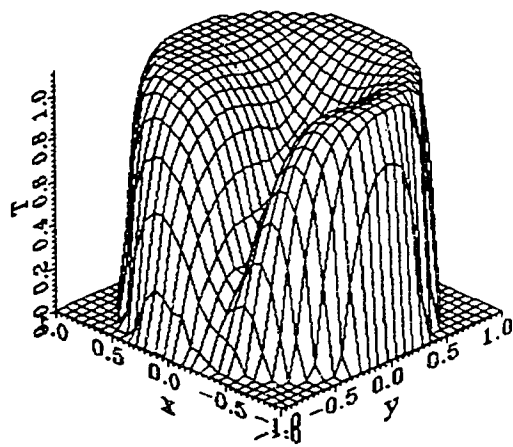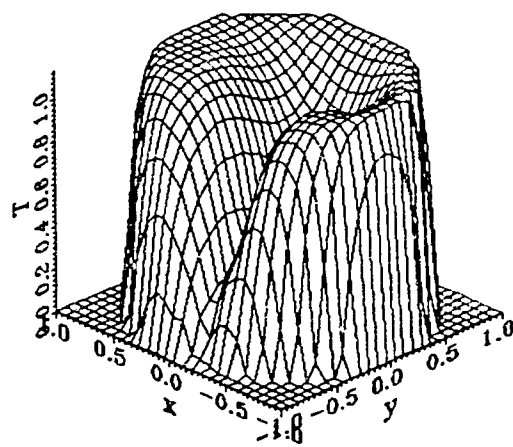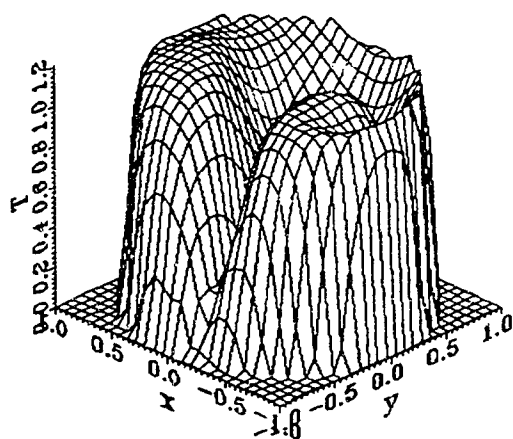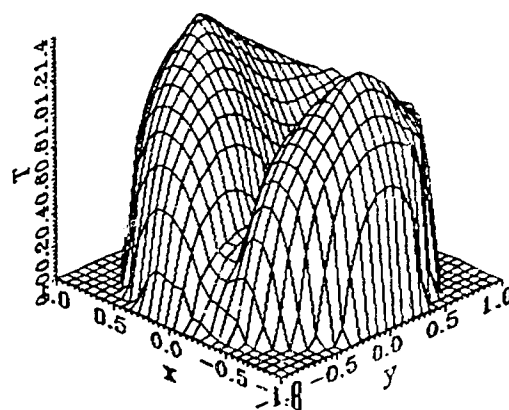
Fig. 5.33.   Temperature profile development for Dn = 100, λ = 0.1, η = 0.15, γ = 0.04743, Pr = 100. Uniform axial velocity entry.

a. s* =0.00401

b. s* =0.02166

c. s* =0.0395

d. s* =0.0801

e. s* =0.2003

f. s*
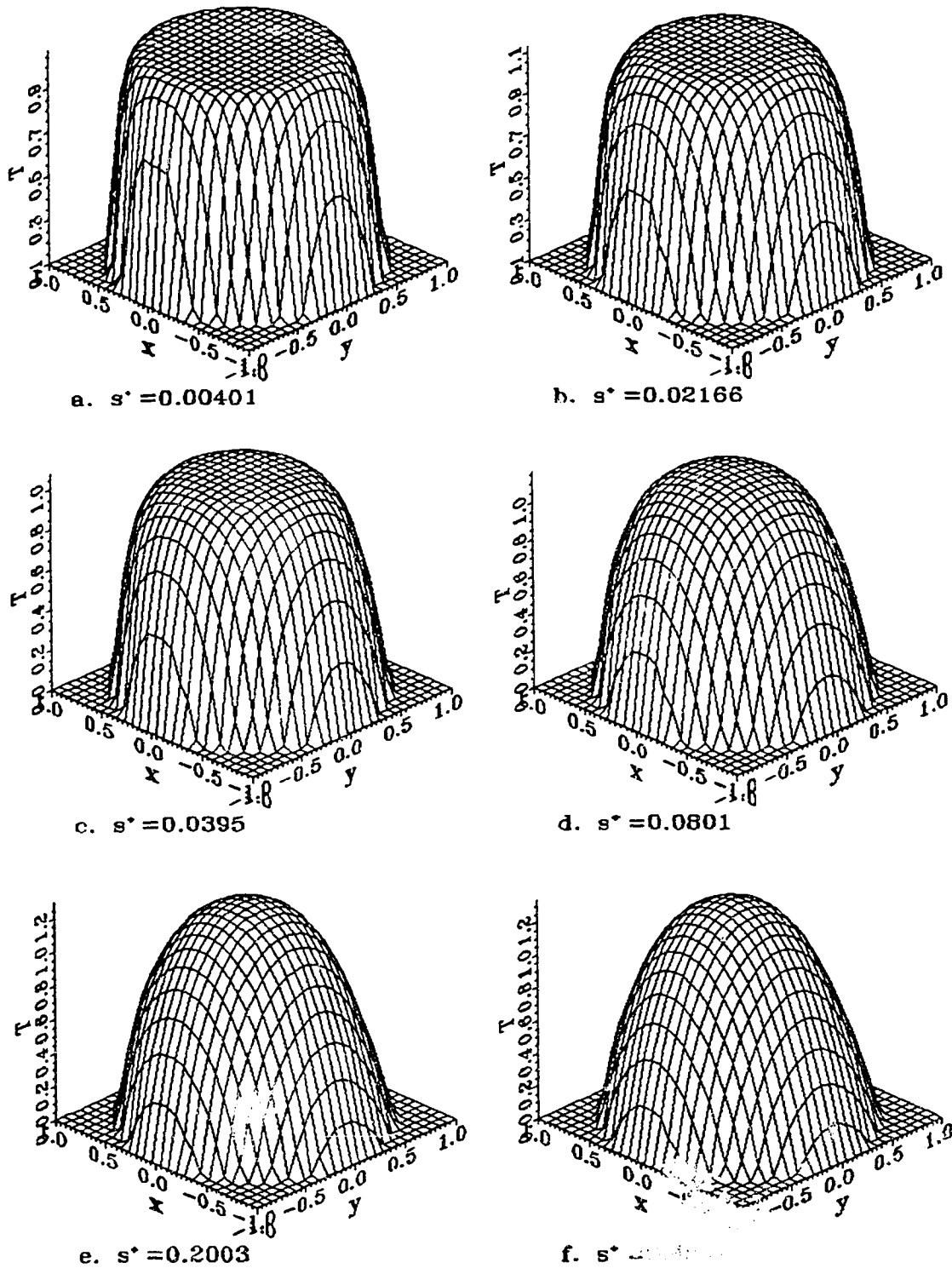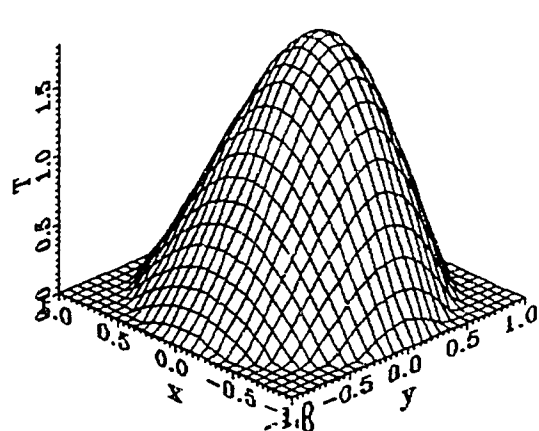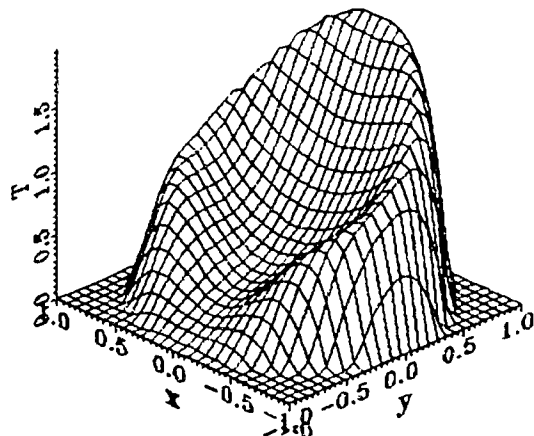
Fig. 5.34.   Temperature profile development for Dn = 200, $\lambda = 0.01$,
$\eta = 0.3535$, $\gamma = 0.25$ and Pr = 500. Uniform axial velocity entry.

a. Dn=21.86, Pr=0.707, λ=0.02439, γ=0

b. Dn=312.3, Pr=0.707, λ=0.02439, γ=0
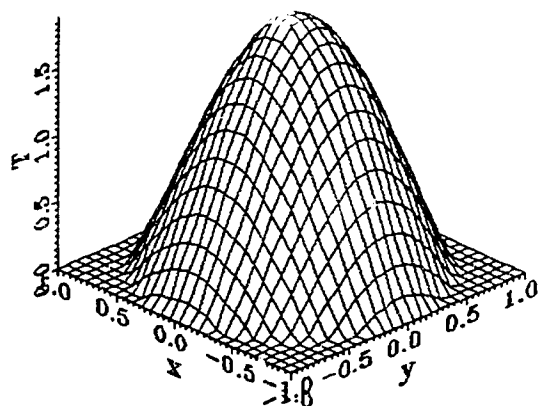
c. Dn=100, Pr=0.01, λ=0.1, γ=0.03162
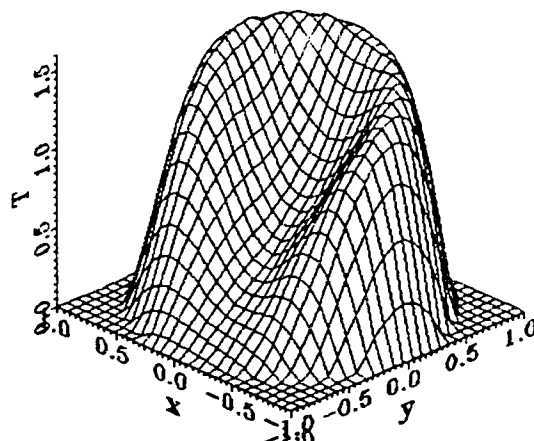
d. Dn=100, Pr=1, λ=0.1, γ=0.03162

e. Dn=200, Pr=0.1, λ=0.01, γ=0.01
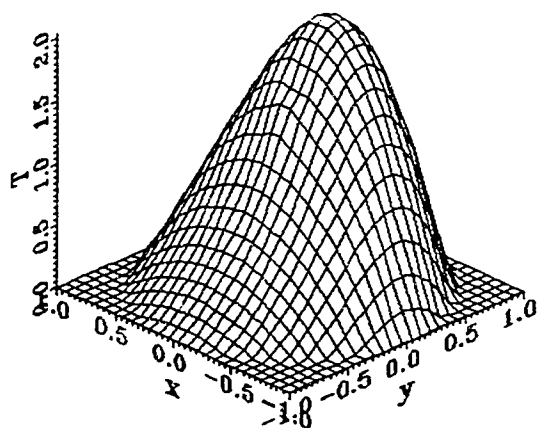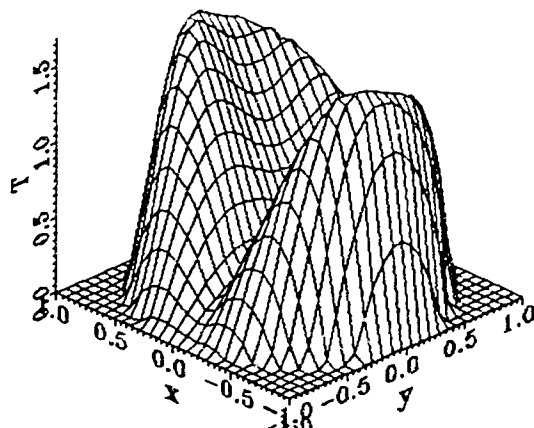
f. Dn=200, Pr=5, λ=0.01, γ=0.01

Fig. 5.35. Developed temperature distributions for various Dn and Pr when the curvature ratio λ and the torsion η are small.
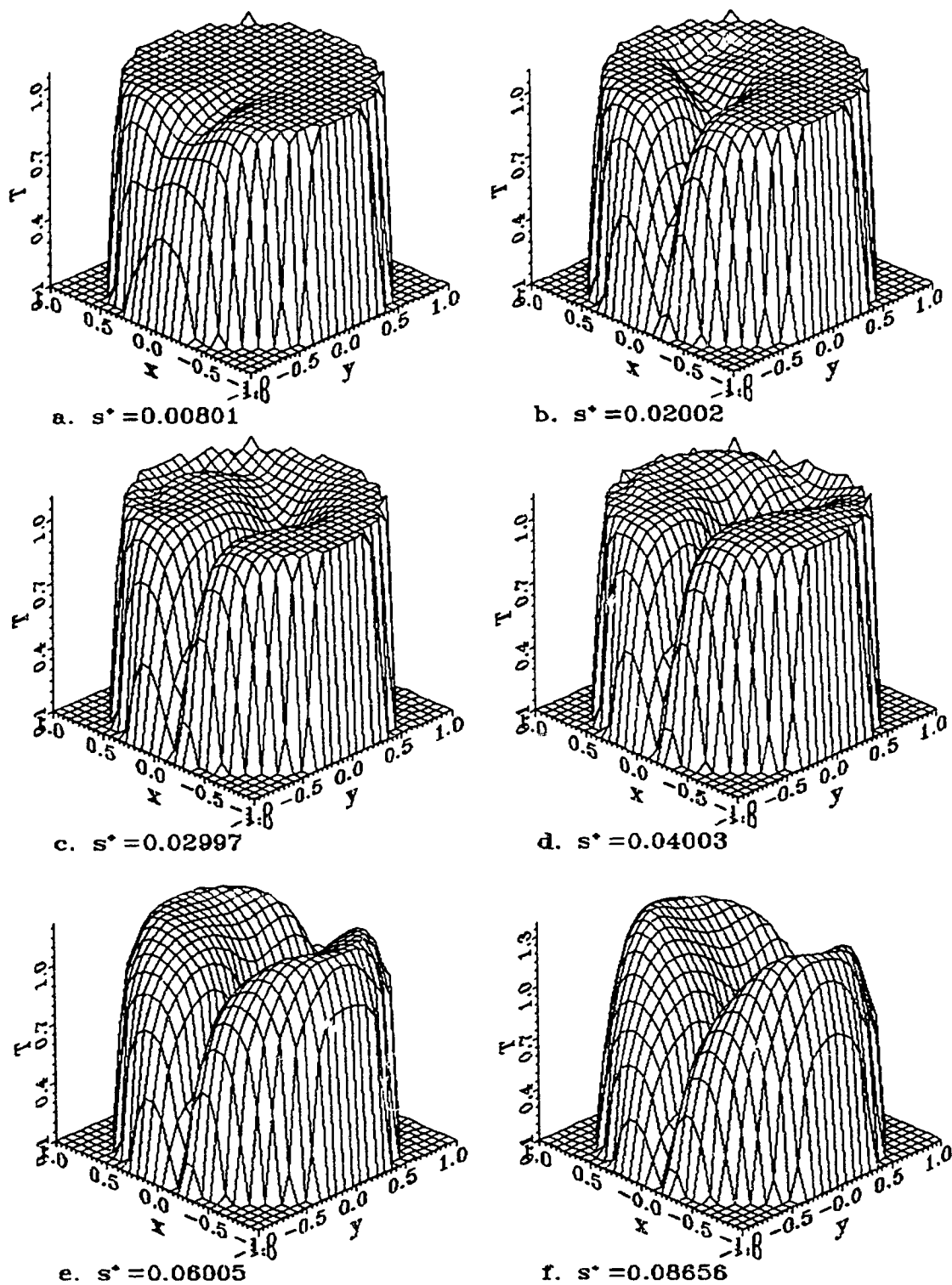
Fig. 5.36. Temperature profile development for Dn = 200, Pr = 500, $\lambda = 0.01$, $\gamma = 0.02$, $\eta = 0.02828$. Parabolic axial velocity entry.

a. s* =0.00801

b. s* =0.01006

c. s* =0.02002

d. s* =0.02997

e. s* =0.04003

f. s* =0.08656

Fig. 5.37. Temperature profile development for $Dn = 200$, $Pr = 5$, $\lambda = 0.01$, $\gamma = 0.02$, $\eta = 0.02828$. Parabolic axial velocity entry.
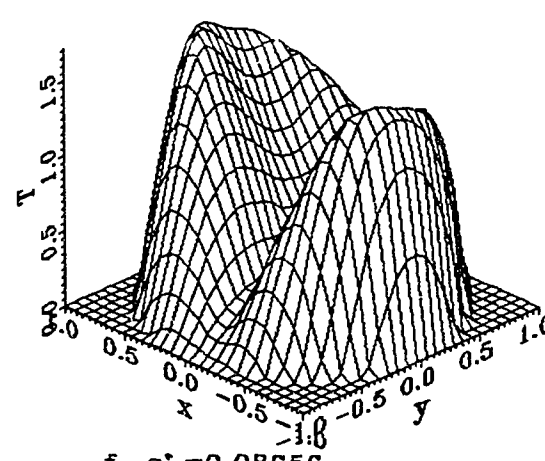
Fig. 5.38.   Temperature profile development for Dn = 200, Pr = 5, λ
γ = 0.02, η = 0.02828. Uniform axial velocity entry.

$$LNu = s^+ |Nu - (Nu)_{fd}| \leq 0.01 \ (Nu)_{fd} \tag{5-48}$$

The computed values of the fully—developed fRe and Nu and the developing lengths are listed in Table 5.1 for the case of the helical flow with a uniform axi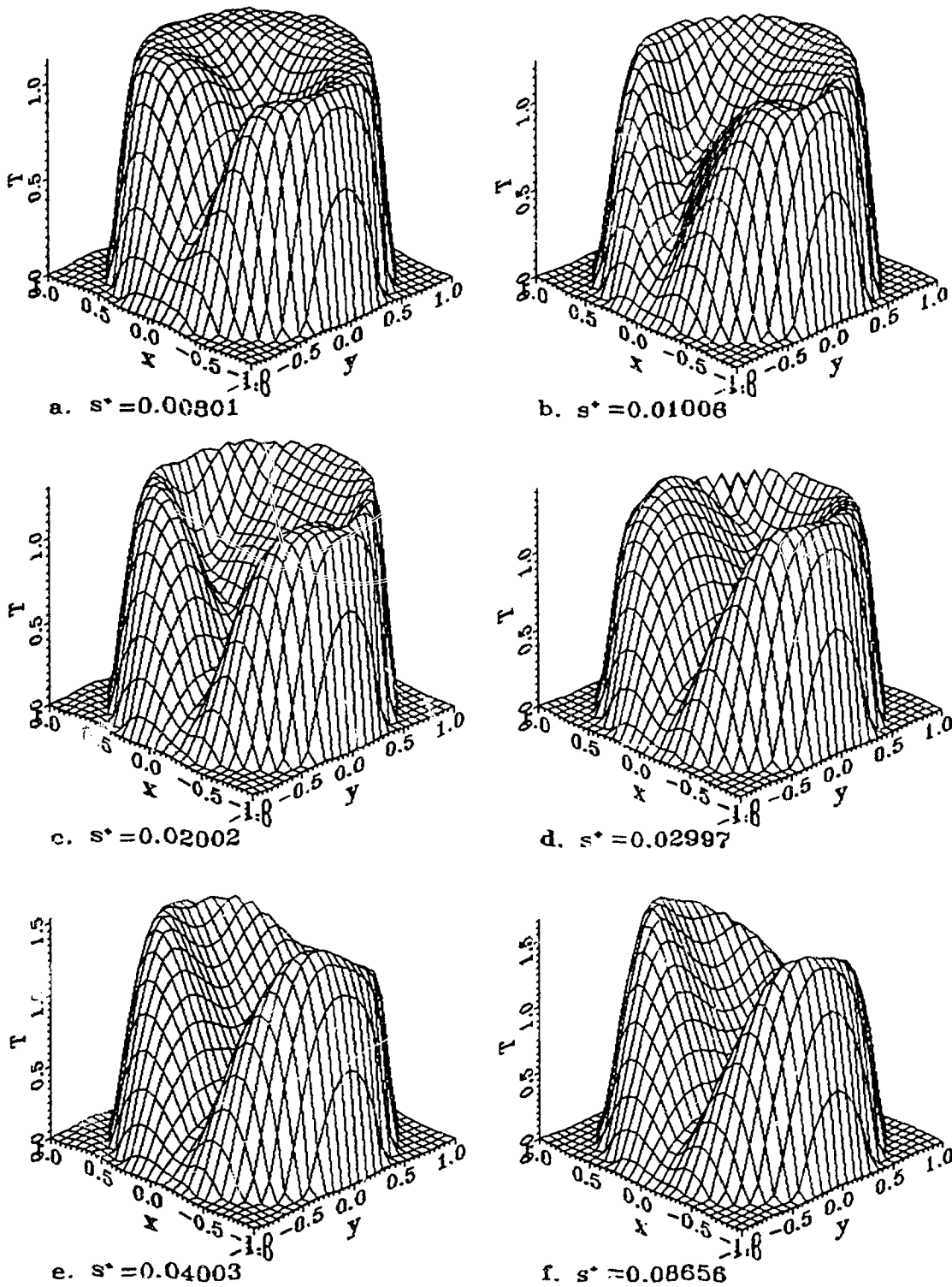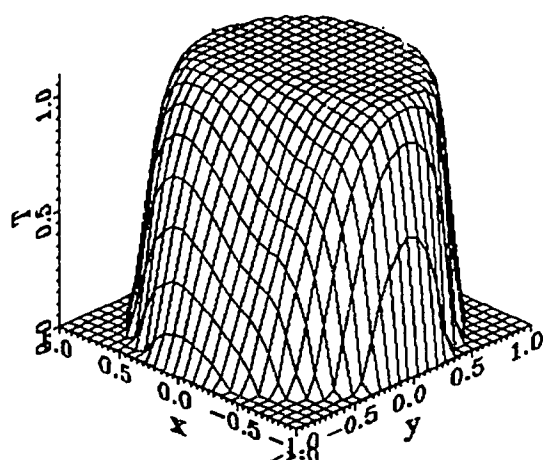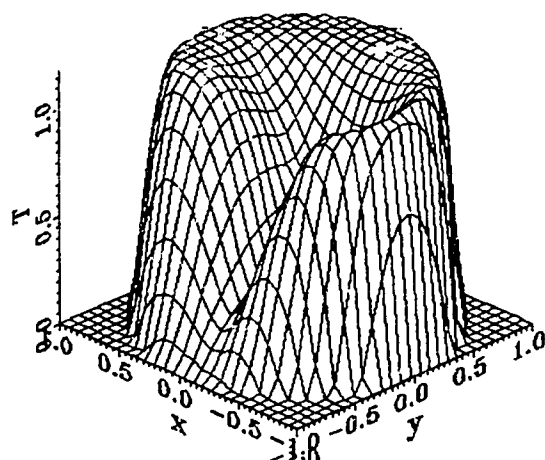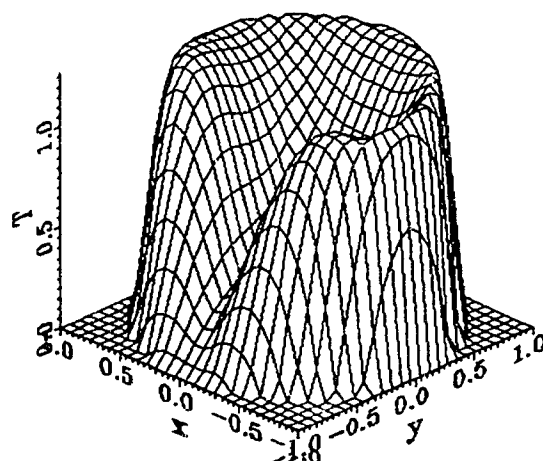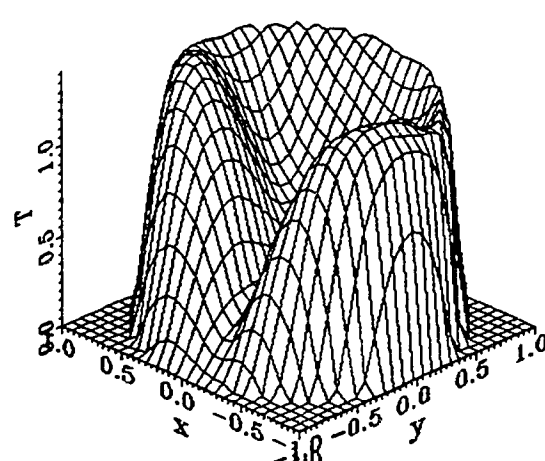al velocity entry. The fully—developed values are listed without the fd subscript. The use in equations (5—46) to (5—48) of the subscript fd is only for the purpose of avoiding confusion with the local values.

From Table 5.1, we can observe that the developing lengths vary slightly with the curvature ratio. However, Lu does not comply with the findings of Yao & Berger (1975) where a strong variation in Lu with λ was presented for a torus. The developing lengths vary with the torsion η. When the torsion is small, $\eta \leq \lambda$, the developing lengths are relatively constant against a change in η. When η increases, the developing lengths increase. Owing to the lack of data on the variation of λ and η, we correlated our computed developing lengths by neglecting the effect of λ and η for $\eta \leq \lambda$ pipes. From equations (5—35) to (5—39) and (5—43), we realize that the hydrodynamic developing lengths are functions of Dn only when the effects of λ and η are neglected. This is in agreement with Yao & Berger (1975). The thermal developing length is a function of both Dn and Pr. The results in Table 5.1 can be best represented for $0.01 \leq \lambda \leq 0.25$, $\gamma \leq 0.1$ and $22 \leq Dn \leq 5000$, by

$$Lu = \frac{0.056 + 0.0120 \ Dn^{1/4}}{1 + 0.0122 \ Dn} \tag{5-49}$$

$$Lp = 0.06 \ (1 + 0.05 \ Dn)^{-0.6} \tag{5-50}$$

and for $0.1 \leq Pr \leq 500$, $0.01 \leq \lambda < 0.15$, $\gamma \leq 0.1$ and $22 \leq Dn \leq 5000$

$$LNu = \frac{0.155 + 0.00604 \ Dn^{\frac{1}{2}} Pr^{\frac{1}{4}}}{1 + 0.0122 \ PrDn} \ Pr \tag{5-51}$$

Table 5.1. Developing lengths and fully developed flow fRe and Nu with uniform axial velocity entry.

Dn	λ	η	fRe	Lp	Lu	Pr(Nu, LNu)
21.86	.0244	0	16.92	.0388	.0659	$\{$ .707(4.012,.0803), 34(8.455,.776) 460(14.80,1.07)
91.47	.1429	0	24.17	.0200	.0416	$\{$ .1(4.590,.0275), 5(10.15,.109) 80(15.52,.362)
100	.1	0	24.53	.021	.0391	1(8.694,.0522)
100	.1	.05	24.60	.0188	.0405	1(8.688,.0513)
100	.1	.1	24.73	.0130	.0428	1(8.675,.0470)
100	.1	.15	24.93	.0130	.0457	1(8.651,.0412)
182.9	.1429	0	30.47	.0152	.0300	.1(5.186,.0224), 5(14.02,.0746)
200	.01	.0141	30.12	.0158	.0300	.1(5.224,.0215), 5(14.35,.0691)
200	.01	.0283	30.20	.0172	.0303	.1(5.260,.0235), 5(14.38,.0691)
200	.01	.2828	17.66	.0550	.0468	.1(3.738,.0343), 5(4.569,.1088)
200	.01	.3535	16.90	.0620	.0602	$\{$ .707(3.744,.0422), 2(3.923,.0868) 500(7.189,.391)
200	.1	0	31.12	.0138	.0305	1(12.27,.0399), 100(25.50,.0905)
200	.1	.05	31.20	.0138	.0326	1(12.03,.0398), 100(27.80,.0950)
200	.1	.1	31.41	.0148	.0326	1(12.30,.0390), 100(28.04,.102)
200	.1	.15	31.76	.0236	.0349	1(12.29,.0380), 100(25.52,.105)
200	.1	.2	32.22	.0261	0417	1(12.32,.0376)
200	.1	.3	33.36	.0293	.0545	1(12.30,.0398)
312.3	.0244	0	35.92	.0105	.0235	$\{$ .707(14.57,.0328), 34(22.33,.123) 460(30.25,.214)
643	.1429	0	49.96	.0071	.0118	$\{$ .1(6.910,.0154), 2(23.00,.034) 5(24.67,.0482)
680.3	.1429	0	51.33	.0071	.0101	$\{$ .707(20.12, .0276), 4(25.15,.0342) 10(27.00,.0527)
721.7	.0833	0	51.42	.0063	.0106	$\{$ .707(21.87,.0269), 43(30.61,.0883) 500(50.18,.1294)
2000	.25	.0200	85.85	.0052	.0054	
2000	.1	.02	81.45	.0044	.0051	$\{$ .1(11.26,.0112), 1(37.74,.0186) 100(63.88,.0485)
5000	.1	.02	124.4	.0021	.0024	$\{$ .1(20.25,.0115), 2(62.85,.0137) 500(122.9,.0358)

The thermal entrance length correlation, equation (5–51), is within the bound of that of Janssen & Hoogendoorn (1978). Janssen & Hoogendoorn's correlation is shown as LNu', where

$$LNu' \le 20 \; Pr^{0.2}/Dn \qquad (5–52)$$

Equation (5–52) is not very accurate in estimating the thermal entrance length. It is only a bound estimate.

To compare the developing lengths of the flow with a parabolic axial velocity entry, we presented some of our results in Table 5.2. It can be seen that the developing lengths are not very different from that of the uniform axial velocity entry case. Comparing Table 5.2 with Table 5.1, we observe that L_u for the parabolic axial velocity entry is slightly shorter than that of the uniform axial velocity entry. L_p for the parabolic axial velocity entry is slightly longer than L_p of the uniform axial velocity entry. LNu for small Pr is shorter, while for large Pr is longer, than LNu of the uniform axial velocity entry.

From Tables 5.1 and 5.2, we observe that the entrance lengths increase with increasing torsion η. When the flow is a one—vortex flow type $(\gamma > 0.2)$, the entrance lengths are similar to those of a straight pipe problem.

Table 5.2. Developing length and fully developed flow fRe and Nu with a parabolic axial velocity entry.

Dn	λ	η	fRe	Lp	L_u	Pr(Nu, LNu)
200	.01	.0141	30.12	.0177	.0253	.1(5.224,.0248), 5(14.35,.0747)
200	.01	.0283	30.20	.0173	.0293	.1(5.260,.0193), 5(14.38,.0741)
200	.01	.2828	17.66	.0483	.0420	.1(3.738,.0294), 5(4.569,.113)
200	.01	.3535	16.90	.0390	.0295	$\{\begin{matrix} .1(3.679,.0232),\ 5(4.276,.161) \\ 500(7.189,.417) \end{matrix}$

For the parabolic axial velocity entry, Austin & Seader (1974) correlated their experimental developing length in a torus. Their correlation is given by

$$Lu = \frac{49\pi}{360} Dn^{-2/3}\lambda^{-1/6}$$

(5—53)

Here, the present notations are used.

From the Lu values of Table 2 for small η cases, we find that our results agree well with the experimental results of Austin & Seader (1974) within about 5%. However, we should point out that equation (5—53) should be re—examined since when $\lambda \to 0$, equation (53) does not reduce to $Lu \sim f(Dn)$.

The fully—developed fRe correlation is consistent with our early study given in Chapter 4 (or Liu & Masliyah 1992c). For $\gamma < 0.1$ or $\eta < 0.1 \sqrt{\lambda Dn}$, it can be represented by

$$fRe = [1 + \frac{(0.0908+0.0233\lambda^{\frac{1}{2}})Dn^{\frac{1}{2}}-0.132\lambda^{\frac{1}{2}}+0.37\lambda+\lambda^2\eta^2-0.2}{1 + 49/Dn}] \cdot$$
$$[16 + (0.378 Dn^{\frac{1}{2}} \lambda^{-\frac{1}{4}} + 12.1 Dn^{-\frac{1}{2}}\lambda^{-\frac{1}{2}})\eta^2]$$

(5—54)

When the torsion is increased but η is small, fRe increases, as shown in Tables 5.1 and 5.2. We also observe that when the torsion effect is significant, fRe decreases with the torsion η and reduces to 16, i.e., a value corresponding to the Poiseuille flow.

For small torsion, $\eta \leq \lambda$, we find our predicted Nu is in agreement with the correlation, Nu$'$, of Manlapaz & Churchill (1981) for $80 < Dn < 400$ and large Pr cases. The correlation due to Manlapaz & Churchill (1981) is given by:

$$Nu' = \left\{1.158(\frac{PrDn}{Pr+0.477})^{3/2} + \left[3.657+4.343(1+\frac{957}{Dn^2Pr})^{-2}\right]^3\right\}^{1/3}$$

(5—55)

The Nu values obtained from this study are substantially lower than that predicted from equation (5—55) for small Pr cases. For $Dn = 200$, $Pr = 0.1$,

equation (5–55) over—predicts by 50%. When Dn is small, the equation (5–55) predicts very poorly as well. For example, at Dn $= 21.86$ and Pr $= 460$, equation (5–55) under—predicts by 75%. However, our results are consistent with those of Akiyama & Cheng (1972), Tarbell & Samuels (1973) and Kalb & Seader (1974). In the range of $21.86 \leq Dn \leq 5000$, $0.1 \leq Pr \leq 500$ and $\eta \leq \lambda < 0.15$, our results can be represented by the following equation.

$$Nu = 3.657 + \frac{(0.75 \ Dn^{\frac{1}{2}} + 0.0028 \ Pr) \ Pr^{1/8}}{(1 + 0.00174 \ Pr^{-3})(1 + 70.6 \ Pr^{-0.6}/Dn)} \qquad (5\text{--}56)$$

When the torsion is increased but remains small, Tables 5.1 and 5.2 show that the fully developed (asymptotic) Nusselt number increases. When the torsion effect is significant, i.e., γ is large, the asymptotic Nusselt number Nu decreases with increasing torsion. Nu values tend to a limit which corresponds to that of the heat transfer under Poiseuille flow conditions.

5.5. Conclusions

Simultaneous developing laminar flow and forced convective heat transfer in a helical pipe of a finite pitch was formulated. Through the loose coiling analysis, we were able to establish some confidence for the parabolization approach. The numerical simulations using the parabolized formulation show good agreement for the axial shear rate, axial velocity and Nusselt number developments for the limiting case of a torus. The developing lengths are correlated with Pr and Dn when the effect of λ and η can neglected. The fully—developed fRe and Nu are found to be in good agreement with published data. A design equation for fully—developed Nusselt number is presented.

When torsion increases, the friction factor, asymptotic Nusselt number and entrance lengths increase. When the torsion is dominant, all the flow and heat transfer properties tend to the limits corresponding to a Poiseuille flow. That is, at large η, an increase in η leads to a decrease in the friction factor and the asymptotic Nusselt number and an increase in the entrance lengths. However, the hydrodynamic entrance lengths of parabolic axial velocity entry decrease with increasing torsion.

References

Agrawal Y., Talbot L. and Gong K., "Laser anemometer study of flow development in curved circular pipes", *J. Fluid Mech.*, 85, 497–518(1978).

Akiyama M. and Cheng K.C., "Laminar forced convection in the thermal entrance region of curved pipes with uniform wall temperature", *Can. J. Chem. Eng.*, 52, 234–240(1974a).

Akiyama M. and Cheng K.C., "Laminar forced convection heat transfer in curved pipes with uniform wall temperature", *Int. J. Heat Mass Transfer*, 15, 1426–1431(1972).

Akiyama M. and Cheng K.C., "Graetz problem in curved pipes with uniform wall heat flux", *Appl. Sci. Res.*, 29, 401–418(1974b).

Austin L.R. and Seader J.D., "Entry region for steady viscous flow in coiled circular pipes", *AIChE J.*, 20, 820–822(1974).

Balejova M., Cakrt J. and Mik V., "Heat transfer for laminar flow in curved pipes with uniform wall heat flux", *Acta Technica Csav*, 22, 183–194(1977).

Bara B.M., "Experimental investigation of developing and fully developed flow in a curved duct of square cross section", PhD dissertation, University of Alberta, 1991.

Bara B., Nandakumar K. and Masliyah J.H., "Experimental investigation of developing and fully developed flow in a curved duct of square cross section", to appear in *J. Fluid Mech.*

Berger S.A., "Flow and heat transfer in curved pipes and tubes", AIAA 91–0030, 1991.

Berger S.A., Talbot L. and Yao L.S., "Flow in curved pipes", *Ann. Rev. Fluid Mech.*, 15, 461–512(1983).

Cheng K.C. and Mok S.Y., "Flow visualization studies on secondary flow patterns

and centrifugal instability phenomena in curved tubes", in: *Fluid Control Measurement*, Vol. 2, ed. M. Harada, p.756–773, Pergamom, Oxford, 1986.

Cheng K.C. and Yuen F.P., "Flow visualization studies on secondary flow patterns in straight tubes downstream of a 180 deg bend and in isothermally heated horizontal tubes", *J. Heat Transfer*, **109**, 49–54(1987).

Choi U.S., Talbot L. and Cornet I., "Experimental study of wall shear rates in the entry region of a curved tube", *J. Fluid Mech.*, **93**, 465–489(1979)

Dravid A.N., Smith K.A., Merrill E.W. and Brian P.L.T., "Effect of secondary fluid motion on laminar flow heat transfer in helically coiled tubes", *AIChE J.*, **17**, 1114–1122(1971).

Germano M., "On the effect of the torsion in a helical pipe flow", *J. Fluid Mech.*, **125**, 1–8(1982).

Germano M., "The Dean equations extended to a helical pipe flow", *J. Fluid Mech.*, **203**, 289–305(1989).

Humphrey J.A.C., "Numerical calculation of developing laminar flow in pipes of arbitrary curvature radius", *Can.J. Chem. Eng.*, **56**, 151–164(1978)

Humphrey J.A.C., Iacovides H. and Launder B.E., "Some numerical experiments on developing laminar flow in circular–sectioned bends", *J. Fluid Mech.*, **154**, 357–375(1985).

Ito H., "Flow in curved pipes", *JSME Int. J.*, **30**(262), 543–552(1987).

Janssen L.A. and Hoogendoorn C.J., "Laminar convective heat transfer in helical coiled tubes", *Int. J. Heat Mass Transfer*, **21**, 1197–1206(1978).

Kalb C.E. and Seader J.D., "Fully–developed viscous–flow heat transfer in curved circular tubes with uniform wall temperature", *AIChE J.*, **20**, 340–346(1974).

Kao H.C., "Torsion effect on fully developed flow in a helical pipe", *J. Fluid Mech.*, **184**, 335–356(1987).

Kluwick A. and Wohlfahrt H., "Hot—wire—anemometer study of the entry flow in a curved duct", *J. Fluid Mech.*, 165, 335–353(1986).

Liu S. and Masliyah J.H., "A decoupling numerical method for fluid flows", submitted to *Int. J. Numer. Methods Fluids*.

Liu S. and Masliyah J.H., "Axially—invariant laminar flow in helical pipes with a finite pitch, part 1. theory and loosely coiled pipes", submitted to *J. Fluid Mech.*

Liu S. and Masliyah J.H., "Axially—invariant laminar flow in helical pipes with a finite pitch, part 2. curvature and torsion effects", submitted to *J. Fluid Mech.*

Manlapaz R. and Churchill S.W., "Fully developed laminar convection from a helical coil", *Chem. Eng. Commun.*, 9, 185–200(1981)

Murata S., Miyake Y., Inaba T. and Ogata H., "Laminar flow in a helically coiled pipe", *Bull. JSME*, 24, 355–362(1981).

Nandakumar K. and Masliyah J.H., "Swirling flow and heat transfer in coiled and twisted pipes", in Mujumdar A.S. and Mashelkar R.A. ed., *Advances in Transport Processes*, IV, Wiley Eastern Ltd., New Delhi, 1986.

Patankar S.V., Pratap V.S. and Spalding D.B., "Prediction of laminar flow and heat transfer in helically coiled pipes", *J. Fluid Mech.*, 62, 539–551(1974).

Sankar S.R., Nandakumar K. and Masliyah J.H., "Oscillatory flows in coiled square ducts", *Physics of Fluids*, 31(6), 1348–1358(1988).

Singh M.P., "Entry flow in a curved pipe", *J. Fluid Mech.*, 65, 517–539(1974).

Soh W.Y. and Berger S.A., "Laminar entrance flow in a curved pipe", *J. Fluid Mech.*, 148, 109–135(1984).

Smith F.T., "Fluid flow into a curved pipe", *Proc. R. Soc. London*, A351, 71–87(1976).

Stewartson K., Cebecei and Chang K.C., "A boundary—layer collision in a curved duct", *Q. J. Mech. Appl. Math.*, **33**, 59—75(1980).

Tarbell J.M. and Samuels M.R., "Momentum and heat transfer in helical coils", *Chem. Eng. J.*, **5**, 117—127(1973).

Talbot L. and Wong S.J., "A note on boundary—layer collision in a curved pipe", *J. Fluid Mech.*, **122**, 505—510(1982).

Yao L.S. and Berger S.A., "Entry flow in a curved pipe", *J. Fluid Mech.*, **67**, 177—196(1975).

Yao L.S. and Berger S.A., "The three—dimensional boundary layer in the entry region of curved pipes with finite curvature ratio", *Physics of Fluids.*, **31**, 486—494(1988).

Chapter 6
General Conclusions and Discussions

6.1. Numerical Method

In Chapter 2, a robust first order non—conforming numerical method for fluid flow with 3—point exponential interpolation was developed. The method employs the separation of a multi—dimensional problem into multiple one—dimensional subproblems that are assembled to form the solution. The resulting algebraic equations are solved iteratively with a tri—diagonal solver. The velocity and pressure are decoupled at each iteration through the pressure perturbation (or pressure correction). The inf—sup condition is satisfied by mesh staggering and velocity—pressure interpolation strategies.

The accuracy of the traditional upwind and exponentially weighted schemes were analyzed and were compared with the proposed scheme for both interpolation and consistency. It is found that the proposed three—point exponential interpolation together with the multi—dimensional separation strategy render a guaranteed first order convergence. The use of the traditional exponential or upwind schemes render such schemes less than first order accurate. The three—point exponential interpolation employs a physical velocity (length) scale to satisfy the V_0—coerciveness of the nonlinear terms.

A two—dimensional direct solver was developed with minimum storage requirement (less than a band solver) and with a partial inversion strategy.

The computational results of the laminar fluid flow in a torus and a square cavity show good agreement with the literature. The flexibility in the mesh distribution makes the proposed scheme competitive. It is shown that the use of exponential functions increases the overall computational time by about 2% for a simple problem of the square driven cavity. The convergence rate of the proposed 3—point exponential scheme is very much the same as that of traditional 2—point upwind or 2—point exponentially weighted scheme.

Future work is needed to implement the exponential type interpolation function in the finite element method. Investigations are needed to relate the stability of a flow solution to the numerical convergence of certain discretization.

6.2. Fully Developed Flow in Helical Pipes of Finite Pitch

In Chapters 3 and 4, fully developed laminar Newtonian flows in helical pipes of a constant circular cross–section with a finite pitch are formulated and numerically studied by the Separation Method. The governing flow equations are constructed from orthogonal helical coordinates. They are used to obtain a loose coiling approximation with two dominant parameters, Dean number, $Dn = Re \, \lambda^{\frac{1}{2}}$, with Reynolds number Re and curvature ratio λ, and Germano number, $Gn = Re \, \eta$, with η being the torsion. The importance of the Germano number is investigated. For high Dean number flows, a new helical flow group evolves, namely, $\gamma = Gn \cdot Dn^{-3/2} = \eta \cdot (\lambda Dn)^{-\frac{1}{2}}$. For very small Dn flows, the counterpart of γ is defined by $\gamma^* = Gn \cdot Dn^{-2} = \eta/(\lambda Re)$. It is further shown that under the loose coiling conditions and negligible Germano number: $\lambda \to 0$, $\gamma \to 0$, and $Re > O(\lambda^{-\frac{1}{2}})$, the helical flow problem reduces to the Dean problem. These qualitative theoretical results are further enhanced by numerical simulations.

It is found that the friction factor and the axial velocity profiles are almost invariant with varying λ and η when the conditions of $Dn = constant$, $Re > O(\lambda^{-\frac{1}{2}})$, $\gamma \leq 0.01$ and most importantly $\lambda \to 0$ are satisfied. A helical flow may be simplified by a toroidal flow if $\gamma \leq 0.01$. As λ changes with the above conditions being held, the cross–plane pressure and the secondary flow stream function (so do the secondary velocities) are proportional to $\lambda^{\frac{1}{2}}$ or Re^{-1} with the contour shapes holding remarkably unchanged. When $\gamma > 0.01$, the flow preserves its pattern and becomes independent of λ and η as long as $\lambda \to 0$ and $\eta \to 0$.

For a given helical pipe, i.e., Rc and H being fixed, the flow field consists of a swirl–like pattern for very small Dn when $\gamma^* > 0.039$ and is a torus–like secondary flow pattern for large Dn when $\gamma < 0.2$.

The center region on the cross–plane of the pipe has a relatively flat axial

velocity profile for large Dn. The flat area becomes broader as Dn increases. The flow field changes more sharply near the wall as Dn increases.

For a given Dn and Rc, the helical flow changes from a torus–like flow to a distorted torus–like flow when the pitch is increased. As $H \to \infty$, the flow patterns tend to stay unchanged with respect to H. For a fixed large H and Dn, the helical flow is more distorted at smaller Rc and changes to a torus–like flow pattern as Rc increases. For helical flow to behave torus–like, it is not necessary to require Rc being greater than H as long as $\gamma \leq 0.01$ condition is met at large Dn flows.

The friction factor varies linearly with curvature for small Dn flows and $fRe \propto \lambda^{\frac{1}{2}}$ for large Dn flows. For $\lambda > 0.2$, the torsion effect on the helical flow consists of more distortion with increasing λ and/or Dn.

The friction factor increases with increasing torsion when γ is small, especially for large Dean number and large λ. When γ is large, the friction factor decreases sharply towards the value of a straight pipe Poiseuille flow as γ increases. The friction factor reaches a maximum at $\gamma \simeq 0.1$ for moderate λ and Dn flows. But for small Dn and/or small λ, the increase of the friction factor with γ is not apparent. Here, the distortion effect of the torsion on the flow field is minimal.

For large λ and large Dn flows, the flow field rotates and distorts as γ increases. This is due to the significance of the terms $\lambda\eta$ and $\lambda^2\eta$ in the governing equations. The maximum axial velocity increases as the torsion increases with its location moving along a curve looking like a half heart starting from the outer–half of the y–axis and a projected end at the center of the pipe.

The secondary flow strength behaves somewhat similar to the friction factor when γ is increased. However, in the limit of large γ for a given Dean number, the secondary flow strength does not reduce to zero (Poiseuille flow). Rather, the secondary flow strength tends to a fixed non–zero value when γ is increased.

When viewing in the orthogonal coordinate system, the secondary flow is

generally of two—vortex pattern with sources and sinks except at $\gamma \simeq 0.18$, it is of nearly one vortex pattern with a very small vortex at the inner upper wall area. When γ is small, the two vortices are in a up—and—down position. When γ is large, the two vortices are left—and—right. Strong sources and sinks exist in the secondary flow. In the limit of large γ, a clear source near the inner bottom wall and a clear sink near the outer upper wall can be observed.

For a given main flow strength, i.e., fixed Re, the helical flow changes from a toroidal flow at zero pitch to a Poiseuille—like flow as $H \rightarrow \infty$.

The stability of the flow downstream in the pipe is studied using axially parabolized three—dimensional Navier—Stokes equations written in the orthogonal helical coordinates. Four—vortex solutions have been found from the numerical experimentation. When $\gamma < 0.01$ and Dn > 130, a four—vortex solution can be observed by disturbing the flow field at the outer half of the y—axis. The four—vortex solutions disappeared when a fine enough mesh is used.

A correlation for the friction factor is developed based on the numerical solutions of more than 250 cases. Accounted are all the controlling parameters Dn, λ and γ. The friction factors in the limit of $\lambda \rightarrow 0$ and $\eta \rightarrow 0$ are in good agreement with previous experimental and numerical observations of $fRe \sim Dn^{\frac{1}{2}}$.

Future work on developed flows in helical pipes is needed both theoretically and experimentally. Theoretically, closed form solutions for large Dn flows should be attempted by including Dn, λ and η. Numerical analysis is welcome for stability analysis and solutions for a wider range of combined effects of Dn, λ and γ. The characterization of the flow pattern needs to be made for a wider Dean number, λ and γ range. More numerical analysis for the turbulent and transition flow is also required to gain insight into helical flows. Experimental work is needed in all aspects of flow in helical pipes of finite pitch and for the limiting case of a large torsion to compare with numerical results.

6.3. Developing Laminar Flow of Incompressible Newtonian Fluid in Helical Pipes

A more general version of loose coiling analysis is used in Chapter 5 to show further the parabolization of the governing equations (momentum and energy). The characteristic length in axial direction evolves from the loose coiling approximation.

The computed axial velocity and axial shear rates are found in good agreement with the published data. The axial shear rate does show a sharp decrease upon entry into a helical pipe from a large reservoir, but it does not vanish, nor does it dip lower than that of its fully—developed value. The maximum axial wall shear rates cross over from the inner wall to the outer wall when γ is small.

The developing flow from a parabolic axial velocity entry is smooth as compared with the uniform axial velocity entry. The developing lengths are, however, very much the same as those corresponding to uniform axial velocity entry flows.

The entrance length measured by the axial pressure gradient is shorter than that measured by the center line axial velocity. Correlations are given for the hydrodynamic developing lengths.

More investigation is needed, especially, for the solution of the full elliptic Navier—Stokes equations to model the developing flows in large curvature pipes. Closed form solutions for large Dn flows as an extension of the type given by Van Dyke is surely a challenge. Experimental work is welcome for helical pipes of finite pitch. More accurate measurements for the axial velocity and axial wall shear rate will be useful to compare with the theoretical analysis.

6.4. Developing Laminar Forced Convective Heat Transfer in Helical Pipes of Finite Pitch

The developing laminar forced convective heat transfer of an incompressible Newtonian fluid having a uniform constant wall temperature with a simultaneous developing flow was studied in Chapter 5. The heat transfer Nusselt number is found to be oscillatory. For a torus, the developing and fully—developed (asymptotic) peripherally averaged Nusselt numbers are in good agreement with the published experimental and numerical results.

For a uniform axial velocity entry, the local maximum Nusselt numbers also cross over from the inner wall to the outer wall, but at a distance much shorter than the crossover of the axial wall shear rates. The crossover occurs closer to the inlet for higher Prandtl number fluid flows. The Nusselt numbers appear to have a deeper "valley" prior to a higher "peak" for higher Prandtl number and higher Dean number flows.

For a parabolic axial velocity entry, the development of the Nusselt number becomes relatively smooth and the magnitude of the oscillation is much lower than that for a uniform axial velocity entry.

For two—vortex ($\gamma < 0.2$) high Dean number and high Prandtl number flows, the local temperature profile has much lower values near the vortex dividing line. However, the maximum Nusselt number (so does the temperature gradient) still occurs at the outer wall and the vortex dividing line intersection. For a one—vortex flow, the temperature distribution is convex (i.e. no local minimum). When the torsion effect is dominant, the thermal developing length increases with the torsion and the asymptotic Nusselt number tends towards the limit of a straight pipe.

The thermal entrance length and asymptotic Nusselt number are correlated for $21.86 \leq \mathrm{Dn} \leq 5000$, $\eta \leq \lambda \leq 0.15$ and $0.1 \leq \mathrm{Pr} \leq 500$.

Future numerical work should be conducted to investigate the influence of λ and η in large curvature pipes. Both developing and fully—developed heat transfer studies would be welcome for flow in helical pipe of finite pitch. Close form solution should also be attempted for large Dn flows.

Free convection and combined convection in helical pipes of finite pitch received little attention. It would be interesting to study the combined convection in helical pipe.

Appendix

Derivation of the Orthogonal Helical Coordinate System

A.I. The Reference System

A helical system can be established in reference to the master cartesian coordinate system $\vec{x}'$ (x_1', x_2', x_3') and the local vectors originated on the generic curve of the helix as follows:

$$\vec{R} = (Rc \cos\varphi, Rc \sin\varphi, B\, s) \tag{A-1}$$

$$\vec{T} = \frac{d\vec{R}}{ds} = (-\sqrt{\kappa Rc} \sin\varphi, \sqrt{\kappa Rc} \cos\varphi, B) \tag{A-2}$$

$$\vec{N} = \frac{1}{\kappa} \frac{d\vec{T}}{ds} = (-\cos\varphi, -\sin\varphi, 0) \tag{A-3}$$

$$\vec{B} = \vec{T} \times \vec{N} = (B \sin\varphi, -B \cos\varphi, \sqrt{\kappa Rc}) \tag{A-4}$$

$$\kappa = \frac{Rc}{Rc^2 + (H/2\pi)^2} \tag{A-5}$$

$$\tau = \frac{(H/2\pi)}{Rc^2 + (H/2\pi)^2} \tag{A-6}$$

$$B = \sqrt{\tau H/(2\pi)} \tag{A-7}$$

$$\varphi = \sqrt{\kappa/Rc}\; s \tag{A-8}$$

Where $\vec{R}$ is the global coordinate vector of the point O on the generic curve; the generic curve is the track of a particle moving along the center of the cross section of the helical pipe; $\vec{T}$ (or $\vec{s}$), $\vec{N}$ and $\vec{B}$ are the tangential, normal and binormal to the generic curve at O respectively; s is the curve length parameter along the generic curve; κ and τ are the curvature and torsion at O respectively; Rc and H are the radius of coil and the pitch for the helix respectively. The orthogonality of a helical system can be achieved by rotating the basis formed by $\vec{B}$ and $\vec{N}$ around the s axis.

A schematic figure showing the coordinate system is presented in Figure A.1. (x_0, y_0, s) represents a set of orthogonal rectangular helical coordinates. (r, θ', s) is a set of orthogonal polar helical coordinates. (x, y, s) and (r, θ, s) are non—orthogonal rectangular and polar coordinates, respectively.
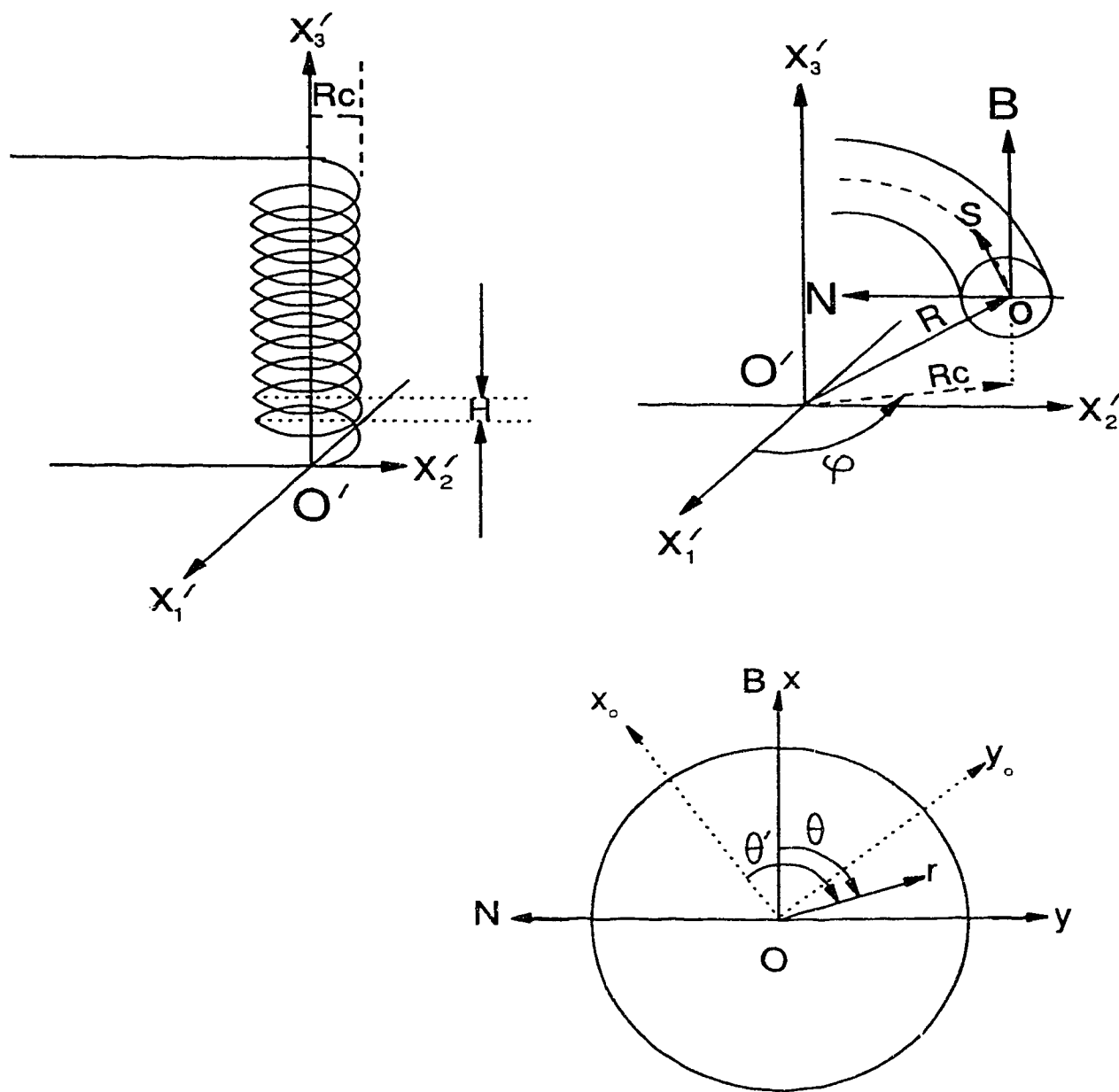

Figure A.1. The helical coordinate system.

A.II. The Metrics for the Circular Helical System

In a circular system, any given point can be mapped to the master cartesian system as follows:

$$\vec{x}' = \vec{R} - r\sin\theta\, \vec{N} + r\cos\theta\, \vec{B} \tag{A-9}$$

The transformation matrix can be represented in the tensor as follows:

$$g_{ij} = \frac{\partial x'_k}{\partial q_i} \cdot \frac{\partial x'_k}{\partial q_j} \tag{A-10}$$

Let $q_1 = s$, $q_2 = r$, $q_3 = \theta'$ and $\theta = \theta' + f(s)$, we can obtain the following transformation matrix coefficients

$$g_{11} = \frac{\partial \vec{x}'}{\partial s} \cdot \frac{\partial \vec{x}'}{\partial s} = (\frac{d\vec{R}}{ds} - r\sin\theta\frac{d\vec{N}}{ds} - r\cos\theta\frac{d\theta}{ds}\vec{N} + r\cos\theta\frac{d\vec{B}}{ds} - r\sin\theta\frac{d\theta}{ds}\vec{B})^2 \tag{A-11}$$

Apply the basic equations of the curve theory

$$\frac{d\vec{N}}{ds} = \tau\vec{B} - \kappa\vec{T} \tag{A-12}$$

and

$$\frac{d\vec{B}}{ds} = -\tau\vec{N} \tag{A-13}$$

The transformation matrix coefficients can be cast out and given by:

$$g_{11} = \frac{\partial \vec{x}'}{\partial s} \cdot \frac{\partial \vec{x}'}{\partial s}$$

$$= [\ \vec{T} - r\sin\theta(\tau\vec{B} - \kappa\vec{T}) - r\cos\theta\frac{d\theta}{ds}\vec{N} - r\cos\theta\tau\vec{N} - r\sin\theta\frac{d\theta}{ds}\vec{B}]^2$$

$$= [(1 + \kappa r\sin\theta)\vec{T} - r\sin\theta(\tau + \frac{d\theta}{ds})\vec{B} - r\cos\theta(\tau + \frac{d\theta}{ds})\vec{N}]^2$$

$$= (1 + \kappa r\sin\theta)^2 + r^2(\tau + \frac{d\theta}{ds})^2 \qquad\qquad \text{(A--14)}$$

$$g_{12} = \frac{\partial \vec{x}'}{\partial s} \cdot \frac{\partial \vec{x}'}{\partial r}$$

$$= -[(1 + \kappa r\sin\theta)\vec{T} - r\sin\theta(\tau + \frac{d\theta}{ds})\vec{B} - r\cos\theta(\tau + \frac{d\theta}{ds})\vec{N}] \cdot (\sin\theta\ \vec{N} - \cos\theta\ \vec{B})$$

$$= -r\sin\theta\cos\theta(\tau + \frac{d\theta}{ds}) + r\sin\theta\cos\theta(\tau + \frac{d\theta}{ds})$$

$$= 0 \qquad\qquad \text{(A--15)}$$

$$g_{13} = \frac{\partial \vec{x}'}{\partial s} \cdot \frac{\partial \vec{x}'}{\partial \theta'}$$

$$= -[(1 + \kappa r\sin\theta)\vec{T} - \quad \tau + \frac{d\theta}{ds})\vec{B} - r\cos\theta(\tau + \frac{d\theta}{ds})\vec{N}] \cdot (r\sin\theta\ \vec{B} + r\cos\theta\ \vec{N})$$

$$= r^2(\tau + \frac{d\theta}{ds}) \qquad\qquad \text{(A--16)}$$

$$g_{22} = \frac{\partial \vec{x}'}{\partial r} \cdot \frac{\partial \vec{x}'}{\partial r}$$

$$= (\cos\theta\ \vec{N} + \sin\theta\ \vec{B})^2$$

$$= 1 \qquad\qquad \text{(A--17)}$$

$$g_{23} = \frac{\partial \vec{x}'}{\partial r} \cdot \frac{\partial \vec{x}'}{\partial \theta'}$$

$$= (\sin\theta \ \vec{N} - \cos\theta \ \vec{B}) \cdot (r\cos\theta \ \vec{N} + r\sin\theta \ \vec{B})$$

$$= 0 \tag{A--18}$$

$$g_{33} = \frac{\partial \vec{x}'}{\partial \theta'} \cdot \frac{\partial \vec{x}'}{\partial \theta'}$$

$$= (r\cos\theta \ \vec{N} + r\sin\theta \ \vec{B})^2$$

$$= r^2 \tag{A--19}$$

By setting

$$0 = g_{13} = r^2(\tau + \frac{d\theta}{ds}) \tag{A--20}$$

one obtains

$$\theta = \theta' - \tau s + \theta_0 \tag{A--21}$$

The transformation of the helical coordinate system defined by (s, r, θ') is orthogonal, i.e., $g_{ij} = 0$ for $i \neq j$. The metrics of the coordinates (s, r, θ'), $h_i = \sqrt{g_{ii}}$, (where ii does not imply summation), can be obtained from the transformation matrix as given by equations (A--14) to (A--19) as follows:

$$\begin{cases} h_1 = 1 + \kappa r\sin(\theta' - \tau s + \theta_0) \\ h_2 = 1 \\ h_3 = r \end{cases} \tag{A--22}$$

For

$$\theta_0 = 0 \tag{A--23}$$

The metrics becomes

$$\begin{cases} h_1 = 1 + \kappa r \sin(\theta' - \tau s) \\ h_2 = 1 \\ h_3 = r \end{cases} \tag{A--24}$$

In terms of the non—orthogonal coordinate system (r, θ, s) but with other dependent and independent variables expressed in the orthogonal coordinate system (r, θ', s), we can write:

$$\begin{cases} h_1 = 1 + \kappa r \sin \theta \\ h_2 = 1 \\ h_3 = r \end{cases} \tag{A--25}$$

$$\vec{x} = \vec{R} - r \sin \theta \, \vec{N} + r \cos \theta \, \vec{B} \tag{A--26}$$

$$\vec{x} = \{\cos\varphi(\text{Rc}+r\sin\theta)+r\text{B}\sin\varphi\cos\theta, \; \sin\varphi(\text{Rc}+r\sin\theta) - r\text{B}\cos\varphi\sin\theta, \; \frac{\text{H}\varphi}{2\pi} + r\sqrt{\kappa\text{Rc}} \, \cos\theta\}$$
$$\tag{A--27}$$

For the limiting cases, we obtain:

Horizontally oriented straight pipe: $\kappa\text{Rc} = 1, \; \varphi = 0, \; \kappa = 0, \; \tau = 0, \; \text{H} = 0;$

Vertically oriented straight pipe: $\text{B} = 1, \; \varphi = 0, \; \kappa = 0, \; \tau = 0, \; \text{Rc} = 0;$

Toroidal pipe: $\tau = 0, \; \text{B} = 0$

This system of coordinates can recover the helical, straight and toroidal pipes.

A.III. The metrics for the rectangular helical system

To establish the rectangular helical coordinates, we choose, again, to rotate the system formed by $\vec{N}$ and $\vec{B}$, that is

$$\vec{x}_0 = \cos\alpha\,\vec{N} + \sin\alpha\,\vec{B} \tag{A-28}$$

$$\vec{y}_0 = -\sin\alpha\,\vec{N} + \cos\alpha\,\vec{B} \tag{A-29}$$

Then, a point of interest can be mapped between the master cartesian coordinate and the helical coordinates by

$$\vec{x}' = \vec{R} + (x\cos\alpha - y\sin\alpha)\,\vec{N} + (x\sin\alpha + y\cos\alpha)\,\vec{B} \tag{A-30}$$

The matrix of transformation can be represented in the following tensor form:

$$g_{ij} = \frac{\partial x'_k}{\partial q_i} \cdot \frac{\partial x'_k}{\partial q_j} \tag{A-31}$$

Let $q_1 = s$, $q_2 = x_0$, $q_3 = y_0$ and $\alpha = \alpha(s)$, we obtain the following coefficients

$$g_{11} = \frac{\partial x'_k}{\partial s} \cdot \frac{\partial x'_k}{\partial s}$$

$$= [\frac{d\vec{R}}{ds} + (x_0\cos\alpha - y_0\sin\alpha)\frac{d\vec{N}}{ds} - (x_0\sin\alpha + y_0\cos\alpha)\frac{d\alpha}{ds}\vec{N} +$$

$$(x_0\sin\alpha + y_0\cos\alpha)\frac{d\vec{B}}{ds} + (x_0\cos\alpha - y_0\sin\alpha)\frac{d\alpha}{ds}\vec{B}]^2 \tag{A-32}$$

Apply the basic equations of the curve theory

$$\frac{d\vec{N}}{ds} = \tau\vec{B} - \kappa\vec{T} \tag{A-33}$$

and

$$\frac{d\vec{B}}{ds} = -\tau\vec{N} \tag{A-34}$$

We can obtain

$$g_{11} = \frac{\partial x'_k}{\partial s} \cdot \frac{\partial x'_k}{\partial s}$$

$$= \{[1 - \kappa(x_0\cos\alpha - y_0\sin\alpha)]\vec{T} + (x_0\cos\alpha - y_0\sin\alpha)(\tau + \frac{d\alpha}{ds})\vec{B} - (x_0\sin\alpha + y_0\cos\alpha)(\frac{d\alpha}{ds} + \tau)\vec{N}\}^2$$

$$= [1 - \kappa(x_0\cos\alpha - y_0\sin\alpha)]^2 + (x_0^2 + y_0^2)(\tau + \frac{d\alpha}{ds})^2 \tag{A-35}$$

$$g_{12} = \frac{\partial x'_k}{\partial s} \cdot \frac{\partial x'_k}{\partial x_0}$$

$$= \{[1 - \kappa(x_0\cos\alpha - y_0\sin\alpha)]\vec{T} + (x_0\cos\alpha - y_0\sin\alpha)(\tau + \frac{d\alpha}{ds})\vec{B} - (x_0\sin\alpha + y_0\cos\alpha)(\frac{d\alpha}{ds} + \tau)\vec{N}\} \cdot (\cos\alpha\,\vec{N} - \sin\alpha\,\vec{B})$$

$$= (\tau + \frac{d\alpha}{ds})y_0 \tag{A-36}$$

$$g_{13} = \frac{\partial x'_k}{\partial s} \cdot \frac{\partial x'_k}{\partial y_0}$$

$$= \{[1 - \kappa(x_0\cos\alpha - y_0\sin\alpha)]\vec{T} + (x_0\cos\alpha - y_0\sin\alpha)(\tau + \frac{d\alpha}{ds})\vec{B} - (x_0\sin\alpha + y_0\cos\alpha)(\frac{d\alpha}{ds} + \tau)\vec{N}\} \cdot (\sin\alpha\,\vec{N} + \cos\alpha\,\vec{B})$$

$$= (\frac{d\alpha}{ds} + \tau)x_0 \tag{A-37}$$

$$g_{22} = \frac{\partial x'_k}{\partial x_0} \cdot \frac{\partial x'_k}{\partial x_0}$$

$$= (\cos\alpha \ \vec{N} - \sin\alpha \ \vec{B})^2$$

$$= 1 \qquad\qquad (A\text{--}38)$$

$$g_{23} = \frac{\partial x'_k}{\partial x_0} \cdot \frac{\partial x'_k}{\partial y_0}$$

$$= (\cos\alpha \ \vec{N} - \sin\alpha \ \vec{B}) \cdot (\sin\alpha \ \vec{N} + \cos\alpha \ \vec{B})$$

$$= 0 \qquad\qquad (A\text{--}39)$$

$$g_{33} = \frac{\partial x'_k}{\partial y_0} \cdot \frac{\partial x'_k}{\partial y_0}$$

$$= (\sin\alpha \ \vec{N} + \cos\alpha \ \vec{B})^2$$

$$= 1 \qquad\qquad (A\text{--}40)$$

Setting

$$0 = (\tau + \frac{d\alpha}{ds}) \qquad\qquad (A\text{--}41)$$

we obtain

$$\alpha = \alpha_0 - \tau s \qquad\qquad (A\text{--}42)$$

The transformation of the rectangular helical coordinate system defined by (s, x_0, y_0) is rendered to be orthogonal by the above choice of rotation along the axis of the tube or generic curve.

The coordinate metrics are

$$\begin{cases} h_1 = 1 - \kappa x \cos(\tau s - \alpha_0) + \kappa y \sin(\tau s - \alpha_0) \\ h_2 = 1 \\ h_3 = 1 \end{cases} \qquad \text{(A--43)}$$

Following the tradition, we take, with a tilted angle of β

$$\alpha_0 = \frac{\pi}{2} - \beta \qquad \text{(A--44)}$$

Denoting

$$\alpha = \beta + \tau s \qquad \text{(A--45)}$$

the metrics become,

$$\begin{cases} h_1 = 1 - \kappa x_0 \sin \alpha + \kappa y_0 \cos \alpha \\ h_2 = 1 \\ h_3 = 1 \end{cases} \qquad \text{(A--46)}$$

At the limiting cases, we obtain:

Horizontally oriented straight pipe: $\kappa Rc = 1, \kappa = 0, \tau = 0, B = 0$;

Vertically oriented straight pipe: $B = 1, \kappa = 0, \tau = 0, Rc = 0$;

Toroidal pipe: $\tau = 0, B = 0$

Hence, this system can recover the helical, straight and toroidal pipes. In case of the toroidal pipe, $\beta = 0$ renders the traditional rotating coordinates.

A.IV. Fluid Flow Equations in a General Orthogonal Coordinate System

Mass balance yields the continuity equation:

$$\frac{D\rho}{Dt} = \frac{\partial \rho}{\partial t} + \nabla \cdot \rho \vec{u} = 0 \qquad (A-47)$$

The momentum balance yields the Navier—Stokes Equation:

$$\rho \frac{D\vec{u}}{Dt} = \rho \vec{g} - \nabla p + \nabla(\lambda \nabla \cdot \vec{u}) + \nabla \cdot (2\mu e) \qquad (A-48)$$

The energy equation is given by

$$\rho c_v \frac{DT}{Dt} = -p\nabla \cdot \vec{u} + \lambda(\nabla \cdot \vec{u})^2 + 2\mu e{:}e + \nabla \cdot (k\nabla T) + Q \qquad (A-49)$$

where $\quad 2e = \nabla \vec{u} + (\nabla \vec{u})^T, \ \lambda = -\frac{2}{3}\mu.$

$$e_{ii} = \frac{1}{h_i}\frac{\partial u_i}{\partial q_i} + \frac{u_j}{h_i h_j}\frac{\partial h_i}{\partial q_j} + \frac{u_k}{h_i h_k}\frac{\partial h_i}{\partial q_k} \qquad (A-50)$$

and

$$e_{ij} = \frac{1}{2}[\frac{h_i}{h_j}\frac{\partial}{\partial q_j}(\frac{u_i}{h_i}) + \frac{h_i}{h_i}\frac{\partial}{\partial q_i}(\frac{u_j}{h_j})] = e_{ji} \qquad (A-51)$$

Note that the summation over the repeated indices is not applicable here. The indexes i, j and k are cyclic in $i=1,2,3$.

Making use of the metrics, the governing equations can be re—formulated as given by the following:

The continuity equation,

$$\frac{\partial \rho}{\partial t} + \nabla \cdot \rho \vec{u} = 0 \tag{A–52}$$

The momentum equations,

$$\rho[\frac{\partial u_i}{\partial t} + \sum_{m=1}^{3} \frac{u_m}{h_m}(\frac{\partial u_i}{\partial q_m} + \frac{u_i}{h_i}\frac{\partial h_i}{\partial q_m} - \frac{u_m}{h_i}\frac{\partial h_m}{\partial q_i}) - g_i]$$

$$= -\frac{1}{h_i}\frac{\partial p}{\partial q_i} - \frac{\mu}{h_j h_k}\{\frac{\partial}{\partial q_j}[\frac{h_k}{h_i h_j}(\frac{\partial h_j u_j}{\partial q_i} - \frac{\partial h_i u_i}{\partial q_j})] - \frac{\partial}{\partial q_k}[\frac{h_j}{h_i h_k}(\frac{\partial h_i u_i}{\partial q_k} - \frac{\partial h_k u_k}{\partial q_i})]\}$$

$$+ \frac{4\mu}{3h_i}\frac{\partial \nabla \cdot \vec{u}}{\partial q_i} + 2\sum_{m=1}^{3}(\frac{e_{im}}{h_m}\frac{\partial \mu}{\partial q_m}) - \frac{2\nabla \cdot \vec{u}}{3h_i}\frac{\partial \mu}{\partial q_i} \tag{A–53}$$

The energy equation,

$$\rho c_v[\frac{\partial T}{\partial t} + \sum_{m=1}^{3}(\frac{u_m}{h_m}\frac{\partial T}{\partial q_m})] + p\nabla \cdot \vec{u} - \frac{2\mu(\nabla \cdot \vec{u})^2}{3} + 2\mu \sum_{\substack{m=1 \\ n=1}}^{3} e_{nm}^2 + Q$$

$$= \frac{1}{h_1 h_2 h_3}[\frac{\partial}{\partial q_1}(\frac{h_2 h_3}{h_1}k\frac{\partial T}{\partial q_1}) + \frac{\partial}{\partial q_2}(\frac{h_3 h_1}{h_2}k\frac{\partial T}{\partial q_2}) + \frac{\partial}{\partial q_3}(\frac{h_1 h_2}{h_3}k\frac{\partial T}{\partial q_3})] \tag{A–54}$$

where

$$\nabla \cdot \vec{a} = \frac{1}{h_1 h_2 h_3}[\frac{\partial(h_2 h_3 a_1)}{\partial q_1} + \frac{\partial(h_3 h_1 a_2)}{\partial q_2} + \frac{\partial(h_1 h_2 a_3)}{\partial q_3}] \tag{A–55}$$

and e is the same as that defined previously.

A.V. Governing Flow Equations in the Rectangular Helical System
for a Constant—Property Fluid

The velocity field is denoted by (u, v, w) for the coordinate system of (s, x_0, y_0). The governing flow equations are given by

The continuity:

$$\frac{1}{h_1}\frac{\partial u}{\partial s} + \frac{1}{h_1}\frac{\partial h_1 v}{\partial x_0} + \frac{1}{h_1}\frac{\partial h_1 w}{\partial y_0} = 0 \tag{A-56}$$

The s momentum:

$$\frac{\partial u}{\partial t} + \frac{u}{h_1}\frac{\partial u}{\partial s} + v\left(\frac{\partial u}{\partial x_0} + \frac{u}{h_1}\frac{\partial h_1}{\partial x_0}\right) + w\left(\frac{\partial u}{\partial y_0} + \frac{u}{h_1}\frac{\partial h_1}{\partial y_0}\right)$$

$$= -\frac{1}{\rho h_1}\frac{\partial p}{\partial s} - \nu\left\{\frac{\partial}{\partial x_0}\left[\frac{1}{h_1}\left(\frac{\partial v}{\partial s} - \frac{\partial h_1 u}{\partial x_0}\right)\right] - \frac{\partial}{\partial y_0}\left[\frac{1}{h_1}\left(\frac{\partial h_1 u}{\partial y_0} - \frac{\partial w}{\partial s}\right)\right]\right\} \tag{A-57}$$

Equation (A-57) can be reduced to

$$\frac{\partial u}{\partial t} + \frac{u}{h_1}\frac{\partial u}{\partial s} + v\frac{\partial u}{\partial x_0} + w\frac{\partial u}{\partial y_0} - \frac{\kappa u}{h_1}(v\sin\alpha - w\cos\alpha)$$

$$= -\frac{1}{\rho h_1}\frac{\partial p}{\partial s} + \nu\left[\frac{1}{h_1}\frac{\partial}{\partial s}\left(\frac{1}{h_1}\frac{\partial u}{\partial s}\right) + \frac{1}{h_1}\frac{\partial}{\partial x_0}\left(h_1\frac{\partial u}{\partial x_0}\right) + \frac{1}{h_1}\frac{\partial}{\partial y_0}\left(h_1\frac{\partial u}{\partial y_0}\right) - \frac{\kappa^2}{h_1^2}u - \right.$$

$$\left.\frac{2\kappa}{h_1^2}\left(\sin\alpha\frac{\partial v}{\partial s} - \cos\alpha\frac{\partial w}{\partial s}\right) - \kappa\tau\left(\frac{\kappa y_0 + \cos\alpha}{h_1^3}v - \frac{\kappa x_0 - \sin\alpha}{h_1^3}w\right)\right] \tag{A-58}$$

The x_0 momentum:

$$\frac{\partial v}{\partial t} + \frac{u}{h_1}\left(\frac{\partial v}{\partial s} - u\frac{\partial h_1}{\partial x_0}\right) + v\frac{\partial v}{\partial x_0} + w\frac{\partial v}{\partial y_0}$$

$$= -\frac{1}{\rho}\frac{\partial p}{\partial x_0} - \frac{\nu}{h_1}\left\{\frac{\partial}{\partial y_0}\left[h_1\left(\frac{\partial w}{\partial x_0} - \frac{\partial v}{\partial y_0}\right)\right] - \frac{\partial}{\partial s}\left[\frac{1}{h_1}\left(\frac{\partial v}{\partial s} - \frac{\partial h_1 u}{\partial x_0}\right)\right]\right\} \tag{A-59}$$

Equation (A—59) can be reduced to

$$\frac{\partial v}{\partial t} + \frac{u}{h_1}\frac{\partial v}{\partial s} + v\frac{\partial v}{\partial x_0} + w\frac{\partial v}{\partial y_0} + \frac{\kappa \sin\alpha}{h_1}u^2$$

$$= -\frac{1}{\rho}\frac{\partial p}{\partial x_0} + \nu[\frac{1}{h_1}\frac{\partial}{\partial s}(\frac{1}{h_1}\frac{\partial v}{\partial s}) + \frac{1}{h_1}\frac{\partial}{\partial x_0}(h_1\frac{\partial v}{\partial x_0}) + \frac{1}{h_1}\frac{\partial}{\partial y_0}(h_1\frac{\partial v}{\partial y_0}) - \frac{\kappa^2\sin^2\alpha}{h_1^2}v +$$

$$\frac{2\kappa\sin\alpha}{h_1^2}\frac{\partial u}{\partial s} + \frac{\kappa\tau}{h_1^3}(\kappa y_0+\cos\alpha)u + \frac{\kappa^2\sin\alpha\cos\alpha}{h_1^2}w] \qquad (A\text{—}60)$$

The y_0 momentum:

$$\frac{\partial w}{\partial t} + \frac{u}{h_1}(\frac{\partial w}{\partial s} - u\frac{\partial h_1}{\partial y_0}) + v\frac{\partial w}{\partial x_0} + w\frac{\partial w}{\partial y_0}$$

$$= -\frac{1}{\rho}\frac{\partial p}{\partial y_0} - \frac{\nu}{h_1}\{\frac{\partial}{\partial s}[\frac{1}{h_1}(\frac{\partial h_1 u}{\partial y_0} - \frac{\partial w}{\partial s})] - \frac{\partial}{\partial x_0}[h_1(\frac{\partial w}{\partial x_0} - \frac{\partial v}{\partial y_0})]\} \qquad (A\text{—}61)$$

Equation (A—61) can be reduced to

$$\frac{\partial w}{\partial t} + \frac{u}{h_1}\frac{\partial w}{\partial s} + v\frac{\partial w}{\partial x_0} + w\frac{\partial w}{\partial y_0} - \frac{\kappa\cos\alpha}{h_1}u^2$$

$$= -\frac{1}{\rho}\frac{\partial p}{\partial y_0} + \nu[\frac{1}{h_1}\frac{\partial}{\partial s}(\frac{1}{h_1}\frac{\partial w}{\partial s}) + \frac{1}{h_1}\frac{\partial}{\partial x_0}(h_1\frac{\partial w}{\partial x_0}) + \frac{1}{h_1}\frac{\partial}{\partial y_0}(h_1\frac{\partial w}{\partial x_0}) - \frac{\kappa^2\cos^2\alpha}{h_1^2}w -$$

$$\frac{2\kappa\cos\alpha}{h_1^2}\frac{\partial u}{\partial s} - \frac{\kappa\tau}{h_1^3}(\kappa x_0-\sin\alpha)u + \frac{\kappa^2\sin\alpha\cos\alpha}{h_1^2}v] \qquad (A\text{—}62)$$

The governing flow and convective heat transfer equations can be summarized in the conservational form as follows:

The continuity,

$$\frac{1}{h_1}\frac{\partial u}{\partial s} + \frac{1}{h_1}\frac{\partial h_1 v}{\partial x_0} + \frac{1}{h_1}\frac{\partial h_1 w}{\partial y_0} = 0 \qquad (A\text{—}63)$$

The s momentum,

$$\frac{\partial u}{\partial t} + \frac{\partial}{h_1 \partial s}(\eta u - \frac{\nu}{h_1}\frac{\partial u}{\partial s}) + \frac{\partial}{h_1 \partial x_0}h_1(vu - \nu\frac{\partial u}{\partial x_0}) + \frac{\partial}{h_1 \partial y_0}h_1(wu - \nu\frac{\partial u}{\partial y_0}) +$$

$$\frac{\kappa u}{h_1}(\frac{\kappa \nu}{h_1} - v\sin\alpha + w\cos\alpha)$$

$$= -\frac{1}{\rho h_1}\frac{\partial p}{\partial s} - \frac{\kappa \nu}{h_1^2}[2\sin\alpha\,\frac{\partial v}{\partial s} - 2\cos\alpha\,\frac{\partial w}{\partial s} + \frac{\tau}{h_1}(\kappa y_0 + \cos\alpha)v - \frac{\tau}{h_1}(\kappa x_0 - \sin\alpha)w]$$

$$(A\text{--}64)$$

The x_0 momentum,

$$\frac{\partial v}{\partial t} + \frac{\partial}{h_1 \partial s}(uv - \frac{\nu}{h_1}\frac{\partial v}{\partial s}) + \frac{\partial}{h_1 \partial x_0}h_1(vv - \nu\frac{\partial v}{\partial x_0}) + \frac{\partial}{h_1 \partial y_0}h_1(wv - \nu\frac{\partial v}{\partial y_0}) + \frac{\kappa^2 \sin^2\alpha}{h_1^2}\nu v$$

$$= -\frac{1}{\rho}\frac{\partial p}{\partial x_0} - \frac{\kappa \sin\alpha}{h_1}u^2 + \frac{\kappa \nu}{h_1^2}(2\sin\alpha\,\frac{\partial u}{\partial s} + \frac{\kappa y_0 + \cos\alpha}{h_1}\tau u + \kappa\sin\alpha\cos\alpha\,w)$$

$$(A\text{--}65)$$

The y_0 momentum:

$$\frac{\partial w}{\partial t} + \frac{\partial}{h_1 \partial s}(uw - \frac{\nu}{h_1}\frac{\partial w}{\partial s}) + \frac{\partial}{h_1 \partial x_0}h_1(vw - \nu\frac{\partial w}{\partial x_0}) + \frac{\partial}{h_1 \partial y_0}h_1(ww - \nu\frac{\partial w}{\partial y_0}) + \frac{\kappa^2 \cos^2\alpha}{h_1^2}\nu w$$

$$= -\frac{1}{\rho}\frac{\partial p}{\partial y_0} + \frac{\kappa \cos\alpha}{h_1}u^2 - \frac{\kappa \nu}{h_1^2}(2\cos\alpha\,\frac{\partial u}{\partial s} + \frac{\kappa x_0 - \sin\alpha}{h_1}\tau u - \kappa\sin\alpha\cos\alpha\,v)$$

$$(A\text{--}66)$$

As we can see from the above momentum equations, the coefficients are functions of the axial curve length. This makes it difficult to realize any fully developed flows. We make use of the following variable changes, with the axial (s–directional) velocity u_1 retained to be that of the orthogonal component.

$$(s, x, y) \Longleftarrow (s, x_0, y_0)$$

$$s = s$$

$$x = x_0 \cos\tau s + y_0 \sin\tau s$$

$$y = -x_0 \sin\tau s + y_0 \cos\tau s$$

$$u_1 = u$$

$$u_2 = v \cos\tau s + w \sin\tau s$$

$$u_3 = -v \sin\tau s + w \cos\tau s$$

By such a choice, we are able to retain the orthogonality of the axial velocity component u_1, while u_2 and u_3 now correspond to the x and y directions.

$$h_1 = 1 - \kappa x \sin\beta + \kappa y \cos\beta \tag{A-67}$$

$$(s, x_0, y_0) \Longleftarrow (s, x, y)$$

$$\frac{\partial}{\partial x_0} = \cos\tau s \frac{\partial}{\partial x} - \sin\tau s \frac{\partial}{\partial y}$$

$$\frac{\partial}{\partial y_0} = \sin\tau s \frac{\partial}{\partial x} + \cos\tau s \frac{\partial}{\partial y}$$

$$\frac{\partial}{\partial s} = \frac{\partial}{\partial s} + \tau y \frac{\partial}{\partial x} - \tau x \frac{\partial}{\partial y}$$

$$u = u_1$$

$$v = u_2 \cos\tau s - u_3 \sin\tau s$$

$$w = u_2 \sin\tau s + u_3 \cos\tau s$$

The field scalar quantity ψ (or the pseudo—secondary flow stream function) can be defined as:

$$\frac{\partial\psi}{\partial y} = h_1 u_2 + \tau y u_1 \tag{A-68a}$$

and

$$\frac{\partial\psi}{\partial x} = -h_1 u_3 + \tau x u_1 \tag{A-68b}$$

The continuity:

$$\frac{1}{h_1}(\frac{\partial}{\partial s} + \tau y \frac{\partial}{\partial x} - \tau x \frac{\partial}{\partial y})u_1 + \frac{1}{h_1}\frac{\partial h_1 u_2}{\partial x} + \frac{1}{h_1}\frac{\partial h_1 u_3}{\partial y} = 0 \qquad (A\text{--}69)$$

The momentum and energy equations can be generalized as:

$$[\mathbf{M}(\nu) + d_\phi]\phi = S_\phi \qquad (A\text{--}70)$$

where d_ϕ and S_ϕ are given by the individual velocity component or temperature ϕ. $\mathbf{M}$ is defined by the following equation:

$$\mathbf{M}(\nu)\ \phi = \frac{\partial \phi}{\partial t} + \frac{\partial}{h_1 \partial s}(u\phi - \frac{\nu}{h_1}\frac{\partial \phi}{\partial s}) + \frac{\partial}{h_1 \partial x_0}h_1(v\phi - \nu\frac{\partial \phi}{\partial x_0}) + \frac{\partial}{h_1 \partial y_0}h_1(w\phi - \nu\frac{\partial \phi}{\partial y_0})$$

$$= \frac{\partial \phi}{\partial t} + \frac{1}{h_1}(\frac{\partial}{\partial s} + \tau y\frac{\partial}{\partial x} - \tau x\frac{\partial}{\partial y})[u\phi - \frac{\nu}{h_1}(\frac{\partial}{\partial s} + \tau y\frac{\partial}{\partial x} - \tau x\frac{\partial}{\partial y})\phi] +$$

$$\frac{1}{h_1}(\cos\tau s\frac{\partial}{\partial x} - \sin\tau s\frac{\partial}{\partial y})h_1[v\phi - \nu(\cos\tau s\frac{\partial}{\partial x} - \sin\tau s\frac{\partial}{\partial y})\phi] +$$

$$\frac{1}{h_1}(\sin\tau s\frac{\partial}{\partial x} + \cos\tau s\frac{\partial}{\partial y})h_1[w\phi - \nu(\sin\tau s\frac{\partial}{\partial x} + \cos\tau s\frac{\partial}{\partial y})\phi]$$

$$= \frac{\partial \phi}{\partial t} + \frac{1}{h_1}\cdot\frac{\partial}{\partial s}[(u_1 - \frac{x\cos\beta + y\sin\beta}{h_1^2}\kappa\tau\nu)\phi - \frac{\nu}{h_1}\cdot\frac{\partial \phi}{\partial s}] +$$

$$\frac{1}{h_1}\cdot\frac{\partial}{\partial x}[(h_1 u_2 + \tau y\ u_1 + \frac{1-\kappa x\sin\beta}{h_1^2}\tau^2 x\nu)\phi - \nu(h_1 + \frac{\tau^2 y^2}{h_1})\frac{\partial \phi}{\partial x}] +$$

$$\frac{1}{h_1}\cdot\frac{\partial}{\partial y}[(h_1 u_3 - \tau x\ u_1 + \frac{h_1+\kappa x\sin\beta}{h_1^2}\tau^2 y\nu)\phi - \nu(h_1 + \frac{\tau^2 x^2}{h_1})\frac{\partial \phi}{\partial y}] +$$

$$2\frac{\tau^2 xy\nu}{h_1^2}\frac{\partial^2 \phi}{\partial x\ \partial y} - 2\frac{\tau^2 y\nu}{h_1^2}\frac{\partial^2 \phi}{\partial s\ \partial x} + 2\frac{\tau^2 x\nu}{h_1^2}\frac{\partial^2 \phi}{\partial s\ \partial y} -$$

$$2\frac{\tau^2 \nu\phi}{h_1^4}(h_1 - \kappa^2 xy\sin 2\beta) \qquad (A\text{--}71)$$

When the energy equation is to be referred, the kinematic viscosity ν in $\mathbf{M}(\nu)$ should be replaced by the thermal diffusivity $k/\rho C_p$.

s—momentum $\mathbf{M}(\nu)\ \phi = S_\phi$:

$$\phi = u_1 \tag{A-72a}$$

$$d_\phi = \frac{\kappa}{h_1}(\frac{\kappa\nu}{h_1} - u_2\sin\beta + u_3\cos\beta) \tag{A-72b}$$

$$S_\phi = -\frac{1}{\rho h_1}(\frac{\partial p}{\partial s} + \tau y\frac{\partial p}{\partial x} - \tau x\frac{\partial p}{\partial y}) - \frac{\kappa\nu}{h_1^2}[2(\frac{\partial}{\partial s} + \tau y\frac{\partial}{\partial x} - \tau x\frac{\partial}{\partial y})(u_2\sin\beta - u_3\cos\beta) -$$

$$\tau u_2(2\cos\beta - \frac{\kappa y + \cos\beta}{h_1}) - \tau u_3(2\sin\beta + \frac{\kappa x - \sin\beta}{h_1})] \tag{A-72c}$$

x—momentum $\mathbf{M}(\nu)\ \phi = S_\phi$:

$$\phi = u_2 \tag{A-73a}$$

$$d_\phi = \frac{\tau^2 + \kappa^2\sin^2\beta}{h_1^2}\nu \tag{A-73b}$$

$$S_\phi = -\frac{1}{\rho}\frac{\partial p}{\partial x} + \tau\frac{u_1 u_3}{h_1} - \frac{\kappa\sin\beta}{h_1}u_1^2 + \frac{\nu}{h_1^2}[2\kappa\sin\beta(\frac{\partial u_1}{\partial s} + \tau y\frac{\partial u_1}{\partial x} - \tau x\frac{\partial u_1}{\partial y}) + \frac{\kappa y + \cos\beta}{h_1}\kappa\tau u_1 -$$

$$2\tau(\frac{\partial u_3}{\partial s} + \tau y\frac{\partial u_3}{\partial x} - \tau x\frac{\partial u_3}{\partial y}) + (\frac{\kappa}{2}\sin2\beta - \frac{x\cos\beta + y\sin\beta}{h_1}\tau^2)\kappa u_3] \tag{A-73c}$$

y—momentum $\mathbf{M}(\nu)\ \phi = S_\phi$:

$$\phi = u_3 \tag{A-74a}$$

$$d_\phi = \frac{\tau^2 + \kappa^2\cos^2\beta}{h_1^2}\nu \tag{A-74b}$$

$$S_\phi = -\frac{1}{\rho}\frac{\partial p}{\partial y} - \tau\frac{u_1 u_2}{h_1} + \frac{\kappa\cos\beta}{h_1}u_1^2 - \frac{\nu}{h_1^2}[2\kappa\cos\beta(\frac{\partial u_1}{\partial s} + \tau y\frac{\partial u_1}{\partial x} - \tau x\frac{\partial u_1}{\partial y}) + \frac{\kappa x - \sin\beta}{h_1}\kappa\tau u_1 -$$

$$2\tau(\frac{\partial u_2}{\partial s} + \tau y\frac{\partial u_2}{\partial x} - \tau x\frac{\partial u_2}{\partial y}) - (\frac{\kappa}{2}\sin2\beta + \frac{x\cos\beta + y\sin\beta}{h_1}\tau^2)\kappa u_2] \tag{A-74c}$$

The energy equation with negligible viscous dissipation:

$$\mathbf{M}(\frac{k}{C_p\rho})\ T = 0 \tag{A-75}$$

A.VI. Governing Flow Equations in the Circular Helical System
with Constant Properties

The circular coordinate system of choice is (s, r, θ'). With the velocity field denoted by (u, v, w), we can obtain the governing equations for this orthogonal coordinate system as

The continuity equation:

$$\frac{1}{h_1} \cdot \frac{\partial u}{\partial s} + \frac{1}{h_1 h_2 h_3} \cdot \frac{\partial(h_1 h_3 v)}{\partial r} + \frac{1}{h_1 h_2 h_3} \cdot \frac{\partial(h_1 h_2 w)}{\partial \theta'} = 0 \tag{A-76}$$

The s momentum balance equation:

$$\frac{\partial u}{\partial t} + \frac{u}{h_1}\frac{\partial u}{\partial s} + \frac{v}{h_2}\left(\frac{\partial u}{\partial r} + \frac{u}{h_1}\frac{\partial h_1}{\partial r}\right) + \frac{w}{h_3}\left(\frac{\partial u}{\partial \theta} + \frac{u}{h_1}\frac{\partial h_1}{\partial \theta}\right)$$

$$= -\frac{1}{\rho h_1}\frac{\partial p}{\partial s} - \frac{\nu}{h_2 h_3}\left\{\frac{\partial}{\partial r}\left[\frac{h_3}{h_1 h_2}\left(h_2\frac{\partial v}{\partial s} - \frac{\partial h_1 u}{\partial r}\right)\right] - \frac{\partial}{\partial \theta}\left[\frac{h_2}{h_1 h_3}\left(\frac{\partial h_1 u}{\partial \theta} - h_3\frac{\partial w}{\partial s}\right)\right]\right\}$$

$$= -\frac{1}{\rho h_1}\frac{\partial p}{\partial s} + \frac{\nu}{h_2 h_3}\left[-\frac{\partial}{\partial r}\left(\frac{h_3}{h_1}\frac{\partial v}{\partial s}\right) - \frac{\partial}{\partial \theta}\left(\frac{h_2}{h_1}\frac{\partial w}{\partial s}\right) + \frac{\partial}{\partial r}\left(\frac{h_3}{h_1 h_2}\frac{\partial h_1 u}{\partial r}\right) + \frac{\partial}{\partial \theta}\left(\frac{h_2}{h_1 h_3}\frac{\partial h_1 u}{\partial \theta}\right)\right]$$

$$\tag{A-77}$$

Manipulating the cross—related term with the aid of equation (A-76), we get

$$-\frac{\partial}{\partial r}\left(\frac{h_3}{h_1}\frac{\partial v}{\partial s}\right) - \frac{\partial}{\partial \theta'}\left(\frac{h_2}{h_1}\frac{\partial w}{\partial s}\right)$$

$$= -\frac{\partial}{\partial r}\left(\frac{1}{h_1^2}\frac{\partial h_1 h_3 v}{\partial s} - \frac{h_3}{h_1^2}\cdot\frac{\partial h_1}{\partial s}\cdot v\right) - \frac{\partial}{\partial \theta'}\left(\frac{1}{h_1^2}\frac{\partial h_1 h_2 w}{\partial s} - \frac{h_2}{h_1^2}\cdot\frac{\partial h_1}{\partial s}\cdot w\right)$$

$$= \frac{2}{h_1^3}\frac{\partial h_1}{\partial r}\frac{\partial h_1 h_3 v}{\partial s} + \frac{\partial}{\partial r}\left(\frac{h_3}{h_1^2}\cdot\frac{\partial h_1}{\partial s}\cdot v\right) + \frac{\partial}{\partial \theta'}\left(\frac{h_2}{h_1^2}\cdot\frac{\partial h_1}{\partial s}\cdot w\right) + \frac{2}{h_1^3}\frac{\partial h_1}{\partial \theta'}\frac{\partial h_1 h_2 w}{\partial s} -$$

$$\frac{1}{h_1^2}\frac{\partial}{\partial s}\left(\frac{\partial h_1 h_3 v}{\partial r} + \frac{\partial h_1 h_2 w}{\partial \theta'}\right)$$

$$= \frac{h_2 h_3}{h_1^2}\frac{\partial^2 u}{\partial s^2} + \frac{2h_3}{h_1^2}\frac{\partial h_1}{\partial r}\frac{\partial v}{\partial s} + \frac{2h_3}{h_1^2}\frac{\partial h_1}{\partial r}\frac{\partial h_1}{\partial s}v + \frac{2h_2}{h_1^2}\frac{\partial h_1}{\partial \theta'}\frac{\partial w}{\partial s} + \frac{2h_2}{h_1^2}\frac{\partial h_1}{\partial \theta'}\frac{\partial h_1}{\partial s}w -$$

$$\frac{h_2 h_3}{h_1^2}\frac{\partial h_1}{\partial s}\frac{\partial u}{\partial s} - h_1 h_3 v\frac{\partial}{\partial r}\left(\frac{1}{h_1^2}\frac{\partial h_1}{\partial s}\right) - h_1 h_2 w\frac{\partial}{\partial \theta'}\left(\frac{1}{h_1^2}\frac{\partial h_1}{\partial s}\right)$$

$$= \frac{h_2 h_3}{h_1} \frac{\partial}{\partial s}(\frac{1}{h_1} \frac{\partial u}{\partial s}) + \frac{2h_3}{h_1^2} \frac{\partial h_1}{\partial r} \frac{\partial v}{\partial s} + \frac{2h_2}{h_1^2} \frac{\partial h_1}{\partial \theta'} \frac{\partial w}{\partial s} -$$

$$\frac{h_3}{h_1^3}(h_1 \frac{\partial^2 h_1}{\partial r \partial s} - \frac{\partial h_1}{\partial r} \frac{\partial h_1}{\partial s})v - \frac{h_2}{h_1^3}(h_1 \frac{\partial^2 h_1}{\partial \theta' \partial s} - \frac{\partial h_1}{\partial \theta'} \frac{\partial h_1}{\partial s})w$$

Substituting the above expression back into the momentum balance equation (A–77), we obtain

$$\frac{\partial u}{\partial t} + \frac{u}{h_1} \frac{\partial u}{\partial s} + \frac{v}{h_2}(\frac{\partial u}{\partial r} + \frac{u}{h_1} \frac{\partial h_1}{\partial r}) + \frac{w}{h_3}(\frac{\partial u}{\partial \theta'} + \frac{u}{h_1} \frac{\partial h_1}{\partial \theta'})$$

$$= -\frac{1}{\rho h_1} \frac{\partial p}{\partial s} + \nu\{\frac{1}{h_1} \frac{\partial}{\partial s}(\frac{1}{h_1} \frac{\partial u}{\partial s}) + \frac{1}{h_1 h_2^2 h_3} \frac{\partial}{\partial r}(h_1 h_3 \frac{\partial u}{\partial r}) + \frac{1}{h_1 h_2 h_3} \frac{\partial}{\partial \theta'}(\frac{h_1 h_2}{h_3} \frac{\partial u}{\partial \theta'}) +$$

$$\frac{1}{h_1^2 h_2}[\frac{h_1-1}{r^2 h_2} + \frac{h_1}{h_3^2}(\frac{1}{h_2} \frac{\partial h_2}{\partial \theta'} - \frac{1}{h_1} \frac{\partial h_1}{\partial \theta'} - \frac{1}{h_3} \frac{\partial h_3}{\partial \theta'})\frac{\partial h_1}{\partial \theta'} + \frac{h_1}{h_3^2} \frac{\partial^2 h_1}{\partial \theta'^2}]u + \frac{2}{h_1^2 h_2} \frac{\partial h_1}{\partial r} \frac{\partial v}{\partial s} +$$

$$\frac{2}{h_1^2 h_3} \frac{\partial h_1}{\partial \theta'} \frac{\partial w}{\partial s} - \frac{1}{h_1^3 h_2}(h_1 \frac{\partial^2 h_1}{\partial r \partial s} - \frac{\partial h_1}{\partial r} \frac{\partial h_1}{\partial s})v - \frac{1}{h_1^3 h_3}(h_1 \frac{\partial^2 h_1}{\partial s \partial \theta'} - \frac{\partial h_1}{\partial \theta'} \frac{\partial h_1}{\partial s})w\}$$

$$(A–78)$$

Hence, the s–momentum equation in the conservational form can be written as:

$$\frac{\partial u}{\partial t} + \frac{1}{h_1} \cdot \frac{\partial}{\partial s}(uu - \frac{\nu}{h_1} \cdot \frac{\partial u}{\partial s}) + \frac{1}{h_1 h_2 h_3} \cdot \frac{\partial}{\partial r} h_1 h_3 (vu - \frac{\nu}{h_2} \cdot \frac{\partial u}{\partial r}) +$$

$$\frac{1}{h_1 h_2 h_3} \cdot \frac{\partial}{\partial \theta'} h_1 h_2 (wu - \frac{\nu}{h_3} \cdot \frac{\partial u}{\partial \theta'}) + \{\frac{h_1-1}{r h_1 h_2}v + \frac{w}{h_1 h_3} \cdot \frac{\partial h_1}{\partial \theta'} -$$

$$\frac{\nu}{h_1^2 h_2}[\frac{h_1-1}{r^2 h_2} + \frac{h_1}{h_3^2}(\frac{1}{h_2} \frac{\partial h_2}{\partial \theta'} - \frac{1}{h_1} \frac{\partial h_1}{\partial \theta'} - \frac{1}{h_3} \frac{\partial h_3}{\partial \theta'})\frac{\partial h_1}{\partial \theta'} + \frac{h_1}{h_3^2} \frac{\partial^2 h_1}{\partial \theta'^2}]\}u$$

$$= -\frac{1}{\rho h_1} \frac{\partial p}{\partial s} + \frac{\nu}{h_1^2}[\frac{2}{h_2} \cdot \frac{\partial h_1}{\partial r} \cdot \frac{\partial v}{\partial s} + \frac{2}{h_3} \frac{\partial h_1}{\partial \theta'} \cdot \frac{\partial w}{\partial s} - \frac{1}{h_2}(\frac{\partial^2 h_1}{\partial r \partial s} - \frac{1}{h_1} \cdot \frac{\partial h_1}{\partial r} \frac{\partial h_1}{\partial s})v -$$

$$\frac{1}{h_3}(\frac{\partial^2 h_1}{\partial \theta' \partial s} - \frac{1}{h_1} \cdot \frac{\partial h_1}{\partial \theta'} \frac{\partial h_1}{\partial s})w]$$

$$(A–79)$$

r—momentum balance equation:

$$\frac{\partial v}{\partial t} + \frac{u}{h_1}\left(\frac{\partial v}{\partial s} - \frac{u}{h_2}\frac{\partial h_1}{\partial r}\right) + \frac{v}{h_2}\frac{\partial v}{\partial r} + \frac{w}{h_3}\left(\frac{\partial v}{\partial \theta'} + \frac{v}{h_2}\frac{\partial h_2}{\partial \theta'} - \frac{w}{h_2}\frac{\partial h_3}{\partial r}\right)$$

$$= -\frac{1}{\rho h_2}\frac{\partial p}{\partial r} - \frac{\nu}{h_1 h_3}\left\{\frac{\partial}{\partial \theta'}\left[\frac{h_1}{h_2 h_3}\left(\frac{\partial h_3 w}{\partial r} - \frac{\partial h_2 v}{\partial \theta'}\right)\right] - \frac{\partial}{\partial s}\left[\frac{h_3}{h_1 h_2}\left(\frac{\partial h_2 v}{\partial s} - \frac{\partial h_1 u}{\partial r}\right)\right]\right\}$$

$$= -\frac{1}{\rho h_2}\frac{\partial p}{\partial r} + \nu\left[\frac{1}{h_1}\frac{\partial}{\partial s}\left(\frac{1}{h_1}\frac{\partial v}{\partial s}\right) - \frac{1}{h_1 h_3}\frac{\partial}{\partial s}\left(\frac{h_3}{h_1 h_2}\frac{\partial h_1 u}{\partial r}\right) - \frac{1}{h_1 h_3}\frac{\partial}{\partial \theta'}\left(\frac{h_1}{h_2 h_3}\frac{\partial h_3 w}{\partial r}\right) +$$

$$\frac{1}{h_1 h_3}\frac{\partial}{\partial \theta'}\left(\frac{h_1}{h_2 h_3}\frac{\partial h_2 v}{\partial \theta'}\right)\right]$$

(A—80)

Manipulating the cross—related term with the aid of equation (A—76) leads to

$$-\frac{1}{h_1 h_3}\frac{\partial}{\partial s}\left(\frac{h_3}{h_1 h_2}\frac{\partial h_1 u}{\partial r}\right) - \frac{1}{h_1 h_3}\frac{\partial}{\partial \theta'}\left(\frac{h_1}{h_2 h_3}\frac{\partial h_3 w}{\partial r}\right)$$

$$= -\frac{1}{h_1 h_2}\frac{\partial}{\partial s}\left(\frac{1}{h_1}\frac{\partial h_1 u}{\partial r}\right) - \frac{1}{h_1 h_3}\frac{\partial}{\partial \theta'}\left(\frac{h_1}{h_2}\frac{\partial w}{\partial r} + \frac{w h_1}{r h_2}\right)$$

$$= -\frac{1}{h_1 h_2}\frac{\partial}{\partial r}\left(\frac{\partial u}{\partial s}\right) - \frac{1}{h_1 h_2^2 h_3}\frac{\partial}{\partial r}\left(\frac{\partial h_1 h_2 w}{\partial \theta'}\right) + \frac{1}{h_1 h_2^2 h_3}\frac{\partial h_2}{\partial \theta'}\frac{\partial h_1 w}{\partial r} - \frac{1}{h_1 h_3}\frac{\partial}{\partial \theta'}\left(\frac{w h_1}{r h_2}\right) +$$

$$\frac{1}{h_1 h_3}\frac{\partial}{\partial \theta'}\left(\frac{w}{h_2}\frac{\partial h_1}{\partial r}\right) - \frac{1}{h_1 h_2}\frac{\partial}{\partial s}\left(\frac{h_1-1}{r h_1}u\right)$$

$$= -\frac{1}{h_1 h_2^2 h_3}\frac{\partial}{\partial r}\left(h_2 h_3\frac{\partial u}{\partial s} + \frac{\partial h_1 h_2 w}{\partial \theta'}\right) + \frac{1}{h_1 h_2 h_3}\frac{\partial h_3}{\partial r}\frac{\partial u}{\partial s} + \cdots$$

$$= \frac{1}{h_1 h_2^2 h_3}\frac{\partial}{\partial r}\left(h_1 h_3\frac{\partial v}{\partial r}\right) + \frac{1}{h_1 h_2^2 h_3}\frac{\partial}{\partial r}\left(v\frac{\partial h_1 h_3}{\partial r}\right) + \frac{1}{h_1 h_2 h_3}\frac{\partial h_3}{\partial r}\frac{\partial u}{\partial s} + \cdots$$

$$= \frac{1}{h_1 h_2^2 h_3}\frac{\partial}{\partial r}\left(h_1 h_3\frac{\partial v}{\partial r}\right) + \frac{2h_1-1}{r h_1^2 h_2^2 h_3}\frac{\partial}{\partial r}\left(h_1 h_3 v\right) - \frac{2h_1^2-2h_1+1}{r^2 h_1^2 h_2^2}v + \frac{1}{h_1 h_2 h_3}\frac{\partial h_3}{\partial r}\frac{\partial u}{\partial s} + \cdots$$

$$= \frac{1}{h_1 h_2^2 h_3}\frac{\partial}{\partial r}\left(h_1 h_3\frac{\partial v}{\partial r}\right) - \frac{2h_1-1}{r h_1^2 h_2}\left(\frac{\partial u}{\partial s} + \frac{\partial h_1 h_2 w}{h_2 h_3 \partial \theta'}\right) - \frac{2h_1^2-2h_1+1}{r^2 h_1^2 h_2^2}v + \frac{1}{h_1 h_2 h_3}\frac{\partial h_3}{\partial r}\frac{\partial u}{\partial s} +$$

$$\frac{1}{h_1 h_2^2 h_3}\frac{\partial h_2}{\partial \theta'}\frac{\partial h_1 w}{\partial r} - \frac{1}{h_1 h_3}\frac{\partial}{\partial \theta'}\left(\frac{w h_1}{r h_2}\right) + \frac{1}{h_1 h_3}\frac{\partial}{\partial \theta'}\left(\frac{w}{h_2}\frac{\partial h_1}{\partial r}\right) - \frac{1}{h_1 h_2}\frac{\partial}{\partial s}\left(\frac{h_1-1}{r h_1}u\right)$$

$$= \frac{1}{h_1 h_2^2 h_3}\frac{\partial}{\partial r}\left(h_1 h_3\frac{\partial v}{\partial r}\right) - \frac{2h_1^2-2h_1+1}{r^2 h_1^2 h_2^2}v - 2\frac{h_1-1}{r h_1^2 h_2}\frac{\partial u}{\partial s} + \frac{1}{h_2^2 h_3}\frac{\partial h_2}{\partial \theta'}\frac{\partial w}{\partial r} -$$

$$\frac{2}{r h_2 h_3}\frac{\partial w}{\partial \theta'} - \frac{2h_1-1}{r h_1^2 h_2 h_3}\frac{\partial h_1}{\partial \theta'}w + \frac{u}{r h_1^3 h_2}\frac{\partial h_1}{\partial s}$$

Hence the reduced r momentum equation can be obtained by substituting the cross—related terms as given above into the momentum balance equation (A—80) as follows:

$$\frac{\partial v}{\partial t} + \frac{u}{h_1}\left(\frac{\partial v}{\partial s} - \frac{u}{h_2}\frac{\partial h_1}{\partial r}\right) + \frac{v}{h_2}\frac{\partial v}{\partial r} + \frac{w}{h_3}\left(\frac{\partial v}{\partial \theta'} + \frac{v}{h_2}\frac{\partial h_2}{\partial \theta'} - \frac{w}{h_2}\frac{\partial h_3}{\partial r}\right)$$

$$= -\frac{1}{\rho h_2}\frac{\partial p}{\partial r} + \nu\left\{\frac{1}{h_1}\frac{\partial}{\partial s}\left(\frac{1}{h_1}\frac{\partial v}{\partial s}\right) + \frac{1}{h_1 h_2^2 h_3}\frac{\partial}{\partial r}\left(h_1 h_3 \frac{\partial v}{\partial r}\right) + \frac{1}{h_1 h_2 h_3}\frac{\partial}{\partial \theta'}\left(\frac{h_1 h_2}{h_3}\frac{\partial v}{\partial \theta'}\right) - \right.$$

$$\left[\frac{2h_1^2 - 2h_1 + 1}{r^2 h_1^2 h_2^2} - \frac{1}{h_2^2 h_3^2}\left(\frac{\partial^2 h_2}{\partial \theta'^2} + \frac{1}{h_1}\frac{\partial h_1}{\partial \theta'}\frac{\partial h_2}{\partial \theta'} - \frac{1}{h_2}\frac{\partial h_2}{\partial \theta'}\frac{\partial h_2}{\partial \theta'} - \frac{1}{h_3}\frac{\partial h_3}{\partial \theta'}\frac{\partial h_2}{\partial \theta'}\right)\right]v -$$

$$2\frac{h_1 - 1}{r h_1^2 h_2}\frac{\partial u}{\partial s} + \frac{u}{r h_1^3 h_2}\frac{\partial h_1}{\partial s} + \frac{1}{h_2^2 h_3}\frac{\partial h_2}{\partial \theta'}\frac{\partial w}{\partial r} - \frac{2}{r h_2 h_3}\frac{\partial w}{\partial \theta'} - \frac{2h_1 - 1}{r h_1^2 h_2 h_3}\frac{\partial h_1}{\partial \theta'}w\right\}$$

$$(A\text{—}81)$$

Then the r—momentum equation can be cast into the momentum conservational form as,

$$\frac{\partial v}{\partial t} + \frac{1}{h_1}\cdot\frac{\partial}{\partial s}\left(uv - \frac{\nu}{h_1}\cdot\frac{\partial v}{\partial s}\right) + \frac{1}{h_1 h_2 h_3}\cdot\frac{\partial}{\partial r}h_1 h_3\left(vv - \frac{\nu}{h_2}\cdot\frac{\partial v}{\partial r}\right) +$$

$$\frac{1}{h_1 h_2 h_3}\cdot\frac{\partial}{\partial \theta'}h_1 h_2\left(wv - \frac{\nu}{h_3}\cdot\frac{\partial v}{\partial \theta}\right) + \left\{\nu\left[\frac{2h_1^2 - 2h_1 + 1}{r^2 h_1^2 h_2^2} - \right.\right.$$

$$\frac{1}{h_2^2 h_3^2}\left(\frac{\partial^2 h_2}{\partial \theta'^2} + \frac{1}{h_1}\cdot\frac{\partial h_1}{\partial \theta'}\frac{\partial h_2}{\partial \theta'} - \frac{1}{h_2}\cdot\frac{\partial h_2}{\partial \theta'}\frac{\partial h_2}{\partial \theta'} - \frac{1}{h_3}\cdot\frac{\partial h_3}{\partial \theta'}\frac{\partial h_2}{\partial \theta'}\right)\right] + \frac{w}{h_2 h_3}\cdot\frac{\partial h_2}{\partial \theta'}\right\}v$$

$$= \frac{h_1 - 1}{r h_1 h_2}u^2 + \frac{w^2}{r h_2} - \frac{1}{\rho h_2}\cdot\frac{\partial p}{\partial r} - \nu\left(2\frac{h_1 - 1}{r h_1^2 h_2}\cdot\frac{\partial u}{\partial s} - \frac{u}{r h_1^3 h_2}\cdot\frac{\partial h_1}{\partial s} - \frac{1}{h_2^2 h_3}\cdot\frac{\partial h_2}{\partial \theta'}\frac{\partial w}{\partial r} + \right.$$

$$\frac{2}{r h_2 h_3}\cdot\frac{\partial w}{\partial \theta'} + \frac{2h_1 - 1}{r h_1^2 h_2 h_3}\cdot\frac{\partial h_1}{\partial \theta'}w\right)$$

$$(A\text{—}82)$$

The θ momentum balance leads to the following:

$$\frac{\partial w}{\partial t} + \frac{u}{h_1}\left(\frac{\partial w}{\partial s} - \frac{u}{h_3}\frac{\partial h_1}{\partial \theta'}\right) + \frac{v}{h_2}\left(\frac{\partial w}{\partial r} + \frac{w}{r} - \frac{v}{h_3}\frac{\partial h_2}{\partial \theta'}\right) + \frac{w}{h_3}\frac{\partial w}{\partial \theta'}$$

$$= -\frac{1}{\rho h_3}\frac{\partial p}{\partial \theta'} - \frac{\nu}{h_1 h_2}\left\{\frac{\partial}{\partial s}\left[\frac{h_2}{h_1 h_3}\left(\frac{\partial h_1 u}{\partial \theta'} - \frac{\partial h_3 w}{\partial s}\right)\right] - \frac{\partial}{\partial r}\left[\frac{h_1}{h_2 h_3}\left(\frac{\partial h_3 w}{\partial r} - \frac{\partial h_2 v}{\partial \theta'}\right)\right]\right\}$$

$$= -\frac{1}{\rho h_3}\frac{\partial p}{\partial \theta'} + \nu\left[\frac{1}{h_1}\frac{\partial}{\partial s}\left(\frac{1}{h_1}\frac{\partial w}{\partial s}\right) + \frac{1}{h_1 h_2}\frac{\partial}{\partial r}\left(\frac{h_1}{h_2 h_3}\frac{\partial h_3 w}{\partial r}\right) - \right.$$

$$\frac{1}{h_1}\frac{\partial}{\partial s}\left(\frac{1}{h_1 h_3}\frac{\partial h_1 u}{\partial \theta'}\right) - \frac{1}{h_1 h_2}\frac{\partial}{\partial r}\left(\frac{h_1}{h_2 h_3}\frac{\partial h_2 v}{\partial \theta'}\right) \tag{A-83}$$

Manipulating the cross-related term with the aid of equation (A-76) leads to

$$-\frac{1}{h_1}\frac{\partial}{\partial s}\left(\frac{1}{h_1 h_3}\frac{\partial h_1 u}{\partial \theta'}\right) - \frac{1}{h_1 h_2}\frac{\partial}{\partial r}\left(\frac{h_1}{h_2 h_3}\frac{\partial h_2 v}{\partial \theta'}\right)$$

$$= -\frac{1}{h_1 h_3}\frac{\partial}{\partial s}\left(\frac{\partial u}{\partial \theta'} + \frac{u}{h_1}\frac{\partial h_1}{\partial \theta'}\right) - \frac{1}{h_1 h_2}\frac{\partial}{\partial r}\left(\frac{h_1}{h_3}\frac{\partial v}{\partial \theta'} + \frac{h_1 v}{h_2 h_3}\frac{\partial h_2}{\partial \theta'}\right)$$

$$= -\frac{1}{h_1 h_3}\frac{\partial}{\partial \theta'}\left(\frac{\partial u}{\partial s}\right) - \frac{1}{h_2 h_3}\frac{\partial}{\partial \theta'}\left(\frac{1}{h_1 h_3}\frac{\partial h_1 h_3 v}{\partial r} - \frac{v}{h_1 h_3}\frac{\partial h_1 h_3}{\partial r}\right) -$$

$$\frac{1}{h_1 h_3}\frac{\partial}{\partial s}\left(\frac{u}{h_1}\frac{\partial h_1}{\partial \theta'}\right) - \frac{1}{h_1 h_2}\frac{\partial}{\partial r}\left(\frac{h_1}{h_3}\right)\frac{\partial v}{\partial \theta'} - \frac{1}{h_1 h_2}\frac{\partial}{\partial r}\left(\frac{h_1 v}{h_2 h_3}\frac{\partial h_2}{\partial \theta'}\right)$$

$$= -\frac{1}{h_1 h_3}\frac{\partial}{\partial \theta'}\left(\frac{\partial u}{\partial s} + \frac{1}{h_2 h_3}\frac{\partial h_1 h_3 v}{\partial r}\right) + \frac{1}{h_2 h_3}\frac{\partial}{\partial \theta'}\left(\frac{v}{h_1 h_3}\frac{\partial h_1 h_3}{\partial r}\right) +$$

$$\frac{1}{h_1^2 h_2 h_3}\left(h_3\frac{\partial h_1}{\partial \theta'} + h_1\frac{\partial h_3}{\partial \theta'}\right)\frac{\partial h_1 h_3 v}{\partial r} - \frac{1}{h_1 h_2 h_3^2}\frac{\partial h_2}{\partial \theta'}\frac{\partial h_1 h_3 v}{\partial r} - \frac{1}{h_1^2 h_3}\frac{\partial h_1}{\partial \theta'}\frac{\partial u}{\partial s} -$$

$$\frac{u}{h_1 h_3}\frac{\partial}{\partial s}\left(\frac{1}{h_1}\frac{\partial h_1}{\partial \theta'}\right) - \frac{1}{h_1 h_2}\frac{\partial}{\partial r}\left(\frac{h_1}{h_3}\right)\frac{\partial v}{\partial \theta'} - \frac{h_3 v}{h_2}\frac{\partial}{\partial r}\left(\frac{1}{h_2 h_3^2}\frac{\partial h_2}{\partial \theta'}\right)$$

$$= \frac{1}{h_1 h_3}\frac{\partial}{\partial \theta'}\left(\frac{1}{h_2 h_3}\frac{\partial h_1 h_2 w}{\partial \theta'}\right) + \cdots$$

$$= \frac{1}{h_1 h_3}\frac{\partial}{\partial \theta'}\left(\frac{h_1}{h_3}\frac{\partial w}{\partial \theta'} + \frac{w}{h_2 h_3}\frac{\partial h_1 h_2}{\partial \theta'}\right) + \cdots$$

$$= \frac{1}{h_1 h_2 h_3}\frac{\partial}{\partial \theta'}\left(\frac{h_1 h_2}{h_3}\frac{\partial w}{\partial \theta'}\right) - \frac{1}{h_2 h_3^2}\left(\frac{\partial h_2}{\partial \theta'} - \frac{1}{h_1}\frac{\partial h_1 h_2}{\partial \theta'}\right)\frac{\partial w}{\partial \theta'} + \frac{w}{h_1 h_3}\frac{\partial}{\partial \theta'}\left(\frac{1}{h_2 h_3}\frac{\partial h_1 h_2}{\partial \theta'}\right) + \cdots$$

$$= \frac{1}{h_1 h_2 h_3}\frac{\partial}{\partial \theta'}\left(\frac{h_1 h_2}{h_3}\frac{\partial w}{\partial \theta'}\right) + \frac{1}{h_1^2 h_2 h_3^2}\frac{\partial h_1}{\partial \theta'}\frac{\partial h_1 h_2 w}{\partial \theta'} - \frac{w}{h_1^2 h_2^2 h_3^2}\left[\left(\frac{\partial h_1 h_2}{\partial \theta'}\right)^2 - h_1 h_2\frac{\partial^2 h_1 h_2}{\partial \theta'^2}\right] + \cdots$$

$$= \frac{1}{h_1 h_2 h_3}\frac{\partial}{\partial \theta'}\left(\frac{h_1 h_2}{h_3}\frac{\partial w}{\partial \theta'}\right) - \frac{w}{h_1^2 h_2^2 h_3^2}\left[\left(\frac{\partial h_1 h_2}{\partial \theta'}\right)^2 - h_1 h_2\frac{\partial^2 h_1 h_2}{\partial \theta'^2}\right] -$$

$$\frac{1}{h_1^2 h_2 h_3^2}\frac{\partial h_1}{\partial\theta'}(h_2 h_3\frac{\partial u}{\partial s} + \frac{\partial h_1 h_3 v}{\partial r}) + \frac{1}{h_2 h_3}\frac{\partial}{\partial\theta'}(\frac{v}{h_1 h_3}\frac{\partial h_1 h_3}{\partial r}) +$$

$$\frac{1}{h_1^2 h_2 h_3^2}(h_3\frac{\partial h_1}{\partial\theta'} + h_1\frac{\partial h_3}{\partial\theta'})\frac{\partial h_1 h_3 v}{\partial r} - \frac{1}{h_1 h_2^2 h_3^2}\frac{\partial h_2}{\partial\theta'}\frac{\partial h_1 h_3 v}{\partial r} - \frac{1}{h_1^2 h_3}\frac{\partial h_1}{\partial\theta'}\frac{\partial u}{\partial s} -$$

$$\frac{u}{h_1 h_3}\frac{\partial}{\partial s}(\frac{1}{h_1}\frac{\partial h_1}{\partial\theta'}) - \frac{1}{h_1 h_2}\frac{\partial}{\partial r}(\frac{h_1}{h_3})\frac{\partial v}{\partial\theta'} - \frac{h_3 v}{h_2}\frac{\partial}{\partial r}(\frac{1}{h_2 h_3^2}\frac{\partial h_2}{\partial\theta'})$$

$$= \frac{1}{h_1 h_2 h_3}\frac{\partial}{\partial\theta'}(\frac{h_1 h_2}{h_3}\frac{\partial w}{\partial\theta'}) - \frac{w}{h_1^2 h_2^2 h_3^2}[(\frac{\partial h_1 h_2}{\partial\theta'})^2 - h_1 h_2\frac{\partial^2 h_1 h_2}{\partial\theta'^2}] - \frac{2}{h_1^2 h_3}\frac{\partial h_1}{\partial\theta'}\frac{\partial u}{\partial s} -$$

$$\frac{u}{h_1^2 h_3}(h_1\frac{\partial^2 h_1}{\partial s\partial\theta'} - \frac{\partial h_1}{\partial\theta'}\frac{\partial h_1}{\partial s}) - \frac{1}{h_2^2 h_3^2}(h_3\frac{\partial h_2}{\partial\theta'} - h_2\frac{\partial h_3}{\partial\theta'})\frac{\partial v}{\partial r} + \frac{h_1 + 2h_1 h_2 - h_2}{r h_1^2 h_3}\frac{\partial v}{\partial\theta'} +$$

$$\frac{1}{r h_2 h_3}[\frac{2}{h_2}\frac{\partial h_2}{\partial\theta'} + \frac{1}{h_1}(\frac{2h_1 - 1}{h_3}\frac{\partial h_3}{\partial\theta'} - \frac{2h_1 - 1}{h_2}\frac{\partial h_2}{\partial\theta'} + \frac{1}{h_1})\frac{\partial h_1}{\partial\theta'}]v$$

Hence, after eliminating the cross—related terms, we can reduce the θ' — momentum equation to:

$$\frac{\partial w}{\partial t} + \frac{u}{h_1}(\frac{\partial w}{\partial s} - \frac{u}{h_3}\frac{\partial h_1}{\partial\theta'}) + \frac{v}{h_2}(\frac{\partial w}{\partial r} + \frac{w}{r} - \frac{v}{h_3}\frac{\partial h_2}{\partial\theta'}) + \frac{w}{h_3}\frac{\partial w}{\partial\theta'}$$

$$= -\frac{1}{\rho h_3}\frac{\partial p}{\partial\theta'} + \nu\{\frac{1}{h_1}\frac{\partial}{\partial s}(\frac{1}{h_1}\frac{\partial w}{\partial s}) + \frac{1}{h_1 h_2 h_3}\frac{\partial}{\partial r}(\frac{h_1 h_3}{h_2}\frac{\partial w}{\partial r}) +$$

$$\frac{1}{h_1 h_2 h_3}\frac{\partial}{\partial\theta'}(\frac{h_1 h_2}{h_3}\frac{\partial w}{\partial\theta'}) - \frac{w}{h_1^2 h_2^2 h_3^2}[(\frac{\partial h_1 h_2}{\partial\theta'})^2 - h_1 h_2\frac{\partial^2 h_1 h_2}{\partial\theta'^2} +$$

$$\frac{h_1 h_3^2}{r^2}] - \frac{2}{h_1^2 h_3}\frac{\partial h_1}{\partial\theta'}\frac{\partial u}{\partial s} - \frac{1}{h_2^2 h_3^2}(h_3\frac{\partial h_2}{\partial\theta'} - h_2\frac{\partial h_3}{\partial\theta'})\frac{\partial v}{\partial r} - \frac{u}{h_1^2 h_3}(h_1\frac{\partial^2 h_1}{\partial s\partial\theta'} -$$

$$\frac{\partial h_1}{\partial\theta'}\frac{\partial h_1}{\partial s}) + \frac{h_1 + 2h_1 h_2 - h_2}{r h_1^2 h_3}\frac{\partial v}{\partial\theta'} + \frac{1}{r h_2 h_3}[\frac{2}{h_2}\frac{\partial h_2}{\partial\theta'} + \frac{1}{h_1}(\frac{2h_1 - 1}{h_3}\frac{\partial h_3}{\partial\theta'} -$$

$$\frac{2h_1 - 1}{h_2}\frac{\partial h_2}{\partial\theta'} + \frac{1}{h_1})\frac{\partial h_1}{\partial\theta'}]v\} \tag{A—84}$$

The θ'—momentum equation can be cast into the momentum conservational form as

$$\frac{\partial w}{\partial t} + \frac{1}{h_1}\frac{\partial}{\partial s}(uw - \frac{\nu}{h_1}\frac{\partial w}{\partial s}) + \frac{1}{h_1 h_2 h_3}\frac{\partial}{\partial r}h_1 h_3(vw - \frac{\nu}{h_2}\frac{\partial w}{\partial r}) +$$

$$\frac{1}{h_1 h_2 h_3}\frac{\partial}{\partial \theta'}h_1 h_2(ww - \frac{\nu}{h_3}\frac{\partial w}{\partial \theta'}) + \{\frac{v}{rh_2} + \frac{\nu}{h_1^2 h_2^2 h_3^2}[(\frac{\partial h_1 h_2}{\partial \theta'})^2 -$$

$$h_1 h_2\frac{\partial^2 h_1 h_2}{\partial \theta'^2} + \frac{h_1 h_3^2}{r^2}]\}w$$

$$= -\frac{1}{\rho h_3}\frac{\partial p}{\partial \theta'} + \frac{v^2}{h_2 h_3}\frac{\partial h_2}{\partial \theta'} + \frac{u^2}{h_1 h_3}\frac{\partial h_1}{\partial \theta'} - \nu\{\frac{2}{h_1^2 h_3}\frac{\partial h_1}{\partial \theta'}\frac{\partial u}{\partial s} +$$

$$\frac{1}{h_2^2 h_3^2}(h_3\frac{\partial h_2}{\partial \theta'} - h_2\frac{\partial h_3}{\partial \theta'})\frac{\partial v}{\partial r} + \frac{u}{h_1^2 h_3}(h_1\frac{\partial^2 h_1}{\partial s \partial \theta'} - \frac{\partial h_1}{\partial \theta'}\frac{\partial h_1}{\partial s}) - \frac{h_1 + 2h_1 h_2 - h_2}{rh_1^2 h_3}\frac{\partial v}{\partial \theta'} -$$

$$\frac{1}{rh_2 h_3}[\frac{2}{h_2}\frac{\partial h_2}{\partial \theta'} + \frac{1}{h_1}(\frac{2h_1 - 1}{h_3}\frac{\partial h_3}{\partial \theta'} - \frac{2h_1 - 1}{h_2}\frac{\partial h_2}{\partial \theta'} + \frac{1}{h_1})\frac{\partial h_1}{\partial \theta'}]v\}$$

(A–85)

The governing flow equations have been obtained for constant density and viscosity and can be summarized in the circular helical coordinate system as follows:

The continuity equation

$$\frac{1}{h_1}\cdot\frac{\partial u}{\partial s} + \frac{1}{h_1 h_2 h_3}\cdot\frac{\partial(h_1 h_3 v)}{\partial r} + \frac{1}{h_1 h_2 h_3}\cdot\frac{\partial(h_1 h_2 w)}{\partial \theta'} = 0$$

(A–86)

The s—momentum equation

$$\frac{\partial u}{\partial t} + \frac{1}{h_1}\cdot\frac{\partial}{\partial s}(uu - \frac{\nu}{h_1}\cdot\frac{\partial u}{\partial s}) + \frac{1}{h_1 h_2 h_3}\cdot\frac{\partial}{\partial r}h_1 h_3(vu - \frac{\nu}{h_2}\cdot\frac{\partial u}{\partial r}) +$$

$$\frac{1}{h_1 h_2 h_3}\cdot\frac{\partial}{\partial \theta'}h_1 h_2(wu - \frac{\nu}{h_3}\cdot\frac{\partial u}{\partial \theta'}) + \{\frac{h_r - 1}{rh_1 h_2}v + \frac{w}{h_1 h_3}\frac{\partial h_1}{\partial \theta'} - \frac{\nu}{h_1^2 h_2}[\frac{h_1 - 1}{r^2 h_2} +$$

$$\frac{h_1}{h_3^2}(\frac{1}{h_2}\frac{\partial h_2}{\partial \theta'} - \frac{1}{h_1}\frac{\partial h_1}{\partial \theta'} - \frac{1}{h_3}\frac{\partial h_3}{\partial \theta'})\frac{\partial h_1}{\partial \theta'} + \frac{h_1}{h_3^2}\frac{\partial^2 h_1}{\partial \theta'^2}]\}u$$

$$= -\frac{1}{\rho h_1}\frac{\partial p}{\partial s} + \frac{\nu}{h_1^2}[2\frac{h_1 - 1}{rh_2}\cdot\frac{\partial v}{\partial s} + \frac{2}{h_3}\cdot\frac{\partial h_1}{\partial \theta'}\cdot\frac{\partial w}{\partial s} - \frac{1}{rh_1 h_2}\frac{\partial h_1}{\partial s}v -$$

$$\frac{1}{h_3}(\frac{\partial^2 h_1}{\partial \theta' \partial s} - \frac{1}{h_1}\cdot\frac{\partial h_1}{\partial \theta'}\frac{\partial h_1}{\partial s})w]$$

(A–87)

The r—momentum equation

$$\frac{\partial v}{\partial t} + \frac{1}{h_1}\frac{\partial}{\partial s}\left(uv - \frac{\nu}{h_1}\frac{\partial v}{\partial s}\right) + \frac{1}{h_1 h_2 h_3}\frac{\partial}{\partial r}h_1 h_3\left(vv - \frac{\nu}{h_2}\frac{\partial v}{\partial r}\right) +$$

$$\frac{1}{h_1 h_2 h_3}\frac{\partial}{\partial \theta'}h_1 h_2\left(wv - \frac{\nu}{h_3}\frac{\partial v}{\partial \theta'}\right) + \left\{\nu\left[\frac{2h_1^2 - 2h_1 + 1}{r^2 h_1^2 h_2^2} - \frac{1}{h_2^2 h_3^2}\left(\frac{\partial^2 h_2}{\partial \theta'^2} + \frac{1}{h_1}\frac{\partial h_1}{\partial \theta'}\frac{\partial h_2}{\partial \theta'} - \right.\right.\right.$$
$$\left.\left.\left.\frac{1}{h_2}\frac{\partial h_2}{\partial \theta'}\frac{\partial h_2}{\partial \theta'} - \frac{1}{h_3}\frac{\partial h_3}{\partial \theta'}\frac{\partial h_2}{\partial \theta'}\right)\right] + \frac{w}{h_2 h_3}\frac{\partial h_2}{\partial \theta'}\right\}v$$

$$= \frac{h_1 - 1}{r h_1 h_2}u^2 + \frac{w^2}{r h_2} - \frac{1}{\rho h_2}\frac{\partial p}{\partial r} - \nu\left(2\frac{h_1 - 1}{r h_1^2 h_2}\frac{\partial u}{\partial s} + \frac{u}{r h_1^3 h_2}\frac{\partial h_1}{\partial s} - \frac{1}{h_2^2 h_3}\frac{\partial h_2}{\partial \theta'}\frac{\partial w}{\partial r} + \right.$$
$$\left.\frac{2}{r h_2 h_3}\frac{\partial w}{\partial \theta'} + \frac{2h_1 - 1}{r h_1^2 h_2 h_3}\frac{\partial h_1}{\partial \theta'}w\right) \tag{A—88}$$

The θ'—momentum equation

$$\frac{\partial w}{\partial t} + \frac{1}{h_1}\frac{\partial}{\partial s}\left(uw - \frac{\nu}{h_1}\frac{\partial w}{\partial s}\right) + \frac{1}{h_1 h_2 h_3}\frac{\partial}{\partial r}h_1 h_3\left(vw - \frac{\nu}{h_2}\frac{\partial w}{\partial r}\right) +$$

$$\frac{1}{h_1 h_2 h_3}\frac{\partial}{\partial \theta'}h_1 h_2\left(ww - \frac{\nu}{h_3}\frac{\partial w}{\partial \theta'}\right) + \left\{\frac{v}{r h_2} + \frac{\nu}{h_1^2 h_2^2 h_3^2}\left[h_1^2\left(\frac{\partial h_2}{\partial \theta'}\right)^2 + h_2^2\left(\frac{\partial h_1}{\partial \theta'}\right)^2 - \right.\right.$$

$$\left.\left. h_1^2 h_2\frac{\partial^2 h_2}{\partial \theta'^2} - h_1 h_2^2(1-h_1) + \frac{h_1 h_3^2}{r^2}\right]\right\}w$$

$$= -\frac{1}{\rho h_3}\frac{\partial p}{\partial \theta'} + \frac{v^2}{h_2 h_3}\frac{\partial h_2}{\partial \theta'} + \frac{u^2}{h_1 h_3}\frac{\partial h_1}{\partial \theta'} - \nu\left\{\frac{2}{h_1^2 h_3}\frac{\partial h_1}{\partial \theta'}\frac{\partial u}{\partial s} + \frac{1}{h_2^2 h_3^2}\left(h_3\frac{\partial h_2}{\partial \theta'} - \right.\right.$$

$$\left. h_2\frac{\partial h_3}{\partial \theta'}\right)\frac{\partial v}{\partial r} + \frac{u}{h_1^3 h_3}\left(h_1\frac{\partial^2 h_1}{\partial s \partial \theta'} - \frac{\partial h_1}{\partial \theta'}\frac{\partial h_1}{\partial s}\right) - \frac{h_1 + 2h_1 h_2 - h_2}{r h_1^2 h_3}\frac{\partial v}{\partial \theta'} -$$

$$\left.\frac{1}{r h_2 h_3}\left[\frac{2}{h_2}\frac{\partial h_2}{\partial \theta'} + \frac{1}{h_1}\left(\frac{2h_1 - 1}{h_3}\frac{\partial h_3}{\partial \theta'} - \frac{2h_1 - 1}{h_2}\frac{\partial h_2}{\partial \theta'} + \frac{1}{h_1}\right)\frac{\partial h_1}{\partial \theta'}\right]v\right\} \tag{A—89}$$

To simplify the numerical implementation, we must extract the coordinate change along the generic curve. To achieve this, we choose to rotate the coordinate back to the corresponding non—orthogonal coordinate system while leaving the velocities intact. By denoting the velocity field to be (u', v', w') for the non—orthogonal coordinate system (s, r, θ), we have the following mapping equations:

$$(s, \, r, \, \theta) \Longleftarrow (s, \, r, \, \theta')$$

$$\theta = \theta' - \tau s, \qquad\qquad w' = w$$

$$s = s, \qquad\qquad u' = u, \qquad P' = p$$

$$r = r, \qquad\qquad v' = v$$

We have the following relationships for $(s, \, r, \, \theta') \Longleftarrow (s, \, r, \, \theta)$:

$$\frac{\partial}{\partial s} = \frac{\partial}{\partial s} - \tau \frac{\partial}{\partial \theta}$$

$$\frac{\partial}{\partial r} = \frac{\partial}{\partial r}$$

$$\frac{\partial}{\partial \theta'} = \frac{\partial}{\partial \theta}$$

The advection—diffusion of any property in the s—direction is given by

$$\frac{1}{h_1} \frac{\partial}{\partial s}\left(u\phi - \frac{\nu}{h_1}\frac{\partial \phi}{\partial s}\right) = \frac{1}{h_1}\frac{\partial}{\partial s}\left[\left(u' - \frac{\tau\nu}{h_1^2}\frac{\partial h_1}{\partial \theta}\right)\phi - \frac{\nu}{h_1}\frac{\partial \phi}{\partial s}\right] -$$

$$\frac{\tau}{r h_1}\frac{\partial}{\partial \theta}\left(r u'\phi + \frac{\tau r \nu}{h_1}\frac{\partial \phi}{\partial \theta}\right) + 2\frac{\tau\nu}{h_1}\frac{\partial^2 \phi}{\partial s\, \partial \theta} \qquad\qquad (A{-}90)$$

From the non—rotating basis of the space variables, all the coefficients of the governing equations are now without any influence of the axial length down the pipe. Hence, we are able to find a solution which is independent of the axial curve length, i.e., the fully developed solution. However, with the orthogonal helical coordinates, the solution will be always axial curve length dependent as long as the peripheral change exists.

The following scales are used to render the governing equations dimensionless.

$$s = \frac{s'}{a}\,, \quad r = \frac{r'}{a}\,, \quad \theta = \theta'\,, \quad t = \frac{\nu t'}{a^2}\,, \quad u = \frac{u'}{2U}\,, \quad v = \frac{v'}{2U}\,, \quad w = \frac{w'}{2U}\,, \quad p = \frac{ReP'}{4\rho U^2}$$

and $\lambda = \kappa a$, $\eta = \tau a$, $Re = \dfrac{2aU}{\nu}$, $Pr = \dfrac{C_p \nu \rho}{k}$

Where a is the radius of the pipe, U is the average axial velocity and the primed variables denote the corresponding dimensional quantities.

The final governing flow equations are given by

The continuity:

$$\frac{1}{h_1}\left(\frac{\partial u}{\partial s} - \eta\frac{\partial u}{\partial\theta}\right) + \frac{1}{rh_1}\cdot\frac{\partial(rh_1 v)}{\partial r} + \frac{1}{rh_1}\cdot\frac{\partial(h_1 w)}{\partial\theta} = 0 \qquad (A-91)$$

The scalar quantity or the pseudo–secondary flow stream function, ψ, can be defined as:

$$\frac{\partial\psi}{\partial r} = h_1 w - \eta r u \qquad (A-92a)$$

and

$$\frac{\partial\psi}{\partial\theta} = -r h_1 v \qquad (A-92b)$$

Momentum/Energy equation:

$$[M(Re) + d_\phi] \phi = S_\phi \qquad (A-93)$$

$$M(Re)\phi = \frac{\partial\phi}{\partial t} + \frac{1}{h_1}\frac{\partial}{\partial s}[(Re\, u - \lambda\eta r\frac{\cos\theta}{h_1^2})\phi - \frac{1}{h_1}\frac{\partial\phi}{\partial s}] + \frac{1}{rh_1}\frac{\partial}{\partial r}[rh_1(Re\, v\,\phi - \frac{\partial\phi}{\partial r})] +$$

$$\frac{1}{rh_1}\frac{\partial}{\partial\theta}[Re(h_1 w - \eta r u)\phi - \frac{h_1}{r}(1 + \frac{\eta^2 r^2}{h_1^2})\frac{\partial\phi}{\partial\theta}] + \frac{2\eta}{h_1^2}\frac{\partial^2\phi}{\partial s\partial\theta}$$

$$(A-94)$$

s—momentum $M(Re) \phi = S_\phi$

$\phi = u$ (A—95a)

$$d_\phi = \frac{v\sin\theta + w\cos\theta}{h_1}\lambda Re + \frac{\lambda^2}{h_1^2} \qquad (A\text{—}95b)$$

$$S_\phi = -\frac{1}{h_1}(\frac{\partial p}{\partial s} - \eta\frac{\partial p}{\partial\theta}) + \frac{1}{h_1^2}[2\lambda\sin\theta(\frac{\partial v}{\partial s} - \eta\frac{\partial v}{\partial\theta}) + 2\lambda\cos\theta(\frac{\partial w}{\partial s} - \eta\frac{\partial w}{\partial\theta}) +$$

$$\frac{\lambda\eta\cos\theta}{h_1}v - \frac{\lambda r + \sin\theta}{h_1}\lambda\eta w] \qquad (A\text{—}95c)$$

r—momentum $M(Re) \phi = S_\phi$

$\phi = v$ (A—96a)

$$d_\phi = \frac{1 + 2h_1\lambda r\sin\theta}{r^2 h_1^2} \qquad (A\text{—}96b)$$

$$S_\phi = -\frac{\partial p}{\partial r} + Re(\frac{\lambda\sin\theta}{h_1}u^2 + \frac{w^2}{r}) - \frac{2\lambda\sin\theta}{h_1^2}(\frac{\partial u}{\partial s} - \eta\frac{\partial u}{\partial\theta}) + \frac{\lambda\eta\cos\theta}{h_1^3}u -$$

$$\frac{2}{r^2}\frac{\partial w}{\partial\theta} - \frac{2h_1-1}{rh_1^2}\lambda\cos\theta w \qquad (A\text{—}96c)$$

θ—momentum $M(Re) \phi = S_\phi$

$\phi = w$ (A—97a)

$$d_\phi = Re\frac{v}{r} + \frac{1}{h_1^2}(\lambda^2 + \frac{2h_1-1}{r}) \qquad (A\text{—}97b)$$

$$S_\phi = -\frac{\partial p}{\partial\theta} + Re\frac{\lambda\cos\theta}{h_1}u^2 - \frac{2\lambda\cos\theta}{h_1^2}(\frac{\partial u}{\partial s} - \eta\frac{\partial u}{\partial\theta}) - \frac{\lambda r + \sin\theta}{h_1^3}\lambda\eta u +$$

$$\frac{3h_1-1}{r^2 h_1^2}\frac{\partial v}{\partial\theta} + \frac{1}{rh_1^2}\lambda\cos\theta v \qquad (A\text{—}97c)$$

The energy equation with negligible viscous dissipation

$$M(Pr\ Re)\ T = 0 \qquad (A\text{—}98)$$